HYDRODYNAMIC CONTROLS ON MULTIPLE TIDAL INLET PERSISTENCE

By

Paulo Salles

B. Sc., National Autonomous University of Mexico, 1993

Submitted in partial fulfillment of the requirements for the degree of

Doctor of Philosophy

at the

MASSACHUSETTS INSTITUTE OF TECHNOLOGY

and the

WOODS HOLE OCEANOGRAPHIC INSTITUTION

February 2001

HYDRODYNAMIC CONTROLS ON MULTIPLE TIDAL INLET PERSISTENCE

By

Paulo Salles

Submitted to the Department of Civil and Environmental Engineering on October 6, 2000 in partial fulfillment of the requirements for the Degree of Doctor of Philosophy in Applied Ocean Sciences and Engineering

The importance of the persistence of multiple inlets in coastal systems is fundamental for issues such as water quality, navigability, and beach/barrier stability. In long embayments, having extended residence times, the stability of multiple inlets can be important for more efficient flushing and water exchange between the embayment and the ocean.

Many approaches have been used to analyze inlet stability, but have focused on single rather than multiple tidal inlet systems, relying solely on measured data to describe and predict the behavior of tidal inlets and/or suggesting empirical stability relationships between inlet morphology and inlet/bay hydrodynamics. At present, the only multiple tidal inlet stability model available combines a linear analytical model for the flow and an empirical relationship for equilibrium, suggesting that multiple inlet systems are unstable and ultimately all inlets will close or, at best, one will remain open.

Focusing on shallow multiple tidal inlet systems and in particular on Ría Formosa, a shallow coastal lagoon in the south of Portugal known to have maintained persistently multiple inlets in a historical time scale, the morphodynamic and hydrodynamic response to disturbances in the physical characteristics of the lagoon and inlets was studied through a) the analysis of historical data of the region, b) the analysis of tidal data (velocity and water surface elevation) collected in the study site, and c) through the numerical modeling of the system hydrodynamics under various inlet scenarios (using RMA-2V, a vertically averaged finite element model), with emphasis on the contribution of the hydrodynamic response (changes in tidal prism, residual discharge and current, sediment transport capacity, tidal distortion, and cross-sectional averaged maximum velocity) to maintain the multiple inlets open.

The model results show that multiple tidal inlet systems can exhibit stable inlet configurations, and that the strong hydrodynamic interaction between inlets, as well as the non-linear distortion of the tide, play a major role in multiple inlet persistence. Some of the results and findings are specific to Ría Formosa, and others can be generalized and used to identify processes contributing to stability in shallow systems with multiple inlets servicing a single embayment.

Thesis Supervisor: Dr. David Aubrey
Title: Adjunct Scientist, Woods Hole Oceanographic Institution

ACKNOWLEDGMENTS

Above all, I would like to express my gratitude towards my advisor, David Aubrey, for all his support and guidance throughout the duration of this study, and extending back to 1993, when I met him in Mexico and he suggested me to apply to the MIT/WHOI Joint Program. His insight and enthusiasm for coastal oceanography were always a motivation for me to pursue and accomplish this project. His friendship towards my family and me made my experience at WHOI very enjoyable.

I would also like to thank the other members of my thesis committee - Ole Madsen, Heidi Nepf, and John Trowbridge - for their valuable advice and encouragement. Many of the ideas expressed in this thesis resulted from meetings and conversations with them. A special thanks goes to Ole, who always showed faith in me and supported me in the difficult moments of my graduate studies. I also thank Mark Grosenbaugh, who acted as my defense chairman and showed interest on my project since I moved to Woods Hole. Thanks also go to the staff of the WHOI Education Office and the Department of Geology and Geophysics, all of whom were very supportive in all aspects of my graduate education, and always available to help me in my multinational and never ending paperwork.

I am also grateful to George Voulgaris, who initiated me in the numerical modeling life, who in part made possible our participation in the European field campaign in Portugal, and with which I had numerous conversations that were very valuable to this work. I shared very good moments with him throughout the last three years.

In what respects the fieldwork campaign in Portugal, I thank Steve O'Malley, Quin Robertson, Wayne Spencer, and Zoe Hughes, for the amazing teamwork during seven weeks to get everything done in Ría Formosa, and with which I had a very good experience and intense relationship. They also helped intensely preparing the fieldwork and processing part of the data. I am indebted to Oscar Ferreira, Alverinho Dias, and Adélio Silva, and all the people involved in the InDIA project, for helping during the fieldwork, providing data and spending time to answer all my questions regarding the Ría Formosa barrier island system. A special thanks goes to Carlos Felizardo, who very generously lent us his boat for six weeks to deploy and recover the instruments, and to perform all the surveys in the lagoon.

Finally, I would like to thank my wife, Irina, for her love, patience and encouragement, and my children, Paloma and Mateo, for their understanding and their big smiles every evening I would go back home after long working days. I have no words to express my gratitude to them. I also thank my parents, Vania and Severo, who always encouraged me to never give up what I set out to do.

My work as a graduate student was mainly funded by the National Autonomous University of Mexico through a fellowship from the Dirección General de Asuntos del Personal Académico, and partly by the WHOI Education Office. The fieldwork was undertaken as part of the MAST3 Project INDIA and is a result of research sponsored jointly by NOAA National Sea Grant College Program Office, Department of Commerce, under Grant No. NA86RG0075, Woods Hole Oceanographic Institution Sea Grant Project No. R/G-27, by the Commission of the European Communities, Directorate-General for Science, Research and Development under MAST Contract No. MAS3-CT97-0106, and by the Mellon Foundation through a grant to David Aubrey.

To Irina, my love

INDEX

LIST OF FIGURES

LIST OF TABLES

Chapter 1

Introduction

Significant portions of the coastlines worldwide are comprised of estuaries or lagoonal systems, which often serve as habitat for diverse species and are increasingly used for human settlement. Many of these systems are connected to the open ocean by one or more inlets, through which most of the water circulation occurs. The physical processes that drive and describe this circulation and the interaction between the flow and the sediment in the coastal ocean and the embayment are responsible for the shape and the evolution of such dynamic systems. The identification, quantification, and analysis of these processes are fundamental in understanding the hydrodynamic response to natural or anthropogenic disturbances. Inlets are a critical part in this picture, since the ability of these systems to maintain their communication(s) with the ocean is essential for their survival.

Focusing on shallow multiple tidal inlet systems and in particular on Ría Formosa, a shallow coastal lagoon in the south of Portugal, the hydrodynamic response to disturbances in the inlet configuration is studied and its contribution to maintaining the inlets open is analyzed. In the following section, tidal inlet systems are described, and their importance is discussed. In section 1.2 the motivation for this study is presented. The main questions and the approach used in this work are shown in section 1.3. In the last section, section 1.4, the outline and an overview of the following chapters is given.

1.1. Tidal Inlet Systems

In a general sense, inlets constitute the communication between coastal lagoons or estuarine systems and the open ocean. They can have a geological origin (e.g., mouths of semi-enclosed bays as San Francisco Bay, Zihuatanejo Bay in Mexico, and Guanabara Bay in Rio de Janeiro), a hydrological origin (e.g., river mouths and deltas), or a littoral drift and tidal/wave action origin (e.g., tidal inlets along sandy coasts).

Tidal inlets are located along barrier beaches (islands or spits), which occur primarily on coastal plain shorelines. Barrier/inlet systems, which represent 10 to 13 percent of the world's continental coastline (Schwartz, 1973), are associated with littoral drift coasts, in which longshore sediment transport is significant, and with coastal systems having small or non-existent freshwater flow, as opposed to inlets in river mouths or deltas, in which the fresh water flow plays a dominant, or at least significant, role in the inlet hydrodynamics. According to Bruun (1978), tidal inlets are usually divided into three main sections: a) the *ocean section*, which is composed of the entrance itself and may include outer shoals (flood tidal delta) and bars and one or more channels, and whose development is significantly influenced by wave action, b) the *gorge*, which is the section having the minimum cross-sectional area, and c) the *bay section*, composed of the inlet channel and the inner shoals (ebb tidal delta). In another study of inlet morphology, (Hayes, 1975) schematizes the main components of tide-dominated inlets as the main ebb channel which ends at a terminal lobe or ebb delta, channel-margin linear bars that flank the main ebb channel, swash bars that form individual bodies on the swash platform, and marginal flood channels (Figure 1-1).

According to Hayes (1979), tidal inlets occur primarily in mesotidal coasts (tidal range = 2 - 4 m), having medium wave energy (mean significant wave height = 60 - 150 cm). Although buoyancy and / or wind-driven motions may be of some importance, the flow through tidal inlets is mainly driven by the tidal oscillation, flooding and draining the back-barrier water body periodically with an intensity depending on the tidal regime and the physical characteristics of the local environment (inlet planform and geometry, lagoon dimensions and complexity, etc). The development and evolution of the planform and geometry of a tidal inlet are a result of the interaction between tidal currents, longshore currents, river flow (when present), and waves. Furthermore, geological features, the location of channels, and the general bay or lagoon geometry play a role (Bruun, 1978; Aubrey and Speer, 1984). Inlets around the world present a wide diversity of hy-

draulic conditions and morphology. For instance, among the approximately 300 majors inlets along the coast of the United States, widths vary from a few tens to more than 6,000 meters and average depths vary from a few meters to more than 16 meters (Vincent and Corson, 1980).

The existence of tidal inlets in coastal lagoons is important from a variety of reasons. Inlet-bay systems play an important role in the biological cycles of many organisms and in nutrient exchange with coastal waters. The flow through inlets provides the main mechanism for flushing of water from the back-barrier lagoon and renewal with coastal water rich in oxygen. Moreover, inlet flow is important when aquaculture activities are present, which often require salt water having stable physical characteristics. Ocean-lagoon water exchange is particularly important from a water quality point of view in instances where human settlement and industrial activities alter the natural contents of organic and inorganic matter in the water.

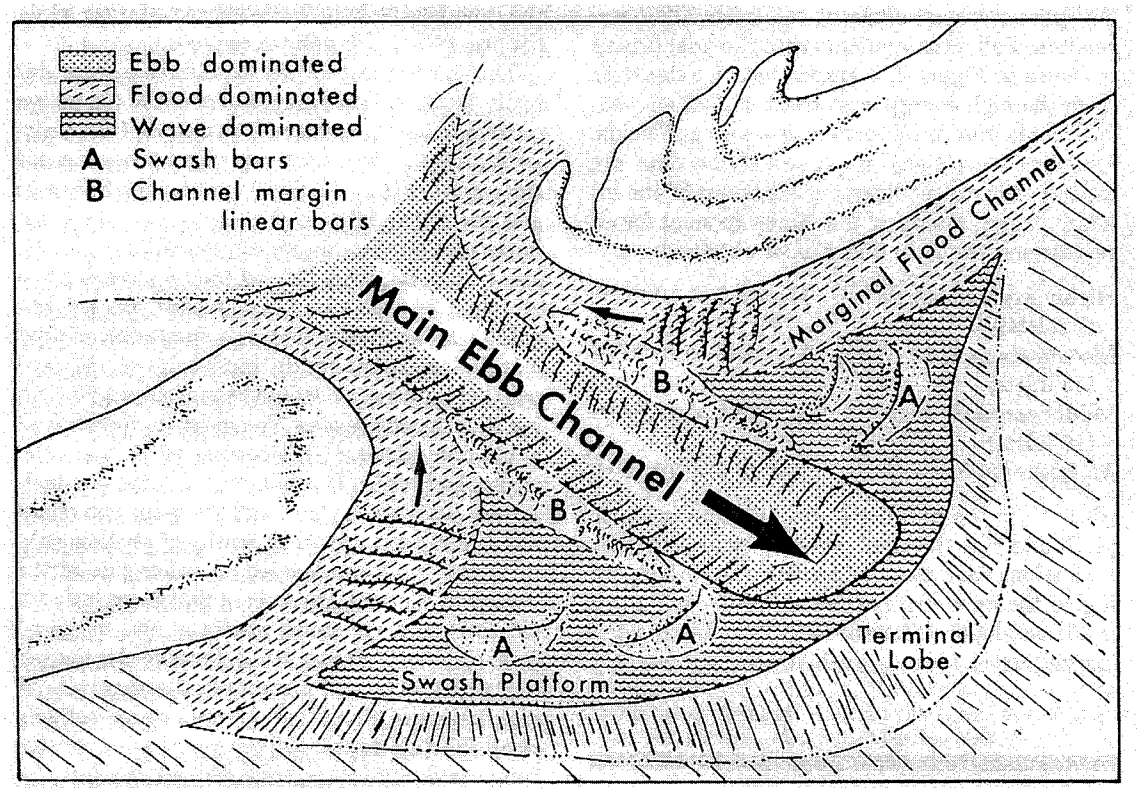

Figure 1-1. Schematic Diagram of the morphology of a tide-dominated inlet, from FitzGerald *et al.* (1976), after Hayes (1975).

In addition, tidal inlets can have strong effects on the barrier islands and beaches along which they are located. Inlet ebb-tidal deltas are large sand reservoirs and may be comparable in

volume to that of adjacent barriers (FitzGerald and Hayes, 1980). Changes in the hydrodynamics of the inlet and its vicinity are likely to modify the sediment transport patterns, which in turn can increase or decrease the sediment supply to the downdrift beaches, resulting in their buildup or erosion. Inlet migration and inlet sediment bypassing are also processes that can account for dramatic shoreline changes along barrier islands. For instance, Fenster and Dolan (1996), investigating barrier island-tidal inlet systems along the United States' mid-Atlantic coast, suggested that inlets impact adjacent shorelines in both the downdrift and the updrift sides of the inlet, and that the maximum extent of inlet influence in barrier beaches ranges from 5 to 13 km, depending on the tidal and wave regime.

Moreover, recreational and in particular fishing and industrial activities in coastal lagoons often require the maintenance of navigational channels to link marinas and ports inside the lagoon with the open ocean, and whose dimensions vary according to the type of vessel. A navigational channel may need a depth ranging from a couple of meters for small recreational boats to 20 meters or more when large cargo vessels having deep drafts plan to enter and exit the lagoon. These requirements are rarely satisfied naturally but often are only met with anthropogenic alterations of the inlet and some areas of the lagoon. These alterations are in most of the cases intrusive and create the need for regular and expensive maintenance operations.

That an inlet stays open, and in some instances in a fixed position and with a fixed geometry, can be of great interest and importance. The period over which inlets are desired to stay open corresponds to a historical time scale (several decades to even centuries), but this period is often reduced to a few decades or at least several years under natural conditions. The capacity of an inlet to stay open can be regarded from the point of view of inlet stability, from the point of view of equilibrium between the different forces and processes acting on the inlet or, in a more general sense, from the point of view of its persistence.

Inlet stability is divided into locational stability, a state in which the inlet remains in a fixed position and does not experience any significant migration through the time scale of interest, and geometrical stability, a state in which the inlet's dimensions and general shape remain relatively constant, experiencing only small deviations through time. Inlets can therefore be considered stable in terms of their location, or of their geometry, or both. However, given the unrestrained nature of tidal inlets in littoral drift coasts, the granular characteristics of their constitutive materials, and the power of the physical processes and hydrodynamics present in such envi-

ronments, stability in a strict locational and/or geometrical sense can practically never be met. Instead, the inlet geometry and/or location experience fluctuations around an average configuration, which constitute a response of the inlet to the changing and often unpredictable environment. This interaction between the inlet and its environment can get further complicated if we consider that the time scale of the inlet response may not be the same as the time scale and frequency of these disturbing events. Stability is then usually associated with a state of quasi-equilibrium, which is the group of conditions met by the littoral drift, the inlet currents, and the local wave regime in order to maintain the inlet open. Conceivably, an equilibrium condition could be reached with zero net accretion or erosion in the inlet, producing little or no change in morphology. This situation would correspond to the stability mentioned above. However, instead of developing this equilibrium condition, inlets more often will exhibit (1) small short-term variations associated with the spring-neap tidal cycle, (2) seasonal variations (associated with storm activity) of the order of 10% of the yearly mean flow area (Byrne *et al.*, 1974), and (3) a long-term gradual decrease in cross-sectional area, which trend is referred as the equilibrium flow area (van de Kreeke, 1985). Strong perturbations (extreme meteorological events, significant dredging in the inlet and adjacent channels, changes in lagoon dimensions) can affect dramatically the inlet hydrodynamics, leading to temporary or even permanent changes in the inlet configuration, as can be the inlet closure or the acquisition of a new equilibrium state.

In a more general sense, inlet persistence is defined here as the ability of the inlet to stay open for long periods, no matter what changes occur in the equilibrium configuration. Even if significant migration and/or irreversible changes in its geometry take place, an inlet can be in a dynamic state of equilibrium and can be said to persist if it is capable of sustaining uninterrupted flow between the ocean and the lagoon. This concept confers increased flexibility in the analysis of inlet morphological behavior, and is particularly useful and applicable when studying multiple tidal inlet systems.

Multiple tidal inlet systems are a special case of inlet/lagoon systems in which more than one inlet links a single back-barrier lagoon with the ocean. These systems are not as common as single-inlet systems but they are equally important in terms of the need to understand their physics. To mention some examples, multiple inlet systems can be found in the east coast of the United States (Cape Cod, Cape Hatteras), in Northern Europe (Wadden Sea), in Mexico (Laguna

Madre, Laguna de Chacahua), in the south coast of Brazil (Lagoa de Patos) and in the south of Portugal (Ría Formosa).

Multiple tidal inlet systems exist in different types of environment but occur primarily in locations characterized by both micro- and mesotidal coasts having medium wave energy (i.e., tidal range from 0 to 4 m and significant wave heights of 0.6 to 1.5 m) (Hayes, 1979), and back-barrier lagoons elongated parallel to the shoreline. Their origin can be linked to the genesis of the barrier island system, to the breaching and formation of companion inlets due to severe storms in single inlet systems, or can be the result of man-made artificial openings. More often though, multiple tidal inlet systems result from a combination of these processes (e.g., Matagorda Bay, Texas; Nauset, Waquoit Bay and Chatham Harbor, Massachusetts; Ría Formosa, Portugal).

The importance of the existence and persistence of multiple inlets in such systems is fundamental for issues such as water quality, navigability, and beach/barrier stability. In the case of long embayments, having extended residence times, the existence and stability of multiple inlets can be important for more efficient flushing and water exchange between the embayment and the ocean.

The stability of such systems depends in part on factors not found in single inlet systems. Morphological changes in a given inlet are likely to modify the hydrodynamic behavior in the inlet and its "area of influence" inside the lagoon, which in turn may affect the hydrodynamics in other inlets and other areas of the lagoon. A simplistic example would be to consider a reduction in the cross-sectional area of a given inlet, which may translate to a reduction of the tidal prism through that inlet. This would result, in a single-inlet system, in a decrease of the flooded area during rising tide and the capture of a smaller volume of water during ebb. In a multiple inlet system, this reduction in flooded area may be compensated by an increase of the tidal prism through adjacent inlets, with the consequent changes in their hydrodynamics.

Given this additional degree of freedom in the hydrodynamic and morphodynamic behavior of multiple inlet systems, the stability of the system should not be regarded in terms of the geometrical or locational stability of each inlet. Instead, the stability should refer to the persistence of the inlets and the capacity of the system, which is often in a dynamic state of equilibrium, to maintain multiple inlets. In fact, a system can show, on a historical time scale, fluctuations in the number of inlets. However, as long as this fluctuation does not result in a monotonic

decrease in the number of inlets, the system can be considered stable in terms of the existence of multiple inlets.

1.2. Motivation

When the inlets are far apart and especially when there is no efficient communication between them in the back-barrier side (e.g., when bathymetric features or shallow areas act as a natural barrier to the flow), the hydrodynamics in multiple tidal inlet systems can be treated as if they were formed by several sub-embayments, each one serviced by a single inlet. For instance, recent work in Nauset (Aubrey *et al.*, 1997) has suggested the possibility of dividing a dual-inlet/bay system into two single-inlet/bay systems, and analyzes each inlet separately. However, this is not the general rule. In cases when such dividing features do not exist or are not present between all the inlets, the flow entering the lagoon during the rising tide has fewer constraints and mixing between waters coming from different inlets is likely to occur, producing in the lagoon a more complex hydrodynamic comportment. As mentioned before, the hydrodynamic interaction between inlets is important since changes in the physical characteristics of one inlet will likely affect the characteristics of the flow in and out of the lagoon, which in turn can interfere in the stability of adjacent inlets. Moreover, the existence inside the embayment of large areas experiencing wetting and drying during the tidal cycle (tidal flats), is an important factor contributing to tidal distortion and flow dominance, which in turn are known to affect stability significantly (e.g., Speer and Aubrey, 1985; DiLorenzo, 1988; de Vriend and Ribberink, 1996; Friedrichs and Perry, in press). The identification and quantification of the hydrodynamic processes present in such systems are fundamental to a better understanding of how the persistence of multiple tidal inlets servicing a single embayment is possible.

Given the variety and complexity of tidal inlet systems and the processes acting in them, and given the many different hydrodynamic and morphodynamic aspects that can be addressed when studying tidal inlets and coastal embayments, many approaches have been used to analyze inlet stability. De Vriend (1996) proposed a classification of the models used to address these problems, distinguishing 1) *data based models*, which use measured data to describe phenomena, 2) *empirical relationships and empirical models*, based on statistical relationships between different state variables, derived from the analysis of field data, 3) *semi-empirical long-term models*, which describe the dynamic interaction between large elements of the system, using empirical

relationships to represent the effects of smaller-scale processes, 4) *process-based models*, which are mathematical models based on first physical principles, and 5) *formally integrated long-term or idealized models*, which are derived from process-based models by formal integration over time (and space), with possible empirical or parametric closure relations. In reality most of the studies conducted to present have been of the types (1), (2) and (3) and have focused on single rather than multiple tidal inlet systems, relying solely on measured data to describe and predict the behavior of tidal inlets and/or suggesting empirical stability relationships between inlet morphology and inlet/bay hydrodynamics.

At present, the only multiple tidal inlet stability model available (van de Kreeke, 1985, 1990) combines a linear analytical model for the flow and an empirical relationship for equilibrium, suggesting that multiple inlet systems are unstable and ultimately all inlets will close or, at best, one will remain open. However, recent research has shown that multiple tidal inlet systems are potentially stable. Research at Gasparilla Sound (Escoffier, 1977), Chatham (Friedrichs *et al.*, 1993; Liu and Aubrey, 1993), Waquoit Bay (Aubrey *et al.*, 1993), Nauset Inlet (Aubrey *et al.*, 1997), and Ría Formosa (Bettencourt, 1994; this study), has documented specific examples where multiple inlets are potentially long-lived and persistent on a historical time scale. Van de Kreeke's model assumes an inlet/lagoon geometry such that linearizing simplifications in the mathematical model can be made, and does not take into account the nonlinear processes usually present in shallow coastal systems. In fact, complex intertidal areas are common in shallow embayments, which can result in important variations in bay surface slopes and friction coefficients throughout the tidal cycle, and in the development of strong nonlinearities. A series of recent studies has shown that these shallow estuarine and lagoonal systems are strongly nonlinear. For instance, some studies have documented the nonlinear interaction of the offshore tidal constituents, showing how the offshore tide becomes strongly distorted as it propagates into shallow estuarine systems (e.g., Speer and Aubrey, 1985; DiLorenzo, 1988; Friedrichs and Aubrey, 1988; Friedrichs and Madsen, 1992). Some other studies have also shown strong nonlinearities, as the generation of phase and amplitude asymmetries in the velocity field due to tidal asymmetries (Boon and Byrne, 1981), and the combined influence of the tidal phase, amplitude, and mean sea-level differences on the generation of tidal residual currents in a multiple inlet system (Liu and Aubrey, 1993). Moreover, this linear type of model does not take into account the dynamic state of equilibrium often present in multiple tidal inlet systems, characterized by relatively high rates of inlet migration. This suggests that, if the interest resides in evaluating the degree of stability of

a realistic multiple inlet system, a linear approach, which only roughly models the true hydrodynamics of the system, may not always be valid.

1.3. Approach

There is evidence that multiple inlets can coexist in a shared single embayment. Inlets in these systems may present different states of stability and dynamic equilibrium, which result from a continuous response and adaptation to the changing environment. However, the mechanisms responsible for maintaining this overall stability have not been properly identified. In addition, the analysis of the evolution of tidal basins and entrances has usually emphasized the stability of an inlet in particular, and almost no attempt has been done to analyze the problem from the point of view of inlet persistence, keeping in mind the high variability in inlet morphology often present in these systems. The main hypothesis in this study is that multiple tidal inlet systems can be stable. More specifically, the hypotheses to be tested are:

- *Observed morphological responses to inlet and lagoon disturbances, and the evolution of the physical characteristics of the system can help explain the inlet persistence,*
- *The hydrodynamic interaction between inlets servicing a single embayment, and the capacity of the system to adjust to inlet disturbances by transferring large portions of the tidal prism from one inlet to another, and by modifying the residual flow and sediment transport patterns, contribute to maintain multiple inlets open,*
- *Hydrodynamic processes not found in single inlet systems play an important role in multiple tidal inlet stability,*
- *Nonlinear hydrodynamics are important to multiple inlet persistence in shallow systems. In other words, changes in nonlinear hydrodynamic processes due to inlet morphological disturbances play an important role in maintaining multiple inlets open.*

In order to test the first hypothesis, the Ría Formosa lagoon, a coastal system in the south of Portugal known to have maintained persistently multiple inlets for centuries, is used as a case study. Analysis of historical data and more recent material, as well as the review of previous studies of the area, serve to identify time scales of stability, patterns in the morphological evolution and the system's response to well-documented disturbances.

The other hypotheses are tested by analyzing field data collected in Ría Formosa, and results from numerical simulations of the hydrodynamics in that system with its present configura-

tion and with other different inlet scenarios. The field campaign was meant to provide hydrodynamic measurements (tidal fluctuations inside the lagoon and flow velocities through the inlets) from a system exhibiting multiple inlet persistence, and to provide detailed data for the calibration and validation of a hydrodynamic numerical model used to simulate responses of the system to disturbances.

The numerical simulations use a two-dimensional, vertically averaged finite-element model, and a computational mesh describing the Ría Formosa system. The approach to the analysis of multiple inlet stability is to create perturbations to the established inlet's cross-sectional areas and then to analyze the hydrodynamic response of the lagoon to these disturbances, in terms of changes in tidal distortion and residual circulation. On one hand, nonlinear tidal distortion plays an important role in controlling the hydrodynamics of tidal inlet systems. As the tide distorts entering shallow coastal systems, tidal asymmetries are produced, which in turn may generate stronger flows during rising tides (flood dominance) or falling tides (ebb dominance). The effects of the flow dominance in the sediment transport in shallow estuaries are important and have been well documented (e.g., Aubrey, 1986). Flood dominance (shorter and stronger floods) tends to enhance accretion in the channels and ebb dominance tends to flush bed-load sediment seaward more effectively. On the other hand, the residual currents, which are the net direction and amplitude of water movement after all the sinusoidal tidal currents have been removed (Zimmerman, 1978), and their changes due to applied disturbances can affect the net direction of sediment transport in the lagoon and the inlet vicinity, which can also contribute to inlet stability. Their contribution is in terms of modification in the flow dominance and the maximum velocity through the inlet, which in turn is a fundamental parameter in the stability criteria adopted.

The changes in tidal distortion and residual circulation, resulting from the system's response to disturbances, are in turn translated to stability arguments by relating them to changes in sediment transport capacity in the inlets with the assistance of widely used stability criteria. The disturbances applied are selected based on natural changes that have actually occurred and have been documented in the Ría Formosa system, and on disturbances applied in the artificially stabilized inlets.

This study is limited to the analysis of multiple tidal inlet persistence from a hydrodynamic point of view, and to the analysis of the hydrodynamic response to inlet morphological disturbances. Moreover, the focus is on the tidally driven motions. In fact, the capacity of an inlet

to stay open depends ultimately on the sediment transport pattern, and in turn sediment transport is locally dependent on many additional factors related to the flow (such as wave action, wave-induced currents, wind-induced circulation, river flow) and to the mechanics of near-bottom flow-sediment interaction, which are beyond the scope of this study.

1.4. Outline

A review of the research performed on inlet stability and on the inlet/bay hydrodynamics is presented on Chapter 2. In the first section, the main studies and the proposed models on single-inlet stability are summarized, which start with the pioneering work done by M. P. O'Brien in 1931 relating the tidal prism to the inlet area. The second section is dedicated to review the studies on multiple inlet stability, in particular the model proposed by van de Kreeke (1985; 1990). The last section presents some of the relevant work done in investigating the contribution for inlet stability of the nonlinear hydrodynamic processes present in shallow embayments.

The Ría Formosa system, which is a complex, shallow multiple tidal inlet system in the Algarve, Portugal, constitutes the study site for this thesis.

In Chapter 3 the Algarve system itself and the analysis of historical data are presented. Its general physical characteristics, as well as the proposed theories about its geologic genesis and evolution, are shown in section 3.1. The analysis of historical data and other more recent materials in order to investigate the morphological evolution of the system can be found in section 3.2. This section shows the data and materials used for this study, the methods adopted, and the results obtained.

Chapter 4 is dedicated to describe the fieldwork campaign undertaken in January-March 1999, the data reduction, and interpretation. A description of the instrumentation used can be found in section 4.2, whereas the field methods and procedures are presented in section 4.3. The process of reducing the data and its analysis, as well as the numerical tools applied to perform that task are shown in section 4.4. Finally, a preliminary interpretation of these data from a multiple inlet system, with an emphasis on testing previously proposed models of hydrodynamic behavior in shallow embayments, is done in section 4.5.

The hydrodynamic numerical modeling performed for this study is presented in Chapter 5. The finite element, two-dimensional, vertically averaged numerical model selected is described

in section 5.2. The setup of the model, which consists of generating the computational mesh based on topo-bathymetric data of the Ría Formosa lagoon, assigning values to the bottom roughness and eddy viscosity coefficients, and determining the boundary and initial conditions, is discussed in section 5.3. The calibration process and verification of the model output are presented in section 5.4. To optimize the reliability of the model output, the spin-up time of the model (time required for the model to provide a solution that repeats itself within some percentage for two consecutive identical tidal cycles) was determined. Then the calibration itself takes place, consisting of an iterative process in which the model inputs (physical attributes of the lagoon, friction, and eddy viscosity coefficients) are refined and adjusted to assure that the model output is consistent with the field observations. The verification follows the general approach used for the calibration. For each inlet's tidal prism and velocity verification, the model is forced with the tide corresponding to the time during which the flow velocity survey was performed in that inlet. The resulting velocity records through each inlet's cross section are then used to compute the modeled discharges and tidal prisms, which in turn are compared with the corresponding measured and processed data.

The numerical simulation setup, which consists of creating a series of modified computational meshes as input for the model, is presented in section 5.5. The results of the numerical simulations (flow velocity and water surface elevation), as well as their processing to extract the tidal distortion and residual circulation information, are presented in section 5.6. The discussion of the results and their ability to answer the questions posed in section 1.3 is done in section 5.7. Finally, the general conclusions of the thesis are shown in Chapter 6.

1.5. References

Aubrey, D. G., 1986. Hydrodynamic Controls on Sediment Transport in Well-Mixed Bays and Estuaries, in: J. van de Kreeke, Ed.: *Physics of Shallow Estuaries and Bays*. Coastal and Estuarine Studies, **16**. Springer-Verlag, New York, NY, pp 245-258.

Aubrey, D. G., McSherry, T. R. and Eliet, P. P., 1993. Effects of Multiple Inlet Morphology on Tidal Exchange. Waquoit Bay, Ma., in: D.G. Aubrey and G.S. Giese, Eds.: *Formation and Evolution of Multiple Tidal Inlets*. Coastal and Estuarine Studies, **44**. American Geophysical Union, Washington D.C., pp 213-235.

Aubrey, D. G. and Speer, P. E., 1984. Updrift Migration of Tidal Inlets. *Journal of Geology,* **92**: pp 531-545.

Aubrey, D. G., Voulgaris, G. and Spencer, W. D., 1997. *Tidal Residence Times within the Nauset Marsh System.* Report to the town of Orleans, WHOI-97-11. Department of Geology and Geophysics, Woods Hole Oceanographic Institution. Woods Hole, MA.

Bettencourt, P., 1994. *Les Environements Sédimentaires De La Côte Sotavento (Algarve, Sud Portugal) Et Leur Évolution Holocène Et Actuelle.* PhD thesis, Université de Bordeaux I.

Boon, J. D. I. and Byrne, R. J., 1981. On Basin Hypsommetry and the Morphodynamic Response of Coastal Inlet Systems. *Marine Geology,* **40**: pp 27-48.

Bruun, P., 1978. Stability of Tidal Inlets, Theory and Engineering. Development in Geotechnical Engineering, **23**. Elsevier.

Byrne, R. J., DeAlteris, J. T. and Bullock, P. A., 1974. Channel Stability in Tidal Inlets: A Case Study. Proc. of the 14th International Coastal Engineering Conference, Copenhagen, **2**: pp 1585-1604.

de Vriend, H. J., 1996. Mathematical Modeling of Meso-Tidal Barrier Island Coasts, Part I: Empirical and Semi-Empirical Models, in: P.L.-F. Liu, Ed.: Advances in Coastal and Ocean Engineering, **2**. World Scientific, pp 115-149.

de Vriend, H. J. and Ribberink, J. S., 1996. Mathematical Modeling of Meso-Tidal Barrier Island Coasts, Part 2: Process-Based Simulation Models, in: P.L.-F. Liu, Ed.: Advances in Coastal and Ocean Engineering, **2**. World Scientific, pp 151-197.

DiLorenzo, J. L., 1988. The Overtide and Filtering Response of Small Inlet/Bay Systems., in: D.G. Aubrey and L. Weishar, Eds.: *Hydrodynamics and Sediment Dynamics of Tidal Inlets.* Lecture Notes on Coastal and Estuarine Studies., **29**. Springer-Verlag, New York, pp 24-53.

Escoffier, F. F., 1977. *Hydraulics and Stability of Tidal Inlets*. General Investigation of Tidal Inlets (GITI) Report, 13. USACE.

Fenster, M. and Dolan, D., 1996. Assessing the Impact of Tidal Inlets on Adjacent Barrier Island Shorelines. *Journal of Coastal Research,* **12**(1): pp 294-310.

FitzGerald, D. M. and Hayes, M. O., 1980. Tidal Effects on Barrier Island Management. Proc. of the Coastal Zone '80, Hollywood, Florida, in: ASCE, Ed.: pp 2355-2379.

FitzGerald, D. M., Nummedal, D. and Kana, T. W., 1976. Sand Circulation Pattern at Price Inlet, South Carolina. Proc. of the 15th Coastal Engineering Conference, in: ASCE, Ed.: pp 1868-1880.

Friedrichs, C. T. and Aubrey, D. G., 1988. Nonlinear Tidal Distortion in Shallow Well-Mixed Estuaries: A Synthesis. *Estuarine, Coastal and Shelf Science,* **27**: pp 521-545.

Friedrichs, C. T., Aubrey, D. G., Giese, G. S. and Speer, P. E., 1993. Hydrodynamical Modeling of a Multiple Inlet Estuary/Barrier System: Insight into Tidal Inlet Formation and Stability., in: D.G. Aubrey and G.S. Giese, Eds.: *Formation and Evolution of Multiple Tidal Inlets*. Coastal and Estuarine Studies, **44**. American Geophysical Union, Washington D.C., pp 95-112.

Friedrichs, C. T. and Madsen, O. S., 1992. Nonlinear Diffusion of the Tidal Signal in Frictionally Dominated Embayments. *Journal of Geophysical Research,* **97**(5637-5650).

Friedrichs, C. T. and Perry, J. E., in press. Tidal Salt Marsh Morphodynamics. *Journal of Coastal Research*.

Hayes, M. O., 1975. Morphology of Sand Accumulations in Estuaries, in: L.E. Cronin, Ed.: *Estuarine Research*, **2**. Academic Press.,, pp 3-22.

Hayes, M. O., 1979. Barrier Island Morphology as a Function of Tidal and Wave Regime., in: S.P. Leathermam, Ed.: *Barrier Islands, from the Gulf of St. Laurence to the Gulf of Mexico*, Academic Press., New York, NY, pp 1-28.

Liu, J. T. and Aubrey, D. G., 1993. Tidal Residual Currents and Sediment Transport through Multiple Tidal Inlets, in: D.G. Aubrey and G.S. Giese, Eds.: *Formation and Evolution of Multiple Tidal Inlets*. Coastal and Estuarine Studies, **44**. American Geophysical Union, Washington D.C.,

Schwartz, M. L., 1973. Barrier Islands. Dowden, Hutchinson & Ross.

Speer, P. E. and Aubrey, D. G., 1985. A Study of Non-Linear Tidal Propagation in Shallow Inlet/Estuarine Systems. Part 2: Theory. *Estuarine, Coastal and Shelf Science,* **21**: pp 207-224.

van de Kreeke, J., 1985. Stability of Tidal Inlets - Pass Cavallo, Texas. *Estuarine, Coastal and Shelf Science,* **21**: pp 33-43.

van de Kreeke, J., 1990. Can Multiple Tidal Inlets Be Stable? *Estuarine, Coastal and Shelf Science,* **30**: pp 261-273.

Vincent, C. L. and Corson, W. D., 1980. *The Geometry of Selected U.S. Tidal Inlets*. General Investigation of Tidal Inlets (GITI) Report, 20. USACE.

Zimmerman, J. T. F., 1978. Topographic Generation of Residual Circulation by Oscillatory (Tidal) Currents. *Geophysical and Astrophysical Fluid Dynamics,* **11**: pp 35-47.

Chapter 2

Previous Studies

Understanding inlet stability and predicting the adjustment of the inlet morphology due to fluctuations in the hydraulic environment require detailed knowledge of the hydrodynamic and sedimentary processes in the vicinity of the inlet, which are governed by complex interactions between tidal currents, waves, and sediment. In spite of steady advances in describing these processes, research has focused on a more pragmatic approach referred to as "stability analysis," limiting the scope of the analysis to the inlet channel and in particular to its cross-sectional area (van de Kreeke, 1990). An inlet is said to be in equilibrium when the net rate of deposition of sediment in the inlet channel is zero. In other words, stability implies that the cross-sectional area continually adapts to the hydraulic environment and fluctuates only around a mean value, called the equilibrium cross-sectional area (Gao and Collins, 1994a).

Given the nature of the problem addressed in this study, the literature review has been divided in single tidal inlet stability studies (section 2.1), multiple tidal inlet stability studies (section 2.2), and studies related with nonlinear processes in shallow embayments (section 2.3).

2.1. Single Tidal Inlet Stability

Numerous studies on stability of single tidal inlets have been conducted from the late 1920's to present and most have recognized that there appears to be some organized structure in the morphology that suggests a relationship with the hydrodynamics, as is the case in the widely used semi-empirical stability principle proposed by Escoffier (1940). Other studies, based on field data and founded on empirical relationships between different inlet/bay parameters, have sug-

gested equilibrium formulas determined from regression analysis of data describing the existing inlet conditions, which are assumed to represent the equilibrium conditions. The best known of these are (a) the relationship between the inlet cross-sectional area, A_E, and the tidal prism, Ω (O'Brien, 1931, 1966), and (b) the relationship between the total littoral drift in the inlet vicinity, M_{tot}, and the tidal prism (Bruun, 1968). These stability models and formulas, as well as related methods and other independent studies, are discussed in sections 2.1.1 to 2.1.3. More recently, the progress in the computational capabilities, as well as the development of powerful software systems for the numerical modeling of mathematical formulations describing various physical processes, have allowed the use of process-based mathematical simulation models for tidal inlet research. These models are presented in section 2.1.4.

2.1.1. Tidal Prism – Cross-Sectional Area Relationship

O'Brien (1931) formalized a relation between the general dimensions of the entrance to a tidal estuary or bay along a sandy coast and the volume of the tidal prism expressed as

$$A_E = \alpha \Omega^n \tag{2.1}$$

where Ω is the volume of the tidal prism for the embayment in cubic feet between mean lower low water and mean higher high water (spring tide), A_E is the area of the entrance section below mid-tide in square feet, and α and n are constants determined from regression analysis. Using data from 14 inlet/bay systems in the Pacific Coast and one in the Atlantic Coast, O'Brien found (after rearranging) that $A_E = 4.69 \cdot 10^{-4} \Omega^{0.85}$.

The explanation he gave to the existence of this relationship was that "the pressure of the littoral sand motion tends to reduce the entrance area until the tidal currents are sufficiently strong to remove material from the ends of the encircling sand spits." He used this relation to show the susceptibility of the inlet to changes in the lagoon morphology. For instance, the reduction of the tidal prism by artificial means is likely to cause a general shoaling and deterioration of the inlet.

In 1966, O'Brien revisited the relationship using additional data that had become available since the initial study. Assuming that the data pertained to inlets that were believed to have reached a state of equilibrium at the time of the survey, he found that the original relationship agreed closely with the new data for inlets having two jetties. However, inlets without jetties ap-

peared to be better represented with the linear relationship $A_E = 2 \cdot 10^{-5} \Omega$. The author concluded that the equilibrium cross-sectional area of an inlet, with or without jetties, is controlled by the tidal prism. Furthermore, O'Brien found that neither the bed material size nor the tractive force appear to provide meaningful criteria for the equilibrium condition of tidal inlets.

Nayak (1971) performed investigations of this relationship in a model inlet. Two series of experiments were conducted: no jetties with and without waves, and twin jetties with and without waves. From the results of his experiments and available prototype data (mainly O'Brien data) the author concluded that the Ω-A_E relationship could be approximated by $A_E = 4.17 \cdot 10^{-4} \Omega^{0.85}$ for jettied inlets and by $A_E = 1.89 \cdot 10^{-5} \Omega$ for unjettied inlets. Nayak observed that (1) the areas developed for unjettied inlets with no waves were similar to the areas found in the jettied experiments, and (2) the experiments with unjettied inlets and long-period waves produced smaller areas than the experiments with short-period waves.

Jarret (1976) reanalyzed the Ω-A_E relationship using data from 108 inlets in the Pacific, Atlantic and Gulf of Mexico coasts. The data were grouped into three main categories (all inlets, unjettied and single-jettied inlets, and inlets with two jetties). Within these categories, he performed regression analysis for the inlets of the three coasts together and for the inlets of each coast separately. The results yielded in all cases an equation of the form $A_E = \alpha \Omega^n$, where α and n vary depending on inlet location and whether or not the inlet has been stabilized with two jetties. The values of α and n are shown in Table 2-1.

The most important conclusions Jarret presented are:

- Unjettied or single-jettied inlets on the Atlantic coast have larger cross-sectional areas than do their counterparts on the Pacific coast. Jarrett suggested that this may be due to differences in the tidal forcing and the wave climate. In addition, he found that the Pacific Coast inlets seem to have a smaller ratio of width over hydraulic radius (W/R), suggesting that these inlets may be hydraulically more efficient than wide and shallow channels. He suggested that the small values of W/R for the Pacific coast inlets are probably related to the higher rates of littoral drift entering the inlets.

- The Gulf coast data exhibit more scatter and the regression curves obtained are less reliable. He suggested that this scatter may be attributable to (1) the fact that the tides are uniformly small and vary from diurnal to semidiurnal, depending upon the declination of the

moon, and (2) the fact that the waves in the Gulf are relatively small, in terms of both height and period, compared with the other two coasts.

Table 2-1 Values of *C* and *n* for the O'Brien (1931; O'Brien, 1966) equilibrium formula (Jarret, 1976).

Inlets	*C*	*n*
Atlantic, Gulf and Pacific Coasts		
All	5.74×10^{-5}	0.95
One or no jetty	1.04×10^{-5}	1.03
Two jetties	3.76×10^{-4}	0.86
Atlantic Coast		
All	7.75×10^{-6}	1.05
One or no jetty	5.37×10^{-6}	1.07
Two jetties	5.77×10^{-5}	0.95
Gulf Coast		
All	5.02×10^{-4}	0.84
One or no jetty	3.51×10^{-4}	0.86
Two jetties*	-----	-----
Pacific Coast		
All	1.19×10^{-4}	0.91
One or no jetty	1.91×10^{-6}	1.10
Two jetties	5.28×10^{-4}	0.85

*: insufficient data for regression analysis.

More recently, many authors have verified and applied this relationship. For instance, Hume (1991) used data from 11 estuarine waterways in New Zealand. He found that $A_E = 6.54 \cdot 10^{-5} \Omega^{1.027}$, with a high coefficient of determination (r^2=0.95). He concluded that Ω-A_E relationships analogous to those derived for open coast sandy inlets hold for waterways in the interior of harbors in the Auckland area, where sediments are fine grained and where there is no wave action. In another study, Hume and Herdendorf (1992) studied 16 inlets in Auckland and suggested that the inlets are geometrically stable in part because of the strong Ω-A_E relationship they found (r^2=0.97), indicating that there is a balance between inlet geometry and tidal flow through the gorge. In yet another study, Hume and Herdendorf (1993) used data from New Zealand and overseas studies to support the hypothesis the Ω-A_E relationship hold for a wide variety of estuary types ranging from lagoons to river mouths to large coastal embayments. Finally, van de Kreeke (1996) suggested a possible path of evolution of the Frisian Inlet (Wadden Sea) using the Ω-A_E relationship. He found the constants α and n from Equation (2.1) with regression analysis of data from five inlets in the Wadden Sea, which were assumed to have similar hydrody-

namic and morphodynamic characteristics and to be subject to the same littoral drift, and he used this expression to estimate the possible magnitude of the cross-sectional area after an anthropogenic reduction of the tidal prism.

Although such Ω-A_E relationship showed good correlation in a *log-log* plot, scatter in the data is significant. The application of the method depends upon data from a number of inlet systems. Therefore, this relationship applied to a single inlet can only give a rough estimate of the equilibrium conditions, due to the statistical nature of the method.

Moreover, in spite of the popularity of the Ω-A_E relationship as a criterion to estimate inlet equilibrium cross-sectional areas due to its simplicity, the values of the constants α and n vary widely (from the data above: $7.75\ 10^{-6} < \alpha < 5.02\ 10^{-4}$; $084 < n < 1.05$) over the different regions studied (see also Gao and Collins, 1994a), which implies that the relationship is not universal and that local conditions may play an important role in equilibrium. Given that, this relationship has limited use in the sense that there appears to be no account for the various local processes known to contribute in inlet stability, such as tidal current intensities and degree of distortion (i.e., flow dominance), longshore currents, wave action, littoral drift and sediment grain size. For instance, Friedrichs (1995) performed a literature survey and found estimates of the cross-sectional area and the peak spring discharge at 242 sections in 26 separate sheltered tidal systems. Assuming the discharge to be sinusoidal (i.e., $Q = \Omega\pi/T$), the relations Ω-A_E and Q-A_E become interchangeable, and the author found that the cross-sectional area of most sheltered tidal channels is larger than that predicted by Jarrett (1976), especially values of A for channels having small Q. This suggests that the presence of waves (and littoral drift) in non-sheltered coastal inlets has the effect of decreasing the equilibrium cross-sectional area.

In addition, the proportionality constants α and n were in all cases obtained assuming that the inlets were in equilibrium. However, since the inlet geometric characteristics often fluctuate around a mean value with seasonal or even shorter time scales (see, e.g., van de Kreeke, 1985), there is some doubt as to when exactly the survey was done and whether or not the regression line actually represents equilibrium.

Finally, given that the Ω-A_E relationship was proposed and calibrated in single inlet systems, it does not make the distinction between flood and ebb tidal prisms. However, multiple inlet systems may exhibit significant differences between inflow and outflow volumes due to the po-

tential existence of large residual flow between inlets, in which case the use of the flood or ebb tidal prisms may lead to different equilibrium interpretations.

Therefore, the equilibrium relationship proposed by O'Brien should be used as a preliminary guidance for evaluation of the equilibrium. A more quantitative physical understanding of inlet stability must necessarily take into account the external conditions that act as "disturbing forces" to close the inlet and the restoring forces to keep the inlet from closing.

2.1.2. Closure Curve and Related Criteria

The stability concept known as *closure curve* was first introduced by Escoffier (1940). He proposed a diagram in which the maximum cross-sectional averaged velocity through the inlet, V_{max}, is plotted as a function of the inlet minimum cross-sectional area below mean sea level, A_c, which varies over a wide range of values as shown in Figure 2-1.

When the cross-sectional area A_c approaches zero, the maximum velocity through the inlet, V_{max}, also approaches zero, as a result of the bottom friction in the inlet being inversely proportional to A_c (van de Kreeke, 1992). Inversely, if A_c is small, V_{max} increases as A_c increases because the growth of the tidal prism will be predominant (de Vriend, 1996). For large values of the cross-sectional area, the maximum velocity decreases as the area increases. This is due to the fact that the tidal prism reaches a maximum value, becoming independent of A_c, and therefore the same amount of flow through a wider channel leads to smaller velocities.

In practice, the computation of the closure curve has been done analytically using Brown's (1928) or Keulegan's (1951) methods, in which the following assumptions are made:

- The water surface in the bay remains horizontal throughout the tidal cycle,
- The walls of the bay are vertical so that the water surface area remains constant,
- The tributary and surface runoff inflow to the bay is zero,
- No density currents are present,
- The tide in the sea is given by a simple sinusoidal curve,
- The depth variation in the inlet during the tidal cycle is small so that the cross-sectional area and hydraulic radius can be assumed to remain constant, and
- The head due to acceleration in the inlet is negligible.

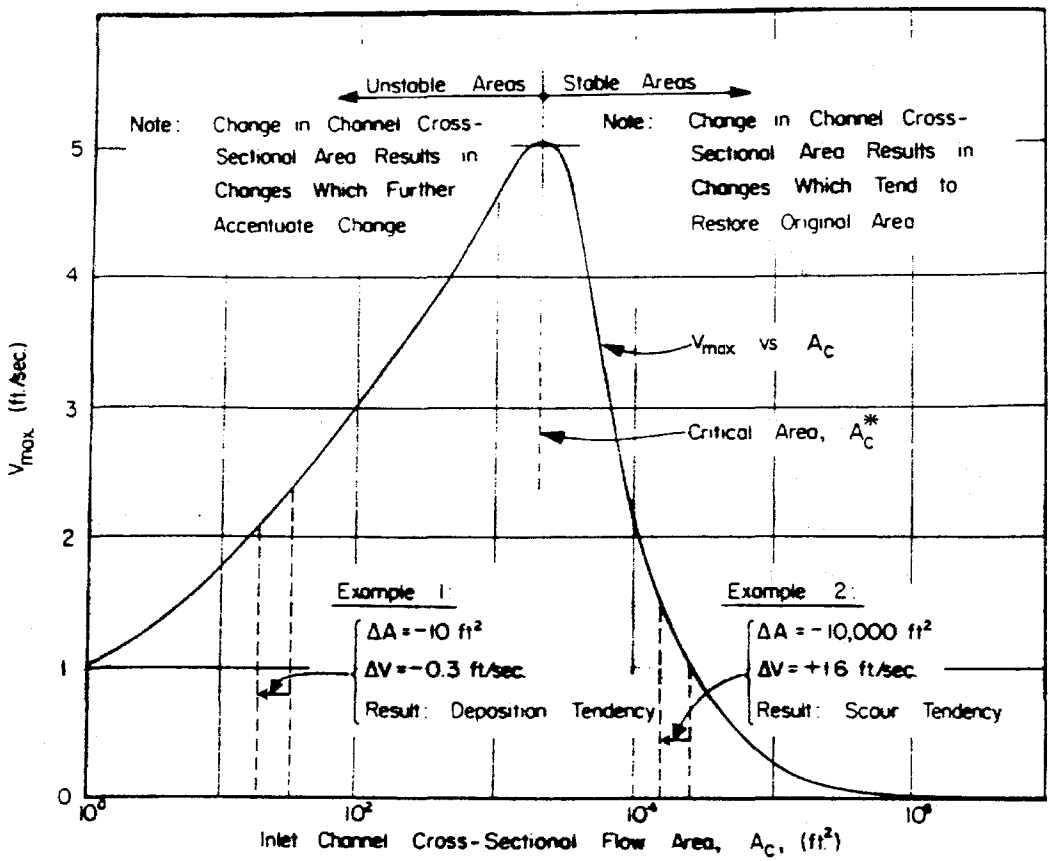

Figure 2-1. Escoffier stability concept (1940)

In addition to the references by Brown and Keulegan, a summary and comparison of the two methods can be found in Escoffier (1977). The method developed by Keulegan (1951) is more accurate than the Brown method in the sense that Brown assumes that both the sea and the bay water surface levels follow a simple sinusoidal curve, whereas Keulegan makes that assumption only for the sea level. The resulting expression for the maximum velocity through the inlet is, for both methods

$$V_{\max} = C\frac{2\pi A_b a_b}{A_c T}, \tag{2.2}$$

where $C = 1$ for the Brown method and is a function of the so-called repletion coefficient K in Keulegan's method, A_b is the bay surface area (m^2), a_b is the tidal amplitude inside the bay (m), which is given by

$$a_b = a_0 \frac{K^2}{\sqrt{2}} \sqrt{\sqrt{1+\frac{4}{K^4}} - 1}, \text{ for Brown and } a_b = a_0 \sin\tau, \text{ for Keulegan.}$$

where a_0 is the sea tidal amplitude (m), τ is also a function of K and is the complement of the phase between the sea and the bay tide, A_c is the inlet gorge cross-sectional area below mean sea level (m^2), and T is the tidal period (s). The repletion coefficient K, is in turn defined by

$$K = \frac{T}{2\pi a_0} \frac{A_c}{A_b} \sqrt{\frac{2gRa_0}{mR+FL}}, \tag{2.3}$$

where m is the sum of the exit and entrance losses, R is the hydraulic radius (m), L is the inlet length (m), and F is a friction coefficient defined in terms of Manning's n as $F = 2gn^2/R^{1/3}$.

The parameters C and $\sin\tau$ are monotonically increasing functions of K as shown in Keulegan (1951), with the range $0.8 < C < 1.0$ for $0.1 < K < 4$, and $0 < \sin\tau < 1.0$ for $0 < K < 4$. Equation (2.2) has been widely used to estimate the maximum velocity through the inlet for different values of the cross-sectional area, given the specification of the parameters mentioned above.

The closure curve of the inlet presents a peak of velocity for a corresponding critical area A_c^*. According to Escoffier (1940), the inlet was said to be stable (i.e., has the ability to return to its initial configuration after a disturbance) if the actual cross-sectional area of the inlet was greater than the critical area, $A > Ac^*$, and unstable if $A < Ac^*$, (see examples 1 and 2 in Figure 2-1). This approach gave an interval of areas for which the inlet would not close but did not specify what would be the actual equilibrium cross-sectional area of the inlet. Recognizing the difference between stability and equilibrium, the author later suggested that equilibrium required a particular value of the maximum velocity, the so-called equilibrium velocity (or V_{cr} by Escoffier). The equilibrium velocity is the velocity for which the sediment transport capacity of the inlet is just sufficient to remove the sediment deposited in the inlet, and depends on the amount of sediment carried into the inlet, the sediment characteristics, the wave climate, and the tidal range and period. In fact, given that the closure curve is by itself independent of the littoral drift in the inlet

region, the equilibrium velocity represents the parameter in which all the forces in play in inlet morphodynamics are collapsed.

The equilibrium velocity, shown in Figure 2-2, was plotted in the closure curve diagram as a straight line corresponding to a constant velocity. That $V_{max}=V_{eq}$ line intersects the closure curve in two points with corresponding cross-sectional areas A_U and A_S, which are the equilibrium flow areas, or, according to Escoffier (1940), are the areas for which the inlet is "stationary in size".

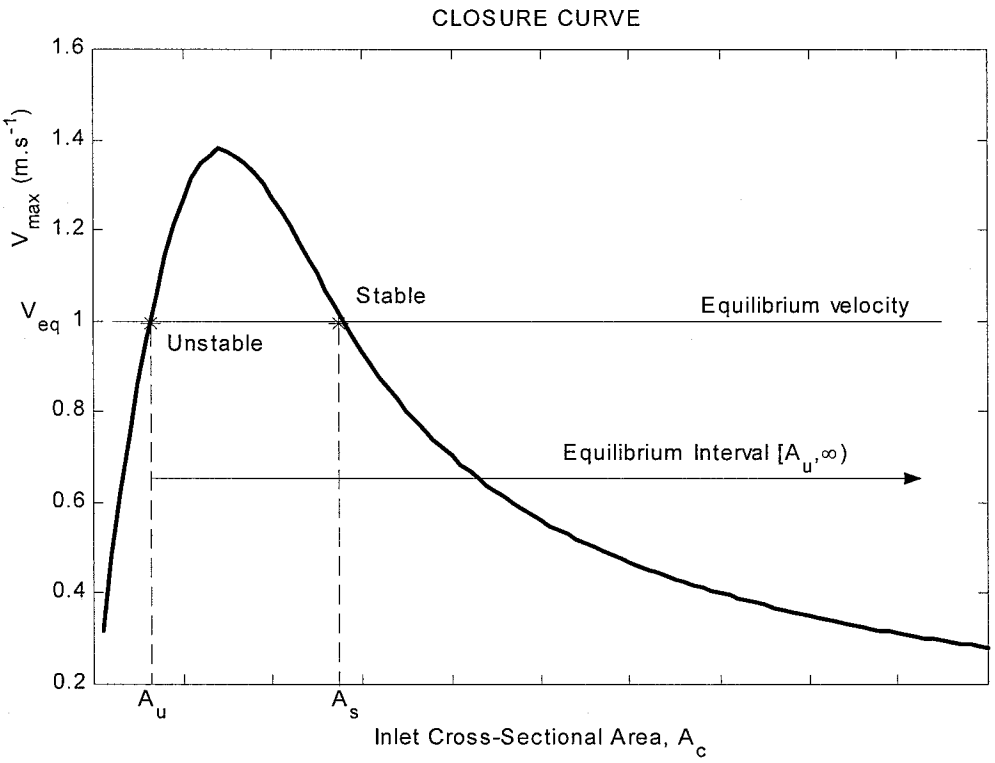

Figure 2-2. Equilibrium velocity, equilibrium interval, and cross-sectional areas exhibiting stable (A_S) and unstable (A_U) equilibrium conditions.

When the inlet cross-sectional area is larger than A_S, its velocity is smaller than V_{eq}. Consequently, the sediment transport capacity is below what is needed to maintain a zero net rate of deposition/erosion in the inlet. The inlet cross-sectional area will then decrease until it reaches the value of A_S. In a similar way, it can be seen that if $A_U < A < A_S$, then $V > V_{eq}$, which means that the sediment transport capacity is larger than that required to remove the sediment carried into the inlet. In that case, the cross-sectional area will increase until it reaches A_S. Following the same idea, when the area is smaller than A_U, the flow through the inlet is not at any time enough to re-

move the sediment deposited, and therefore the cross-sectional area will decrease and ultimately the inlet will close. In that sense, when the inlet cross-sectional area is A_U, the inlet is said to be in a state of unstable equilibrium, whereas when having a cross-sectional area equal to A_S, the inlet is in a state of stable equilibrium.

Given the above, an inlet is said to be *stable* when its cross-sectional area is located in the *equilibrium interval*, which is the range of areas extending from the smaller equilibrium flow area, A_U, to infinity (van de Kreeke, 1992).

For closure of the problem, and to make the closure curve useful in practice, the equilibrium velocity has to be estimated. Many authors, based on field data from inlets assumed to be in equilibrium, have suggested similar values. Escoffier (1940) argued that the equilibrium velocity " varies somewhat, being largely determined by the grain size of the sand occurring in the channel", and suggested that "a value of about 3 feet per second ($\cong$1 m.s^{-1}) can be considered as a fair approximation in most cases." Bruun (1968) observed that V_{max} at spring tide conditions to be close to 1 m.s^{-1} ($\pm$ 15%) in seventeen inlets (8 in the U.S., 6 in the Netherlands and 1 in Denmark) forced by different types of tides (diurnal, semi-diurnal and mixed) and with hydraulic radius ranging from 2.5 to 15 m. For the inlets in the Netherlands, the maximum velocity was found to be 1 m.s^{-1} in the ebb channels and 0.85 m.s^{-1} in the flood channels. This value of the maximum velocity in inlets assumed to be in equilibrium has been confirmed by other researchers and field surveys (Bruun, 1978, Tables 5.4.2.2 and 5.4.2.3). Jarrett (1976) used the annual average maximum velocities from NOS tidal current tables to determine the Ω-A_E relationships shown in Table 2-1, and he found the average for all the inlets to be 0.98 m.s^{-1} during ebb. Van de Kreeke and Haring (1980) investigated the stability of the Rotterdam waterway and reported that the maximum velocity at the estuary mouth was 0.85 m.s^{-1} for average tide conditions and 1 m.s^{-1} for spring tide conditions.

Alternatively, some authors (see, e.g., van de Kreeke, 1985; Friedrichs, 1995) have used the bottom shear stress instead of the velocity as a measure of equilibrium. According to Bruun and Gerritsen (1960), the "determining shear stress for inlet stability", τ_s, varies between 3.5 and 5.5 $N.m^{-2}$, the lower and upper limits pertaining to inlets having light and heavy littoral drift, respectively. However, the uncertainty in the estimation of the shear stress is greater than that of the velocity since the computation of the shear stress includes, in all cases, the estimation of a friction coefficient, which, in turn, has some degree of uncertainty.

The narrow range of the cross-sectional averaged maximum velocity through the inlet (or the corresponding shear stress) is remarkable. An attempt to explain this by Bruun (1968) suggested that a shear stress corresponding to velocities of about 1 $m.s^{-1}$ is common because this velocity is just sufficient to flatten dunes and produce a smoother bed, over which the frictional loss is minimized and the fraction of shear stress transferred directly into sediment transport capacity is maximized. In addition, Bruun (1978) suggested that the sediment transport through the inlet happens mainly in the form of bedload and that the flushing capacity is independent of the depth and therefore the same velocity is needed for equilibrium, regardless of the inlet depth. However, the existence of bedforms in inlet mouths is common, and complex combinations of bedforms (ripples, megaripples, dunes...) often occur, as a result of the interaction between waves and a reversing current. This simple observation suggests that velocity is well below 1 $m.s^{-1}$ in many stable inlets, and therefore flat bed flow conditions may be an inadequate representation of the hydrodynamics for inlet stability theory. For instance, Riedel and Gourlay (1980) studied four inlets in a sheltered region on the southeast Queensland coast (Australia), and the equilibrium velocities they found range from 0.29 to 0.42 $m.s^{-1}$. Gao and Collins (1994a) found that $V_{eq} = 0.67$ $m.s^{-1}$ in the Yangpu Harbor entrance, which also has a small sediment supply from the ocean. Therefore, the amount of wave action and littoral drift in the vicinity of a given inlet, as well as the sediment and bedform characteristics, play an important role in defining the equilibrium velocity. The 1 $m.s^{-1}$ figure should then be used cautiously. Some authors have proposed other methods, based on the closure curve, to compute the degree of stability and to estimate the stable equilibrium area.

O'Brien and Dean (1972) incorporated the closure curve concept and the deposition in the inlet in another stability model. They first assumed that (1) the deposition of sand occurs primarily in the ocean side of the inlet channel within a length Δ , and (2) the head loss across the inlet can be translated into an "equivalent length" , and proposed a new expression of the repletion coefficient, which included Δ and . In addition they introduced the parameter κ as the ratio of the critical area, A_c^* (see Figure 2-1), to the equilibrium area, A_{cE}, and the stability index defined as

$$\beta_s = \int_{A_c^*}^{A_{cE}} (V_{\max} - V_t)^3 \, dA_c \,, \tag{2.4}$$

where A_c is the cross-sectional area, V_{max} is the maximum velocity, and V_t is the "threshold velocity for sand transport." They proposed that β_s represents the capacity of the inlet to resist closure under conditions of deposition. Finally, by constructing closure curves as a function of Δ / , they found that as the deposition length increases, both κ and β_s decrease. This approach allows the determination of the equilibrium cross-sectional area as a function of the critical area and introduces the stability index as a measure of the degree of inlet stability. However, this method only considers depositions in the seaward area of the inlet and ignores the deposition that can take place elsewhere in the channel and on the ebb and flood deltas, which is equally detrimental for stability.

Escoffier (1977) proposed yet another stability criterion, namely a stability number, λ, which estimates the degree of stability in an inlet. Combining the Ω-A_E relationship proposed by O'Brien, Equation (2.1) with Keulegan's expression for maximum velocity, Equation (2.2), and assuming that the tidal prism is $\Omega = 2a_bA_b$ (where a_b is the bay tidal amplitude and A_b is the bay area), he defined the equilibrium maximum velocity as

$$V_{eq} = C\frac{2\pi A_b a_b}{A_E T} = C\frac{\pi}{\alpha T}\left(2a_b A_b\right)^{1-n}, \tag{2.5}$$

where α and n come from Equation (2.1). The equilibrium velocity is not a constant value anymore but rather a monotonically increasing function of the cross-sectional area (Equation (2.5)). He finally defined the stability number as the ratio of the maximum velocity (at the peak of the closure curve) to the corresponding equilibrium velocity,

$$\lambda = \left(\frac{V_{\max}}{V_{eq}}\right)\Bigg|_{\frac{dV_{\max}}{dA_c}=0} = \frac{V^*_{\max}}{V_{eq}} = \alpha\frac{\left(2A_b a_b\right)^n}{A_c^*}. \tag{2.6}$$

Escoffier suggested that an inlet is potentially stable if, and only if $\lambda > 1$. If this condition is met, this parameter is a measure of stability in the sense that it indicates how much larger the maximum velocity through the inlet (for a specific area A_c^*) is compared to the velocity needed for equilibrium. In other words, an inlet with a large λ has (a) a greater range of areas for which stability is granted than an inlet having a small λ, and (b) greater chances to remain within the equilibrium interval after a sudden decrease in its cross-sectional area.

In another study, Skou and Fredsøe (1990) introduced the concept of "response ability," R_A, which they used to estimate the optimal cross-sectional area of an inlet. If the cross-sectional area of an inlet is in the stable region of the closure curve, the degree at which the velocity through the inlet changes after a disturbance in the cross-sectional area can be seen as a measure of the resistance against change. In mathematical terms they defined the response ability as the slope of the closure curve, i.e., $R_A = -dV_{max}/dA$. Taking into account only the action of the tidal flow as the disturbing force, the authors showed that the inlet is stable (in Escoffier's sense) for $R_A > 0$, and suggested that the optimal equilibrium flow area of an inlet corresponds to the point on the closure curve where R_A is maximum, i.e., at the point of inflexion. On one hand, the *maximum response ability* approach is interesting in the sense that it does not take the $V_{eq} = 1$ m.s^{-1} as granted, but on the other hand it does not take into account many of the forces acting on the inlet as littoral drift and waves (which are in some way incorporated in the equilibrium velocity parameter), and may lack of physical basis. Some authors have questioned the validity of the closure curve approach to analyze inlet stability as it has been presented above, and have suggested new criteria and models for its improvement.

The maximum velocity through the inlet may be a reasonable determining factor for stability since this velocity corresponds to the highest sediment transport rate throughout the tidal cycle. Bruun (1978) showed that for a tidal entrance having a simple geometry subject to a simple-harmonic semi-diurnal tidal forcing, ignoring wave effects, and assuming the sediment transport proportional to the velocity to the fifth power, about 80% of the sediment transport takes place between 85% and 100% of the peak velocity. However, while the closure curves are constructed for a single tidal range (spring), the ratio of spring to neap tidal ranges, R_{SP}/R_N, can vary considerably in nature, from 1.2 to 1.8 or more (see, e.g., O'Brien and Dean, 1972; this study; Friedrichs, 1995). This means that the condition $V > 0.85\ V_{max,\,spring}$ is satisfied more frequently throughout the spring/neap tidal cycle in inlets with small R_{SP}/R_N than in inlets having large R_{SP}/R_N. Consequently, significant sediment transport occurs also more frequently when the spring/neap tidal range ratio is small. Moreover, given that the distortion of the tide varies, depending on local physical characteristics and external conditions, the duration for which the velocity is close to the maximum velocity may vary considerably from one inlet to another, and even from one part of the tide to another (spring, neap, flood, ebb).

Another aspect of the closure curve model that has been questioned is the choice of the absolute maximum velocity through the inlet, without taking into account whether this velocity occurs during ebb or flood. The fact that a system has stronger flows during ebb ("ebb dominant") or flood ("flood dominant") may be determinant for inlet stability. It is well known that lagoons and bays with higher flood velocities tend to carry sediment inside the embayment, with the consequent tendency to form flood deltas and infill the channels with coarse sediment (e.g., Aubrey and Speer, 1985; DiLorenzo, 1988). That situation is hardly reversible since the ebb flows are not strong enough to remove the material deposited during flood, and may eventually lead to "clogging" of the inlet. Inversely, ebb-dominant systems tend to flush bed-load sediment seaward more effectively and may represent for the inlet a more stable situation. Following van de Kreeke (1996), a simplified mechanism of sediment transport in inlets presenting conditions of equilibrium can be described as follows: (1) after entering the inlet region, part of the littoral drift enters the inlet and part is bypassed via the ebb tidal delta to the downdrift region of the inlet, (2) the material that entered the inlet is then transported by the flood currents and deposited at the next slack water, and (3) the sand deposited in the inlet channel is transported seaward by the ebb currents.

Many authors have found that the ebb flows are usually stronger than the flood flows in inlets considered in equilibrium. The data used by Jarrett (1976) for his Ω-A_E empirical relationship contained information about the ebb and flood intensities, and it was found that the average flood velocities for all the inlets was 0.94 $m.s^{-1}$, whereas during ebb the velocity was 1.02 $m.s^{-1}$. The data from the Dutch inlets used by Bruun (1968) for his observed V_{max} = 1 $m.s^{-1}$ result showed that the maximum velocity was found to be 1 $m.s^{-1}$ during ebb and 0.85 $m.s^{-1}$ during flood. Skou (1990) performed experiments in a flume with a movable bed to simulate the hydrodynamics in an inlet, without considering waves or longshore currents. As expected, the ebb flow formed a jet with return flow along the sides when leaving the inlet channel while the flood flow developed a more uniform velocity field when entering the channel. The author found that the ebb flow discharge has the dominant influence on how the bed topography is formed. Therefore, the extent to which V_{max} is representative of the inlet flow for stability purposes is not universal.

2.1.3. Ω/M_{tot} and Related Criteria for Overall Stability

The overall stability of an inlet refers to the entire length of the inlet channel, as opposed to cross-sectional stability, which refers only to the inlet gorge. Bruun (1978) proposed a criterion based not only on "internal" factors such as tidal prism, but rather he added "external" factors, i.e., longshore sediment transport rates. He used the ratio of tidal prism per spring tidal cycle, Ω, to the total quantity of sediment transported due to longshore drift, M_{tot}, as a criterion to evaluate the degree of stability, and suggested that this ratio has a minimum value under which the inlet is not stable. Bruun found the following to hold:

$\Omega / M_{tot} > 150$	Conditions are relatively good, little bar formation and good flushing.
$150 > \Omega / M_{tot} > 100$	Conditions become less satisfactory, and offshore bar formation becomes more pronounced.
$100 > \Omega / M_{tot} > 50$	Entrance bar may be rather large, but there is usually a channel through the bar.
$50 > \Omega / M_{tot} > 20$	Typical "bay-bypassers". Existence depends on flushing by increased fresh-water discharge during storms and monsoons.
$\Omega / M_{tot} < 20$	Mainly "overflow channels" rather than inlets.

For instances when the cross-sectional area measurements are more reliable than the tidal prism, Bruun also related the littoral drift to the area with

$$\frac{\Omega}{M_{tot}} = \frac{A\bar{V}T}{2M_{tot}}, \tag{2.7}$$

where A is the inlet cross-sectional area, $\bar{V}$ is the mean velocity over the half tidal cycle, and T is the tidal period. Using the value of $\bar{V} = (2/3)V_{max} = 0.67 \text{m.s}^{-1}$ he suggested the following ranges for stability:

$(2/3)\, A/M_{tot} > 0.9 \cdot 10^{-2}$	for good stability
$0.9 \cdot 10^{-2} > (2/3)\, A/M_{tot} > 0.45 \cdot 10^{-2}$	for fair stability
$(2/3)\, A/M_{tot} < 0.45 \cdot 10^{-2}$	for poor stability

Some authors have supported this criterion by verifying it with their own data (see, e.g., Hume and Herdendorf, 1992; Gao and Collins, 1994a). Gao and Collins (1994b) modified the

parameter Ω / M_{tot} to account for fresh-water input. However, this approach suffers of the following problems. First, the sediment transport taken into account in this criterion is the total littoral drift. However, given the fact that the ratio of M_{tot} and the amount of sand that actually enters the inlet is not constant for all inlets (a function of offshore bathymetry, ebb tidal delta and wave climate), the Ω/M_{tot} ratio may not be a good parameter to use for a general equilibrium criterion. Second, for coasts having similar littoral drift, this expression would imply that the tidal prism would have to be larger than a minimum value. However, according to van de Kreeke (1996), this "minimum tidal prism" requirement is not always met in stable inlets, since it has been observed that flows in small inlets having small tidal prisms can be strong enough to maintain the inlet stable.

Besides the Ω/M_{tot} criterion, other studies have explored the overall stability (Byrne *et al.*, 1974; Mehta and Hou, 1974). These studies include in their formulation some form of external action (wave height and direction, longshore energy) and propose parameters such as "channel maintenance ratio" and "stability coefficient," which are a function of these external processes. Bruun (1990) suggested that these approaches are similar to the Ω/M_{tot}, assuming that the littoral drift is proportional to the wave height and the longshore energy. Yet another study taking into account the wave action is the work done by Johnson (1972), in which he analyzed the ratio of the annual wave power to the area of the lagoon for 46 inlets in the coast of California, concluding that the wave power is the single most important factor affecting inlet stability. Although these approaches have not been adopted in subsequent studies, they constitute at least an empirical attempt to incorporate the wave action in the stability analysis.

2.1.4. Other Criteria and Approaches

The approaches to inlet stability presented in the previous sections are of empirical or semi-empirical nature, and have been shown to be valuable tools for tidal inlet modeling and stability analysis. The empirical approach (e.g., O'Brien, 1931; Bruun, 1978) is based on observations and data from inlets in different locations and environments. Semi-empirical models (e.g., Escoffier, 1940) combine the empirical knowledge with one or more basic physical processes and principles. More recently, other types of semi-empirical models have been proposed (see de Vriend, 1996 for a review). For instance, the basin models (e.g., Di Silvio, 1989; van Dongeren and de Vriend, 1994) are models in which channels and flats are represented as idealized boxes

and interaction rules are defined between these boxes. On one hand, these models can be a powerful tool to predict the long-term morphodynamic behavior and stability of inlet/bay systems, and, on the other hand, they only describe the large features of the inlets, and no attempt is made to improve our knowledge on the basic processes in tidal inlets.

In recent years, researchers have gone beyond the empirical and semi-empirical approach to inlet stability, through the mathematical modeling of many of the complex physical processes, which take place in the vicinity of an inlet (waves, currents, sediment transport, morphological changes). Given the complexity of the equations of motion and the mathematical models of flow-sediment interaction, these models are solved numerically and some approaches may consider idealized geometries, allowing the use of simplifying assumptions with respect of the water motion. From a scientific point of view, such models are useful to develop and test hypotheses on how an inlet works, and from an engineering point of view they can help to analyze the response of the system to natural or anthropogenic disturbances.

Process-based models consist of modules describing the different processes in play (waves, currents, and sediment transport). De Vriend and Ribberink (1996) distinguish two types of process-based models: the Initial Sediment/Erosion (ISE) models and the Medium-Term Morphodynamic (MTM) models. The ISE models use the modules sequentially and do not take into account the interaction between the flow and the bathymetric changes due to the sediment transport. These models only describe phenomena in a short time scale, such as the accretion/erosion rate on the bathymetry at a given time. The MTM models use the modules iteratively in a time-loop, and are able to describe in longer time scales the dynamic formation and behavior of morphological features such as channels, bars, sandwaves, and ebb and flood deltas. An example of the use of an MTM model can be seen in Wang *et al.* (1995), who performed an analysis of the long-term morphological development of an inlet system in the Wadden Sea. In spite of the limitations in reproducing reality in detail, especially in the areas not sheltered by the waves, the model proved to be a useful research tool to investigate the relative importance of the physical processes in the morphological system.

Although the computational time to run the simulations has decreased steadily, the process-based models are not yet practical tools to analyze the long-term morphological evolution of coastal systems. Furthermore, given the lack of a complete understanding of the complex physical processes present in inlet/bay systems and the need of further development in that area, these

models are inherently unreliable to make morphodynamic predictions in decadal time scales (Schuttelaars, 1997). These arguments have been the motivation to combine numerical simulation models of one or various physical processes with a semi-empirical approach. The former is used to obtain a realistic hydrodynamic and/or morphodynamic behavior of the system, and the latter constitutes the closure for equilibrium and stability arguments. For instance, Yassuda and Sheng (1994), used the results of a numerical simulation hydrodynamic model, combined with Escoffier (1940) closure curve concept, to explain the closure of an inlet in Florida.

2.2. Multiple tidal inlet stability

Multiple tidal inlet systems are a particular case of inlet/bay systems where a single embayment communicates with the ocean through more than one inlet. Some authors who original focused on empirical and semi-empirical approaches to analyze single-inlet stability, have also commented on aspects of multiple inlet stability (e.g., O'Brien, 1966; Escoffier, 1977; Bruun, 1978). The major contribution using a semi-empirical approach is the work done by J. van de Kreeke, in which he developed a linear analytical model to study the stability of a specific dual tidal inlet system (van de Kreeke, 1984, 1985), and generalized the model for any multiple inlet system (van de Kreeke, 1990). Some other authors have focused on the formation and evolution of multiple tidal inlets in case specific studies, identifying some of the hydrodynamic processes that may affect stability, and analyzing some aspects of the hydrodynamic response to morphological changes (e.g., Aubrey and Giese, 1993). These studies present evidence of multiple inlets that can be stable on a decadal time scale. At present, the most promising approach to multiple inlet stability is the use of process-based models to simulate the hydrodynamics and morphodynamics of the system, or the use of a hydrodynamic numerical model in combination with semi-empirical models for closure (see section 2.1.4). The present review will focus on empirical and semi-empirical models, given that the use of process-based models for multiple tidal inlet stability analysis is only in early stages of development.

2.2.1. Empirical and Semi-Empirical Models

O'Brien (1966) used his Ω-A_E equilibrium relationship to conclude that the equilibrium minimum flow area of an inlet is controlled by the tidal prism, and that a reduction of the tidal

prism by sedimentation, vegetation, or artificial fill would reduce the flow area. He later extended this idea to the case of multiple tidal inlet systems and suggested that the reduction in cross-sectional area (or closure) of one or more inlets would enlarge the flow area of the others. This conclusion seems intuitively reasonable, but is rather optimistic since it is based on the assumption of a linear response where the total tidal prism remains approximately constant, which may not always be the case, in particular in unstable systems.

Escoffier (1977) suggested that the closure curve concept could also be applied to multiple tidal inlet systems. He first wrote the repletion coefficient as

$$K = \sigma \frac{A_{c_i}}{A_b} \xi, \tag{2.8}$$

where i is the inlet number, and

$$\sigma = \frac{T\sqrt{2ga_0}}{2\pi a_0}, \text{ and } \qquad \xi = \sqrt{\frac{R}{FL + mR}} \tag{2.9}$$

and the notation is the same as in Equation (2.3).

Assuming that the water surface in the bay remains horizontal, he suggested that such systems have a repletion coefficient K_T equal to the sum of the values of that coefficient for the individual inlets. He then adopted the Ω-A_E relationship from O'Brien (1931) and expressed the coefficient ξ for equilibrium of the entire system as

$$\xi_E = \frac{\Sigma(K)}{\sigma} \frac{A_b}{\alpha \Omega^n} \tag{2.10}$$

where Ω is the tidal prism of the entire system. He suggested that equilibrium of the system requires that the value ξ for each inlet shall be equal to ξ_E. From Equations (2.8) and (2.10) this would imply that

$$A_{c_i} = \frac{K_i}{\Sigma(K)} \alpha \Omega^n. \tag{2.11}$$

This means that for equilibrium, the cross-sectional area of each inlet has to be a fraction of a total equivalent area ($A_T = \alpha \Omega^n$), given that this fraction is equivalent to the inlet's contribution to the total repletion coefficient. Escoffier concluded that the system is unstable because if

the value of ξ for any inlet is slightly greater than the values for the other inlets, that inlet will develop a higher velocity than the others and will enlarge until it captures the entire tidal prism.

2.2.2. Van de Kreeke multiple inlet stability semi-empirical model

Van de Kreeke (1984; 1985) developed a linear analytical model to study the stability of a dual tidal inlet system. Borrowing the concept of closure curve from Escoffier (1940) and using Keulegan's (1951) approximate analytical solution for the maximum tidal velocity as a function of the cross-sectional area, he constructed a series of closure curves for each inlet varying the cross-sectional area of the other inlet, as shown qualitatively in Figure 2-3, and obtained for each inlet a so-called closure surface of the maximum bottom shear stress as a function of both cross-sectional areas. The values of τ_{II} decrease with increasing values of A_I, and vice-versa (Figure 2-3).

The equilibrium condition adopted corresponds to the shear stress estimates suggested by Bruun (1978), which range from 3.5 $N.m^{-2}$ to 5.5 $N.m^{-2}$ for inlets having small to high littoral drift, respectively. The equilibrium flow curves for each inlet are the intersection of the equilibrium shear stress plane and these closure surfaces, as shown for the closure surface corresponding to Inlet II in Figure 2-3 and projected in the $\tau = 0$ plane for both closure surfaces in Figure 2-4. These curves represent all the combinations of equilibrium areas (stable an unstable) for each inlet as a function of the cross-sectional areas of both inlets, for a given equilibrium shear stress.

Van de Kreeke used these equilibrium flow curves as a geometrical tool to analyze the stability conditions for each inlet. For instance, using the same reasoning as for the single inlet stability analysis presented in Section 2.1.2, and assuming the cross-sectional area of Inlet I to remain constant, Figure 2-4 shows that when

$A_{II} = A_A$, Inlet II is unstable. It will shoal and ultimately close;

$A_{II} = A_B$, Inlet II is in the equilibrium interval since $\tau_{II} > \tau_{eq}$. Erosion will take place until A_{II} attains the value A_S; and

$A_{II} = A_C$, Inlet II is also in the equilibrium interval but $\tau_{II} < \tau_{eq}$. The inlet will shoal until A_{II} attains the value A_S;

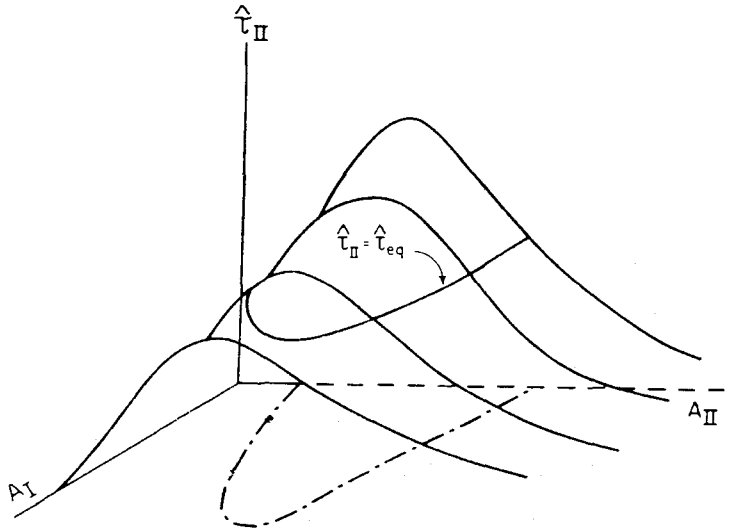

Figure 2-3. Closure curves of a hypothetical inlet II, for different cross-sectional areas of inlet I. This family of curves generates a closure surface, whose intersection with an equilibrium shear stress plane forms the equilibrium flow curve for inlet II, where $\hat{\tau}_{II} = \hat{\tau}_{eq}$ (adopted from van de Kreeke, 1985).

Figure 2-4 also shows with enhanced lines the ranges of the equilibrium flow curves corresponding to a stable equilibrium condition for each inlet. Hence, van de Kreeke suggested that the condition for the existence of stable cross-sectional areas for both inlets is that the enhanced parts of the equilibrium flow curves intersect.

The author applied the stability analysis to Matagorda Bay, Texas, a historically stable single inlet/bay system in which a companion inlet was dredged in 1963 to serve as the entrance of the shipping channel. Since the opening of the companion inlet, the original inlet has experienced a gradual reduction in cross-sectional area. Assuming that the original inlet had reached equilibrium in 1959, the author used measured data relative to the geometry of the system and constructed the corresponding closure curves, closure surfaces and equilibrium flow curves. Van de Kreeke found that the equilibrium flow curves did not intersect in their stable equilibrium sections, and concluded that for this particular two-inlet bay system, neither of the two inlets was stable, resulting in the closure of the natural inlet and the increase in cross-sectional area of dredged inlet.

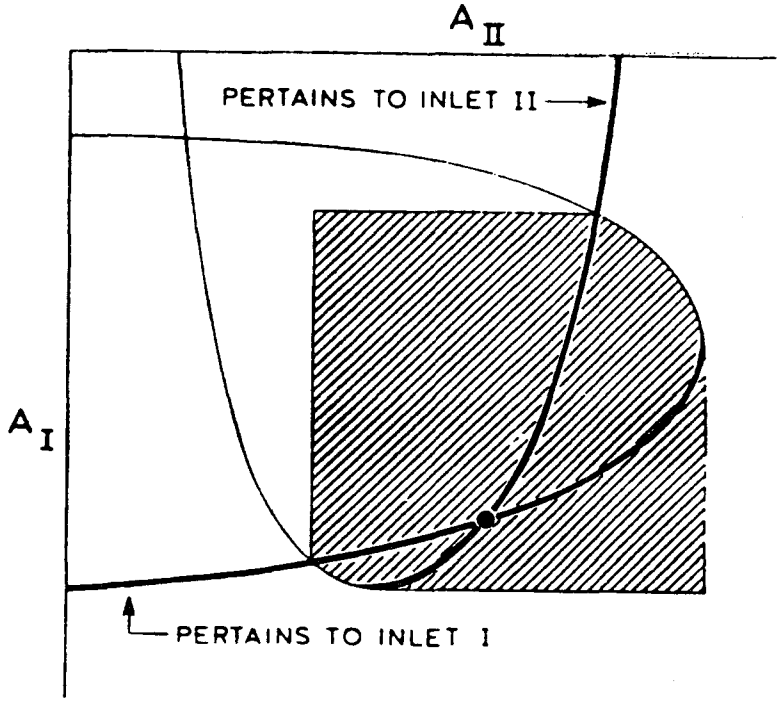

Figure 2-4. Equilibrium Flow Curves for Inlets I and II (adapted from van de Kreeke, 1985)

The model presented by van de Kreeke is based on the approximate analytical solution presented by Keulegan (1951), which assumes 1) constant and uniformly fluctuating bay surface area, 2) simple harmonic ocean tide, and 3) negligible tidal variations in cross-sectional area, hydraulic radius, friction coefficient, and exit and entrance loss coefficients. However, in reality, complex intertidal areas are common in shallow embayments, with the consequent important variations in bay surface slopes and friction coefficients throughout the tidal cycle. Moreover, the analysis by van de Kreeke ignores the nonlinear processes, which, as will be shown in the following section, are usually present in shallow coastal systems.

More recently, van de Kreeke (1990) showed that, for inlets assumed to have rectangular or triangular cross-sections, the equilibrium flow curves cannot intersect in more than two points, which would then exclude the configuration of the curves shown in Figure 2-4. Furthermore, starting with the same approach as for the dual-inlet/bay system, he generalized the model for systems with more than two inlets. In principle, given that more than two cross-sectional areas are in play, the geometrical solution based on the closure surfaces (presented above) is not possible. However, the author made a series of assumptions regarding the inlet geometries to apply the

equilibrium flow curves for equilibrium analysis. For the construction of the closure curves using Keulegan's (1967) linear solution, he first assumed that all the inlets have the same values of entrance and exit loss coefficients, friction coefficient, channel length, and that all the inlets have the same shape (i.e., the same dependency of the hydraulic radius on the cross-sectional area). Given that, the theoretical closure curves are identical for all the inlets. In addition, van de Kreeke assumed that all the inlets respond identically to disturbances. Considering that the system is initially in equilibrium and that a sudden change in the cross-sectional area of one inlet occurs, the author suggested that the system enters in an unstable mode that will lead to the closure of all the inlets or, at best, only one will remain open.

This approach is interesting in the sense that it uses a semi-empirical model originally meant for single-inlet systems to analyze multiple tidal inlet stability. However, the assumption of an identical response of all the inlets is unrealistic, since a disturbance in a given inlet will affect in greater extent adjacent inlets and in lesser extent inlets far from it. In addition, the use of the total bay surface area for the computation of the repletion coefficient and the maximum velocity through each inlet appears to be an oversimplification. Indeed, Aubrey *et al.* (1993), adopting the closure curve approach and using a one-dimensional diagnostic model, studied the effect of the opening of a third inlet in a two-inlet shallow system, in terms of flushing, water exchange and residual transport. Their main conclusion relevant to the closure curve analysis validation was that stability calculations cannot be based on equal bay areas for all the inlets, implying that some hydrodynamic decoupling occurs. Another example showing the strong hydrodynamic interaction between inlets servicing the same embayment is the study done by Kraus and Militello (1999). They examined the hydrodynamics in a two-inlet system in Texas by applying a two-dimensional, depth-averaged hydrodynamic model, and analyzed the overall stability implications of the opening of a proposed third inlet. As opposed to the linear closure curve approach, the authors found that the tidally-driven currents are not always the sole process controlling discharge through the inlets and that the wind-induced setup in one extremity of the embayment produced a quasi-steady ebb current at the location of the proposed inlet, implying the existence of strong residual flows between the inlets.

Finally, van de Kreeke's results from analytical models, suggesting that multiple tidal inlets are unstable, are in disagreement with other studies. For instance, research at Gasparilla Sound in Florida (Escoffier, 1977), Waquoit Bay (Aubrey *et al.*, 1993) and Nauset Inlet (Aubrey

et al., 1997) in Massachusetts, Matagorda Bay in Texas (Kraus and Militello, 1999), and Ría Formosa in Portugal (this study) has documented specific examples where multiple inlets servicing the same embayment are potentially long-lived and persistent on a historical time scale.

2.3. Nonlinear hydrodynamics in shallow systems

Nature is nonlinear. The question is whether nonlinear processes are important to describe a physical phenomenon. Many problems in physics and in particular in coastal hydrodynamics and morphodynamics, whose mathematical description is based on the laws of conservation of momentum, mass, and energy, can be solved using a linear approach, leading to a linear analytical solution. However, this approach was often adopted, not because it was the best, but because it was the only practical way to obtain a solution. At present and since the last few decades, the increasing feasibility of numerical-based modeling has permitted the analysis of the coastal hydrodynamic and morphodynamic processes using the full nonlinear equations of motion. These numerical, process-based simulation models are used to identify and investigate the relative importance of such nonlinearities in the behavior and evolution of inlet/bay systems, and have shown to be a powerful tool to implement more realistic short- and long-term prognostic models.

Relevant to shallow coastal systems, the most important nonlinear processes are associated with different forms of tidal asymmetry, which concern (1) higher frequencies, i.e., the distortion of the tide as it propagates from the open ocean to the embayment and the generation of compound and higher harmonic tidal constituents, and (2) lower frequencies, i.e., subharmonics and tidal rectification, leading to the generation of residual currents. Both processes have strong effects in the morphology of these systems since they are important controlling factors of the sediment transport pattern. Indeed, as the response of sediment transport to velocity is nonlinear, the net transport through an inlet is considerably sensitive to asymmetries in the tidal velocity and water surface elevation (e.g., van de Kreeke and Robaczewska, 1993).

On one hand, the distortion of the tide, which is a result of specific morphological features in the basin and the inlet, can lead to flow dominance, i.e., a consistent and predictable imbalance between the duration and intensity of ebb and flood flows. Boon and Byrne (1981), based on simulations of the response to changes in basin hypsometry, showed that this imbalance is a

plausible mechanism for long-term, net transport of bed material through the inlet and within the embayment. According to Friedrichs and Aubrey (1988), flood-dominant systems (with higher velocity and shorter duration floods) tend to infill their channels with bed-load transported coarse sediment, and ebb-dominant systems (with higher velocity, shorter ebbs) tend to flush bed-load sediment seaward more effectively, and may represent more stable geometries.

On the other hand, tidally driven residual currents are usually one to two orders of magnitude less than the tidal currents themselves. However, they are important because their persistence may allow them to dominate the overall distribution and transport of characteristic water properties such as temperature and salinity (Pugh, 1987). In particular, residual flows may play an important role in producing a net landward or seaward transport of sediment, which in turn is determinant for the overall long-term stability of inlet/bay systems.

2.3.1. Tidal distortion

When the tide propagates from the deep ocean towards shallower coastal regions approaching an inlet, the spectral composition of the tide changes as energy from the offshore tidal constituents is transferred to higher harmonic components called "overtides" (DiLorenzo, 1988; van de Kreeke, 1988), due to the nonlinear filter characteristics of the inlet. In particular, tidal distortion in coastal embayments can be represented by the nonlinear growth or decay of compound constituents and harmonics of the principal astronomical tidal constituents from the mouth of the embayments to the inner regions. Since the dominant astronomical constituent is M_2 (semidiurnal lunar tide) in most of the coastlines, the most significant overtide formed by nonlinearities (such as the dependence on the square of the velocity) in these systems is M_4, the first harmonic of M_2. Therefore, authors have frequently focused in these constituents when analyzing the tidal distortion (e.g., Boon and Byrne, 1981; Uncles, 1981; Aubrey and Speer, 1985; Friedrichs and Aubrey, 1988; van de Kreeke and Robaczewska, 1993), and have suggested that a measure of the distortion can be the M_4 to M_2 velocity and water-surface amplitude ratios. In addition, the relative velocity and water-surface phase angle of M_4 relative to M_2 ($2\phi_{M2}-\phi_{M4}$) is an indication of the type of flow dominance to expect, as summarized in Figure 2-5.

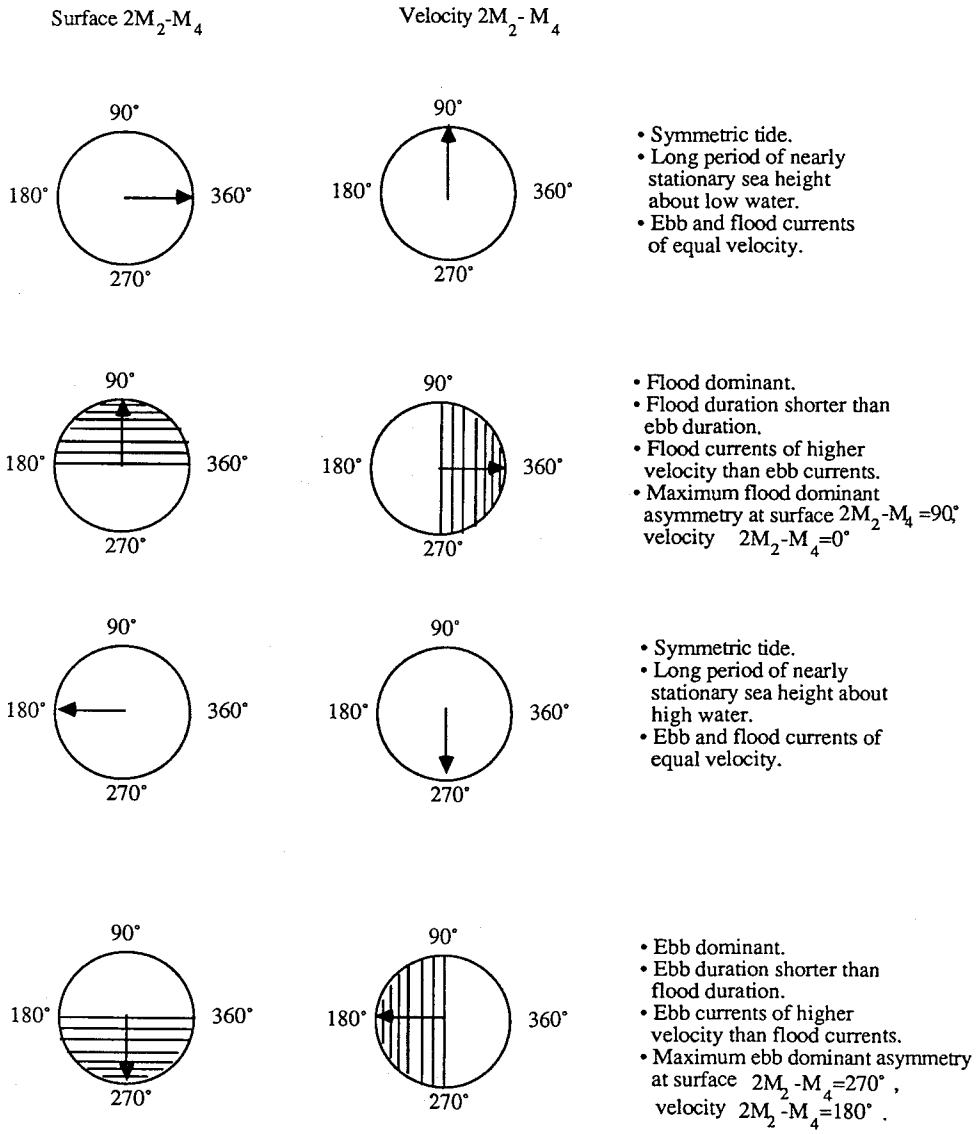

Figure 2-5. Linear relationships between phase and tidal distortion for velocity and water surface $M_4/M_2 > 0$ (from Friedrichs and Aubrey, 1988).

In the case of a shallow, frictionally dominated embayment, Friedrichs and Madsen (1992) showed that the principal sources of nonlinearity in the generation of overtides are: quadratic friction, time-varying channel depth in the friction term, and time-varying channel depth coupled with time-varying embayment width in the continuity equation. Restating the 1-D equations of motion in terms of characteristics scales (and using 0.5 $m.s^{-1}$, 10^{-2}-10^{-3}, $4.5 \cdot 10^4$ s, and 1-10 m as typical values for velocity, drag coefficient, tidal period, and channel depth, respectively), they suggested that ratio of the acceleration terms to the friction term ranges from $5 \cdot 10^{-1}$

to $5 \cdot 10^{-3}$, suggesting that the acceleration terms are negligible. In order to say that the advection and local acceleration terms are of the same order, they assumed the ratio of the embayment width to the channel width to be of the same order as the ratio of the channel depth to the tidal amplitude. Given that tidal embayments often occur in mesotidal environments (Hayes, 1979), the latter ratio may be of the order of unity in shallow systems (e.g., Kjerfve, 1975; Speer and Aubrey, 1985). Therefore, the assumption the authors make would require the channel and embayment widths to be of the same order, which may not always be the case. For instance, Uncles (1981), using a one-dimensional, nonlinear hydrodynamic model, did not make that assumption and suggested that advection may play an important role in the generation of nonlinearities. In addition, he showed the existence of frictional interaction between the tidal flow and the Stokes drift as another source of generation of overtides. In another study, Flather and Heaps (1975) found that the overall influence of advection on the tidal regime was very small, but its effect on currents appeared to be larger. They suggested that the advective accelerations should be retained in the equations if the interest resides in analyzing residual currents.

A series of studies have been conducted to identify the processes and inlet/bay characteristics that control nonlinear tidal distortion.

Boon and Byrne (1981), using a numerical model featuring a hypsometric (area-height) representation of the basin storage to describe nonlinear distributions of basin surface area with water surface height in coastal basins, showed that both channel configuration and basin hypsometry are controlling factors in determining the characteristics of the distorted tide in the inlet region and in the basin. Their results suggested that the dominant tidal component, M_2, and its first overtide, M_4, account for most of the flood and ebb duration differences, which in turn are capable of producing net flood or ebb sediment transport. Moreover, they suggested that (1) the tidal distortion appears to favor the ebb (flood) dominance when basin infilling is advanced (small), and (2) the channel configuration and the tidal range to depth ratio may decide the sense of the flow dominance near inlet entrances. FitzGerald and Nummedal (1983) studied the response characteristics of an ebb dominated tidal inlet channel (Price Inlet, South Carolina), and found that the intertidal marsh of the back-barrier lagoon experiences a change in surface of about 670% during an average tidal cycle. They suggested that the tidal current asymmetries can be explained by changing hydraulic efficiency at the inlet during the tidal cycle at high tide, and low velocities in intertidal areas cause a delay in the turn to ebb, causing relatively shorter ebb, longer flood, and

highest velocity currents during the ebb. In other studies, Speer and Aubrey (1985), Friedrichs and Aubrey (1988), and Di Lorenzo (1988) showed that large tidal amplitude to channel depth ratio causes relatively shorter floods (i.e., flood dominance), and the existence of tidal flats can produce a longer rising tide and stronger ebb currents (i.e., ebb dominance), if the intertidal storage is large enough to overcome the effects of time-variable channel geometry.

The implications of the tidal distortion on the sediment transport pattern have been qualitatively mentioned by several authors, as mentioned above, and they all concur in suggesting that flood-dominance has a tendency to transport sediment landward, with the consequent development of important flood deltas in the bay side of the inlet and the gradual shoaling of the channels (e.g., Aubrey, 1986). This scenario is therefore associated with a long-term instability of the inlet. Inversely, ebb-dominant inlets have the tendency of exporting material to the outer deltas, and, depending on the amount of sediment deposited during flood and slack by the tidal currents and the wave action, this scenario may be associated with increased chances of stability. Fry and Aubrey (1990) performed a more thorough analysis of the bedload transport due to tidal velocity asymmetries in shallow embayments and found the same trends as in earlier studies. In addition, they found that the flood to ebb sediment transport ratio is dependent mainly on (1) the water surface M_4/M_2 amplitude ratio when the flood- or ebb dominance is strong, and (2) the water surface $2M_2$-M_4 relative phase when the flood- or ebb dominance is weak.

Lincoln and FitzGerald (1988) studied the tidal distortion in five shallow tidal inlets in southern Maine (channels shallower than the ocean tide amplitude), and found that an additional factor can contribute to flow dominance at inlets. Namely, they showed that the topographic truncation of the lower portion of the ocean tide curve contributes significantly to a negative tide asymmetry (shorter and stronger flood), producing net landward sediment transport. Similarly, Speer *et al.* (1991) describe a particular class of flood-dominant estuaries where shoaling channels effectively truncate the lowest portion of the tide, resulting in an extended falling tide and a slow shallow ebb flow. This scenario may not be common in nature, in particular for inlets in or near equilibrium on sandy coasts, but suggests that (1) a stable, ebb-dominant inlet can experience a flow dominance reversal if it becomes suddenly shallow, and (2) a positive feedback in a closing inlet can occur with a decrease in ebb dominance (or even a reversal from ebb-to flood-dominance), further increasing the instability and accelerating the closure.

2.3.2. Residual circulation

Many authors have recognized that residual circulation, which can be regarded in terms of the mean (Lagrangian) velocity or the mass transport (discharge), depending on the process to be analyzed, has direct control in the net transport of material through the inlet, and in general in the tidal-mean exchange of salt, pollutants, and suspended material (e.g., Mei *et al.*, 1974; Liu, 1992; Liu and Aubrey, 1993; Bakker and de Vriend, 1995; de Vriend, 1996). The residual current is the tidally averaged velocity, which, in the case of inlet stability analysis focusing on tidal-induced currents, is often expressed as the tidally averaged mean cross-sectional velocity through the inlet or channel. The vertically averaged transport per unit width in a tidal channel is defined as:

$$\bar{q} = \bar{u}(h+\eta) \tag{2.12}$$

where $\bar{u}$ is the vertically averaged instantaneous velocity per unit width, h is the water depth below the mean water level and η(t) is the water surface elevation. Assuming a simple harmonic tidal oscillation, the time average of the vertically averaged transport over the tidal cycle divided by the water depth yields the residual mean current:

$$\langle \bar{u}_L \rangle = \frac{\langle \bar{q} \rangle}{h} = \langle \bar{u} \rangle + \frac{\langle \bar{u}\eta \rangle}{h} = \langle \bar{u}_E \rangle + \langle \bar{u}_S \rangle \tag{2.13}$$

where $\langle \cdot \rangle$ denotes the tidal average, $\langle \bar{u}_L \rangle, \langle \bar{u}_E \rangle$, and $\langle \bar{u}_S \rangle$ are respectively the mean Lagrangian velocity, which refers to the mean velocity of a particle, the mean Eulerian velocity, which refers to the mean velocity at a fixed location in space, and the Stokes drift, which accounts for the change in velocity a particle encounters when moving from one position to another.

Research has focused on the total residual current and its implications on mass transport, but an analysis of its individual components (i.e., Eulerian mean current and Stokes drift) may reveal more information about the residual trends. For instance, Liu (1992) found that the Eulerian, Stokes and Lagrangian residual currents are lagoonward during normal conditions in Sebastian Inlet, Florida, which may be used to explain the long-term trends of flood-delta shoaling, but found that storm events could cause the Eulerian residual current in the inlet to flow seaward temporarily.

The generation of residual flow through the inlet can in fact be due to either local or remote processes (tides), the latter being more relevant for this study. Local processes likely to affect the mean water level in parts or the entire lagoon and to create an imbalance in the flood and ebb tidal prisms, thus affecting the residual current generation, include river and groundwater discharges, surface runoff, local wind forcing on the lagoon at subtidal frequencies, and processes associated with storm events such as storm surge and increased fresh water input (see, e.g., Liu, 1992; Kraus and Militello, 1999). In turn, the generation of tide-induced residual flow in shallow bays and channels is generated by different mechanisms, depending on the dimensions and geometry of the domain studied and on the timescales considered.

Zimmerman (1978; 1980) studied the topographic generation of residual circulation by tidal currents and, through the analysis of vorticity dynamics, he showed that irregular bottom topography can transfer vorticity from the tidal velocity field to the mean (residual) field by advection, with the consequent generation of residual circulation. In another study, van de Kreeke and Chiu (1980), considering the tidal motion in a relatively shallow canal, showed that tidally generated residual currents are generated by (a) mean sea level differences, and (b) by tidal amplitude and phase differences between the two open boundaries of the canal. Writing the one-dimensional governing equations in terms of the discharge per unit width q (rather than the velocity), they also showed, by expanding the discharge and the water surface (e.g., $q = \overline{q} + q_1(x,t) + q_2(x,t) + \ldots$) and neglecting the high order terms, that the residual flow is reduced by (a) the gradient of the tidally averaged momentum flux associated with the tidal velocities, (b) the gradient of the tidally averaged momentum flux associated with the nonlinear part of the pressure gradient, (c) the gradient of the mean water level, and (d) a residual stress resulting from the nonlinear bottom friction. In their review article, de Vriend and Ribberink (1996) suggested that the tidal rectification can also be due to inertial effects (ebb-jet), Coriolis effects (ebb- and flood- branches of a channel), and induced by the topography.

The relative importance of the residual circulation compared to the tidal distortion, and their joint implications in the sediment transport patterns in inlets and embayments have not yet been extensively studied. In general, the studies on nonlinear hydrodynamic processes in coastal systems have focused on the residual current generation or the tidal distortion. However, some studies have analyzed the net transport with the two processes taken into account. Van de Kreeke and Robaczewska (1993) showed for the tide-dominated Ems-Dollard estuary that the contribu-

tion of the residual current to the long-term residual transport is even larger than that of the tidal distortion. Uncles (1981) separated the residual stress on an estuary's bed into two contributing parts: the residual due to tidal asymmetry, and the residual due to the presence of the Stokes drift. By using a one-dimensional, nonlinear numerical model, he showed that the total residual stress (which is proportional to the square root of the velocity) is always seaward. However, he also found that (1) the residual due to tidal asymmetry is seaward near the mouth of the estuary and landward in the inner parts of the embayment, and (2) that the residual stress due to the Stokes drift (which he finds to be dominant for all but neap tides) is always seaward. This shows the importance of considering both the tidal distortion and the residual circulation when analyzing the nonlinear response of inlet/bay systems to disturbances

2.3.3. Nonlinear processes in multiple inlet systems

The existence of multiple inlets servicing a single embayment confers another complication in the systems hydrodynamics, since the flow is not only between the ocean and the bay, but also between the inlets themselves. Thus, the interaction of flows entering the lagoon from different inlets is likely to render the generation of nonlinear processes more complex.

The generation of residual currents and tidal distortion in multiple tidal inlets has been analytically studied and evidenced in the field by many authors. For instance, some authors have shown that the existence of an asymmetric constriction in a channel produces residual flows (Mei *et al.*, 1974; van de Kreeke, 1976; van de Kreeke and Chiu, 1980). Mei *et al.*(1974) examined theoretically the wave transmission through narrow passages (e.g., holes in breakwaters and constrictions in channels), and predicted the presence of a mean current and a mean sea level change for asymmetrical constrictions, suggesting possible applications to flushing of coastal channels "so that the channel may be freed of undesirable deposits." Van de Kreeke (1976) performed laboratory experiments in which a submerged weir was placed in a channel whose both ends communicated to the same bay, and also identified the presence of a mean current in the direction of less friction loss. A similar study was formulated mathematically by van de Kreeke and Chiu (1980)(see p 66), and the authors found that certain geometric features can play an important role in generating mass flows. For instance, the occurrence of a mean flow is possible when inlets with different dimensions are added at each end of a shallow canal, even if the tidal oscillation is identical at both open boundaries (i.e., channel connected to the same oscillating body of water).

These results can be qualitatively extrapolated to a two-inlet system, as suggested by van de Kreeke (1988), showing that significant residual currents can occur in a multiple inlet system.

Aubrey *et al.* (1993), assuming the two-inlet scenario to be historically stable in a system with a newly formed third inlet (Waquoit Bay, Massachusetts), and using the closure curve approach (Escoffier, 1940), found that the theoretical bay area needed for the actual measured values of velocity and cross-sectional area to fall in the theoretical closure curve is appreciably greater than the measured bay area. This may reflect nonlinear tidal dissipation and propagation within the embayment, as well as significant tidal residuals between the different areas of the system. Friedrichs *et al.* (1993) were successful in capturing some of the fundamental nonlinear processes (amplitudes and relative phases of M_4 elevations and velocities) evidenced in field measurements, using a one-dimensional nonlinear tidal propagation model to simulate the hydrodynamics in a multiple inlet system. Liu and Aubrey (1993), using multiple inlets in Chatham, Massachusetts, as a case study, and comparing the results from a linear analytical (van de Kreeke and Chiu, 1980) and a one-dimensional nonlinear models, showed that the combined influence of tidal phase, amplitude, and mean sea level differences between the two ends of an idealized channel on the generation of residual currents is complex and nonlinear, and can be predicted properly only by nonlinear numerical modeling. Forcing the model with a simple harmonic M_2 tide, they found that (1) the residual currents are primarily caused by the mean sea-level differences, (2) the generation of the M_4 overtide is mainly due to the tidal phase difference between the two open boundaries of the channel, and (3) sediment transport patterns in a tidal inlet can be attributed in part to residual currents, implying that the mean sea level differences between the coastal ocean and the inner sections of the embayment is an important controlling factor in morphodynamic evolution.

2.4. References

Aubrey, D. G., 1986. Hydrodynamic Controls on Sediment Transport in Well-Mixed Bays and Estuaries, in: J. van de Kreeke, Ed.: *Physics of Shallow Estuaries and Bays*. Coastal and Estuarine Studies, **16**. Springer-Verlag, New York, NY, pp 245-258.

Aubrey, D. G. and Giese, G. S., Eds., 1993. Formation and Evolution of Multiple Tidal Inlets. Coastal and Estuarine Studies, **44**. American Geophysical Union, Washington, D.C.

Aubrey, D. G., McSherry, T. R. and Eliet, P. P., 1993. Effects of Multiple Inlet Morphology on Tidal Exchange. Waquoit Bay, Ma., in: D.G. Aubrey and G.S. Giese, Eds.: *Formation and Evolution of Multiple Tidal Inlets*. Coastal and Estuarine Studies, **44**. American Geophysical Union, Washington D.C., pp 213-235.

Aubrey, D. G. and Speer, P. E., 1985. A Study of Non-Linear Tidal Propagation in Shallow Inlet/Estuarine Systems. Part I: Observations. *Estuarine, Coastal and Shelf Science,* **21**: pp 185-205.

Aubrey, D. G., Voulgaris, G. and Spencer, W. D., 1997. *Tidal Residence Times within the Nauset Marsh System.* Report to the town of Orleans, WHOI-97-11. Department of Geology and Geophysics, Woods Hole Oceanographic Institution. Woods Hole, MA.

Bakker, W. T. and de Vriend, H. J., 1995. Resonance and Morphological Stability of Tidal Basins. *Marine Geology,* **126**: pp 5-18.

Boon, J. D. I. and Byrne, R. J., 1981. On Basin Hypsommetry and the Morphodynamic Response of Coastal Inlet Systems. *Marine Geology,* **40**: pp 27-48.

Brown, E. I., 1928. Inlets on Sandy Coasts. *Proceedings of the American Society of Civil Engineers,* **54**: pp 505-553.

Bruun, P., 1968. Tidal Inlets and Littoral Drift. Oslo University Book Company.

Bruun, P., 1978. Stability of Tidal Inlets, Theory and Engineering. Development in Geotechnical Engineering, **23**. Elsevier.

Bruun, P., 1990. Port Engineering, **2**. Gulf Publishing Company.

Bruun, P. and Gerritsen, F., 1960. Stability of Coastal Inlets. North Holland Publishing Co.

Byrne, R. J., DeAlteris, J. T. and Bullock, P. A., 1974. Channel Stability in Tidal Inlets: A Case Study. Proc. of the 14th International Coastal Engineering Conference, Copenhagen, **2**: pp 1585-1604.

de Vriend, H. J., 1996. Mathematical Modeling of Meso-Tidal Barrier Island Coasts, Part I: Empirical and Semi-Empirical Models, in: P.L.-F. Liu, Ed.: Advances in Coastal and Ocean Engineering, **2**. World Scientific, pp 115-149.

de Vriend, H. J. and Ribberink, J. S., 1996. Mathematical Modeling of Meso-Tidal Barrier Island Coasts, Part 2: Process-Based Simulation Models, in: P.L.-F. Liu, Ed.: Advances in Coastal and Ocean Engineering, **2**. World Scientific, pp 151-197.

Di Silvio, G., 1989. Modeling the Morphological Evolution of Tidal Lagoons and Their Equilibrium Configuration. Proc. of the 23rd IAHR Congress, Ottawa, Canada., pp C.169-C.175.

DiLorenzo, J. L., 1988. The Overtide and Filtering Response of Small Inlet/Bay Systems., in: D.G. Aubrey and L. Weishar, Eds.: *Hydrodynamics and Sediment Dynamics of Tidal Inlets.* Lecture Notes on Coastal and Estuarine Studies., **29**. Springer-Verlag, New York, pp 24-53.

Escoffier, F. F., 1940. The Stability of Tidal Inlets. *Shore and Beach,* **8**: pp 114-115.

Escoffier, F. F., 1977. *Hydraulics and Stability of Tidal Inlets*. General Investigation of Tidal Inlets (GITI) Report, 13. USACE.

FitzGerald, D. M. and Nummedal, D., 1983. Response Characteristics of an Ebb Dominated Tidal Inlet Channel. *Journal of Sedimentary Petrology,* **53**: pp 833-845.

Flather, R. A. and Heaps, N. S., 1975. Tidal Computations for Morecambo Bay. *Geophysical Journal of the Royal Astronomical Society,* **42**: pp 489-517.

Friedrichs, C. T., 1995. Stability Shear Stress and Equilibrium Cross-Sectional Geometry of Sheltered Tidal Inlets. *Journal of Coastal Research,* **11**(4): pp 1062-1074.

Friedrichs, C. T. and Aubrey, D. G., 1988. Nonlinear Tidal Distortion in Shallow Well-Mixed Estuaries: A Synthesis. *Estuarine, Coastal and Shelf Science,* **27**: pp 521-545.

Friedrichs, C. T., Aubrey, D. G., Giese, G. S. and Speer, P. E., 1993. Hydrodynamical Modeling of a Multiple Inlet Estuary/Barrier System: Insight into Tidal Inlet Formation and Stability., in: D.G. Aubrey and G.S. Giese, Eds.: *Formation and Evolution of Multiple Tidal Inlets*. Coastal and Estuarine Studies, **44**. American Geophysical Union, Washington D.C., pp 95-112.

Friedrichs, C. T. and Madsen, O. S., 1992. Nonlinear Diffusion of the Tidal Signal in Frictionally Dominated Embayments. *Journal of Geophysical Research,* **97**(5637-5650).

Fry, V. A. and Aubrey, D. G., 1990. Tidal Velocity Asymmetries and Bedload Transport in Shallow Embayments. *Estuarine, Coastal and Shelf Science,* **30**: pp 453-473.

Gao, S. and Collins, M., 1994a. Tidal Inlet Equilibrium, in Relation to Cross-Sectional Area and Sediment Transport Patterns. *Estuarine, Coastal and Shelf Science,* **38**: pp 157-172.

Gao, S. and Collins, M., 1994b. Tidal Inlet Stability in Response to Hydrodynamic and Sediment Dynamic Conditions. *Coastal Engineering,* **23**(61-80).

Hayes, M. O., 1979. Barrier Island Morphology as a Function of Tidal and Wave Regime., in: S.P. Leatherman, Ed.: *Barrier Islands, from the Gulf of St. Laurence to the Gulf of Mexico*, Academic Press., New York, NY, pp 1-28.

Hume, T. M., 1991. Empirical Stability Relationships for Estuarine Waterways and Equations for Stable Channel Design. *Journal of Coastal Research,* **7**(4): pp 1097-1111.

Hume, T. M. and Herdendorf, C. E., 1992. Factors Controlling Tidal Inlet Characteristics on Low Drift Coasts. *Journal of Coastal Research,* **8**(2): pp 355-375.

Hume, T. M. and Herdendorf, C. E., 1993. On the Use of Empirical Stability Relationships for Characterising Estuaries. *Journal of Coastal Research,* **9**(2): pp 413-422.

Jarret, J. T., 1976. *Tidal Prism-Inlet Area Relationships*. General Investigation of Tidal Inlets (GITI) Report, 3. U.S. Army Corps of Engineers, CERC. Ft. Belvoir, VA.

Johnson, J. W., 1972. *Tidal Inlets on the California, Oregon, and Washington Coasts*. Report HEL 24-12, Hydraulic Engineering Laboratory, University of California. Berkeley, CA.

Keulegan, G. H., 1951. *Third Progress Report on Tidal Flow in Entrances, Water-Level Fluctuations of Basins in Communication with Seas*. National Bureau of Standards.

Keulegan, G. H., 1967. *Tidal Flow in Entrances*. Technical Bulletin, 14. Committee on Tidal Hydraulics, USACE.

Kjerfve, B., 1975. Velocity Averaging in Estuaries Characterized by a Large Tidal Range to Depth Ratio. *Estuarine, Coastal and Shelf Science,* **3**: pp 311-323.

Kraus, N. C. and Militello, A., 1999. Hydraulic Study of Multiple Inlet System: East Matagorda Bay, Texas. *Journal of Hydraulic Engineering,* **125**(3): pp 224-232.

Lincoln, J. M. and FitzGerald, D. M., 1988. Tidal Distortions and Flood Dominance at Five Small Tidal Inlets in Southern Maine. *Marine Geology,* **82**: pp 133-148.

Liu, J. T., 1992. The Influence of Episodic Weather Events on Tidal Residual Currents: A Case Study at Sebastian Inlet, Florida. *Estuaries,* **15**(2): pp 109-121.

Liu, J. T. and Aubrey, D. G., 1993. Tidal Residual Currents and Sediment Transport through Multiple Tidal Inlets, in: D.G. Aubrey and G.S. Giese, Eds.: *Formation and Evolution of Multiple Tidal Inlets*. Coastal and Estuarine Studies, **44**. American Geophysical Union, Washington D.C.,

Mehta, A. J. and Hou, H. S., 1974. *Hydraulic Constants of Tidal Entrances*. Report, 23. Coastal Engineering Department. Gainesville, FL.

Mei, C. C., Liu, P. L.-F. and Ippen, A. T., 1974. Quadratic Loss and Scattering of Long Waves. *Journal of the Waterways, Harbors, and Coastal Engineering Division,* **100**(WW3): pp 217-239.

Nayak, I. V., 1971. *Tidal Prism-Area Relationship in a Model Inlet*. Technical Report, HEL 24-1. Hydraulic Engineering Laboratory, University of California at Berkeley. Berkeley, CA.

O'Brien, M. P., 1931. Estuarine Tidal Prism Related to Entrance Areas. *Civil Engineering,* **1**: pp 738-739.

O'Brien, M. P., 1966. Equilibrium Flow Areas of Inlets on Sandy Coasts. Proc. of the 10th Coastal Engineering Conference, **1**: pp 676-686.

O'Brien, M. P. and Dean, R. G., 1972. Hydraulics and Sedimentary Stability of Coastal Inlets. Proc. of the 13th Conference on Coastal Engineering, (Location?), ASCE., pp 761-780.

Pugh, D. T., 1987. Tides, Surges and Mean Sea Level, a Handbook for Engineers and Scientists. John Wiley & Sons.

Riedel, H. P. and Gourlay, M. R., 1980. Inlets/Estuaries Discharging into Sheltered Waters. Proc. of the 17th Coastal Engineering Conference, Sydney, Australia, ASCE., pp 2550-2564.

Schuttelaars, H. M., 1997. *Evolution and Stability Analysis of Bottom Patterns in a Tidal Embayment*. PhD thesis, Utrecht University.

Skou, A., 1990. *On the Geometry of Cross-Section Areas in Tidal Inlets*. Series Paper, 51. Institute of Hydrodynamics and Hydraulic Engineering, Technical University of Denmark. Lyngby, Denmark.

Skou, A. and Fredsøe, J., 1990. Prediction of the Dimensions of Tidal Inlets. Proc. of the Skagen Symposium, Skagen, Denmark, in: P. Bruun and N.K. Jacobsen, Eds.: Journal of Coastal Research, Special Issue No. 9, pp 894-910.

Speer, P. E. and Aubrey, D. G., 1985. A Study of Non-Linear Tidal Propagation in Shallow Inlet/Estuarine Systems. Part 2: Theory. *Estuarine, Coastal and Shelf Science,* **21**: pp 207-224.

Speer, P. E., Aubrey, D. G. and Friedrichs, C. T., 1991. Nonlinear Hydrodynamics of Shallow Tidal Inlet/Bay Systems, in: B.B. Parker, Ed.: *Tidal Hydrodynamics*. John Wiley & Sons, Inc.,

Uncles, R. J., 1981. A Note on Tidal Asymmetry in the Severn Estuary. *Estuarine, Coastal and Shelf Science,* **13**: pp 419-432.

van de Kreeke, J., 1976. Increasing the Mean Current in Coastal Channels. *Journal of the Waterways, Harbors, and Coastal Engineering Division,* **102**(WW2): pp 223-234.

van de Kreeke, J., 1984. Stability of Multiple Inlets. Proc. of the 19th Coastal Engineering Conference, (Location?), pp 1360-1370.

van de Kreeke, J., 1985. Stability of Tidal Inlets - Pass Cavallo, Texas. *Estuarine, Coastal and Shelf Science,* **21**: pp 33-43.

van de Kreeke, J., 1988. Hydrodynamics of Tidal Inlets, in: D.G. Aubrey and L. Weishar, Eds.: *Hydrodynamics and Sediment Dynamics of Tidal Inlets.* Lecture Notes on Coastal and Estuarine Studies., **29**. Springer-Verlag, New York, pp 1-23.

van de Kreeke, J., 1990. Can Multiple Tidal Inlets Be Stable? *Estuarine, Coastal and Shelf Science,* **30**: pp 261-273.

van de Kreeke, J., 1992. Stability of Tidal Inlets; Escoffier Analysis. *Shore and Beach,* ----------: pp 9-12.

van de Kreeke, J., 1996. Adaptation of the Frisian Inlet to a Reduction in Basin Area with Special Reference to the Cross-Sectional Area of the Inlet Channel. Proc. of the Physics of Estuaries and Coastal Seas (PECS) 1996,

van de Kreeke, J. and Chiu, S. S., 1980. Tide-Induced Residual Flow, in: J.S.a.K.-P. Holz, Ed.: *Mathematical Modelling of Estuarine Physics*. Lecture Notes on Coastal and Estuarine Studies, **1**. Springer-Verlag, pp 133-144.

van de Kreeke, J. and Haring, J., 1980. Stability of Estuary Mouths in the Rhine-Meuse Delta. Proc. of the 17th Coastal Engineering Conference, Sydney, Australia, ASCE., pp 2627-2639.

van de Kreeke, J. and Robaczewska, K., 1993. Tide-Induced Residual Transport of Coarse Sediment; Application to the Ems Estuary. *Netherlands Journal of Sea Research,* **31**(3): pp 209-220.

van Dongeren, A. R. and de Vriend, H. J., 1994. A Model of Morphological Behavior of Tidal Basins. *Coastal Engineering,* **22**: pp 287-310.

Wang, Z. B., Louters, T. and de Vriend, H. J., 1995. Morphodynamic Modelling for a Tidal Inlet in the Waden Sea. *Marine Geology,* **126**: pp 289-300.

Yassuda, E. A. and Sheng, Y. P., 1994. Use of Three Dimensional Hydrodynamics Model for Tidal Inlet Studies. Proc. of the 24th Coastal Engineering Conference, pp 3432-3446.

Zimmerman, J. T. F., 1978. Topographic Generation of Residual Circulation by Oscillatory (Tidal) Currents. *Geophysical and Astrophysical Fluid Dynamics,* **11**: pp 35-47.

Zimmerman, J. T. F., 1980. Dynamics, Diffusion and Geomorphological Significance of Tidal Residual Eddies. *Nature,* **290**: pp 549-555.

Chapter 3

Historical Data Analysis of the Ría Formosa Lagoon

The Ría Formosa lagoon is a barrier island system that has maintained multiple inlets on a historical time scale. This chapter synthesizes the evolution of the coastline, in particular the inlets and the barrier islands in the Ría Formosa region, to clarify the response of the system to natural and artificial alterations of the general configuration of the various features, and the capacity of the system to maintain these multiple inlets.

An overview of the general characteristics of the system, as well as the possible sequence of events that originated it, are presented in section 3.1. The analysis of the inlet and barrier evolution is based on various materials: 13 old charts dating from the 14th century to the mid-19th century, 7 series of recent charts (from 1870 to 1978), 4 sets of aerial photographs (1978, 1985, 1989, 1991), and a set of orthophotomaps (1991). Results from previous studies also assisted in the analysis. Given the differences in the quality and reliability of each type of material, the information extracted is not homogeneous. Therefore, the study is divided in (a) historical evolution, based on ancient documents and charts (section 3.2), and (b) recent evolution, supported by the recent maps and aerial photographs (section 3.3).

3.1. General Characteristics of the Site

3.1.1. Location and Physical characteristics

The Ría Formosa system is located in the extreme south of Portugal, in the Province of Algarve (Figure 3-1), adjacent to a cliffed coast of moderate relief. This natural coastal system consists of a large tidal lagoon (50 km in length) with an approximate surface area of 111 km^2 and a maximum width of 6 km opposite to Faro. It is presently bounded on the seaward side by 5 barrier islands: Barreta (8 km long), Culatra (6.5 km), Armona (8 km), Tavira (10.5 km) and Cabanas (4.5 km) and by two shore-attached barriers at the extremities: Ancão (10 km) and Cacela (6 km) (Bettencourt, 1988). Six inlets link the lagoon with the ocean: New Ancão Inlet (also referred in this study as New Inlet), which was opened artificially in 1997 to improve the exchange of water between the western end of the lagoon and the ocean; Faro Inlet (also referred as Main Inlet), Armona Inlet, Fuzeta Inlet, Tavira Inlet, and Cabanas (or Cacela) Inlet. All the inlets are free to migrate and evolve naturally, except the Faro (or Main) Inlet and Tavira Inlet, which are stabilized with jetties.

The Ría Formosa region, in particular the lagoon coast, is almost continuously urbanized (2,000 habitants per square kilometer),Faro, Olhão and Tavira being the bigger towns. The region is an important center of economic activity. Tourism is the first source of revenue for the region, and is responsible for a significant increase in population during summer. In addition, agriculture, fishing and traditional micro-industry are well developed. Olhão is the most important fishing port in the south of Portugal (the second in Portugal), and Faro is the most important commercial port in Algarve. Aquaculture is well developed, representing 80% of the national shellfish production. In spite of this active economy and relatively large population density, the region is not significantly polluted (Freire de A., 1990b). The lagoon and the barrier islands constitute a rich natural ecosystem, protected under the status of Natural Park.

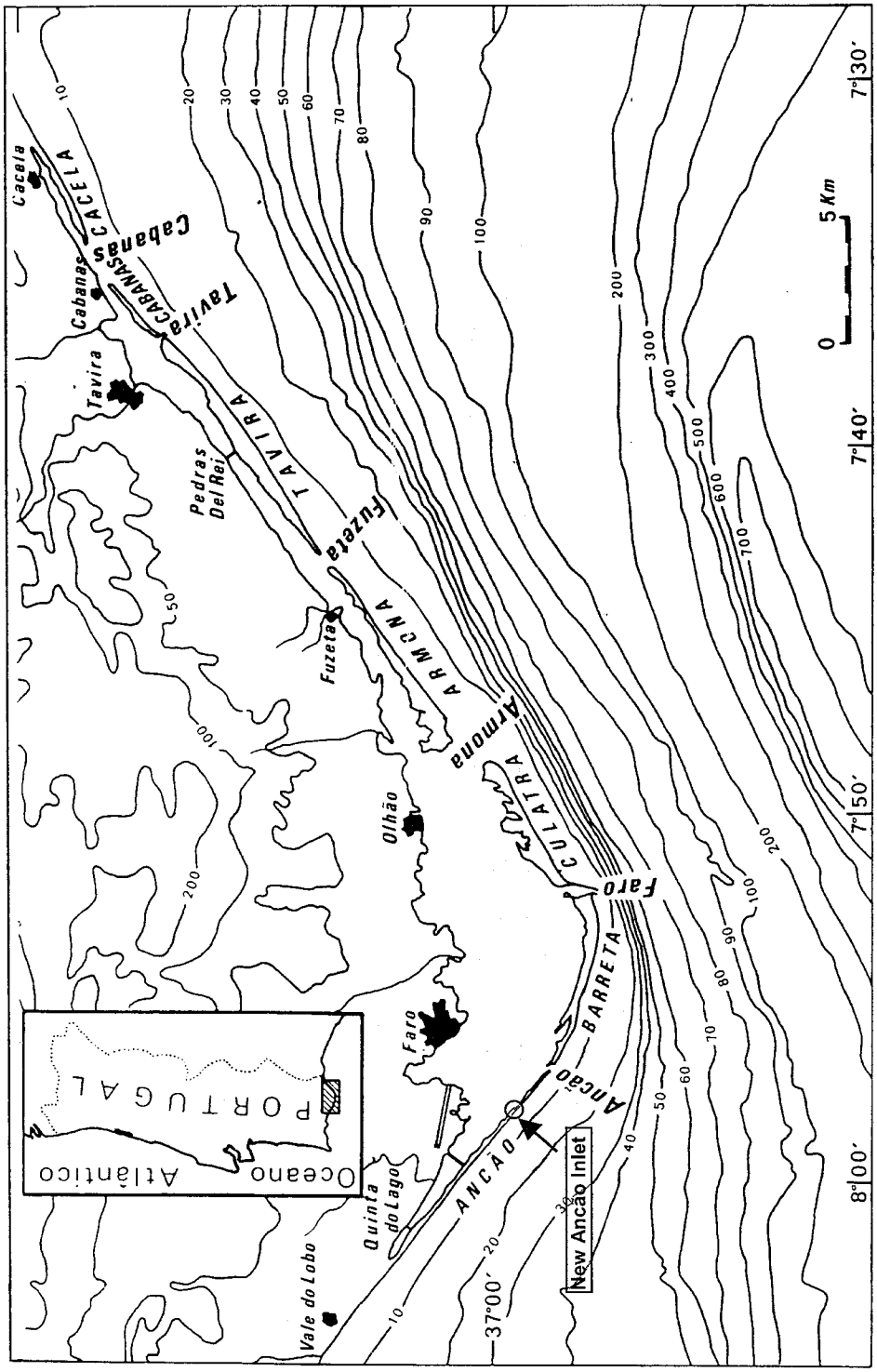

Figure 3-1. Location Map of the Ría Formosa System (after Dias, 1988), with approximate location of the New (Ancão) Inlet (offshore bathymetry in meters).

The embayment is characterized by i) large salt marsh areas with a high density of shallow meanders, largely composed by silt and fine sand (Bettencourt, 1988), ii) large sand flats (overwash fans, incorporated recurved spits, and incorporated flood tidal deltas) partially flooded and reworked during spring tides (Pilkey *et al.*, 1989), and iii) by a complex net of natural and partially-dredged channels throughout the lagoon, which narrow and shoal in the upper regions of the system . Figure 3-2 shows an example of this complexity, where a section of the main channel from the Main (Faro) Inlet to the Faro Port and Marina, as well as secondary channels, and intertidal vegetated flats can be seen.

Figure 3-2. Selected aerial photograph showing the complexity of the system.

Bettencourt (1994), who estimated the tidal flats and salt marshes to represent more than $^2/_3$ of the total area of the lagoon, subdivided the intertidal zone into four areas according to their elevation:

a) Low stage (-1.5 to -0.5 m relative to Mean Sea Level): this area represents roughly 15% of the surface of the lagoon, and is occupied almost solely by *Zoostera noltii*. It covers the mudflats and the low tidal flats, the bottom of the secondary channels and the margins of the main channels. These plants play an important role in the retention of sediments, accelerating the accretion in the channels and the progressive increase in elevation of the tidal flats.

b) Intermediate stage (-0.5 to 0.5 m relative to MSL): This sector is formed by large tidal flats ranging from silty to sandy texture. It occupies around 30% of the area of the lagoon and is characterized by a gradual replacement of the *Zoostera noltii* (low stage) by *Spartina maritima*, which becomes the dominant species around the salicornia salt marshes (transition stage).

c) Transition stage (0.5 to 1.0 m relative to MSL): this zone corresponds to approximately 20% of the surface of the lagoon and is characterized by a gradual substitution of the *Spartina maritima* population by a salicornia, the *Arthrocnemun perrene*. These salt marshes occupy a transition zone between the tidal flats and higher areas that rarely wet.

d) high stage (1.0 to 1.5 m relative to MSL): this stage corresponds to the higher salt marshes and is characterized by the presence of salicornia species (*Arthrocnemun perrene* and *Arthrocnemun pruticosum*). It surface is less than 5% of the surface of the lagoon.

Climatic Framework

The history of the hydrologic evolution of the system is not well documented. However, some ruins dating from the Roman occupation suggest that the Seco River (between Faro and Olhão) was navigable, implying that the fresh water input to the system was larger. At present, the Faro region is a semi-arid region with small fluctuations in air temperature (17°C average temperature, ranging from 11°C in winter to 24°C in summer). The yearly average precipitation ranges from 480 mm in Faro to 580 mm in Tavira. The catchment area of the Ría Formosa system has an area of approximately 740 km^2, and an estimated effective precipitation (precipitation – evapotranspiration) of 152 mm/year, which represents a volume of $112 \cdot 10^6$ m^3/year. Considering

infiltration, the surface runoff has been estimated to be of the order of $70 \cdot 10^6$ m^3/year ($\cong 2.2$ $m^3.s^{-1}$ on average),. Although this value is negligible compared to the tidal driven flows, acute precipitation events may result in significant fresh-water and sediment input into the system, with potential strong long-term effects in the system morphology.

Analysis of 15 years (1971 to 1985) of wind data performed by Freire (1990a) showed that the wind is on average moderate (3 $m.s^{-1}$) and predominantly from the west. This regime is sometimes interrupted by stronger south-easterly and south-westerly winds (see below), which affect the wave climate and the longshore sediment transport along the Algarve coast.

Oceanographic Framework

The area in the vicinity of Faro has an open ocean coast whose wave climate is characterized by dominant smooth and moderate sea states, and by the occurrence of two different types of storms – from SW and from SE – that generate sea states with different wave characteristics.

Most of the time the waves are mainly generated by local winds, associated with the local sea-land breeze system. The largest storms are from South-West, occur mainly during winter, and are associated with atmospheric low pressure centers in the south-eastern region of the North-Atlantic Ocean. The south-easterly storms can occur in all seasons, when a strong "Levante" (strong Mediterranean easterly wind) is blowing in the Gibraltar Strait, producing waves that reach the coast of Algarve as an almost unidirectional swell.

Wave heights are in the range 1-4 m and wave periods in the range 6-13 seconds, with fair-weather wave height typically less than 1 meter. The mean direction from which waves come is 227° (west and southwest directions represent 67% of occurrences). The results from wave measurements performed offshore Faro (water depth = 80 m) during the period 1976-1984 (Oliveira Pires, 1998) are summarized in Table 3-1 and Table 3-2.

The tide in Ría Formosa is semi-diurnal (see section 4.4.4). The mean tidal range is approximately 2.1 m and the spring and neap ranges are 3.1 and 1.3 m, respectively. The equinoctial spring tides can reach 3.8 m.

Table 3-1 Significant wave height and mean period at Faro (from Oliveira Pires, 1998)

	Mean	Maximum	Minimum	Standard Deviation
Significant wave height (m)	0.92	4.93	0.14	0.56
Mean period (s)	6.30	13.30	4.00	1.50

Table 3-2 Probability of occurrence (%) of wave mean direction at Faro Buoy (from Oliveira Pires, 1998)

NE	E	SE	S	SW	W	NW	N
0.5	4.2	25	2.1	16.3	51.5	0.3	0.1

Morphodynamic and Sediment Transport Framework

The general shape and morphologic evolution of the barrier island chain result from (1) the geological origin and evolution of the system, and its response to relative sea-level rise, on time scales of thousands of years, (2) the exposure to different wave and current conditions on each side of the chain (southwest- and southeast-facing sides), on time scales of years, and (3) from the effects of storms and the subsequent adaptation processes, on time scales of weeks. According to Pilkey *et al.* (1989), the major processes of barrier evolution are: shoreline retreat, longshore drift, overwash, vegetated dune formation, tidal delta incorporation, inlet migration, and erosion of the back-barrier regions of the islands by spring tides.

The net direction of the longshore current is west to east, because of the prevailing local winds in that direction, as well as a response to the waves generated over the large fetch of the open Atlantic Ocean to the west. However, during short periods (a few days several times each year) the current direction is reversed, due to strong southeasterly winds (the so-called "Levante" events).

The coastline west of the Ría Formosa system is characterized by 5-50 m high cliffs cut into poorly consolidated Pliocene-Pleistocene sediments. Abundant sediment supply to the islands is derived principally from the erosion of the cliffs located updrift from Ría Formosa. The rates of cliff erosion have been estimated to range from a few meters to up to 15 meters per year. The construction of coastal structures in that area has resulted ultimately in increased rates of

coastal retreat (Correia *et al.*, 1996). However, studies of the sand budgets in and out of the island chain suggest that the inner continental shelf is another important source of sediments (Freire de A., 1990b). In addition, on the other side of the system, the Guadiana River (along the border between Portugal and Spain, whose mouth is approximately 15 km east of Cacela) represents also a source of sediment to the Ría Formosa system, in periods where the littoral drift is westward. The supply from the river is characterized by finer material (silt and fine sands), resulting in smaller grain size distribution along the eastern part of the system. A comprehensive study of the sedimentary environments in Ría Formosa and the adjacent areas can be found in Bettencourt (1994).

According to Hayes' (1979) classification of morphological features in costal-plain environments, the Ría Formosa system lies in the upper tidal range limit for the existence of barrier islands, (Figure 3-3). This may be related to the fact that the system is not located in a coastal plain in the strict sense, since the lagoon is adjacent to a cliffed coast providing large amounts of sediment for the formation of the barrier islands. Moreover, the curved shape of the Ría Formosa system, similar to the configuration encountered in Cape Haterras, does not fall in the general classification, which suggests that inlet-barrier systems occur usually in linear coastlines.

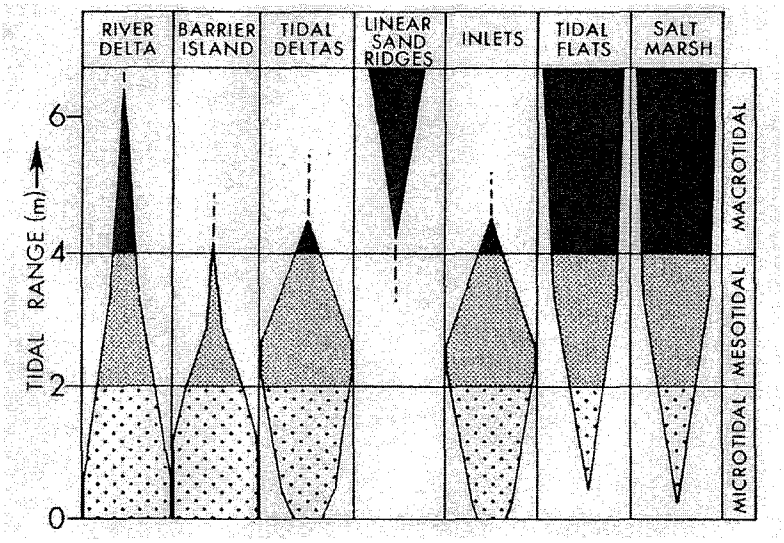

Figure 3-3. Variation of morphology of coastal plain shorelines with respect to mean tidal range (from Hayes, 1979).

3.1.2. Origin of the Ría Formosa system

Several different theories about the origin of the system have been proposed since the early 1900s (Bettencourt, 1994). For instance, some authors suggest the formation of the barrier islands due to a strong transgression (Dunkerquian transgression; see Aubouin *et al.*, 1981) that occurred around 2,000 B.P., followed by a regression. However, there is only evidence that this transgression happened in localized areas in Europe (e.g., Emery and Aubrey, 1991; García-Gil *et al.*, 1999), and there is no proof that it took place in the Algarve Coast. Moreover, it has been estimated that this transgression was of the order of 2 m, which is not considered sufficient for the formation of Ría Formosa (Bettencourt, 1994). Another study explains the formation and the shape of the barrier system with the "cuspate foreland" model (Swift, 1976), i.e., the transformation of a delta into a cape due to the convergence of the littoral drift coming, in this case, from west and east. This theory seems also unlikely given (a) the predominance of the easterly littoral drift, and (b) the lack of an important river (and delta) in the Ría Formosa region.

The geological evolution of the system has been studied previously by Dias (1988) and by Pilkey *et al.* (1989), who suggested an explanation for the formation of the barrier islands. Following Hoyt's (1967) model, they suggested that the origin of the islands is related to the changes in sea level during and after the glacial period, as in previous models (Bettencourt, 1994). In addition, they suggested that the shape of the system is related to the angular shape of the bathymetry offshore (see Figure 3-1). The hypothesized sequence of events leading to the formation of the barrier island system is shown in Figure 3-4 (A, B, C, and D). When the sea level was close to the continental shelf break, the shoreline started retreating and beach-ridges formed parallel to the coast (A). The progressive sea-level rise flooded the areas between the ridges and the continent, forming spits and barrier islands, which in turn suffered transgression, leading to an onshore migration across the continental shelf (B and C). Furthermore, based on Hoyt's model and on the bathymetry of the continental shelf in the eastern Algarve, Monteiro *et al.* (1984) suggested a migration pattern to explain the geometrical form of the barrier island system. In front of the Santa Maria Cape (the southern tip of Barreta Island), the continental shelf has a steeper slope than in the eastern and western parts of the system (see Figure 3-1). Consequently, given that the rate of migration is inversely proportional to the slope of the continental shelf (Dias, 1988), the onshore migration rate in front of the cape has been low, and the sides have experienced a higher onshore mobility, explaining the v-shape of the barrier island system (D).

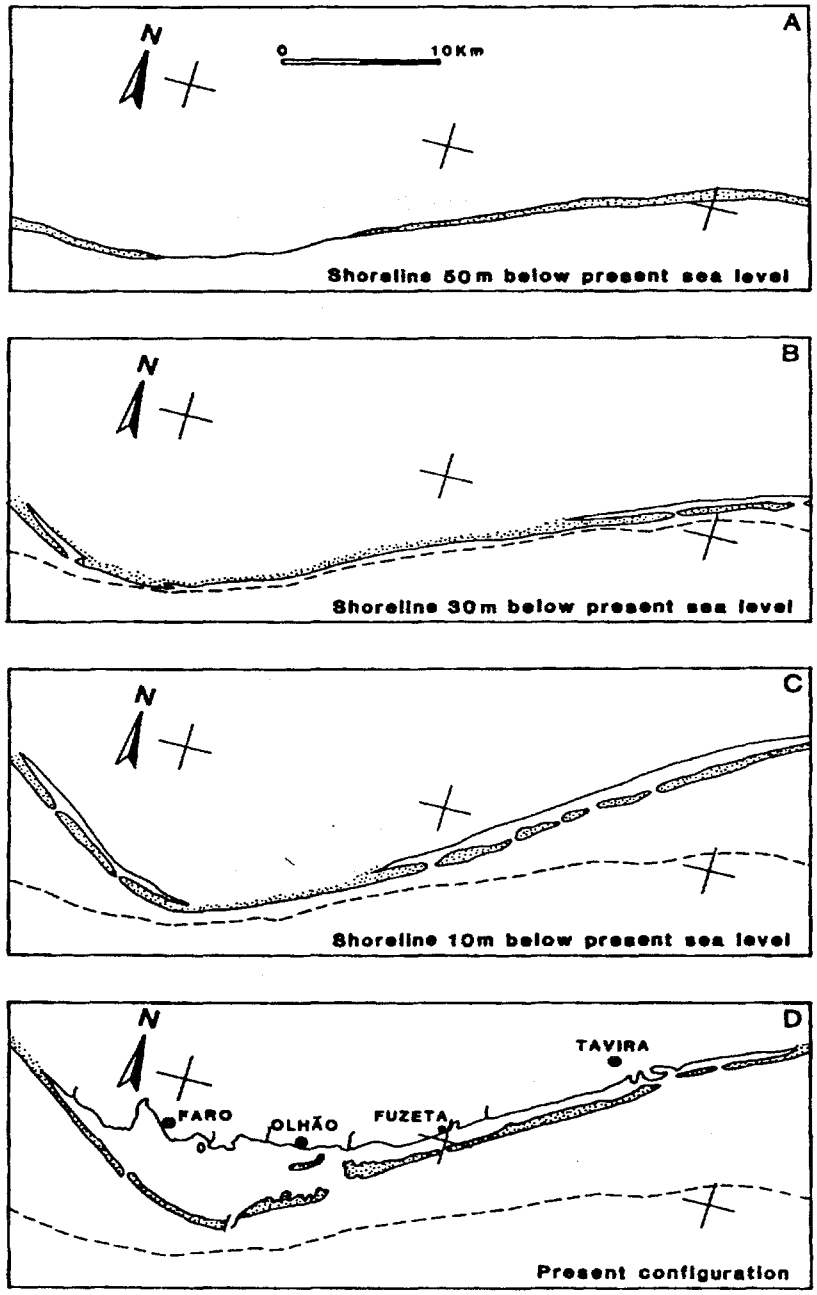

Figure 3-4. Hypothesized sequence of the Ría Formosa formation (from Pilkey *et al.*, 1989). The dashed reference line represents the isobath at 50m below present sea level.

3.2. Historical evolution

Although it is difficult, if not impossible, to reconstruct rigorously the evolution of a given coastline since historical times, the observation and comparison of old charts assisted to determine qualitatively the evolution of the large-scale features of the system (shape and orientation, number of inlets, existence of shore-attached barriers). Copies of old charts were acquired from the National Library in Lisbon, and consist of 10 maps having different degrees of detail in the drawing of the various features. The maps were transferred to electronic format using a large format drum scanner in the Computer Resources Laboratory of the Department of Urban Studies and Planning at MIT. In addition, four maps from Bettencourt (1994) are included.

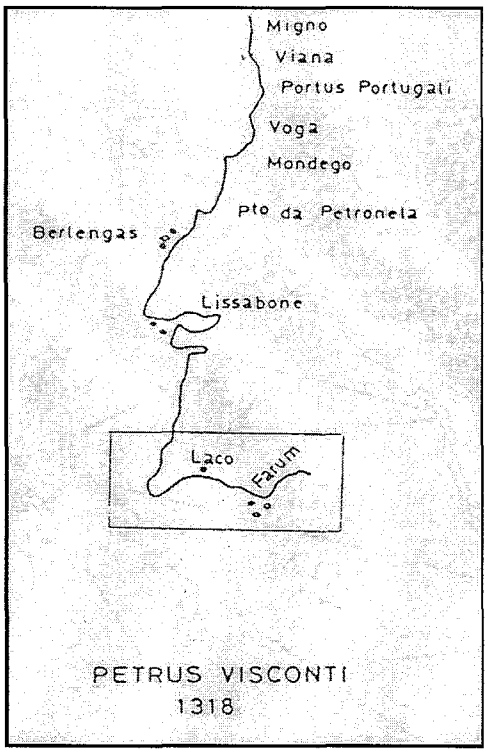

Figure 3-5. Historical chart of the Portuguese Coast, by Petrus Visconti, 1318 (from Bettencourt, 1994)

The first map known of the area (Figure 3-5), is dated on 1318 (from Bettencourt, 1994), and shows schematically the existence of the barrier islands and the angular shape of the system.

Important modifications occurred in the system throughout the period analyzed. The following observations can be made from the chart and documents consulted:

1) The existence of vast sand bodies and lagoons is confirmed since the Roman occupation, around 200 B.C. (Bettencourt, 1994). The author also mentions the infilling of the lagoons as the most cited morphological process in the historical references he consulted (from the 10th to the 18th century), as opposed to the more recent coastal erosion problems. For instance, as mentioned in section 3.1.1, there is evidence from Roman ruins that the Seco River (East of Faro; see Figure 3-18 for location) was navigable, suggesting deeper channels in the upper areas of the lagoon. Another example is the port of Farrobilhas (west of Faro, Figure 3-6), which was abandoned in the early 18th century because of infilling of its channels and the welding of the westernmost barrier island into the mainland.

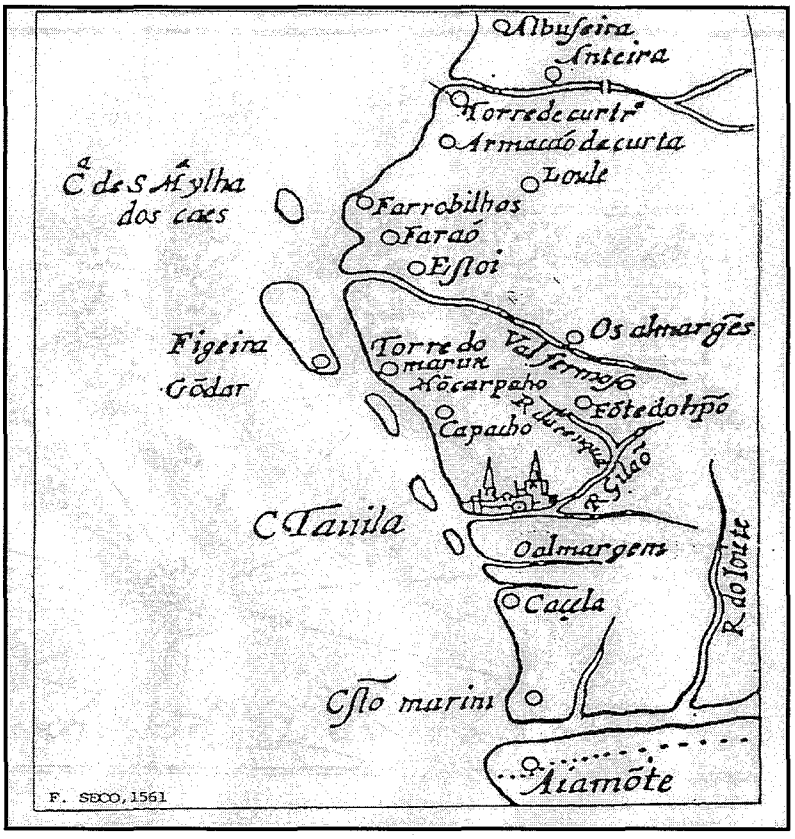

Figure 3-6. Historical chart of the Algarve Coast. Chart from Fernando Alvares Seco, 1561 (from Bettencourt, 1994). The author shows poorly developed barrier islands and the inlets (6) appear to be wide. No shore attached barriers are present.

2) The barrier system experienced a phase of enlargement in the East-West direction until the mid 18th century (see Figure 3-6 to Figure 3-8), with the formation of barrier islands extending from west of Faro to the Guadiana River mouth. The shore-attached barriers do not seem to have developed by that time.

A catastrophic earthquake occurred on November 1st, 1755, in the south of Portugal, accompanied by a large tsunami (estimated 15 m high) that modified significantly the configuration of the Algarve Coast, in particular the Ría Formosa system. The barrier islands were overwashed and reworked (Bettencourt, 1994). The large number of charts produced during the second half of the 18th century, after the earthquake, evidence the interest to have frequent updates of the Algarve Coast in that period, and suggests that this extreme event was the single cause that started these rapid changes. The charts reflect these changes and the evolution of the system to a new configuration.

3) The middle panel in Figure 3-9 (dated on 1760) shows how the eastern barrier islands have disappeared after the 1755 earthquake. The easternmost inlet was near Tavira. The upper panel shows a narrow Fuzeta Inlet, and the lower panel shows Armona Inlet ("Barra Grande"), an inlet approximately in the location of the current Main Inlet ("Barra Nova"), and "Barreta", an inlet separating the newly formed Ancão peninsula from the westernmost barrier island, similar to the actual New Inlet. In spite of its simplicity, this chart shows long and narrow barrier islands to the west, similar to their present form, and is the first chart showing the existence of a barrier attached to the mainland to the west.

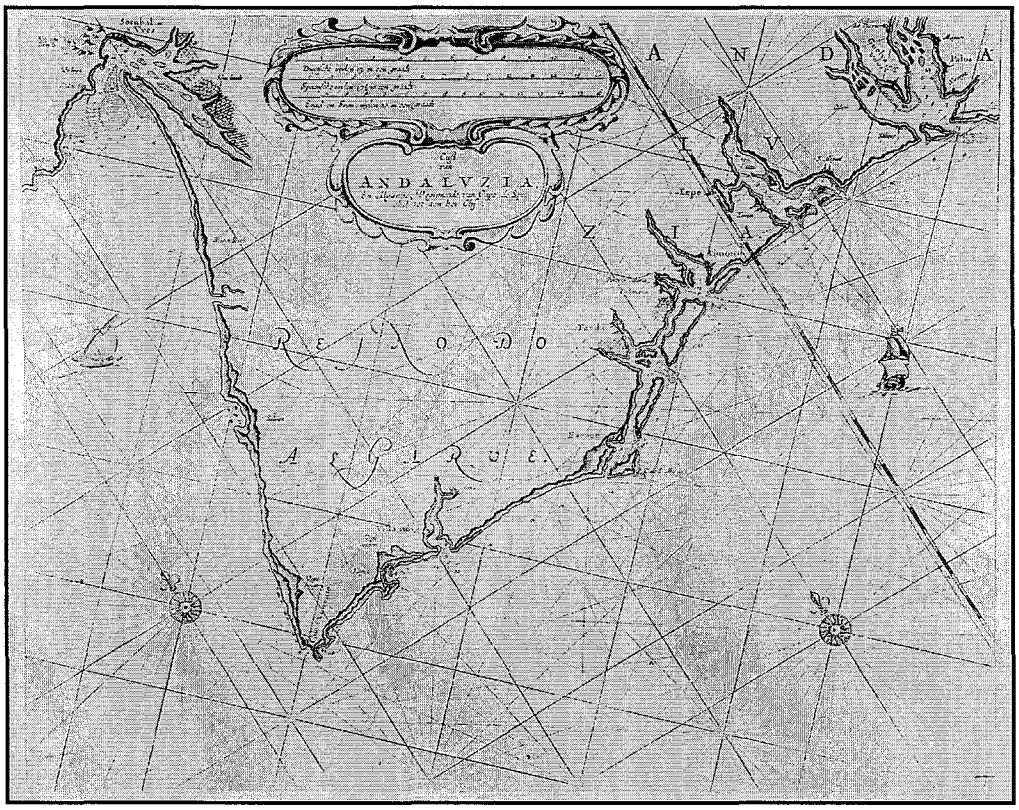

Figure 3-7. Historical chart of the Algarve Coast (unknown author, circa 1610). A large lagoon extends from the West of Faro to East of the Guadiana River Delta. The inlets appear narrower than in previous charts. No shore-attached barriers are present.

4) Figure 3-10 and Figure 3-11 (1762 and 1772, respectively) suggest that the barrier islands that extended from Cacela to the Guadiana River have disappeared, which is attributed to the 1755 Tsunami. In both maps, the westernmost barrier island extends almost to Quarteira, 15 km west of Faro. Figure 3-11 shows large sand banks in the western side of the Guadiana River mouth, where barrier islands existed before the Tsunami of 1755, suggesting that the

attachment of the barrier islands to the mainland through overwash and flattening. This resulted in the abandonment of the important port in Castro Marim (compare Figure 3-6, Figure 3-10, and Figure 3-13)

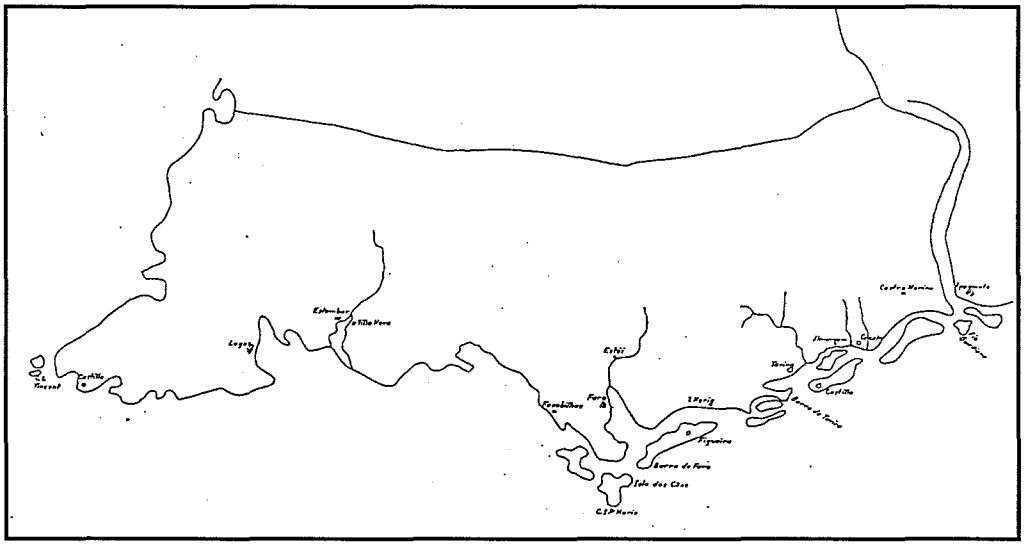

Figure 3-8. Historical chart of the Algarve Coast. Outline of a Chart by Robert, 1751 (from Bettencourt, 1994). The barrier islands extend past the Guadiana River to the east. Their complexity in shape may be due to the high mobility of the sand bodies in the system (low barriers and tidal flats), and in part attributed to cartographic imprecision. No shore-attached barriers are present.

5) Figure 3-12 and Figure 3-13 show maps dated on 1773, in which a shore-attached barrier at the western end of the system (Ancão peninsula) coincides with the modern configuration. In addition, a barrier island is shown in front of Cacela almost in contact with the mainland. Apparently, this barrier was not attached on its eastern end to the mainland, but may represent the early stage of the present-day Cacela shore-attached barrier island.

6) In Figure 3-14, which shows a map dated on 1792, the lagoon appears large and well defined. The angular shape of the system is more pronounced than in the previous maps. The western shore-attached barrier exists and the eastern barrier island ends between Tavira and Cacela.

7) Figure 3-15 and Figure 3-16 (1795 and 1798, respectively) are simple drawings of the Algarvian Coast. They both show a shore-attached barrier to the west which is longer in the second figure. Figure 3-16 also shows (i) a wide and angular Barreta barrier island, with which the cartographer apparently reproduced the v-shape of the system, and (ii) the easternmost lagoon barrier island attached to the mainland.

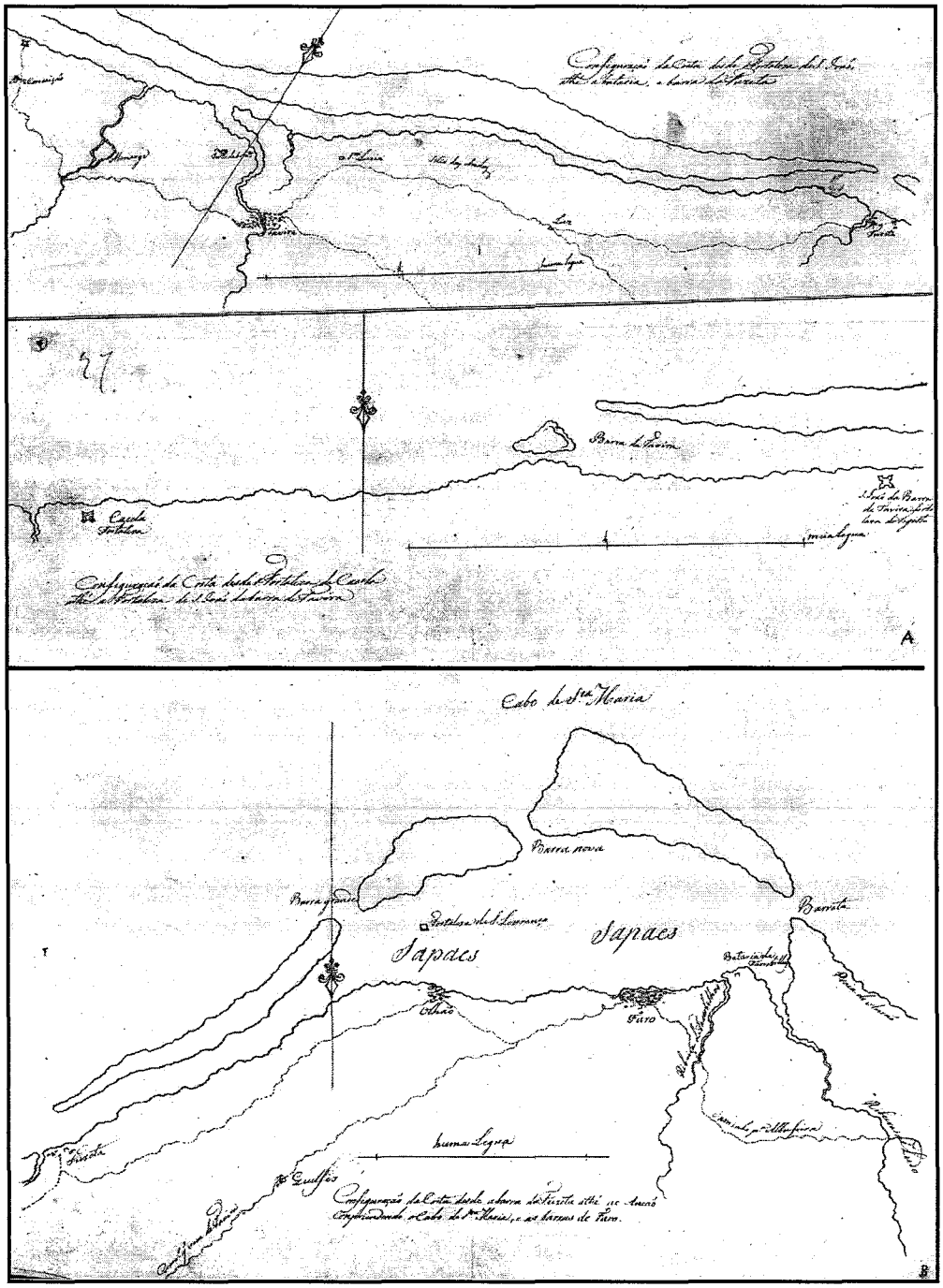

Figure 3-9. Historical chart of the Algarve Coast (no author, circa 1760). This chart is divided in three panels. The middle panel shows the easternmost area of the system, the upper panel represents the central part, and the lower panel shows the western side of the lagoon.

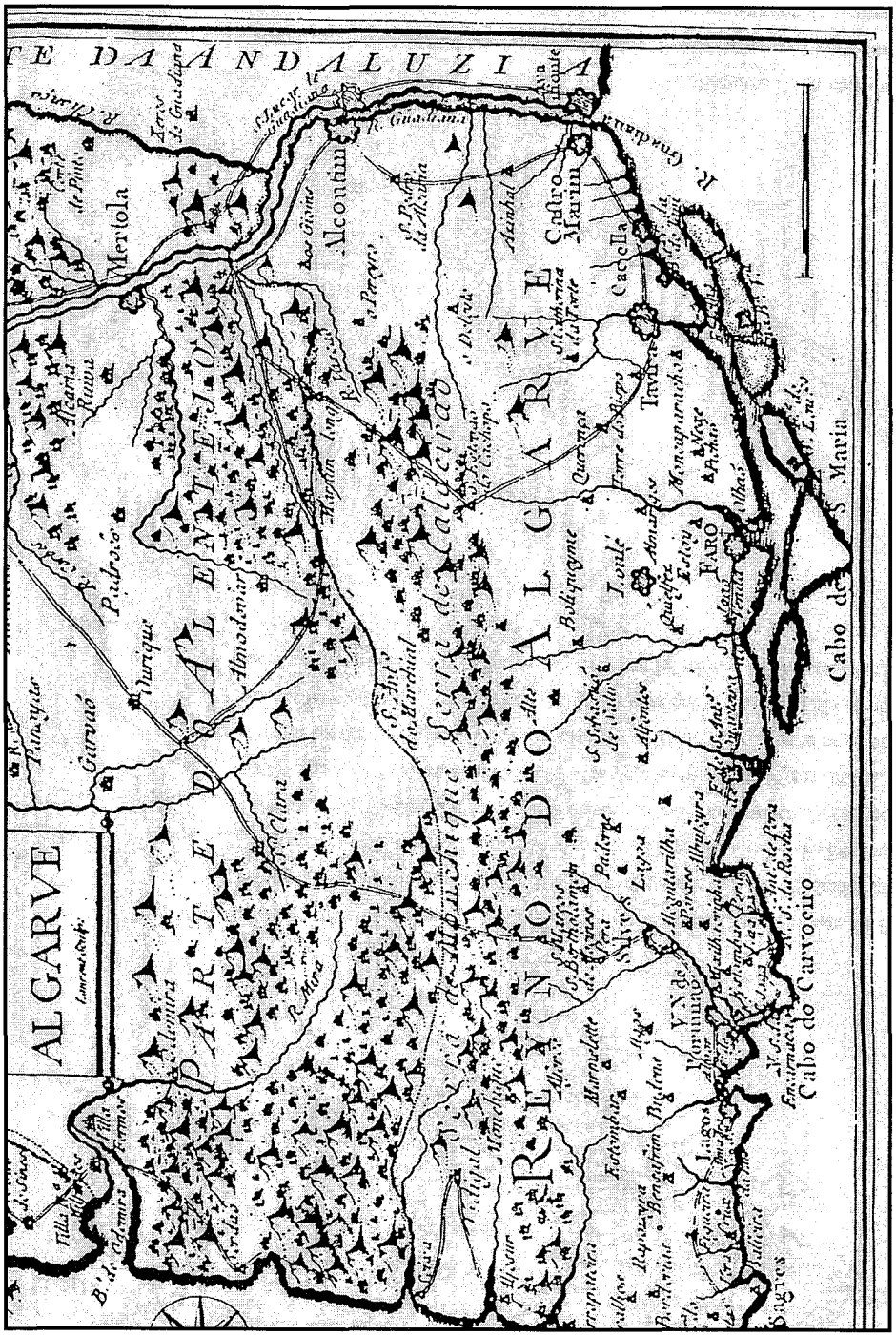

Figure 3-10. Historical chart of the Algarve Coast. Map (detail) of the Kingdom of Algarve, by Carpinetti in 1762 (from Bettencourt, 1994).

8) Figure 3-17 and Figure 3-18 show a map from 1842, which is considered the first modern map of the area. Details of the back-barrier shoals and intertidal areas are clear. Six inlets are

shown, including Barreta (in a location close to the actual New Inlet), Armona, Fuzeta and Cacela. Tavira and Faro (Main) inlets did not exist. Instead, the map shows an inlet west of Armona ("Barra Nova") and an inlet between the towns of Tavira and Cacela.

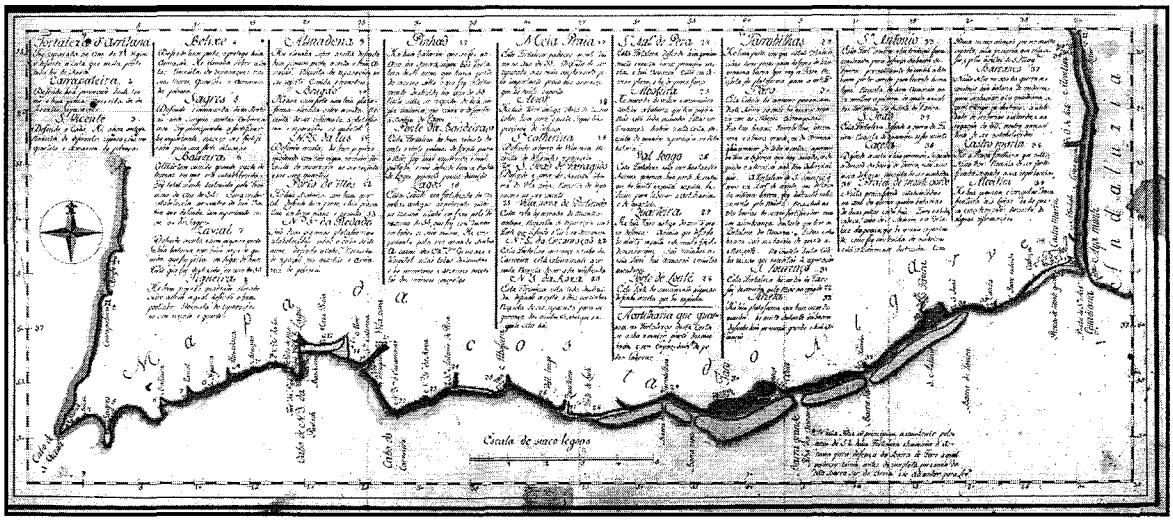

Figure 3-11. Historical chart of the Algarve Coast by J. Vasconcellos (1772). The map shows five barrier islands and no shore attached barriers.

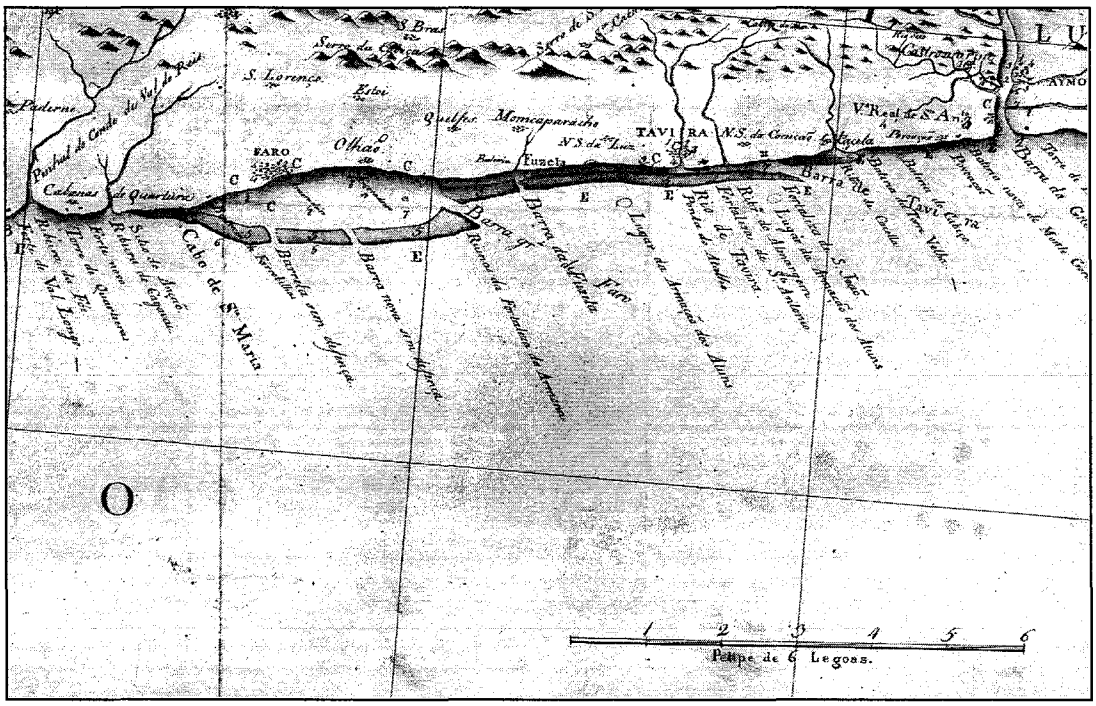

Figure 3-12. Historical chart of the Algarve Coast (no author, circa 1783). The map shows a shore-attached barrier along the western end of the Ría and a barrier in front of Cacela.

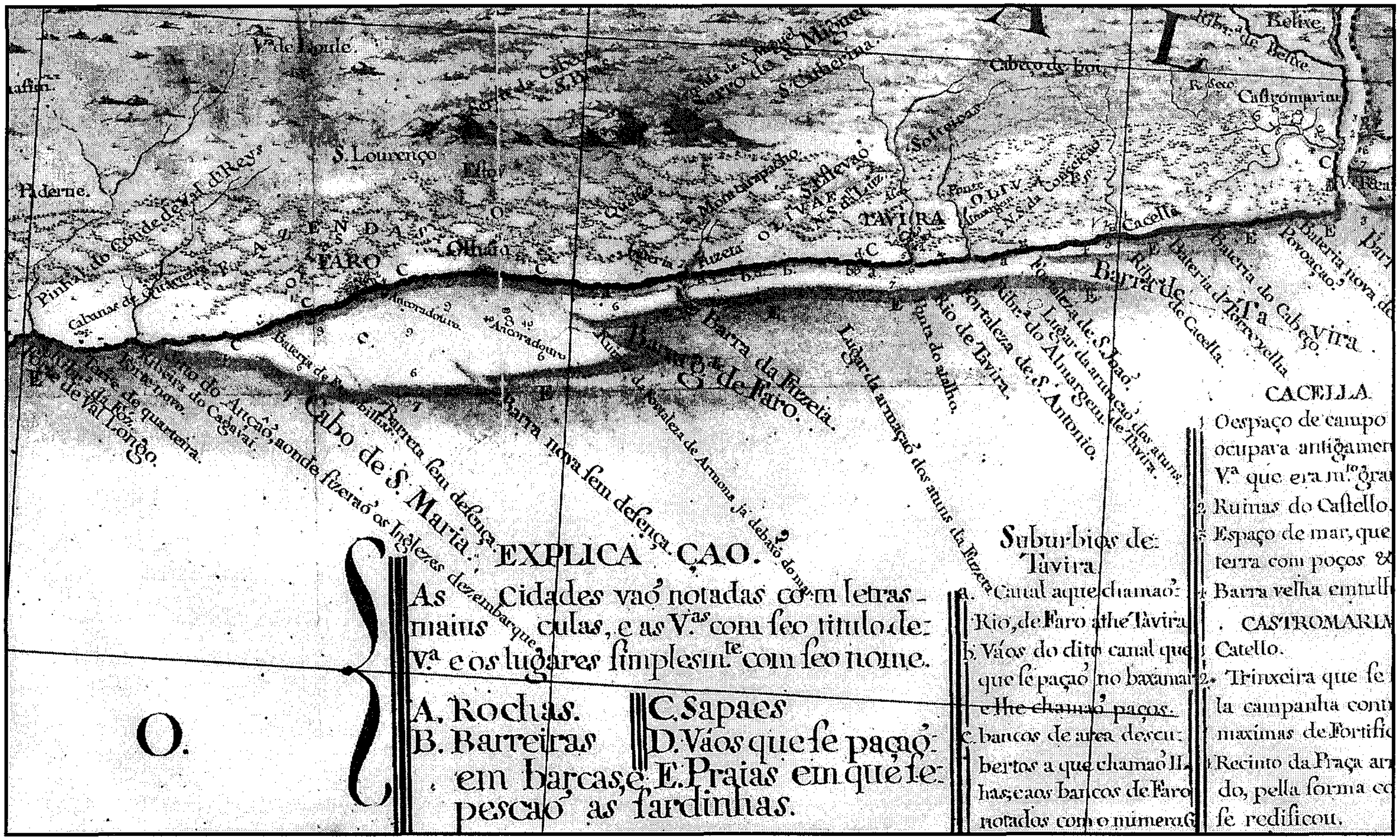

Figure 3-13. Historical chart of the Algarve Coast. Map of the Kingdom of Algarve, by J. Vasconcelos (1783). This map is similar to that shown in Figure 3-12.

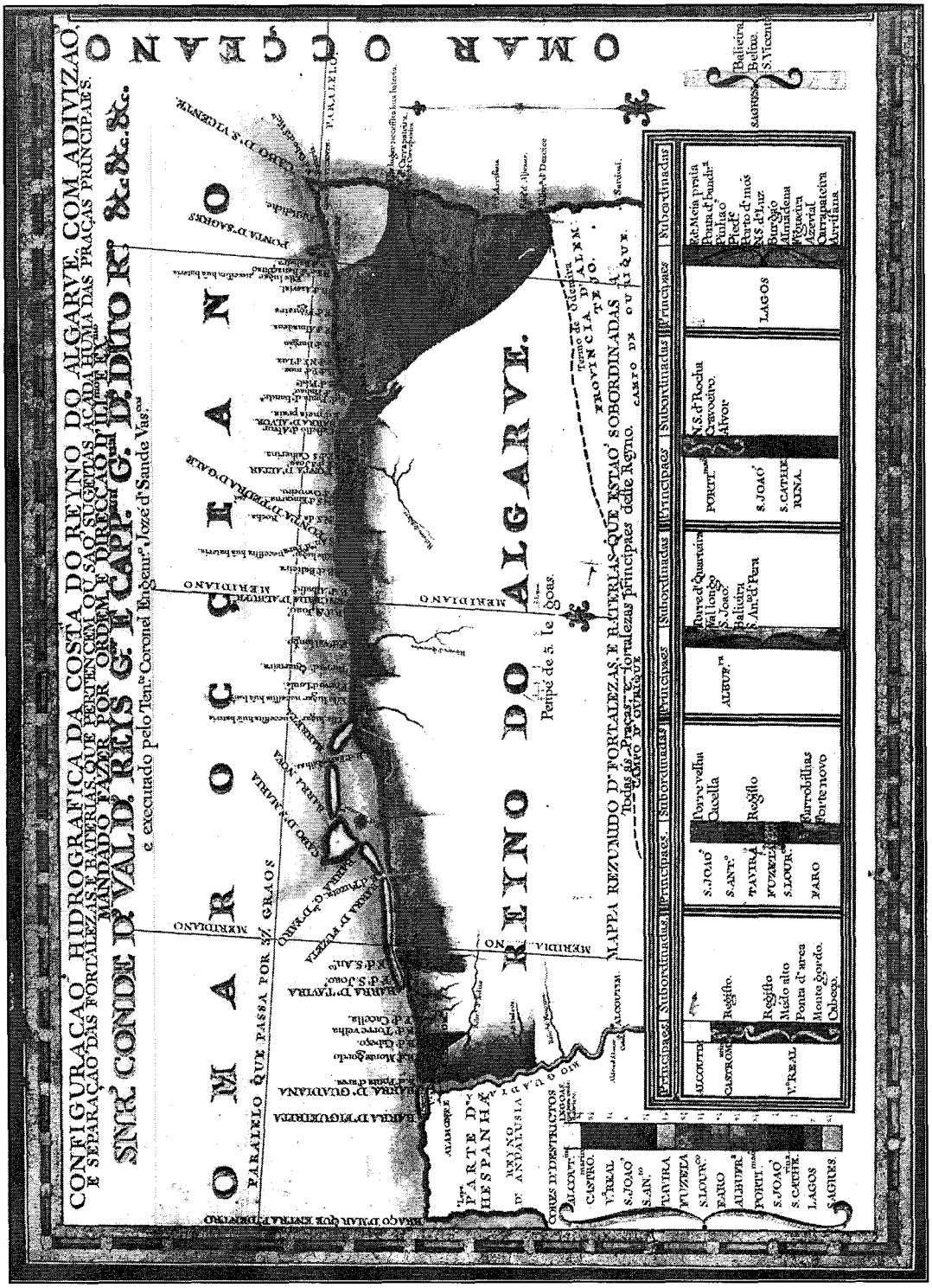

Figure 3-14. Historical chart of the Algarve Coast, by J. Vasconcellos (circa 1792). Five inlets, four barrier islands, and one shore-attached barrier are shown.

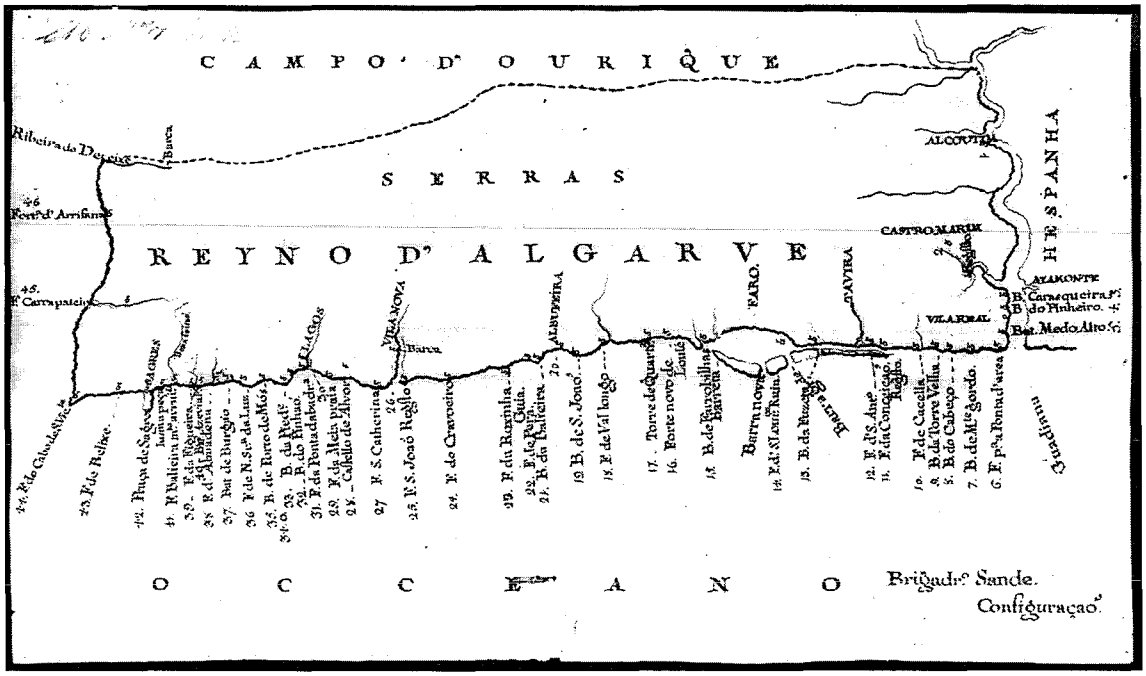

Figure 3-15. Historical chart of the Algarve Coast, by Brig. Sande (1795). The shore-attached barrier to the west appears smaller than in previous maps. No shore-attached barrier to the east.

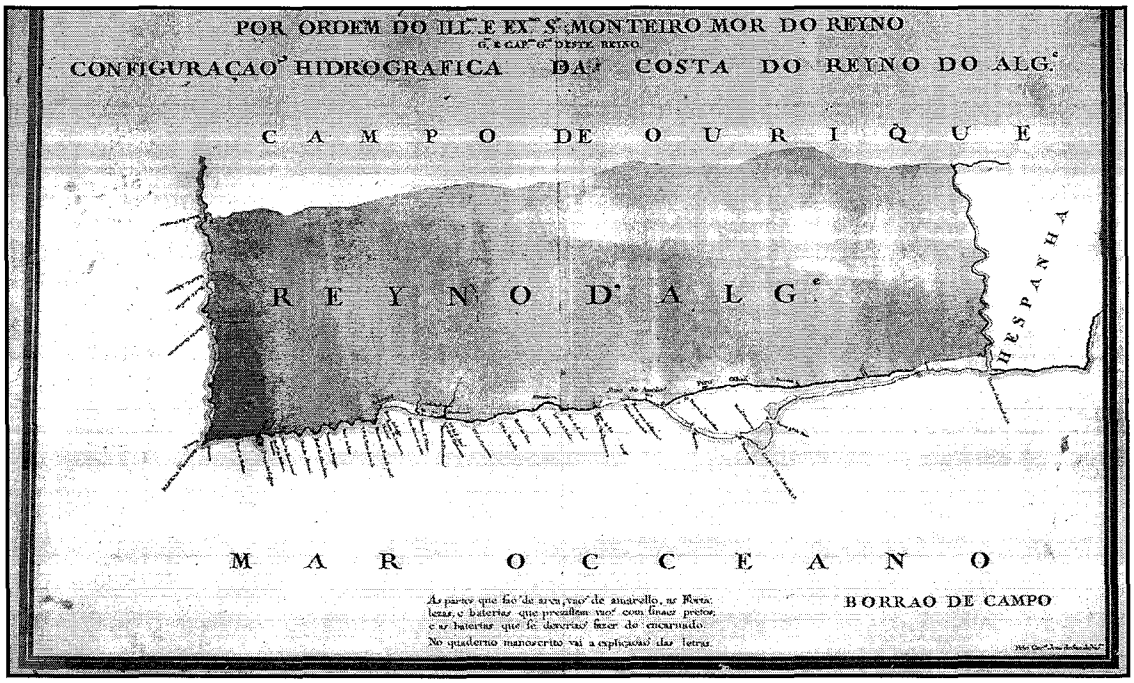

Figure 3-16. Historical chart of the Algarve Coast. Field draft by J. Vasconcellos (circa 1798). Similar map to the map shown in

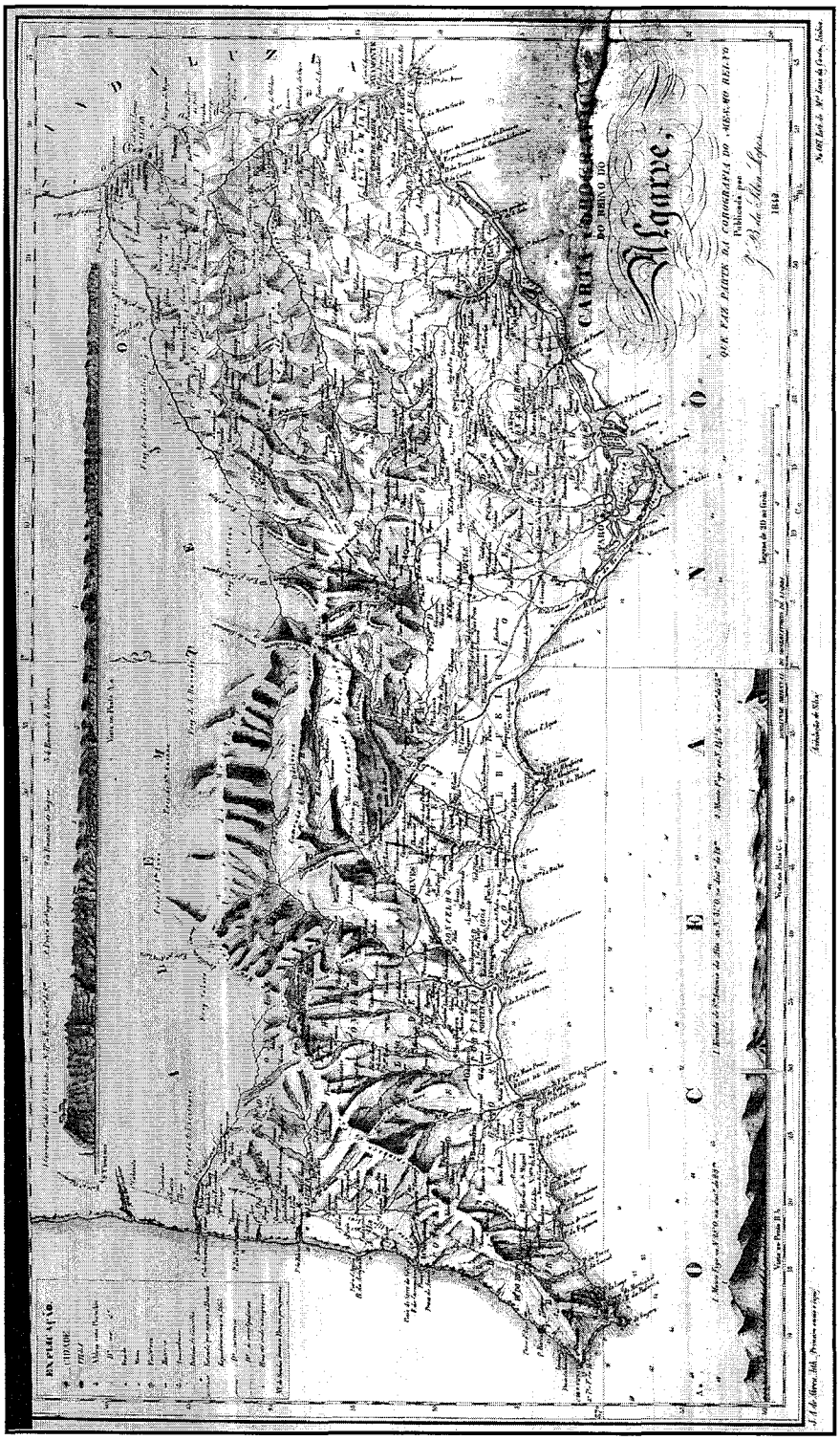

Figure 3-17. Historical chart of the Algarve Coast. Published by Silva Lopes in 1842. Very detailed map showing the Ría with a general configuration similar to the present. The detail of the barrier island area is shown in the next figure.

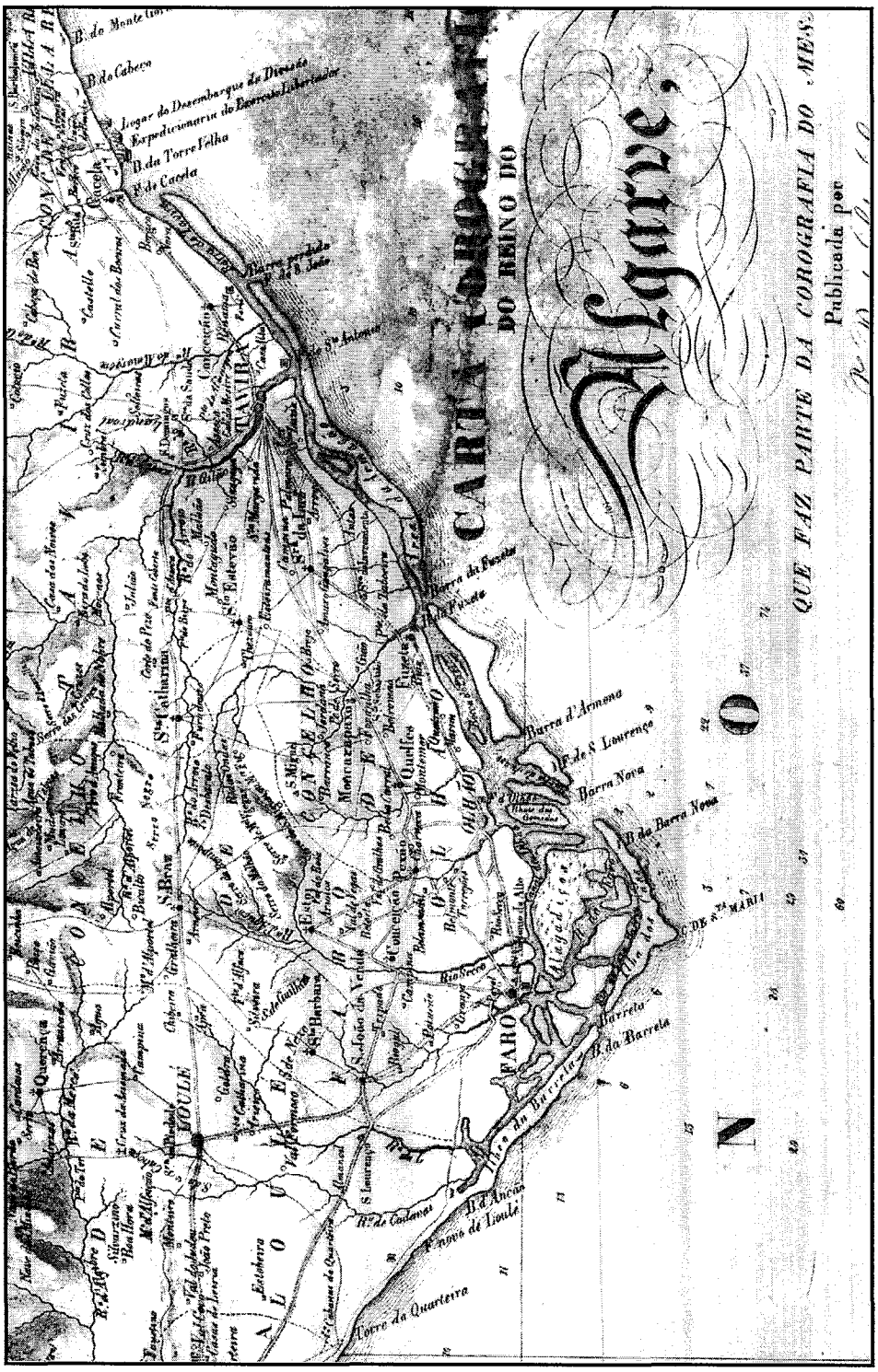

Figure 3-18. Historical chart of the Algarve Coast. Detail from previous map. The intertidal areas and tidal flats inside the lagoon are clearly shown. The number and position of inlets differs from the present configuration. No shore-attached barrier existed in front of Cacela.

In summary, the ancient cartography shows that the system maintained multiple inlets (from five-to-seven) between the 15th and the 18th centuries. Until the mid 18th century, the barrier island system exhibited a phase of expansion (extending east as far as the Guadiana River mouth), regression of the beaches, with abundant sediment supply shoaling and infilling the ports and channels inside the lagoon. In 1755, a single event triggered rapid and profound modifications, shortening the system, narrowing the barrier islands, and attaching the outermost barrier islands to the mainland.

3.3. Recent evolution

The recent evolution of the Ría Formosa was analyzed with more accurate maps and aerial photographs. This allowed the superposition of the geomorphic features from each period to perform more quantitative analysis of the evolution of (a) inlet and barrier island position (to analyze inlet migration and barrier island regression/transgression), and (b) inlet separation.

Initial visual comparison between the maps from the late 19th century and the old maps suggests a decrease in inlet width, as well as narrower barrier islands. This apparent change in morphology may be in part real, and in part attributed to the fact that the representation of the various features in the maps was done more and more precisely, giving the impression of larger changes in the physical characteristics of the barrier island chain. However, all sources of information coincide in suggesting that the island chain became thinner, the inlets narrowed, and that the rate of shoaling and infilling of the lagoon decreased.

3.3.1. Materials

The materials used in this analysis of recent changes consisted of:

1) Seven sets of maps from 1870 (one map, scale 1:20,000), 1893 (one map, 1:100,000), 1915 (one map, scale 1:150,000), 1923 (2 maps, scale 1:50,000), 1951, 1964, and 1976 (4 maps each, scale 1:25,000), obtained from the Portuguese Cartographic Institute and from the Portuguese Army Geographic Institute.

2) Three sets of aerial photographs from 1978 (16 photos scale 1:33,000), 1989 (75 photos scale 1:10,000), and 1991 (14 photos scale 1:33,000) obtained from the Portuguese Cartographic Institute.

3) One set of 16 orthophotomaps from 1991, scale 1:10,000, with topographic and bathymetric information superimposed, which was used as the geocoded image for the orthorectification of the aerial photograph sets.

In addition, the studies by Esaguy (1984; 1985; 1986a; 1986b; 1987), Dias (1988), Pilkey (1989), Freire de A. (1990b), Bettencourt (1994), and Vila (1999) were consulted.

3.3.2. Methods

Prior to analysis of the recent evolution of the Ría Formosa system, the maps, aerial photographs, and orthophotomaps were (a) transferred to electronic format, (b) processed to eliminate geometric distortions, and (c) referenced into a common coordinate system. The resulting images were used to digitize the lagoon and barrier island shorelines. The methods to achieve that varied for each source type:

1) Maps and orthophotomaps

The maps were first scanned using a large format drum scanner in the Computer Resources Laboratory of the Department of Urban Studies and Planning at MIT, as for the old maps described in section 3.2.

Although the map hardcopies are already referenced to a coordinate system, the raw digital images contain geometric distortions due to the quality of the hardcopy and to the scanning process itself. In order for these images to be useful, they must be geometrically corrected and georeferenced, so that they could overlay in perfect registration with other cartographic information.

The correction and georeferencing of the source images was performed using the PCI GCPWorks software package (PCI, 1997). The process involves the collection of points with known coordinates (the so-called ground control points, or GCPs), distributed evenly over the whole image. A least square regression analysis was used to determine the transformation equations, which related the distorted image to the desired true map projection. In some instances,

when the sets for a given year consisted of more than one map, the corresponding images were grouped into a single mosaic image prior to digitization of the shoreline.

2) Aerial Photographs

Aerial photographs are subject to a number of distortions introduced at various stages in the photographic process. These distortions affect both image space, which refers to the "world" inside the camera (the lens, the film, and the photographic image and measurements obtained from it), and the object space, which refers to the real-world outside the camera (Thieler and Danforth, 1994). On one hand, the sources of distortion affecting the image space are mainly the lens distortion, film deformation during the survey and later in processing, deformations during the generation of prints, and deformation of the photographic paper itself. On the other hand, displacement (as opposed to distortion) of the photographed objects from their true position is a result of (a) relief displacement (changes in ground elevation within a photo), (b) tilt (pitch and roll) displacements due to the inability to keep the camera perfectly leveled during the survey, and (c) atmospheric refraction, which is usually considered minor and neglected.

Given the above, more sophisticated processes than used for the maps were performed for the aerial photographs in order to use them for shoreline mapping. These processes are termed orthorectification, which is the process of finding the correct position of each scanned image projected onto the earth's surface, and to resample the image into a given coordinate system after the removal of the distortions and displacements. The aerial photos were first scanned using a large-format high-definition flatbed scanner, with which the distortion in the scanning process is negligible.The orthorectification of the aerial photographies was performed with the PCI Airphoto OrthoEngine software package (PCI, 1998). More specifically, the airphoto ortorectification process consists of:

1) Collect ground control points (GCP) on each digitally-scanned aerial photo. These points have to be easily recognizable in the geocoded image from which the position and elevation information is extracted (e.g., road intersections, buildings). In the present case, the georeferenced orthophotomaps were used as the source of GCPs. The image coordinates of these points and their corresponding geographic coordinates are used to establish the relationship between the image space and the object space.
2) Collect "pass points" in each aerial photo, which appear in two or more photos and for which the corresponding ground position is not known. These points are used to transfer

the ground position information between overlapping photos, and to establish the orientation of photos relative to each other.

3) Collect fiducial marks (i.e., crosses at the corners of the photo or marks at the midpoint of all four sides) in each photo, as well as the information regarding the position of this marks in the camera. This information is used by the program to determine the position of the central point in the photo (principal point), and to eliminate the distortion due to film and paper deformation.

4) Provide the program with information about the calibration of the camera used in each survey, in order to correct the image for lens distortion.

5) Perform the pixel-by-pixel correction of each photo (rotation, translation, stretching) to eliminate the distortions and displacements, and provide the image with the appropriate position, orientation and scale.

6) Create the mosaic image with all the photos from a given year.

The final output from this stage was a series of mosaics from each year, from which the shoreline was digitized. The estimated error in the georeferencing or orthorectification process for each data set resulted to be, in most cases, smaller than 5 m (Figure 3-19). An example of the resulting mosaic from aerial orthorectification can be seen in Figure 3-28 (section 3.3.3, p 111), in which a detail constructed with approximately 24 aerials shows Armona Inlet.

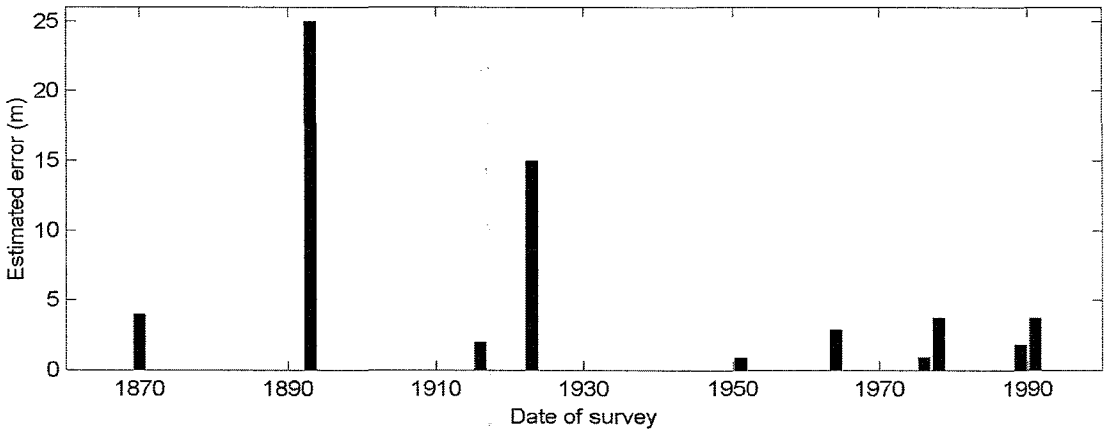

Figure 3-19. RMS error estimates (m) in the georeferencing process.

The areas of the system covered by each data set are shown in Figure 3-20. Maps available from 1870 and 1916 do not show the entire system and were only used for the analysis of the

western and central inlets, respectively. The aerial photographs from 1978 have also a gap in the center (as shown in the figure), but all the inlets were visible for analysis.

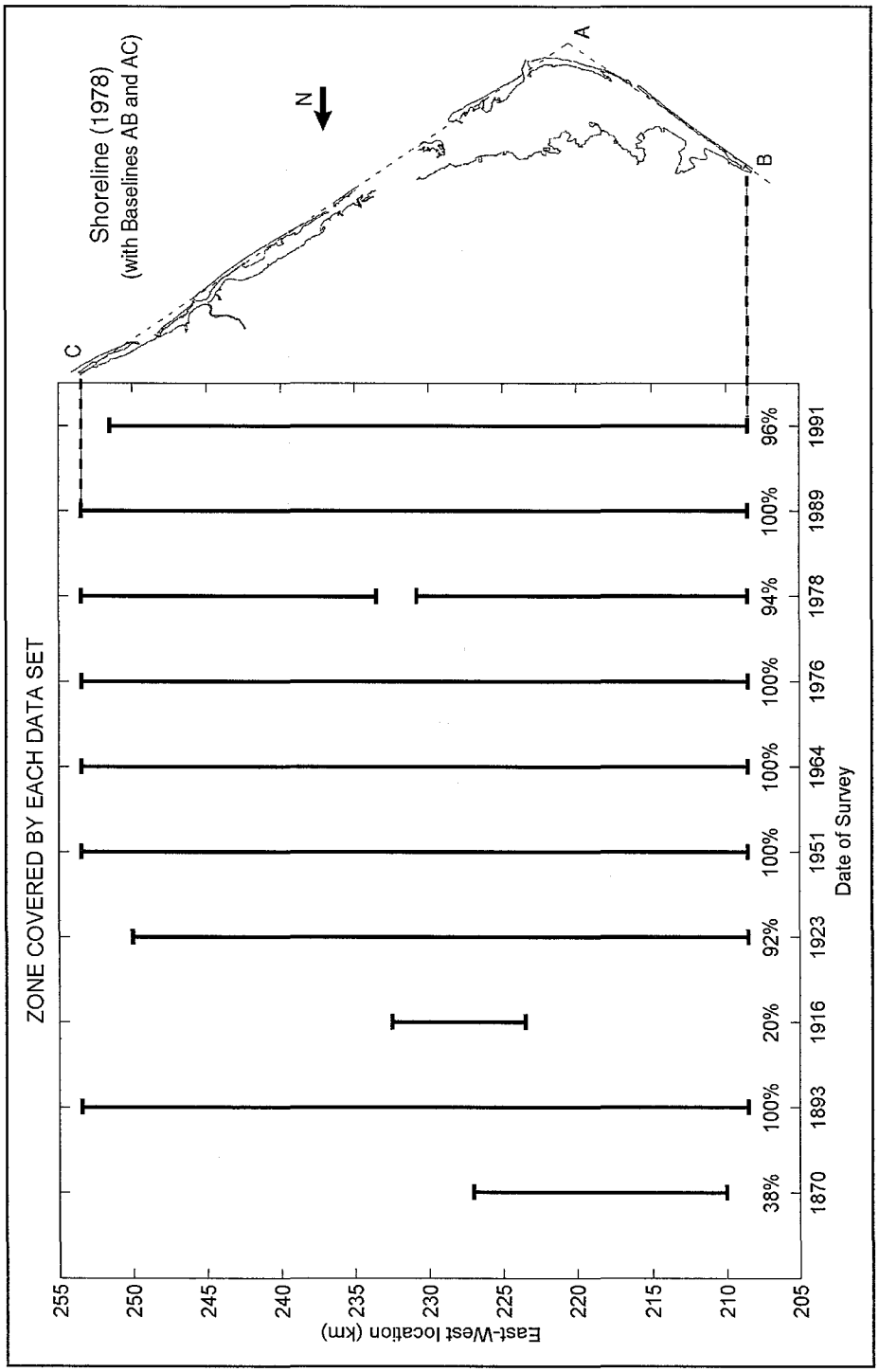

Figure 3-20. Areas of the system covered by each "recent" data set.

3.3.3. Results

The analysis of the inlet evolution addressed: (a) inlet number, (b) inlet and barrier island position (to analyze inlet migration and barrier island regression/transgression), and (c) inlet separation. The inlet width corresponds to the minimum width of the inlet gorge. Inlet position was computed as the distance of the center of the gorge channel (projected perpendicularly on the baseline) to point A (see Figure 3-20). The distance from the center of the inlet gorge to the baseline (line AB or AC in Figure 3-20) was also computed. Finally, the barrier island length was computed as the distance between two adjacent inlets along a curve parallel to the island's coastline.

Inlet Number

The first observation from the data analyzed is that, although the system is characterized by high rates of inlet migration, inlet closure and new inlet formation (Pilkey *et al.,* 1989), the existence of multiple inlets in Ría Formosa has been documented in maps since the 16th century. Figure 3-21 is a plot of the evolution in number of inlets through time (28 data points), where the data from old maps has been included, as well as data from 5 additional maps from 1648, 1662, 1730, 1772, and 1778 (Bettencourt, 1994), and the recent configuration (7 inlets in 1997 just after the opening of the New Ancão Inlet, and 6 inlets since 1998). The figure shows that the data are concentrated in two periods: the 50 years following the earthquake in 1755, and the last 50 years. The data are scarce in the other periods, and may not represent accurately the actual variation in number of inlets.

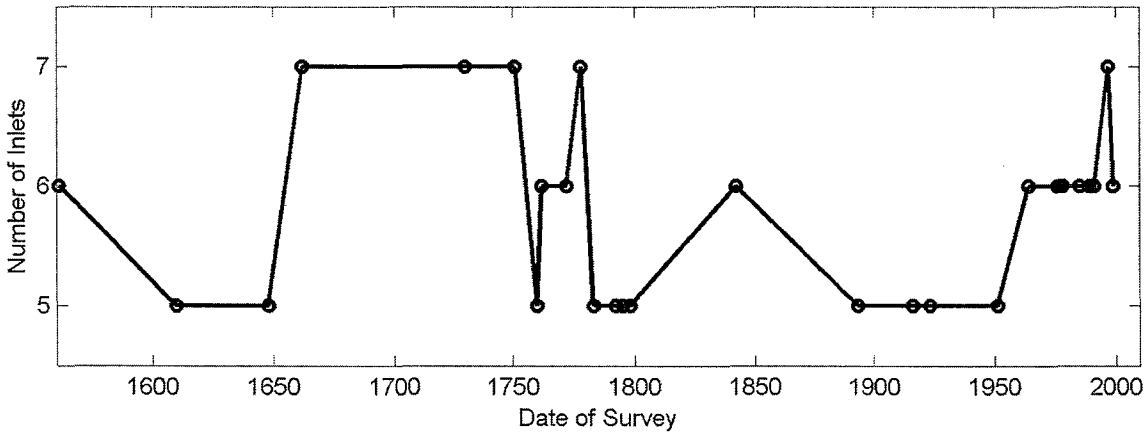

Figure 3-21. Evolution in number of inlets through time

However, the number of inlets has fluctuated from five to seven, and these variations have sometimes occurred quite rapidly. On one hand, a rapid increase in number of inlets can be explained by the breaching and formation of new inlets, or even by artificial opening, which are events that occur in a matter of days or weeks. On the other hand, a rapid decrease in number of inlets may be an indication of (i) the fragility of the equilibrium in some inlets, and (ii) of the surplus in sediment supply, which can shift due to a sudden change in sediment transport conditions, and close an inlet in short periods.

Inlet position

1. Western sector

The western region of Ría Formosa is the region west of the Cape of Santa María (southern tip of Barreta island, see Figure 3-1), in which usually only one inlet is present, the Ancão Inlet, separating the Ancão Peninsula from the Barreta Island. According to Freire de A. (1990b), two inlets coexisted during short periods (1941, 1964, and 1979/80), after the breaching and formation of a second ephemeral inlet in that sector of the system.

The Ancão Peninsula, whose origin resulted from the attachment of the westernmost barrier island to the mainland at the end of the 18th century, is at present a narrow transgressive spit (50-250 m wide), with a length varying from 5.5 km (1870) to 12 km (1998), depending on the Ancão Inlet position. The spit is a single dune ridge of approximately 10 m high. Erosion is taking place in both sides of the shore-attached barrier . Severe erosional events occur in winter, with frequent overwash, especially in the central sector where human occupation has destroyed the dune ridge (Vila *et al.*, 1999). This morphology is similar in the western section of Barreta Island, which is narrow, low in elevation, mostly unvegetated, and frequently overwashed.

According to the cartographic information available for this study, there is no apparent cyclic behavior of (a) opening in a western location, (b) easterly migration, (c) closure, and (d) opening of a new inlet at roughly the original western position, as some other studies have suggested. Figure 3-22 summarizes the Ancão inlet evolution in terms of width and location, which can be divided in 4 phases: before 1893, between 1893 and 1923, between 1923 and 1978, and between 1978 and 1997.

a) The first phase, for which only two maps are available (1870 and 1893), is characterized by a relative stability in inlet location. The inlet width decreased from 490 to 230 m in that period.

It is hypothesized here that this reduction in width is related to the breaching and formation of the Bispo Inlet at the Cape of S^{ta} María in 1861 after a storm (roughly where the Main (Faro) Inlet is presently located), which captured part of the tidal prism originally flowing through the Ancão Inlet. The Bispo Inlet was approximately 1,000 m wide in 1870, and was virtually closed by the turn of the century; a small, meandering, and hydraulically inefficient channel remained until the artificial opening of the Main Inlet in 1927. This progressive closure may have led to the gradual capture of a larger tidal prism by the Ancão, but no cartographic data are available to confirm a reversal in the width evolution pattern. The only information available in that respect is a document from 1891 (cited in Freire de A., 1990b), which mentions the existence of a zone of flow convergence and divergence in the main channel near the city of Faro. This zone represented the limit of the area of influence of the Ancão inlet at that time, which was, for instance, significantly larger to what numerical hydrodynamic simulations suggest is the present-day average area of influence of the New Ancão Inlet.

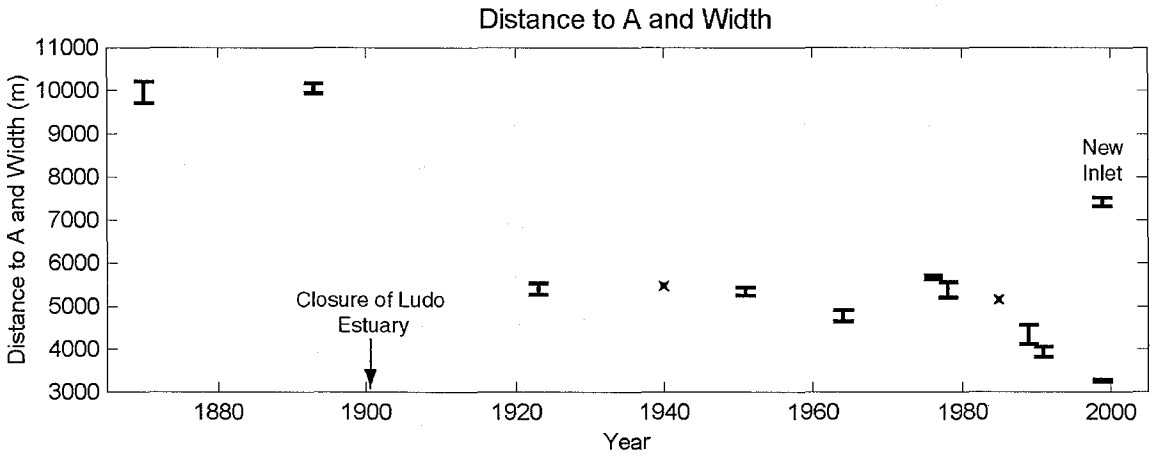

Figure 3-22. West Side inlet evolution. Width (represented by the error bars, and with the scale shown in the y-axis), and position with respect to baseline origin, point A (see Figure 3-20). The stars are data points from Vila *et al.* (1999).

b) The second phase (1893 to 1923) is characterized by a significant change in the inlet position. The inlet in 1923 was approximately 4,500 meters east of the position it had in 1893. Due to the lack of data between these two years, it is not possible to determine if the inlet experienced a continuous "grain-to-grain" migration, or if the former inlet closed and a new inlet opened in an easterly position. In any case, this event has been attributed in part to the artificial closure in the early 1900s of a large portion of the western sector of the lagoon (approximately 5.4 km^2) as part of a land reclamation campaign (Figure 3-23 and Figure 3-24).

This reduction of lagoonal area is significant, considering that, for instance, the area of influence of the New Inlet is at present roughly 10 km^2, or approximately 10% of the lagoon area.

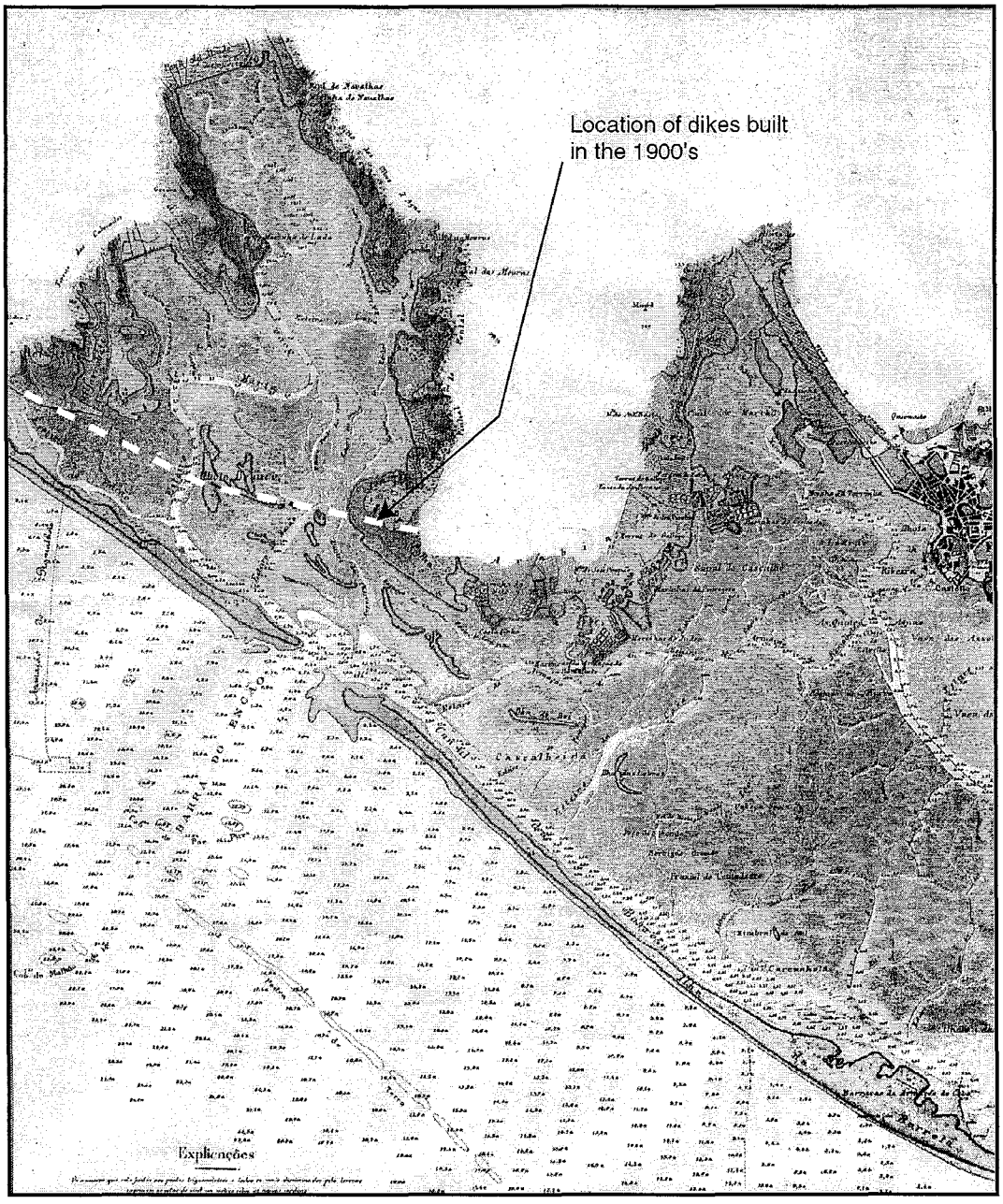

Figure 3-23. Detail of 1870 map showing the approximate position of the dikes constructed in the early 1900s to close the Ludo estuary. The dashed line corresponds to the dikes shown in the map from 1978 (Figure 3-24).

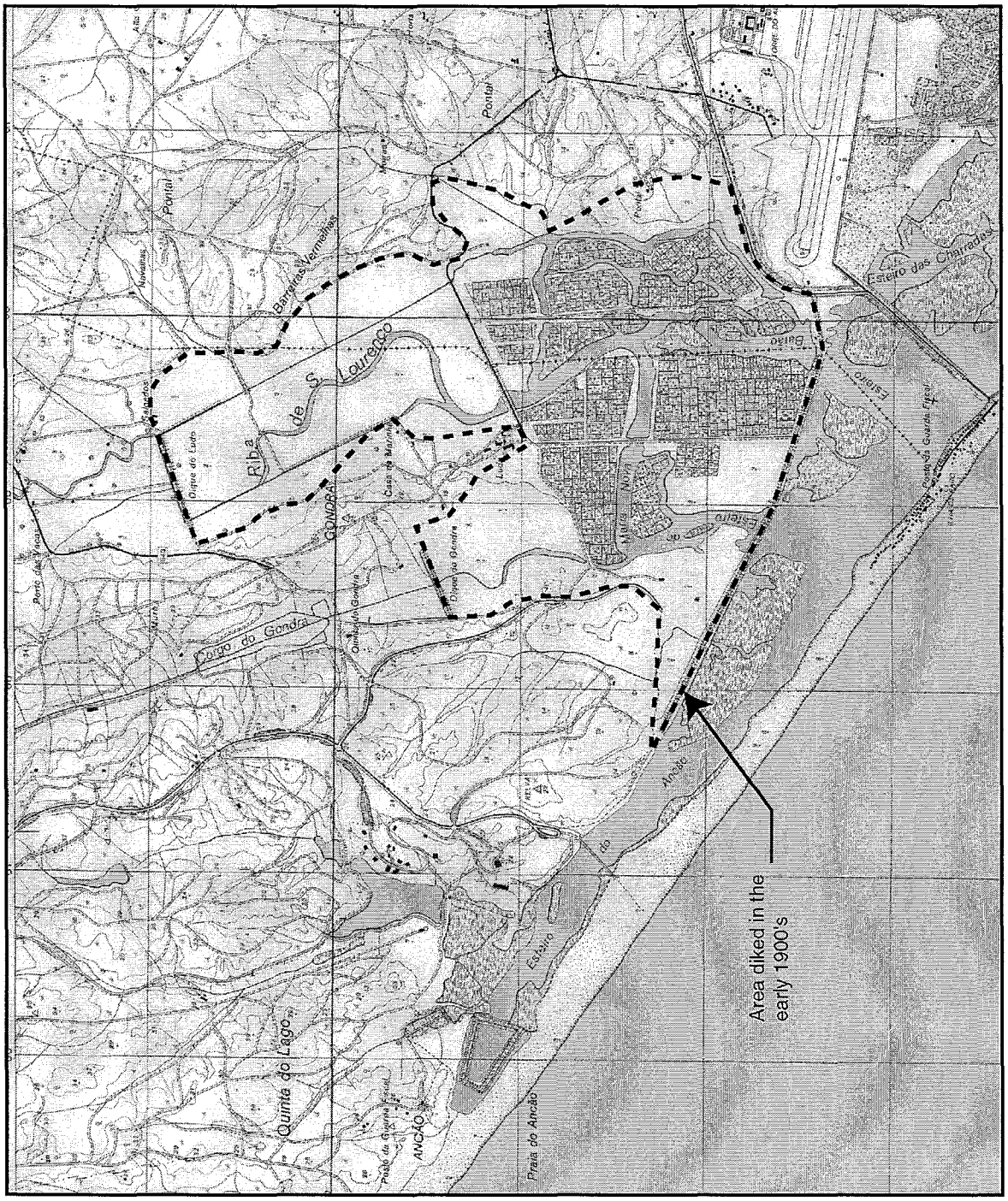

Figure 3-24. Detail of 1978 map showing the dikes and the limits of what once was the Ludo estuary, with an approximate area of 5.4 km^2 (the grid is 1x1 km). The dashed line corresponds to the Ludo Estuary, as shown in the map from 1870 (Figure 3-23).

This reduction in lagoonal area produced a significant decrease of the tidal prism, but more importantly, it may have slowed the flow coming from the west and shifted the inlet channel

to the east bank adjacent to Barreta Island, creating the necessary conditions to initiate an easterly migration process that lasted roughly 20 years and moved the inlet roughly 4,600 m at an average rate of 230 m/year. Additionally, the closure of the Bispo Inlet around 1900 may also have contributed to the easterly migration of Ancão inlet, whose tidal prism increasingly embraced eastern areas of that sector of the lagoon. The inlet width does not seem to have varied significantly in that period (230 m in 1893 and 250 in 1923).

c) The third phase, spanning from 1923 to 1978, is characterized by relatively moderate migration of the inlet in both easterly and westerly directions, the position in 1978 being almost the same as in 1923. The inlet width fluctuated more and was 250, 220, 180, 270, 90, and 360 meters in 1923, 1940, 1951, 1964, 1976, and 1978, respectively. The small value in 1976 results from the existence of a large flood tidal delta, which, according to the 1976 map, is supratidal and attached to Barreta Island. However, this feature may have been only temporary (Vila *et al.* (1999) estimated from aerial photographs the width in that period to be of order of 400 m). This position therefore represents a condition of locational stability for 55 years, and something triggered in 1978 a return to an easterly migration behavior.

d) The fourth and last phase (from 1978 to 1998) corresponds to a period of further easterly migration, instability, and ultimately closure of the inlet. The cause of this last migration is unclear, but the inlet became geometrically unstable, and started an irreversible process of gradual updrift overlapping offset, shoaling and meandering of the main channel, and closure (Figure 3-25).

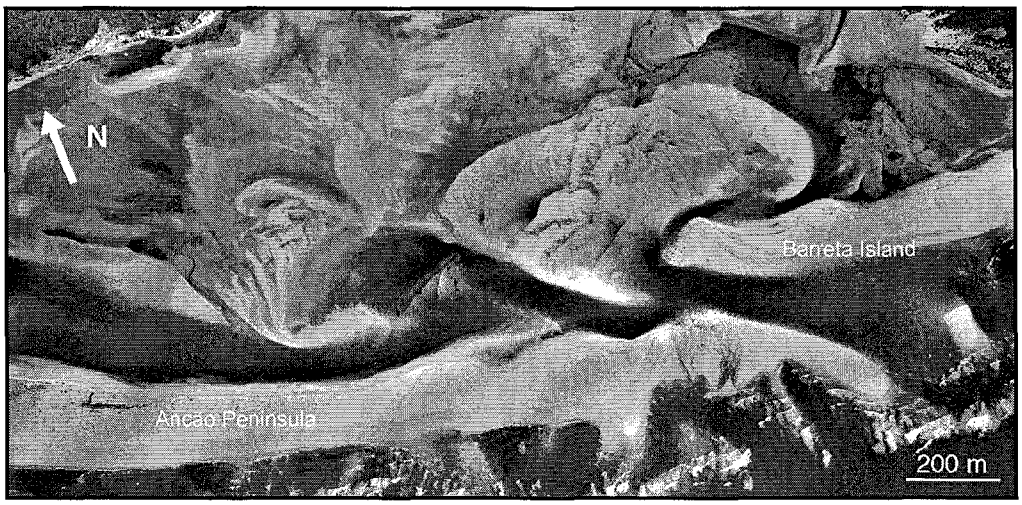

Figure 3-25. Ancão Inlet in 1989.

2. Eastern Sector

The eastern sector extends from the Cape of Santa María to the eastern end of the Ría. The evolution of the width and the position relative the baseline point A are shown in Figure 3-26, where the width and depth of the persistent inlets are plotted through time.

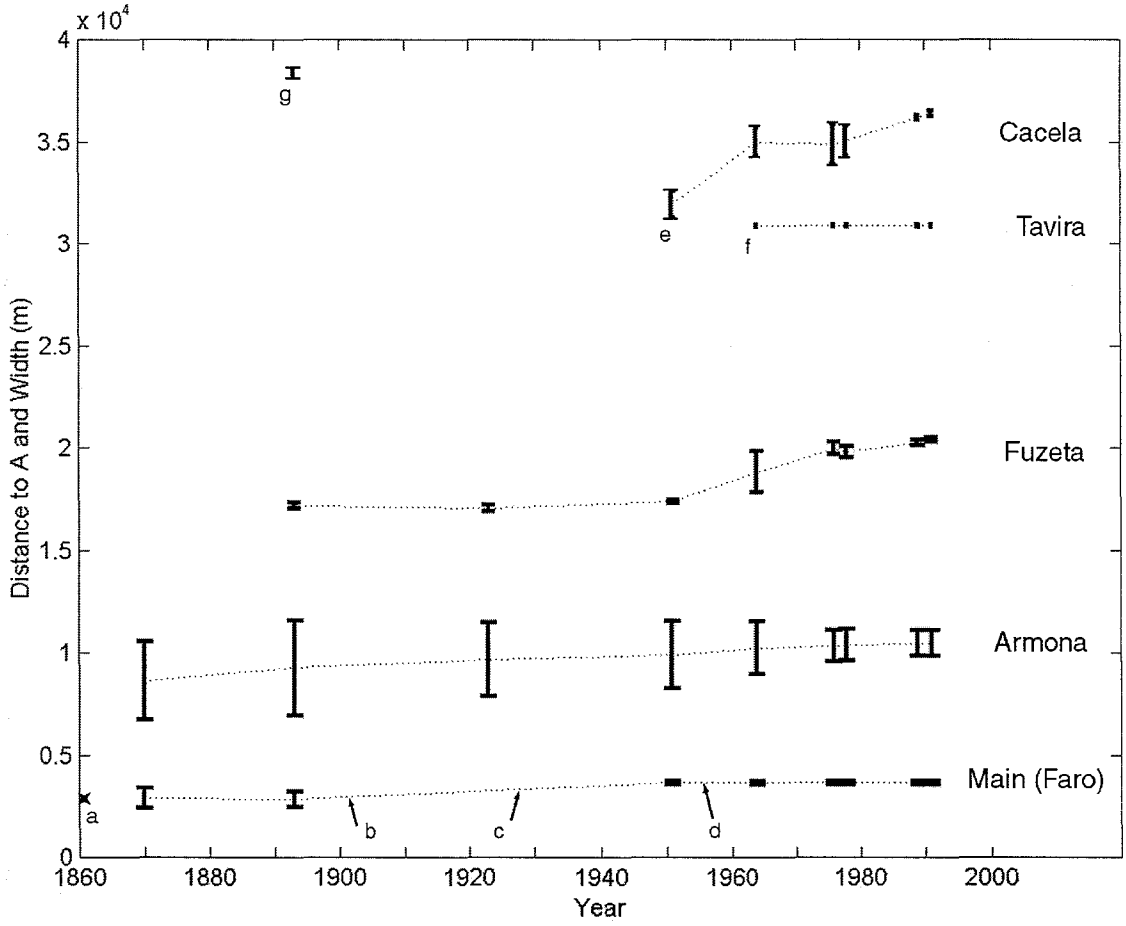

Figure 3-26 Eastern inlet evolution. Width (represented by the bars, and with the scale shown in the y-axis), and position with respect to baseline origin, point A (see Figure 3-20). Notes: a, opening of Bispo Inlet; b, virtual closure of Bispo Inlet; c, artificial opening of Main (Faro) Inlet; d, conclusion of Main Inlet stabilization; e, natural Cochicho Inlet; f, stabilized Tavira Inlet; g, Cacela Inlet at the end of the lagoon (no shore-attached barrier present).

a) Main (Faro) Inlet.

The first inlet encountered in that sector of the lagoon is the Main (or Faro) Inlet, which was opened in 1927 at approximately the same location as the former Bispo Inlet. The stabilization of the inlet with jetties was a long process that lasted almost 30 years, and was finally concluded in 1955. The width of the inlet with jetties is 165m in its narrowest part.

The opening of the Main Inlet had important effects on the littoral physiography in the Ría Formosa area, as well as in the hydrodynamic behavior of the lagoon, as a consequence of the capture of a large tidal prism, the disruption of the natural longshore transport pattern, and the erosion induced by the large ebb jet flow (Freire de A., 1990b).

The most evident consequence of the stabilization is the considerable updrift beach accretion and the downdrift shoreline retreat. The updrift progradation caused the shoreline to move south approximately 450 m between 1923 (before the inlet opening and beginning of stabilization) and 1991, and its occurrence is noticeable 3 km updrift of the western jetty. The updrift and downdrift effects of the stabilization can be seen in Figure 3-27.

Figure 3-27. Main Inlet in 1991.

The hydraulic efficiency of this inlet is due to its proximity to the Faro (Main) Channel, which is the most hydraulically efficient channel in the western area of the Ría (numerical hydrodynamic simulations show that at present, the Main inlet carries approximately 60% of the total flow between the ocean and the lagoon). Added to that, the efficiency of the jetties to prevent the potential deposition of large volumes of sand in the inlet gorge has triggered an ongoing process of erosion, resulting in the deepening of the inlet channel from 5 m in 1962 to 31 m in 1980 (Freire de A., 1990b). This process has produced steep slopes in the jetties' foundations, and the consequent increase in risk of damage of the structures. The bathymetric survey performed during

the field campaign in 1999, in which the maximum depth recorded was 30 m, suggests that the depth has not experienced significant variations in the last 20 years. In fact, one hypotheses to explain that is that the bottom of the inlet channel has reached a more consolidated stratum that prevents further deepening (Oscar Ferreira, personal communication). Therefore, the present geometry represents either an equilibrium cross-sectional area for the average hydrodynamic conditions, or a configuration in which the inlet has a tendency to grow but is limited by the jetties and the hard stratum in the bottom.

This erosive process, that lead to the increase of the gorge cross-sectional area until 1980, also affected the channel in the ocean side. According to Freire de A. (1990b), the ebb jet created a small canyon in front of the inlet entrance. This canyon extends offshore until the -10 m isobath, where the ocean floor becomes steeper, and has in turn prevented the formation of ebb deltas, since the ebb sediment load tends to be exported to deeper areas offshore. Therefore, the offshore morphology of the Main Inlet entrances represents another natural barrier to the littoral drift, conferring to that inlet a low sediment bypass capacity under fair-weather conditions.

In addition, the inner section of the inlet experiences a continuous process of sediment deposition. The Main Channel leading to the port in Faro is frequently dredged to maintain the required depths for navigation, and sand mining activities take place in the flood tidal delta (see Figure 3-27). This accretion, which occurs only in the lagoon side of the inlet, indicates that the flow through the inlet gorge is strong enough to maintain the inlet open.

The major global effect of the opening and stabilization of the Main Inlet is the drastic reduction of the downdrift sediment budget, making the barriers more vulnerable to erosion and decreasing the sediment supply to the eastern inlets.

b) Armona Inlet

Armona Inlet, which separates the barriers of Culatra (West) and Armona (East), is the only natural inlet in the Ría that has been, to some extent, locationally stable for at least the last century, although its width has varied significantly. The apparent migration rate from Figure 3-26 is approximately 15 m/year from 1870 to 1991. However, this value is due to the way the inlet position is determined (as the midpoint of the inlet gorge). In fact, the eastern bank of the inlet (western tip of Armona Island), experienced erosion from 1870 to 1893 and moved east approximately 1,000 m (at a rate of 44 m/year), but accreted back to the west 520 m from 1893 to 1991(at an average rate of 5.3 m/year). The updrift migration of the Armona Island tip is a phe-

nomenon that has been observed, described and modeled in other systems (e.g., Finley, 1975; Hayes, 1975; Aubrey and Speer, 1984), and is related to a local reversal of the sediment transport on the downdrift side of the inlet due to wave refraction around the ebb-tidal delta, and confers to the island the so-called "drumstick" shape (Hayes, 1979). The other side of the inlet (i.e., the eastern tip of Culatra Island) accreted more than 3,000 to the east from 1870 to 1893, at an average rate of 25.3 m/year. This eastward accretion, which occurs in the form of recurved spits incorporated in the eastern tip of the island, suggests that the availability of sediment is still significant, in spite of the construction of the jetties in Main Inlet that caused the obstruction of the littoral drift to the eastern sector of the island chain. The sources of sediment for this process have not been properly identified, but may be a combination of (i) partial bypassing of the littoral drift through the Main Inlet, (ii) shoreline retreat in the island itself, downdrift from the eastern jetty in the Main Inlet, and (iii) local supply from the large ebb tidal deltas, which, according to Freire de A. (1990b), extend 1,500 m offshore. The configuration of Armona Inlet in 1989 can be seen in Figure 3-28.

Figure 3-28. Armona Inlet in 1989 (detail of orthorectified mosaic).

The important morphological process in Armona Inlet in terms of lagoon hydrodynamics and inlet stability is its significant variation in width, which first increased from 3820 to 4670 meters between 1870 and 1893, most likely as a result of the shoaling and virtual closure of the

Bispo Inlet in that period, and then decreased to 1250 m by 1989. The gradual reduction in width of this inlet is the result of the opening and growth (in cross-sectional area) of the Main (Faro) Inlet, which increasingly captured the tidal prism originally flowing through Armona Inlet. Given its width, this inlet was believed to be responsible for approximately half of the tidal prism entering the lagoon. This may have been the case when the Main Inlet was not as deep as now. However, numerical hydrodynamic simulations with the 1991 inlet configuration (and bathymetry from 1994) show that Main Inlet captures almost half of the total tidal prism and Armona Inlet captures 28%. From 1976 to 1989, the rate of width reduction decreased, suggesting that the inlet approached a condition of equilibrium (the width in 1991 was actually 20 m larger than in 1989).

c) Fuzeta Inlet

Fuzeta Inlet is the first inlet in the narrow eastern area of Ría Formosa (see Figure 3-1). It separates Armona Island from Tavira Island. The eastern half of Armona Island and Tavira Island consist of a long continuous frontal dune (8-10 m high), behind which are broad back-barrier areas (100-200 m) of overwash aprons or incorporated tidal deltas (Pilkey *et al.*, 1989).

According to the data in Figure 3-26, the evolution of Fuzeta Inlet from 1893 to 1991 is characterized by:

- a period of relative stability in location and geometry (1893 to 1951),
- a period of rapid migration (1951-1976; migration rate of ~100m/year) during which the width first increased dramatically from 130 m to 2,050 m by 1964, and then decreased to 570 m by 1976, and
- a period of decrease in the migration rate to 29 m/year, and further decrease in width to 290 m by 1991.

The dramatic increase in width shown in the 1964 map is the result of a large storm that hit the Algarvian coast in March of 1962, and opened an inlet west of Fuzeta Inlet (Esaguy, 1985). This situation was ephemeral, as the portion of island between Fuzeta and the newly formed inlet was frequently overwashed and eventually disappeared. By 1964, the two inlets had merged to form a wide single inlet. This new configuration was in turn not stable, as the flow velocities through the inlet were not large enough to maintain the large cross-section. The eastern tip of Armona Island accreted rapidly, and the inlet recovered progressively its original dimensions.

Figure 3-29 shows a vertical aerial view of the inlet in 1991.This configuration is qualitatively similar to what was found during the field survey in 1999.

Figure 3-29. Fuzeta Inlet in 1991.

d) Tavira Inlet

The region of Ría Formosa where Tavira Inlet is located now has experienced several changes during the past centuries. The number and position of inlets have varied, as storms opened new inlets and closed others. Tavira Inlet, as it is now, is the last in a series of attempts to maintain an inlet open in that area. This task has revealed to be difficult, given the abundance of sediment supply from the littoral drift. The first project took place in 1852, and consisted of dredging the inlet channel. Several others projects followed (1855, 1860, 1879), but were not successful to keep the inlet open, as evidenced in the maps from 1893 and 1923, where no inlet is present in that area of the island chain. The inlet was reopened in 1925-27, and further stabilization occurred in 1936 (Esaguy, 1987). A cyclone struck the area in 1941, opening a wide inlet, Cochicho Inlet, which in 1944 was 1,100 meters east of Tavira Inlet. This new opening resulted in the infilling and closure of the artificial Tavira Inlet by 1950, which was opened artificially again in 1961. Since that opening, periodical dredging of the channel has been required to maintain adequate circulation and the required depths for navigation. Figure 3-30 shows the inlet in

1991. The updrift progradation of the beach as well as the considerable downdrift erosion, which has been locally mitigated with the construction of two small groins next to the downdrift jetty, can be observed.

Figure 3-30. Tavira Inlet in 1991.

e) Cacela (or Cabanas, or Cochicho) Inlet

The recent history of the Cacela Inlet is related to the opening and persistence of Tavira Inlet. Until 1928, the westernmost inlet of the system was located in what now is the junction between the Cacela Peninsula and the mainland. Documents from the late 19th and early 20th centuries (cited in Freire de A., 1990b), suggest that this extremity of the lagoon was already experiencing severe shoaling, and the vessel traffic diminished considerably. The closure of that inlet was apparently triggered by the artificial opening of Tavira Inlet in 1925-27. Cochicho Inlet opened during a storm in 1942, and has migrated east with an irregular pattern to its present position. The migration pattern has been observed to be both in a continuous "particle-to-particle" process, and through "jumps", i.e., shoaling and choking with sand bars until a better defined inlet forms in a vulnerable sector of the barrier island.

After the attachment of Cacela Island to the mainland, the formation of new inlets in that area occurred over a wide area during storms, as the low front dune in Cabanas Island is easily

overwashed and breached. Although the Cacela Peninsula is higher and more vegetated than Cabanas Island (see Figure 3-31), overwash also occurs in that sector of the island chain, resulting in the accretion of the peninsula backside. This process has enhanced the shoaling of the lagoon behind the peninsula, which may ultimately close and shorten the length of the barrier chain by moving the existing mainland attachment to the west (Pilkey *et al.*, 1989). Impending closure of the inlet has been mentioned for more than twelve years (Dias, 1988; Freire de A., 1990b). However, the inlet maintained in 1999 a configuration similar to what is present in Figure 3-31 (two shallow channels, downdrift recurved spit, well-developed flood and ebb deltas), suggesting that the inlet has been able to stay open, in spite of the shallowness of its channels.

Figure 3-31. Cacela Inlet in 1991.

Inlet separation

One last point to be mentioned is the separation between inlets. The results shown in Figure 3-32, suggest that the barrier islands can be divided in two groups for which the barrier island length has had a tendency to become uniform. Three observations can be made:

- The separation between the inlets that cover the wide western basin of the Ría (Ancão, Main and Armona Inlets) has become similar (6,500-7,000m),
- The first two (Ancão-Faro) and last two inlets (Tavira-Cacela) also are gradually becoming separated by a similar distance, and
- The distance between Fuzeta and Armona Inlet has become similar to the distance between Fuzeta and Tavira Inlets. Assuming the migration of Armona Inlet to be

small, and given that Tavira Inlet is artificially stabilized, this event is attributable to the migration of Fuzeta Inlet.

These observations may be, at least in part, fortuitous. However, the uniformity of the inlet separation may also be an indication of a self-adjustment of the system. For instance, uniformity in inlet separation in the narrow sector of the Ría may suggest that the system is trying to distribute evenly the tidal prism in each inlet.

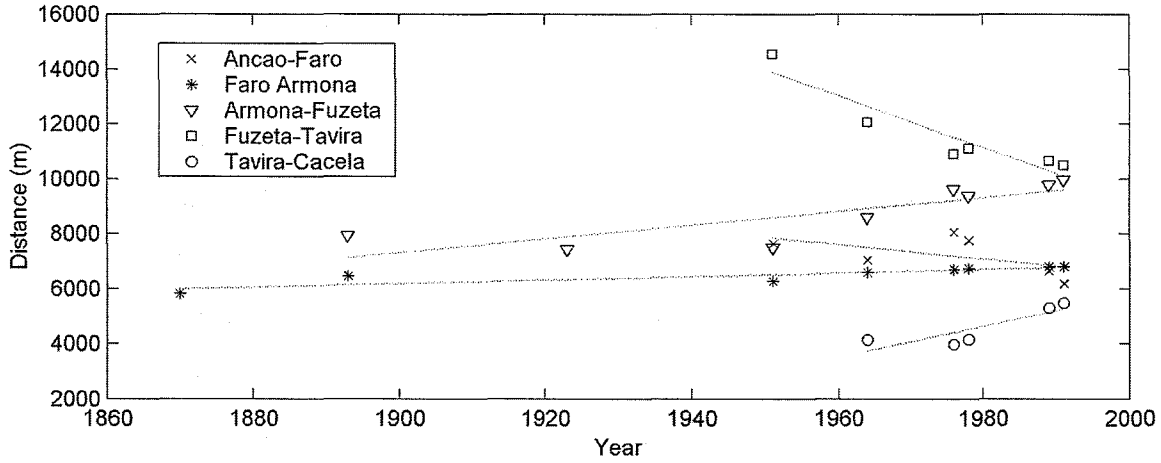

Figure 3-32. Evolution of inlet separation. The coefficients of determination, r^2, for the regression curves shown are (following the same order of the legend): 0.55, 0.87, 0.82, 0.94, and 0.86.

3.4. Summary an Conclusions

The system has historically responded to disturbances with significant changes in its morphology, always maintaining multiple inlets open. In some cases the disturbances have favored the overall stability of the system (Tsunami of 1755, opening and stabilization of Main Inlet), and others (closure of the Ludo estuary, stabilization of Tavira Inlet) have resulted in the adaptation of adjacent areas and inlets to new states of equilibrium.

In summary, the most relevant events that occurred in the past centuries are:

- Prior to the earthquake of 1755, the lagoon was open to the ocean on both sides (East and West), and experienced a clear process of shoaling and infilling with sediment coming from the ocean. After 1755, the easternmost and westernmost barrier islands gradually attached to the mainland (probably due to strong overwash caused by the Tsunami), conferring to the lagoon a more enclosed configuration, which resulted in a decrease in the rate of capture of

sediment from the ocean. This new configuration in turn triggered a series of morphodynamic processes that favored the overall stability of the system: the inlets narrowed (in part due to an increase of the littoral drift reaching the inlets), which resulted in an increase of the flow intensity through the inlets, and favored their capacity to flush sediment.

- The Ancão Inlet easterly migration was apparently triggered by the closure of the Ludo Estuary and the Bispo Inlet, until the inlet reached a condition of locational stability. No satisfactory explanation has been given to the last period of migration (1978-1999), which resulted in the inlet closure.
- The opening (1927) and stabilization (1927-1955) of the Main Inlet, and the consequent trapping and diversion of the littoral drift resulted in significant shoreline retreat in the barrier immediately downdrift, but had no evident effect in inlet behavior downdrift, as suggested by the persistent accretion of the Culatra Island eastern tip. The narrowing of Armona Inlet is in fact attributed to changes in the lagoon hydrodynamic, as the increasingly larger Main Inlet cross-sectional area captured a significant fraction of the Armona Inlet tidal prism. The enlargement of Main Inlet and the reduction of Armona inlet ultimately stopped, suggesting that both inlets ended the phase of adaptation and reached a new stable configuration, which, for the case of Main Inlet, may be imposed by the jetties and, possibly, by the existence of a less erodible bed at the depth of 30 m.
- Main Inlet is a net importer of sediment, as evidenced by the frequent dredging that takes places in the lagoon side of the inlet (flood tidal delta), and in general in the navigational channel leading to the industrial port in Faro.
- Due to a major storm in 1962, Fuzeta Inlet enlarged dramatically (from 130 m to 2,050 m), as it merged with a newly formed inlet. However, the inlet has gradually recovered its original cross-sectional area.
- The increasing uniformity of the separation of the inlets may be an indication of a self-adjustment of the system, with which the system is trying to distribute more evenly the tidal prism through each inlet, at least in the central sector of the system (Armona-Fuzeta-Tavira).

The Ría Formosa multiple inlet system is a dynamic system that has experienced several changes in its configuration. The persistence of multiple inlets can be explained in part by the

capacity of the system to respond to disturbances, which in turn is enhanced by the strong hydrodynamic interaction between inlets.

3.5. References

Aubouin, J., Brousse, R. and Lehman, J.-P., 1981. Paleontología, Estratigrafía. Tratado De Geología, **2**. Omega.

Aubrey, D. G. and Speer, P. E., 1984. Updrift Migration of Tidal Inlets. *Journal of Geology,* **92**: pp 531-545.

Bettencourt, P., 1988. Apports De L'étude Sedimetologique a La Comprehension De L'evolution D'un System D'iles Barrières (Algarve, Sud Portugal). *Bull. Inst. Geol. Bassin D'Aquitaine,* **44**: pp 81-96.

Bettencourt, P., 1994. *Les Environements Sédimentaires De La Côte Sotavento (Algarve, Sud Portugal) Et Leur Évolution Holocène Et Actuelle.* PhD thesis, Université de Bordeaux I.

Correia, F., Dias, J. M. A., Boski, T. and Ferreira, Ó., 1996. The Retreat of the Eastern Quarteira Cliffed Coast (Portugal) and Its Possible Causes, in: Jones, Healy and Williams, Eds.: *Studies in European Coastal Management.* Samara Publishing Limited, Cardigan,

Dias, J. M. A., 1988. Aspectos Geológicos Do Litoral Algarvio. *Genonovas,* **10**: pp 113-128.

Emery, K. O. and Aubrey, D. G., 1991. Sea Levels, Tide Levels, and Tide Gauges. Springer-Verlag.

Esaguy, A. S., 1984. *Ría De Faro, "Barra De Armona", Evolução 1873-1983.* Direcção Geral de Portos, Divisão de Costas Marítimas e Estuários.

Esaguy, A. S., 1985. *Ría De Faro, "Barra De Fuseta", Evolução 1944-1984.* Direcção Geral de Portos, Divisão de Costas Marítimas e Estuários.

Esaguy, A. S., 1986a. *Ría De Faro, "Ilha De Tavira", Evolução 1950-1985.* Direcção Geral de Portos, Divisão de Costas Marítimas e Estuários.

Esaguy, A. S., 1986b. *Ría De Faro, "Ilha Do Ancão", Evolução 1950-1985.* Direcção Geral de Portos, Divisão de Costas Marítimas e Estuários. Lisbon.

Esaguy, A. S., 1987. *Ría De Faro, "Barra De Tavira", Evolução 1950-1985.* Direcção Geral de Portos, Divisão de Costas Marítimas e Estuários.

Finley, R., 1975. Hydrodynamics and Tidal Deltas of North Inlet, South Carolina, in: L.E. Cronin, Ed.: *Estuarine Research,* **2**. Academic Press.,, pp 277-292.

Freire de A., C., 1990a. Estudo Da Susceptibilidade Ao Galgamento Da Ría Formosa. *Geolis,* **IV**: pp 69-76.

Freire de A., C., 1990b. *O Ambiente De Barreira Da Ría Formosa, Algarve - Portugal.* Ph. D. thesis, University of Lisbon.

García-Gil, S., Vilas-Martin, F., Muñoz, A., Acosta, J. and Uchupi, E., 1999. Quaternary Sedimentation in the Ría De Pontevedra (Galicia), Northwest Spain. *Journal of Coastal Research,* **15**(4): pp 1083-1090.

Hayes, M. O., 1975. Morphology of Sand Accumulations in Estuaries, in: L.E. Cronin, Ed.: *Estuarine Research*, **2**. Academic Press.,, pp 3-22.

Hayes, M. O., 1979. Barrier Island Morphology as a Function of Tidal and Wave Regime., in: S.P. Leatherman, Ed.: *Barrier Islands, from the Gulf of St. Laurence to the Gulf of Mexico*, Academic Press., New York, NY, pp 1-28.

Hoyt, J. H., 1967. Barrier Island Formation. *Geological Society of America Bulletin,* **78**: pp 1124-1136.

Oliveira Pires, H., 1998. *Preliminary Report on the Wave Climate at Faro*. Report to the InDIA Project, Insituto de Meteorologia - Instituto Superior Tecnico.

PCI., 1997. Pci Gcpworks Version 6.2 Reference Manual.

PCI, 1998. Pci Orthoengine Airphoto Edition Version 6.2 Reference Manual.

Pilkey, O. H., Neal, W. J., Monteiro, J. H. and Dias, J. M. A., 1989. Algarve Barrier Islands: A Noncoastal-Plain System in Portugal. *Journal of Coastal Research,* **5**(2): pp 239-261.

Swift, D. J. P., 1976. Coastal Sedimentation, in: D.J. Stanley and D.J.P. Swift, Eds.: *Marine Sediment Transport and Environmental Management*, John Wiley., New York, pp 255-310.

Thieler, E. R. and Danforth, W. W., 1994. Historical Shoreline Mapping (I): Improving Techniques and Reducing Positioning Errors. *Journal of Coastal Research,* **10**(3): pp 549-563.

Vila, A., Dias, J. M. A., Ferreira, Ó. and Matias, A., 1999. Natural Evolution of an Artificial Inlet. Proc. of the Coastal Sediments 1999, Long Island, NY., pp 1478-1488.

Chapter 4

Field Data and Analysis

4.1. Introduction

The fieldwork conducted for this study in the lagoon of Ría Formosa in Algarve, Portugal, is part of the field campaign of the MAST3 Project InDIA (Inlet Dynamics Initiative: Algarve). Whereas the InDIA fieldwork partners focused on the New Ancão Inlet in the Ancão Peninsula, with intensive field measurement in its vicinity (2.5 km^2), the work presented here covers the entire lagoon and its six inlets. The field campaign was designed to: (1) obtain hydrodynamic measurements from a persistent multiple inlet system, in order to assist in the identification of processes that may control such persistence, and (2) to provide detailed data for the calibration and validation of the hydrodynamic numerical modeling (Chapter 5).

For the model setup, the field measurements were needed to provide detailed bathymetric surveys of each inlet. In situ measurements of water level fluctuations within the estuary and current velocities are required for calibration purposes, as well as for validation (in instances where more than a single data set is available).

The bathymetric survey of the inlets was conducted from a survey vessel using Differential Global Positioning (DGPS) and a high precision Fathometer.

The water level fluctuations within the estuary were measured using tide recorders. Internally recording pressure/temperature loggers (PTL) were deployed at different locations in the lagoon in order to document the tidal characteristics throughout the system. The approximate lo-

cation of the deployments was designed to cover the entire lagoon and its various morphological environments. The actual locations were eventually determined *in situ* to ensure an optimal location in terms of navigability, security , and data quality. In addition, an Acoustic Doppler Velocimeter was deployed offshore, seaward from Cacela Inlet (eastern end of the system), in order to record the offshore tide and the wave climate. Offshore tidal data from a location near the western end of the lagoon (see Figure 4-2) were made available by the Proudman Oceanographic Laboratory, within the InDIA project..

Finally, the current velocities at the inlets and other selected locations were obtained using a broadband high frequency Acoustic Doppler Current Profiler (ADCP) mounted to a vessel.

This chapter gives first a brief description of the instrumentation used in the field (section 4.2), then describes the methods used to deploy the instruments, perform the surveys, and gather the data (section 4.3), explains the procedures for data reduction, and shows some results (section 4.4 and Appendix).

4.2. Instrumentation

4.2.1. Tide Gauges

Tidal data were acquired using internally recording pressure/temperature loggers. For this program, Brancker TG205 gauges were used. The Brancker instruments were chosen because of their usual reliability, ease in use, and because they provide measurement accuracies appropriate for this project. Each instrument was calibrated at the Woods Hole Oceanographic Institution prior to deployment. The accuracy and nominal operating range for each instrument are provided in Table 4-1.

These instruments use a Druck strain gauge to measure total pressure ($P_{atm} + P_{H2O}$). Within each sampling period, a user-defined number of "burst" samples were taken and then averaged to provide a single value for that period. Although the number of bursts is programmable, the interval between each measurement is fixed at 0.5 seconds. Battery and data storage limitations during the length of deployment defined the maximum amount of data that could be acquired. The typical sample interval was six minutes, which when deployed over a full lunar cycle provided adequate data to derive the harmonic constituents of the local tides.

Table 4-1. Tide Gauge Specifications.

Instrument	Accuracy (cm)	Resolution (cm)
TG 1	0.5	± 1.0
TG 2	0.7	± 1.5
TG 3	1.1	± 2.2
TG 4	1.2	± 2.5
TG 5	1.2	± 2.5
TG 6	1.2	± 2.5
TG 7	1.2	± 2.5
TG 8	1.2	± 2.5
TG 9	1.1	± 2.2

4.2.2. ADCP

An Acoustic Doppler Current Profiler (ADCP) was used to measure and record current velocity profiles at each inlet in the Ría Formosa system. The instrument was deployed from a moving boat, and was connected by cable to a power source and to a portable computer. The computer was used to program the instrument, monitor its operation, and collect and store the data.

The ADCP measures velocity magnitude and direction using the Doppler shift of acoustic energy reflected by material suspended in the water column. The instrument transmits short acoustic pulses of known frequency (1200kHz), along a narrow beam from each of four transducers. As the pulses travel through the water column, they strike suspended sediment and organic particles (referred to as "scatterers") that reflect some of the acoustic energy back to the ADCP. The reflected pulses are separated by time differences into successive, uniformly spaced volumes called "depth cells" (or bins). The change in frequency (Doppler shift) and the time-lag between successive reflected pulses are proportional to the velocity of the scatterers relative to the ADCP.

The water velocity relative to the ADCP is obtained assuming that the scatterers move on average at the same velocity as the water. In addition, since the ADCP was mounted on a moving vessel to measure the velocity profile of an entire cross-section, its velocity had to be subtracted from the ADCP-measured water velocities. The boat speed and direction are also computed by

the instrument. The channel bottom depth and velocity relative to the instrument are computed using the same technique as for the water column, assuming that the bottom is stationary. The direction is determined using an on-board compass. The data provided by the instrument consist of velocity magnitude and direction (in an orthogonal space) from the multiple samples taken within each bin. The sampling rate and the depth of the bins are set by the operator, and can vary depending on the boat speed, the maximum depth of water to be measured and the resolution required. In turn, the length of the bins depends on the boat speed and the sampling rate. The group of pulses that generate data from each set of vertically stacked bins is called an "ensemble." The crossing of the channel from one side to the other, referred as a "transect", usually contains many ensembles and is used to compute the discharge through the channel cross-section.

The instrument is subject to operational limitations that influence directly the quality of the discharge computations, namely the inability to measure the entire cross-section of the channel. First, the sides or edges of the channel are not measurable due to the limitations in the draft of the vessel. In inlets with large intertidal side banks, these unmeasured sections can be significant and have to be accounted for in the final discharge computations. Second, data are not provided in the top layer near the surface due to (a) the partial submergence of the instrument, (b) the "lag" distance between successive portions of the transmission of pulses, and (c) a "blanking period" during which the ADCP does not listen for returns immediately after transmit due to the ringing effect. Third, data at the bottom layer (approximately 6% of the water column) are usually not valid due to interference from return signals from the side lobes of the transmit pulse. The velocity at these unmeasured sections of the cross-section is usually estimated during post-processing. More details about the ADCP operational principles and limitations can be found in Morlock (1996) and in the instrument manuals (R.D.Instruments, 1996, 1998).

4.2.3. ADV

An internally recording Acoustic Doppler Velocimeter (ADV) was used to measure the current velocity and surface wave conditions at a site located seaward of the easternmost inlet. The ADV, manufactured by Sontek, measures current in a control volume of approximately one cubic centimeter by transmitting a 5 MHz acoustic pulse and determining the Doppler shift of the return signal. The ADV senses three components of flow velocities of up to five meters per second. The instrument was chosen for this application because of its excellent low flow perform-

ance, and because the ADV internal power and recording systems allow long term remote deployments.

Table 4-2. ADV Specifications.

Acoustic frequency	5 MHz
Dynamic range	1 mm/s to 5 m/s
Resolution	0.1 mm/s
Sampling rate	Programmable from 0.1 to 25 Hz

The sampling strategy was designed to record both tidal and wave data. For the pressure alone, the sampling rate for each burst was 0.2 Hz, and twenty four samples were averaged to record a data point every six minutes. This burst type is consistent with the sampling design adopted for the tide gauges. For wave measurement, the instrument sampled at a frequency of 2 Hz for a period of 5 minutes (i.e., 600 samples), repeating the sampling once every hour. Details of the ADV deployment set-up can be found in Salles *et al.* (2000). The wave data were post-processed and analyzed by other members of the European InDIA project.

4.2.4. Navigational Control

Positioning of all fixed instrumentation and survey vessel tracking was accomplished using differential global positioning system technology (DGPS). A Trimble AgGPS 132 receiver was installed on the survey vessel. A single deep cycle battery (car battery) provided 12-volt DC power. Positions were referenced to the WGS-84 ellipsoid and later transformed to the Universal Transverse Mercator projection, zone 29.

The largest source of error in stand-alone GPS data (at the time of the experiment) is due to Selective Availability (S/A). S/A is introduced by the U.S. government for the purpose of restricting full GPS accuracy to all but authorized users. The magnitude of S/A combined with other error sources (variable atmospheric conditions) results in horizontal errors of up to 100 meters. In order to remove the selective availability error, a differential correction signal was received and applied to the raw GPS positions. These differential data were created by determining the difference between a known position and that provided by GPS at precisely the same location. The resulting horizontal accuracy of the DGPS data used in this program is less than one meter, as shown in Figure 2.1.

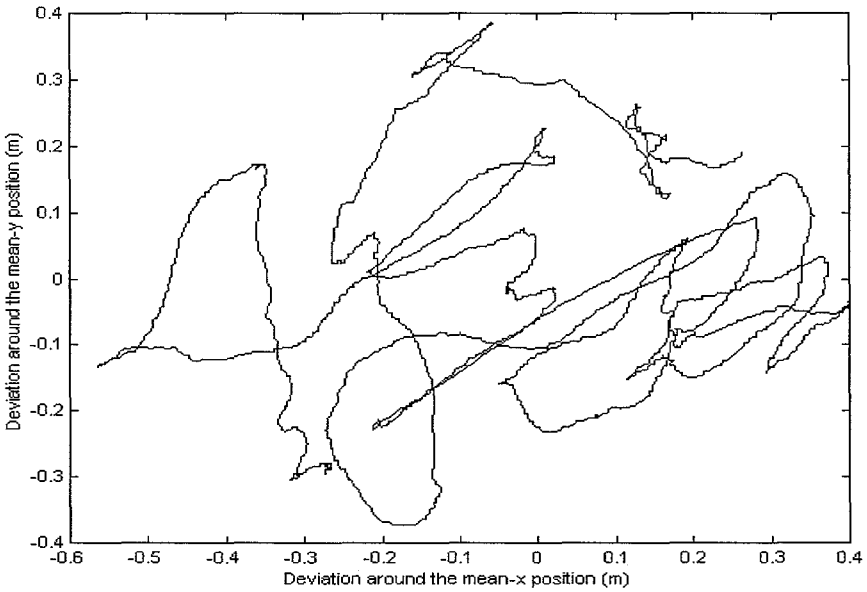

Figure 4-1. DGPS Test results.

Figure 2.1 provides results of a position repeatability test performed prior to the field-work campaign with the Trimble AgGPS 132. 3600 measurements were recorded over one hour at a fixed position. The deviation of each recorded position from the mean position is less than 0.6 m. This high horizontal resolution was particularly valuable when recovering bottom-mounted instruments in low visibility water, whose positions were marked at the surface. The vertical resolution was approximately of the same order, and was not acceptable for the acquisition of the vertical position of the pressure transducers.

4.2.5. Fathometer

Bathymetric data were collected with an Odom Echotrac, dual-frequency fathometer. Echo sounder transmitted frequency is manually selected (either 200 or 24 kHz, or both) to provide the best resolution over variable bottom compositions. Instrument precision is $\pm$ 0.25 cm. This Odom depth sounder provides a paper chart record and digital depth data that are output via RS-232 serial line to the recording computer. One sounding per second is the typical update frequency when working in shallow coastal areas, which provides a depth value every 2 meters at average survey speed.

The Odom Fathometer was calibrated at the start of each survey day by adjusting the speed of sound value the Odom uses to calculate depths. Shallow water survey areas allow the operators to measure the true water depth with a surveyor's stadia rod or a "bar test" and then adjust the speed of sound value accordingly until the measured and calculated values agree.

4.2.6. Land Survey Instrumentation

In order to obtain the absolute vertical elevation of the pressure transducer, transfer of vertical control from provided benchmarks to the installed tide gauges was performed using a Topcon model GTS 3-B total station. System components consist of the measuring unit, tripod, triple prism reflector and stadia rod. The distance measurement capability under worst case conditions (haze with visibility of 7km, sunlight and ordinary heat shimmer) is $\pm$ 5mm. Vertical accuracy under similar conditions is $\pm$ 00° 00' 3".

4.3. Field Methods and Procedures

4.3.1. Bathymetry

Bathymetry data were collected at the Ría Formosa during 29-30 January, 1999, and were acquired using an integrated hydrographic surveying software system (Hypack). Positioning of the vessel was accomplished using differential global positioning system while soundings were taken with an Odom Fathometer. Electrical power for system operation was provided by a 100 watt 110 AC generator.

A 6-meter outboard motor powered vessel was configured to serve as the survey platform. The computer, Fathometer electronics and DGPS unit were installed inside the vessel cabin and the generator in the front. The Fathometer transducer was mounted to the hull via an aluminum gimbal mount, which could be rotated 90° to bring the transducer out of the water during transit to and from survey sites.

4.3.2. ADCP Surveys

The ADCP was usually configured to record and average 20 current velocity values at 0.25 m depth increments (bins) each throughout the water column. The larger depth of the Main Inlet required the use of bin depths of 0.5 m, and the uniformly shallow depths of the Cacela inlet allowed for improved measurement resolution by reducing the bin size to 0.10 m.

Cross-channel ADCP surveys were performed at the six inlets of the Ría Formosa system. The dynamic morphology of some inlets is such that the gorge cross-sectional area is composed of one or more channels and shallow banks on each side, which are not submerged during the entire tidal cycle. In order to ensure consistency throughout the duration of the survey, and to maximize the area over which measurements were taken, the transect in each location was designed in a preliminary visit to the site during low tide. The ADCP transducer unit was mounted to the boat in the same manner as the bathymetry unit, that is, mounted to a gimbaled device with the DGPS antenna located directly above. During each survey, the vessel was run between two buoys that were placed at recorded positions on each side of the channel. DGPS guidance was again provided to the helmsman through the real-time display. Given the different morphological characteristics and wave agitation at each location, the instrument was configured before each survey to optimize the data quality.

The transect line was repeated approximately every 30 minutes over the course of a full tidal cycle (12-13 hours). In addition to the transects of the inlet cross-sections, which were surveyed on average in 6 minutes, measurements of flow velocity were also performed in the adjacent channels. The designed transects are provided in the Appendix (section 4.6), where they are plotted over orthophotomaps from a 1991 aerial coverage, except for the transect line in the New Inlet, which is plotted over a bathymetric map from recent bathymetry. The designed transect for Cacela Inlet is not shown due to (i) the lack of recent bathymetric data of the area, and (ii) to the fact that the inlet has migrated significantly in recent years, preventing the use of orthophotomaps to illustrate its location. Finally, in order to estimate the flow in the intertidal side banks during post-processing, the distance from the shoreline to the beginning and end of each surveyed transect line was visually estimated and recorded. The specific instrument configuration files for each survey and the actual lines run at each inlet (in UTM with WGS-84 datum) can be found in Salles *et al.* (2000).

4.3.3. Tidal Measurements

The tide gauges were deployed at nine different locations throughout the system (Figure 4-2). These sites were chosen to maximize spatial coverage and to record data in areas that were considered important for the numerical modeling calibration. The gauges were set at depths that assured the pressure transducers would remain submerged at spring low water and that they would not cause a hazard to local boating or fishing activity.

Sixteen sample bursts were taken at a rate of 2 Hz and then averaged to provide a single averaged data point for each six-minute sampling interval. This rate provided 240 samples/day. The instruments were mounted to sub-surface pipes that had been water jetted into the sea floor. Instrument positions were obtained using the differential global positioning system (DGPS) referenced to the WGS-84 ellipsoid. Positions were recorded for use during recovery and later tidal analysis. In order to minimize the possibility of the instrument being tampered with during the deployment, the stations were not marked at the surface. Elevations of the pressure recorders were established with the land survey equipment and referenced to the Portuguese Vertical Datum (hydrographic zero = – 2.00 m with respect to the mean sea level in the port of Cascais, near Lisbon).

In addition to the data provided by the Brancker tide gauges, sea surface elevations were also recorded by the Acoustic Doppler Velocimeter/wave gauge (ADV) deployed offshore, south of Cacela. Because of the difficulty in obtaining vertical position of the pressure transducer at such a distance offshore, the data were not directly referenced to a measured datum. It was assumed that the MWL offshore of Faro is the same as that at Cascais.

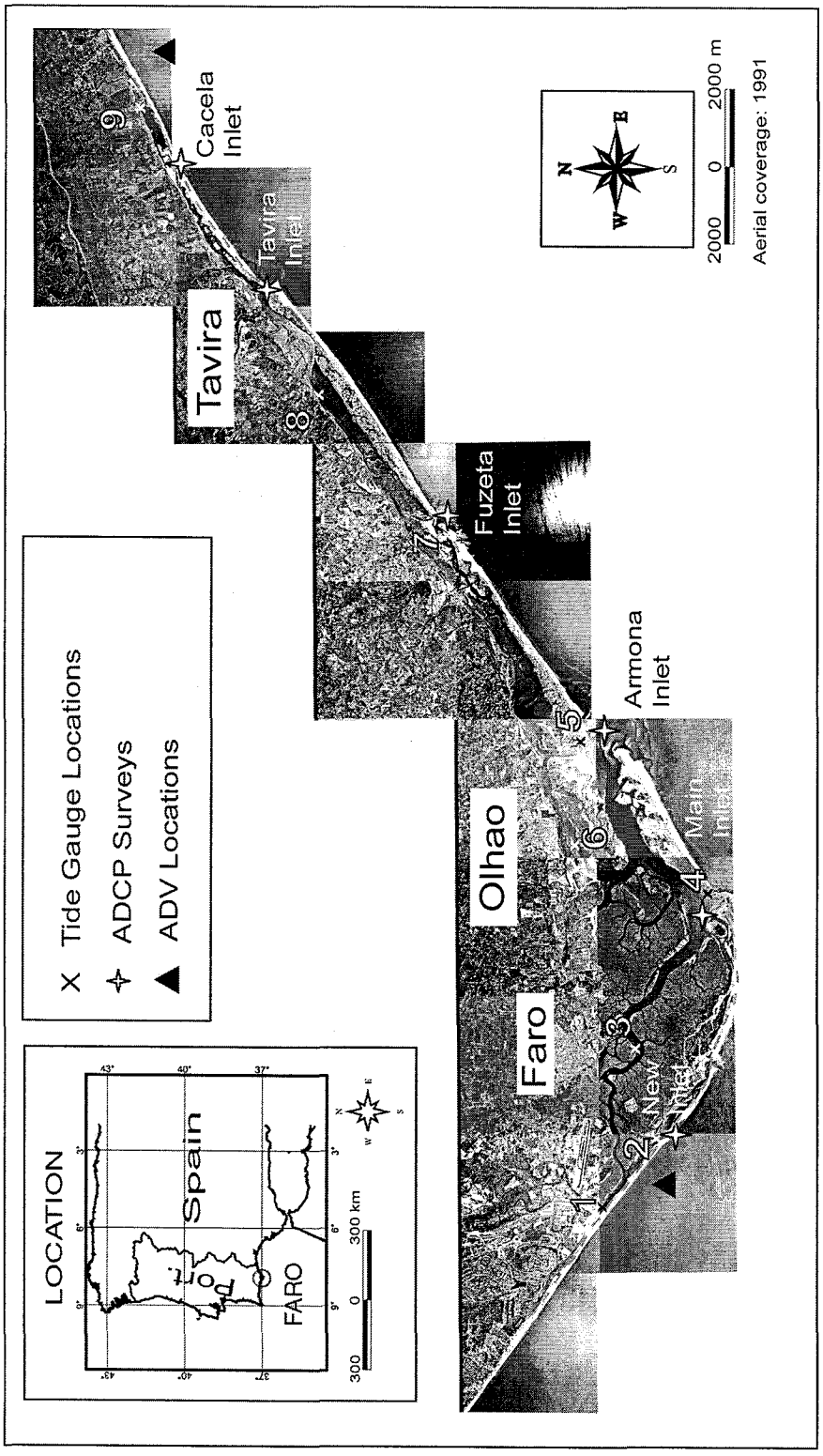

Figure 4-2. Deployment and Survey Locations.

4.4. Data Reduction and Results

4.4.1. Bathymetry Data Processing

Processing of the bathymetric data was performed at WHOI and consisted on tide correction, and elimination of spikes and interpolation. Following are the locations for which valid data were acquired and the total length of the corresponding surveys:

New Ancão Inlet	5.3 km	Armona	15.9 km
Main Channel	17.5 km	Fuzeta	7.3 km
Main Inlet (Faro)	4.1 km	Tavira	2.3 km

Data were processed using the Hypack® hydrographic software package. The detailed bathymetry of the inlets was used for the construction of the computational mesh for the numerical model, as will be discussed in Chapter 5. Plots of the bathymetric survey coverage can be found in Salles *et al.*(2000).

4.4.2. ADCP Data

The ADCP delivered real time data to a computer screen and to a storage device during the length of the surveys. While these data were gathered in one computer, another computer was used to store geographic position data from the DGPS, as explained in section 4.2.4. These two sets of data form the bulk of the ADCP data.

Matlab® routines were created to format and reduce the data, and to compute time series of average cross-sectional velocities and discharges throughout the tidal cycle. Selected velocity profiles for each survey are plotted in the Appendix (Section 4.6). These plots show the magnetic North and East velocities throughout the measured region. The bottom of the channel (lower black line) and the water surface (depth = 0 m) are plotted to indicate the size of the unmeasured upper and bottom layers. The velocity in these layers was linearly extrapolated. The unmeasured sections of the side banks of the surveyed cross-sections were also extrapolated assuming a triangular section from the last (or first) measured point to the closest shoreline.

Due to problems with the DGPS, signal reception during the ADCP surveys, not all the lines had an accurate geographic position. This problem was solved by obtaining the average position of the start point of the lines with valid DGPS information and by assuming that the rest of the lines started in the same point. This assumption is considered to be an adequate approximation since (1) the start point was always marked with a buoy, as explained in Section 4.3.2, and (2) since the objective of the ADCP surveys was not to measure the variation of the velocity in a precise location (for which it would be needed to have a fixed ADCP), but rather to obtain the cross-sectionally averaged velocity and total discharge through the inlet and channel cross-sections.

The total discharge through the inlet and channel cross-sections was computed by integrating the velocity profiles along the area covered by each line. Different numerical methods to compute the cross-section total discharge and averaged velocity were tested. The procedure that gave better results, in terms of capturing most of the flow through the cross-section, and was selected to compute the discharges consisted of:

- Subdivision of the surveyed cross-sections, when appropriate, into subsections as shown by the vertical dashed lines in the velocity profiles (see Appendix, Section 4.6). This was done in instances where the same transect included different channels (e.g., Tavira Inlet) and to differentiate discharges from the main channel of the cross-section to discharges from the banks.
- Projection of the vertically averaged north and east velocities for each ensemble of each subsection in the direction perpendicular to the ensemble orientation.
- The resulting velocity for a given ensemble was multiplied by the total area corresponding to this ensemble (= length of the ensemble times the total depth) to account for the unmeasured layers.
- The total discharge was computed as the sum of all the ensemble discharges for a given line at a given time. In instances where the velocity profile for a given line had bad ensembles such that the average velocity was visibly wrong, an estimate was computed by interpolating the adjacent velocities.

This procedure is similar to that used by the numerical hydrodynamic model (see chapter 5), with the difference that it computes the area of every single ensemble instead of calculating an average area for groups of three ensembles. This procedure is therefore considered to be more accurate. The results of the discharge computations are shown in the Appendix (Section 4.6).

4.4.3. Tide Data Reduction

The tidal data were collected by the 9 PTLs deployed inside the lagoon and by the ADV deployed offshore. The field campaign was designed to collect tidal data for at least a lunar cycle. The ADV was deployed offshore as planned. Due to problems with the analog board, the ADV instrument had to be replaced and its deployment was delayed. In addition, since the deployment sites of the last two tide gauges and the ADV were close together in the easternmost part of the system, it was decided for logistical reasons to wait for the new ADV and deploy the three instruments the same day. Although the selection of the deployment site of the ADV was consulted and discussed with researchers from the University of Algarve and with local fishermen, an accident with a trawling net occurred and the ADV stopped recording nine days after deployment.

Table 4-3 shows the deployment duration and the percentage of data recovered from each instrument. TG 4 and TG 6 failed 23 and 25 days after deployment, respectively.

Table 4-3. Tide Gauges and ADV Deployment Duration and Data Return.

Instrument	Location	Distance to inlet (m)	Deployment dates	Duration (days)	Data return
TG 1 (#8096)	Faro Beach (near bridge)	3,500	1/21 to 2/28	38	100%
TG 2 (#5078)	New Ancão Inlet	160	1/21 to 2/29	39	100%
TG 3 (#3853)	Main Channel	7,700	1/21 to 2/28	38	100%
TG 4 (#8711)	Main (Faro) Inlet	1,250	1/22 to 2/28	37	62%
TG 5 (#8712)	Armona Inlet	900	1/22 to 2/28	37	100%
TG 6 (#8710)	Olhão	5,700	1/22 to 2/28	37	68%
TG 7 (#8709)	Fuzeta	850	1/25 to 2/28	34	100%
TG 8 (#8713)	Tavira (Santa Luzia)	5,450	2/4 to 2/28	24	100%
TG 9 (#5081)	Cacela	2,600	2/4 to 2/28	24	100%
ADV (#9001)	Cacela (offshore)	N/A	2/4 to 2/13	9	100%

The pressure readings were translated to water surface elevation using the elevation of the pressure transducers, removing the atmospheric pressure and assuming a constant water density of 1,024.5 $kg.m^{-3}$. The hourly values of atmospheric pressure, obtained from the Faro Airport, are shown in Figure 4-3.

Figure 4-4 shows the records of Sea Surface Elevation. The data from the offshore instrument #1000 were provided by the Proudman Oceanographic Laboratory. For both offshore instruments (#1000 and #9001), the mean sea surface elevation was assumed to be 2.00 m above

datum, as the Mean Water Level in Cascais. As for the other instruments, the large variability of the mean water level between stations, as shown in Figure 4-4, does not seem to be realistic. Given that the topographic survey to link the pressure transducer elevations with the Portuguese benchmark network closed within the acceptable range of error, the most likely source of error in the determination of the mean water surface at each station is the quality of the benchmarks themselves, which in most cases were located in remote places and not properly maintained. Therefore, the absolute value of the mean water level at each station was not used in the tidal distortion analysis.

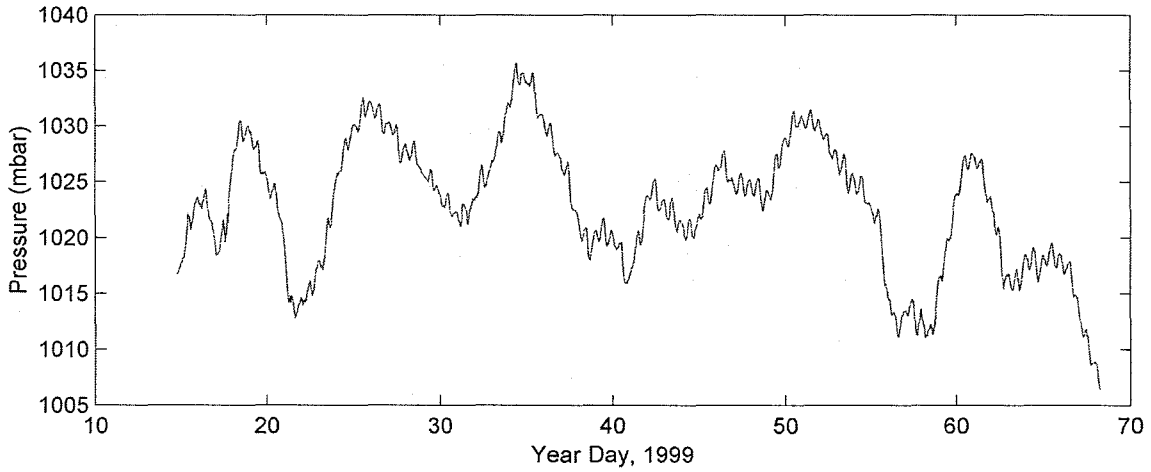

Figure 4-3. Hourly values of Atmospheric Pressure in Ría Formosa (source: Faro Airport)

The water surface elevation records shown in Figure 4-4 were analyzed in order to derive the amplitude and phases of the primary tidal constituents. The results of this analysis were used (i) to study the tidal distortion inside the estuary and thus contribute in the understanding of the nonlinear hydrodynamics of this multiple tidal inlet system, and (ii) for the calibration of the numerical model.

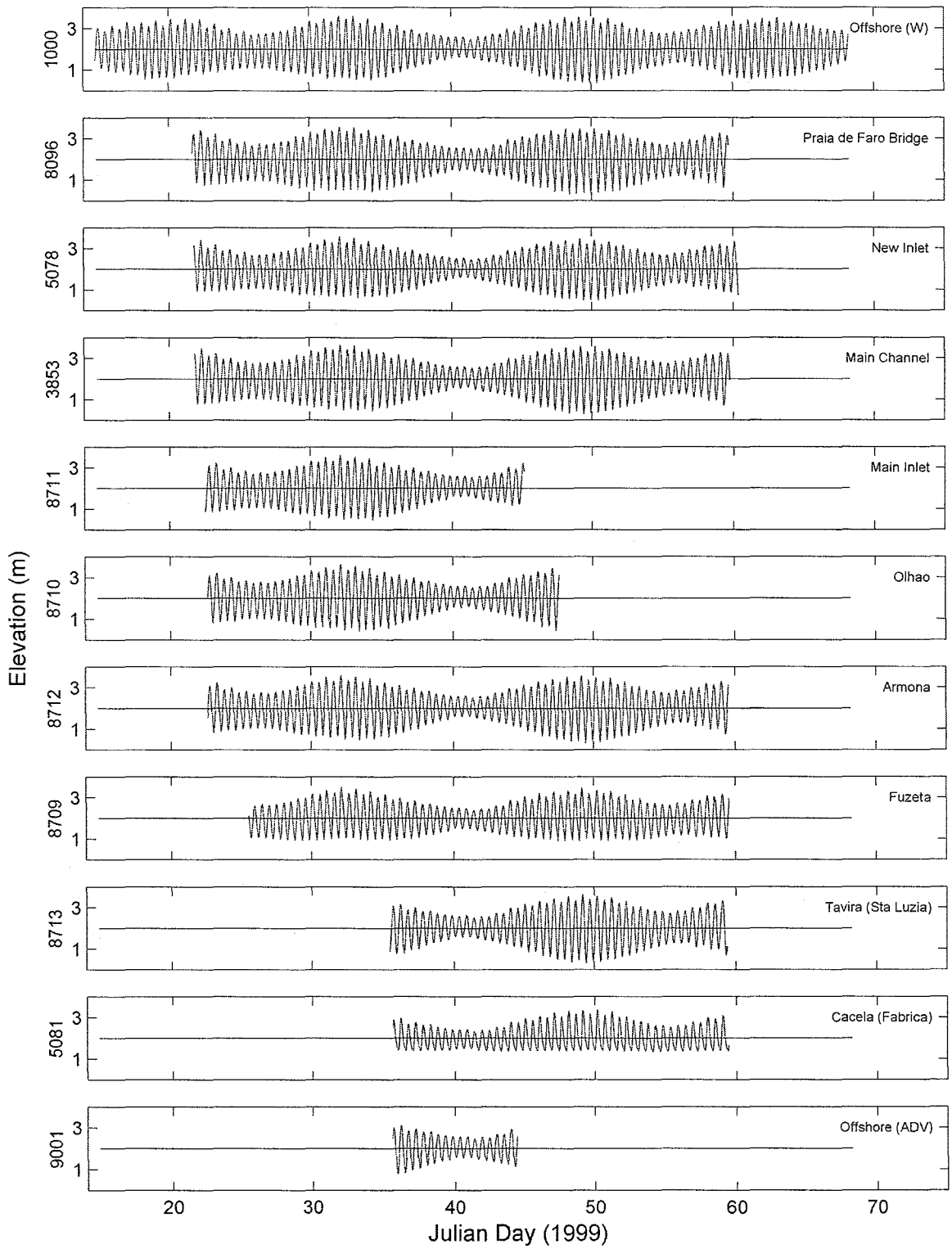

Figure 4-4. Tidal Records for Each Instrument. The mean water surface elevation was shifted to 2.00 m (i.e., the local datum) for all instruments.

The harmonic analysis of the tides from the data of each instrument was performed using the software package developed by the Institute of Ocean Sciences (Foreman, 1977). The program analyzes hourly tide gauge data for a given period. Amplitudes and Greenwich phase lags are calculated via a least squares fit method coupled with nodal modulation for only those constituents that can be resolved over the length of the record. For short records with which certain important constituents cannot be resolved from the data, provision is made for the inference of the amplitude and phase of these constituents from others.

Prior to tidal analysis, the data were decimated to hourly observations and the time base corrected to GMT. Then the data were reformatted in the format needed for the program's input file. The record lengths used for the analysis and the number of constituents for which amplitudes and phases were derived, are listed in Table 4-4.

Table 4-4. Record lengths and constituents derived for each data set.

Instrument	Hours analyzed	Constituents Derived
TG 1 (#8096)	914	36
TG 2 (#5078)	928	36
TG 3 (#3853)	912	36
TG 4 (#8711)	544	18
TG 5 (#8712)	888	36
TG 6 (#8710)	600	18
TG 7 (#8709)	819	36
TG 8 (#8713)	574	18
TG 9 (#5081)	572	18
ADV (#9001)	213	10

The preliminary analysis of the tidal distortion inside the lagoon focuses on the dominant diurnal and semi-diurnal constituents in Ría Formosa and the corresponding relevant overtides, as well as the fortnightly constituent, MS_f, which consists of a weak astronomical term and a potentially larger hydrodynamic term arising from M_2-S_2 interactions (see Table 4-5).

In addition, filtering tests were performed to the data for all instruments in order to detect possible spikes and noise in the data. For this purpose, Godin's filter was used (see e.g., Emery and Thomson, 1998), as suggested by Foreman (1977). This filter is a triple moving average filter, which performs three consecutive convolutions to the original 6-minute spaced data with a

10, 10, and 11 points averaging impulse response, respectively, prior to hourly decimation. The program applies suitable amplitude corrections to compensate for the smoothing effect of these filters. After performing the harmonic analysis to both the original and the filtered data, it was found that the differences in amplitude and phase between both data sets were minimal (less than 1%). The results also show that the standard deviations of the amplitude, A, and phase, φ, for each tidal constituent are much larger for the filtered data than for the original data (2 to 3 times and 3 to 4 times for the short and long data sets, respectively), suggesting a higher confidence in the unfiltered data results. Furthermore, the unfiltered data results show values of A and φ which fall within the confidence intervals of the corresponding values from the filtered data results with a 68.3% confidence level (± one standard deviation). Therefore, it was concluded that the data did not need filtering prior to the harmonic analysis computations.

Table 4-5. Tidal species, constituents, and periods of interest

Species	Constituent	Period (hours)	Record Length required (h)
Fortnightly	MS_f	14.77 days	355
Diurnal	O_1	25.82	328
	K_1	23.93	24
Semi-diurnal	N_2	12.66	662
	M_2	12.42	13
	S_2	12.00	355
Quarter-diurnal	MN_4	6.27	662
	M_4	6.21	25
	MS_4	6.10	355
Sixth diurnal	M_6	4.14	26

The results of the harmonic analysis for all the constituents derived can be found in Salles *et al.*(2000), and the results for the dominant tidal constituents and their corresponding overtides and compound tides are shown in Table 4-6 and Table 4-7, where the tide gauges are listed in order of distance to the closest inlet (following the channel's talweg; see Table 4-3), followed by the results from the ADV.

Table 4-6. Amplitude and Phase of relevant diurnal and semi-diurnal tidal constituents

Station	O_1		K_1		N_2		M_2		S_2	
	a (cm)	θ	a (cm)	θ	a (cm)	θ	a (cm)	θ	a (cm)	θ
1000 (Off.)	**6.7** (± 0.4)	**310** (± 4)	**7.3** (± 0.4)	**65** (± 3)	**17.4** (± 0.1)	**40** (± 1)	**99.3** (± 0.2)	**55** (± 0)	**38.5** (± 0.3)	**94** (± 0)
5078 (TG 2)	**6.4** (± 0.4)	**322** (± 4)	**6.7** (± 0.4)	**83** (± 4)	**16.2** (± 0.1)	**57** (± 1)	**93.9** (± 0.2)	**68** (± 0)	**34.6** (± 0.2)	**112** (± 1)
(1000)[1]	**6.6** (± 0.4)	**306** (± 4)	**7.4** (± 0.4)	**65** (± 3)	**17.8** (± 0.2)	**40** (± 1)	**100.0** (± 0.3)	**56** (± 0)	**38.7** (± 0.3)	**94** (± 0)
8709 (TG 7)	**6.4** (± 0.3)	**335** (± 3)	**6.3** (± 0.4)	**95** (± 4)	**13.1** (± 0.3)	**64** (± 1)	**83.0** (± 0.1)	**74** (± 0)	**26.7** (± 0.1)	**120** (± 1)
(1000)[1]	**6.8** (± 0.4)	**309** (± 4)	**7.4** (± 0.4)	**67** (± 3)	**18.1** (± 0.2)	**41** (± 1)	**100.3** (± 0)	**56** (± 0)	**38.9** (± 0.3)	**95** (± 0)
8712 (TG 5)	**6.5** (± 0.4)	**317** (± 4)	**6.8** (± 0.4)	**75** (± 3)	**17.2** (± 0.3)	**53** (± 1)	**98.4** (± 0.4)	**65** (± 0)	**36.9** (± 0.4)	**108** (± 1)
(1000)[1]	**6.6** (± 0.3)	**308** (± 3)	**7.4** (± 0.3)	**66** (± 3)	**17.9** (± 0.4)	**40** (± 1)	**100.1** (± 0.4)	**56** (± 0)	**38.8** (± 0.4)	**95** (± 1)
8711 (TG 4)	**6.8** (± 0.5)	**319** (± 11)	**7.4** (± 0.5)	**75** (± 10)	---[2]	---[2]	**99.0** (± 0.8)	**67** (± 1)	**36.1** (± 1.0)	**113** (± 2)
(1000)[1]	**6.7** (± 0.9)	**311** (± 10)	**7.9** (± 0.9)	**65** (± 8)	---[2]	---[2]	**99.5** (± 1.3)	**58** (± 1)	**36.3** (± 1.3)	**101** (± 2)
5081 (TG 9)	**5.4** (± 0.8)	**336** (± 10)	**5.4** (± 0.8)	**90** (± 9)	---[2]	---[2]	**66.5** (± 0.8)	**80** (± 1)	**20.0** (± 0.7)	**113** (± 2)
(1000)[1]	**6.7** (± 0.9)	**307** (± 11)	**6.8** (± 0.9)	**65** (± 10)	---[2]	---[2]	**100.1** (± 1.3)	**54** (± 1)	**39.7** (± 1.2)	**90** (± 2)
8096 (TG 1)	**6.3** (± 0.4)	**331** (± 6)	**6.8** (± 0.4)	**93** (± 4)	**16.7** (± 0.6)	**73** (± 2)	**97.1** (± 0.5)	**80** (± 0)	**35.0** (± 0.6)	**128** (± 1)
(1000)[1]	**6.7** (± 0)	**306** (± 4)	**7.5** (± 0.1)	**65** (± 4)	**17.8** (± 0.1)	**40** (± 1)	**100.0** (± 0.1)	**56** (± 0)	**38.7** (± 0.1)	**94** (± 1)
8713 (TG 8)	**6.8** (± 1.1)	**266** (± 11)	**6.6** (± 1.1)	**72** (± 10)	---[2]	---[2]	**102.2** (± 0.1)	**62** (± 1)	**39.1** (± 0.5)	**100** (± 2)
(1000)[1]	**6.7** (± 1.3)	**305** (± 13)	**6.9** (± 1.3)	**66** (± 11)	---[2]	---[2]	**100.1** (± 0.1)	**54** (± 1)	**39.4** (± 0.3)	**90** (± 2)
8710 (TG 6)	**6.1** (± 1.3)	**319** (± 14)	**7.0** (± 1.0)	**78** (± 9)	---[2]	---[2]	**100.0** (± 0.9)	**70** (± 1)	**34.4** (± 1.2)	**117** (± 2)
(1000)[1]	**6.2** (± 1.1)	**309** (± 12)	**7.6** (± 0.7)	**65** (± 54)	---[2]	---[2]	**99.4** (± 1.0)	**57** (± 1)	**34.9** (± 1.1)	**98** (± 2)
3853 (TG 3)	**6.4** (± 0)	**318** (± 4)	**6.9** (± 0.1)	**80** (± 4)	**17.6** (± 0)	**59** (± 1)	**100.9** (± 0)	**70** (± 0)	**38.0** (± 0.1)	**113** (± 1)
(1000)[1]	**6.7** (± 0.1)	**306** (± 4)	**7.5** (± 0.1)	**65** (± 4)	**17.7** (± 0.1)	**40** (± 1)	**100.0** (± 0.1)	**55** (± 0)	**38.6** (± 0.1)	**94** (± 1)
ADV	---[2]	---[2]	**3.9** (± 2..3)	**77** (± 58)	---[2]	---[2]	**69.7** (± 2.8)	**53** (± 2)	---[2]	---[2]
(1000)[1]	---[2]	---[2]	**4.8** (± 2.4)	**74** (± 60)	---[2]	---[2]	**68.9** (± 2.8)	**52** (± 2)	---[2]	---[2]

1: results from the offshore record after truncation to cover only the period covered by the other instrument (see text).
2: the record length is too short for the computation of this constituent (see Table 4-4).

Table 4-7. Amplitude and Phase of relevant low and high frequency (relative to diurnal/semi diurnal tides) tidal constituents

Station	MS_f		MN_4		M_4		MS_4		M_6	
	a (cm)	θ	a (cm)	θ	a (cm)		a (cm)	θ	a (cm)	θ
1000 (Off.)	**3.0** (± 0.3)	**266** (± 7)	**0.5** (± 0.4)	**101** (± 17)	**1.4** (± 0.3)	**164** (± 14)	**0.9** (± 0.1)	**275** (± 24)	**0.2** (± 0.1)	**4** (± 20)
5078 (TG 2)	**3.7** (± 0.1)	**3** (± 7)	**0.7** (± 0.3)	**256** (± 31)	**3.1** (± 0.2)	**258** (± 7)	**3.1** (± 0.3)	**325** (± 6)	**1.0** (± 0.3)	**239** (± 21)
(1000)[1]	**3.5** (± 0.4)	**266** (± 7)	**0.5** (± 0.4)	**119** (± 37)	**1.4** (± 0.4)	**166** (± 15)	**0.9** (± 0)	**269** (± 25)	**0.3** (± 0.1)	**353** (± 30)
8709 (TG 7)	**10.8** (± 0)	**25** (± 2)	**3.4** (± 0.3)	**68** (± 5)	**6.6** (± 0.4)	**77** (± 3)	**5.9** (± 0.4)	**122** (± 4)	**2.3** (± 0.2)	**284** (± 9)
(1000)[1]	**4.5** (± 0.4)	**275** (± 5)	**0.5** (± 0)	**116** (± 37)	**1.4** (± 0)	**164** (± 16)	**0.9** (± 0.2)	**267** (± 22)	**0.4** (± 0.4)	**348** (± 27)
8712 (TG 5)	**2.9** (± 0.3)	**300** (± 7)	**0.8** (± 0.4)	**1** (± 27)	**1.3** (± 0.2)	**319** (± 16)	**2.4** (± 0.3)	**18** (± 8)	**2.1** (± 0.4)	**172** (± 10)
(1000)[1]	**4.1** (± 0.4)	**271** (± 6)	**0.5** (± 0.2)	**115** (± 34)	**1.4** (± 0)	**167** (± 16)	**0.9** (± 0.3)	**271** (± 26)	**0.4** (± 0.1)	**355** (± 20)
8711 (TG 4)	**2.0** (± 0.6)	**329** (± 38)	---[2]	---[2]	**3.6** (± 0.9)	**239** (± 17)	**3.3** (± 0.4)	**310** (± 20)	**1.8** (± 1.1)	**157** (± 53)
(1000)[1]	**1.4** (± 0.7)	**312** (± 56)	---[2]	---[2]	**1.2** (± 0.3)	**178** (± 59)	**1.1** (± 1)	**288** (± 25)	**0.4** (± 0.1)	**341** (± 64)
5081 (TG 9)	**11.5** (± 0.7)	**34** (± 4)	---[2]	---[2]	**17.7** (± 0.6)	**113** (± 2)	**10.9** (± 0.3)	**151** (± 4)	**3.8** (± 0.6)	**115** (± 9)
(1000)[1]	**6.9** (± 1.2)	**255** (± 10)	---[2]	---[2]	**1.5** (± 0.1)	**158** (± 39)	**0.7** (± 0.7)	**273** (± 61)	**0.4** (± 0.1)	**355** (± 34)
8096 (TG 1)	**5.8** (± 0.3)	**19** (± 4)	**1.7** (± 0.5)	**297** (± 16)	**5.5** (± 0.4)	**291** (± 4)	**4.9** (± 0.5)	**360** (± 6)	**3.3** (± 0.6)	**213** (± 9)
(1000)[1]	**3.5** (± 0.4)	**268** (± 7)	**0.5** (± 0)	**115** (± 27)	**1.4** (± 0.2)	**166** (± 30)	**0.9** (± 0.4)	**269** (± 25)	**0.4** (± 0.2)	**351** (± 52)
8713 (TG 8)	**5.8** (± 1.1)	**266** (± 11)	---[2]	---[2]	**2.5** (± 0.8)	**206** (± 77)	**2.1** (± 1.1)	**283** (± 27)	**0.8** (± 0.7)	**150** (± 64)
(1000)[1]	**7.2** (± 1.1)	**257** (± 9)	---[2]	---[2]	**1.5** (± 0)	**159** (± 39)	**0.9** (± 1)	**261** (± 64)	**0.4** (± 0.4)	**342** (± 54)
8710 (TG 6)	**2.7** (± 0.4)	**6** (± 20)	---[2]	---[2]	**2.4** (± 0.4)	**301** (± 26)	**2.9** (± 0.1)	**6** (± 22)	**3.1** (± 1.3)	**169** (± 20)
(1000)[1]	**1.5** (± 1.1)	**307** (± 17)	---[2]	---[2]	**1.2** (± 1.1)	**178** (± 49)	**1.0** (± 1.0)	**281** (± 52)	**0.4** (± 0.4)	**341** (± 47)
3853 (TG 3)	**2.6** (± 0.2)	**325** (± 9)	**2.1** (± 0.4)	**233** (± 10)	**6.9** (± 0.3)	**241** (± 3)	**5.5** (± 0.4)	**302** (± 4)	**1.9** (± 0.3)	**167** (± 63)
(1000)[1]	**3.6** (± 0.4)	**268** (± 7)	**0.5** (± 0.3)	**117** (± 24)	**1.4** (± 0.1)	**167** (± 16)	**0.9** (± 0.3)	**269** (± 26)	**0.4** (± 0.2)	**351** (± 62)
ADV	---[2]	---[2]	---[2]	---[2]	**1.7** (± 0.4)	**147** (± 57)	---[2]	---[2]	**0.4** (± 0.5)	**72** (± 60)
(1000)[1]	---[2]	---[2]	---[2]	---[2]	**1.3** (± 0.3)	**146** (± 64)	---[2]	---[2]	**0.4** (± 0.1)	**338** (± 51)

1: results from the offshore record after truncation to cover only the period covered by the other instrument (see text).
2: the record length is too short for the computation of this constituent (see Table 4-4).

The data recovered from each instrument do not correspond to the same period (as shown in Table 4-3 and Figure 4-4), and in fact include different sections of the neap/spring cycle, which can lead to results of the harmonic analysis that do not describe the water surface fluctuations in full, rendering difficult a study of the offshore tidal distortion as it enters the lagoon. Therefore, consistency in the comparison between offshore and lagoonal tidal records is provided by using the same period for both records, i.e., by truncating the offshore data to cover only the period for which the lagoonal data is available. The harmonic analysis results of the corresponding truncated offshore data are included below the results for each instrument.

The errors shown in the tables are computed with error propagation using the following expressions provided by Foreman (1977) to compute the amplitude and phase for each harmonic component

$$a = \sqrt{\left(C \pm \sigma_C\right)^2 + \left(S \pm \sigma_S\right)^2}, \quad \theta = \tan^{-1}\left(\frac{S \pm \sigma_S}{C \pm \sigma_C}\right), \tag{4.1}$$

where the parameters C and S, and their corresponding standard deviations σ_C and σ_S, are output by the harmonic analysis program.

The harmonic analysis results show large phase errors for (1) the quarter-diurnal components, in particular for the data from the instruments having short tidal records (stations 8711, 5081, 8713, 8710, and ADV), and (2) for the phase of M_6 for 4 stations (8711, 3853, 8713, and ADV) and all the truncated offshore records. In addition, the results from the ADV show the amplitudes of K_1 and M_2 to be significantly smaller than for the other offshore record.

An attempt to reduce the error estimates mentioned above was done using the admittance technique. The admittance function, also known as the frequency response function, has shown to be valuable when analyzing short series of observations (Filloux, 1971; Godin, 1976). Given two sets of observations *x(t)* (i.e., the *long* input series, for which we assume to have a detailed knowledge of the spectral structure) and *y(t)* (i.e., the *short* output series, for which we want to improve knowledge of its spectral structure), whose power spectra $X(\sigma)$ and $Y(\sigma)$, as well as their cross-spectrum $S_{xy}(\sigma)$, are known to exist over the frequencies of interest, the admittance function is defined by:

$$Z(\sigma) = \frac{S_{xy}(\sigma)}{X(\sigma)}. \tag{4.2}$$

The new amplitude and phase of each constituent of the short record as a function of the long record results and the admittance function are given by

$$a_s = a_l \times \left(|Z| \pm e_Z\right), \quad \theta_s = \theta_l - \left(\arg(Z) \pm e_Z\right), \tag{4.3}$$

where s and l are for the short and long records, respectively, and e_Z is the probable error in amplitude and phase (radians) of Z, which, provided it is small, is given by

$$e_Z(\sigma) \sim \sqrt{\left(\frac{1-\gamma^2(\sigma)}{\gamma^2(\sigma)}\right)\left(\frac{1}{(1-P)^{1/(\Delta T)}}-1\right)} \tag{4.4}$$

where P is the probability that the error will not exceed e_Z, T is the duration of the observations over which Z has been evaluated, Δ is the resolution (bandwidth) chosen, and γ is the coherence (the spectral equivalent of the cross-correlation), which measures the degree to which the individual bands of the spectra of *x(t)* and *y(t)* are related, is given by

$$\gamma(\sigma) = \frac{|S_{xy}(\sigma)|}{\sqrt{X(\sigma)Y(\sigma)}}. \tag{4.5}$$

In turn, the coherence γ is itself an estimate of the true coherence, and the expressions to estimate its own confidence limits can be found in Godin (1976).

The bandwidth for the computation of the power and cross spectra was optimized by minimizing the error and maximizing the coherence. The optimal size was found to be $\Delta = 0.01$ cph for all the instruments, except for the ADV (shortest record), for which $\Delta = 0.02$ cph.

The results of the admittance technique represent in some stations an improvement in terms of the error in the phase estimates of some of the constituents listed in Table 4-5, as shown in Table 4-8, and of some other constituents (in particular μ_2, L_2, η_2, and S_4). This technique also represents an improvement, compared to the harmonic analysis method, in terms of the estimate of the M_2 amplitude from the eastern offshore tidal record (ADV). While the harmonic analysis method estimate is 69.7 ± 2.8 cm, the estimate using the admittance function is 100.3 ± 1.9 cm, which is, as expected, similar to the value obtained from the long western offshore record (99.3 ± 0.2 cm). However, the improvement in the estimate of the phase errors is not consistent in all the constituents for which the harmonic analysis estimates large errors.

Table 4-8. Phase error comparison between Harmonic Analysis and Admittance Technique.

Station	Tidal constituent	Phase angle θ		
		Offshore (truncated)	Harmonic	Admittance
Main I. (8711)	MS_f	**312** (± 56)	**329** (± 38)	**239** (± 2)
	O_1	**311** (± 10)	**319** (± 11)	**319** (± 7)
Cacela (5081)	O_1	**307** (± 11)	**336** (± 10)	**335** (± 8)
Tavira (8713)	M_4	**159** (± 39)	**206** (± 77)	**204** (± 20)
ADV	M_4	**146** (± 64)	**147** (± 57)	**165** (± 12)

Moreover, the results also show that the admittance technique does not seem to estimate properly the amplitude of the different tidal constituents, due to the effects of frequency aliasing, with which the energy is not assigned to specific discrete frequencies, but rather to a "bandwidth" averaged across frequencies. This is summarized in Table 4-9, which shows the sum of all the amplitudes resolved from each station using the two methods, and from the corresponding truncated offshore record using the harmonic analysis method. It is assumed that the sum of amplitudes can roughly represent the tidal energy. The table shows that for stations 5078, 8709, and 8712 (which have relatively long records and for which there is no reason to believe that the harmonic analysis estimates are inaccurate), the loss of energy is reasonably small, 3 to 5 times smaller than what the admittance technique suggests. The stations that show an apparent "gain" of energy suggest that the growth of amplitude of the higher harmonics is not only caused by tidal distortion, but possibly to co-oscillation (due to tidal wave reflection from the head of the embayment) and localized resonant effects. The apparent agreement between the offshore tidal energy and the result from the admittance technique seems in fact fortuitous, resulting from the compensation between the suggested resonant and/or co-oscillation effects and the numerical aliasing. Finally, the apparent gain of energy in the eastern offshore station is due to the fact that the admittance technique corrected the M_2 amplitude from what the neap period data suggested to what a larger data set would indicate.

In summary, it can be said that the overall comparison between the least-square harmonic analysis method and the admittance technique indicates that the latter is not a significant improvement. Therefore, the harmonic analysis was selected for the analysis of tidal distortion.

Table 4-9. Sum of amplitudes resolved (cm)

Station	Offshore (truncated) Σ(a)	Harmonic		Admittance	
		Σ(a)	Rel. diff. (%)[2]	Σ(a)	Rel. diff. (%)[2]
New I. (5078)	183.3	177.2	-3.3	167.7	-8.5
Fuzeta (8709)	188.3	181.0	-3.9	152.3	-19.1
Armona (8712)	184.6	184.8	0	171.2	-7.3
Main I.[1] (8711)	154.7	160.9	+4.0	156.1	+0.1
Cacela[1] (5081)	163.0	145.3	-9.0	121.0	-25.8
Bridge (8096)	185.7	2.00	+7.7	177.8	-4.3
Tavira[1] (8713)	163.2	166.1	+1.8	154.4	-5.4
Olhão[1] (8710)	152.7	162.9	+6.7	155.4	+1.8
Main Ch. (3853)	185.9	2.02	+7.7	186.5	0
ADV	75.3	75.7	+0.1	105.8	+40.5

[1]: stations with short records.
[2]: (station value –offshore value) / offshore value

4.4.4. Tide Data Results

The tide in Ría Formosa is semi-diurnal (Figure 4-4 and Table 4-6). The relative importance of the diurnal and semi-diurnal tidal constituents is expressed in terms of the Form Factor defined as (see, e.g., Pugh, 1987)

$$F = \frac{a_{K_1} + a_{O_1}}{a_{M_2} + a_{S_2}} \tag{4.6}$$

and the tide may be roughly classified as: semi-diurnal for $0 < F < 0.25$, mixed (mainly semi-diurnal) for $0.25 < F < 1.50$, mixed (mainly diurnal) for $1.50 < F < 3.00$, and diurnal for $F > 3.00$. For Ría Formosa F ≅ 0.1, which corresponds to a semi-diurnal tide.

The mean spring and neap tidal ranges, which, according to Uncles (1981), can be parameterized as twice the amplitude ($a_{M2} + a_{S2} + a_{M4} + a_{S4} + a_{MS4}$) and ($a_{M2} - a_{S2} + a_{M4} + a_{S4} - a_{MS4}$), respectively, are 2.80 m and 1.23 m. The measurements show a maximum spring range of

3.08 m, and minimum neap range of 0.99 m. The mean tidal range is 2.13 m (considering only three spring-neap cycles of the offshore record, i.e., 44.3 days out of the 53.4 days record).

The amplitudes of the relevant tidal constituents, as shown in Tables 4-6 and 4-7, are plotted for each station in Figure 4-5. In general terms, it can be seen that there is no definite trend of the tidal distortion as a function of the distance from the station to the closest inlet for any of the constituents, as has been observed in other studies for single-inlet systems (e.g., Aubrey and Speer, 1985). However, the figure shows the strong distortion of the tide within the lagoon, which is the result of dissipation due to friction and nonlinear spectral energy transfer. The friction translates in the reduction of the tidal amplitude and creation of phase lags, while the nonlinear distortion translates in (a) the decay of diurnal and semi-diurnal tides, (b) generation of M_2 overtides and compound tides, and (c) in the generation of the forced MS_f fortnightly compound tide.

The effect of friction on the tide is demonstrated by the decay of all diurnal and semi-diurnal constituents, and by the generation of phase lags. The decay of M_2 is generally small, with the exception of the stations Cacela and Fuzeta (33% and 17%, respectively), which are close the small and shallow inlets. The M_2 phase lag is consistently positive for all the stations and ranges from 8 to 26°. In addition, the semi-diurnal components show larger decay rates than the diurnal components for some stations. While the diurnal decays (averaged over K_1 and O_1) for Cacela and Fuzeta are 20% and 11%, the semi-diurnal decays (averaged over N_2, M_2 and S_2) are 38% and 22%, respectively. The other stations show similar decay rates in the diurnal and semi-diurnal bands, of the order of 5%. The phase is again consistently positive for all the diurnal and semi-diurnal constituents analyzed (with the exception of O_1 in Tavira), of the order of 18°, ranging from 6 to 34°.

The effect of the nonlinear growth of the M_2 overtides and its dominant compound tides can be seen in Table 4-7 and Figure 4-5. For all the stations, there is a significant growth of the amplitude of MN_4, M_4, MS_4 and M_6, which are the dominant high frequency components in Ría Formosa. In the offshore station (averaging the results from truncated tidal records), these components have amplitudes of 0.5 cm, less than 1.5 cm, less than 1 cm, and 0.4 cm, respectively. Inside the lagoon, the average amplitudes of these components are 1.7 cm, 4.2 cm (without including a_{M4}=17.7 cm at Cacela), 4.6 cm, and 2.3 cm, respectively.

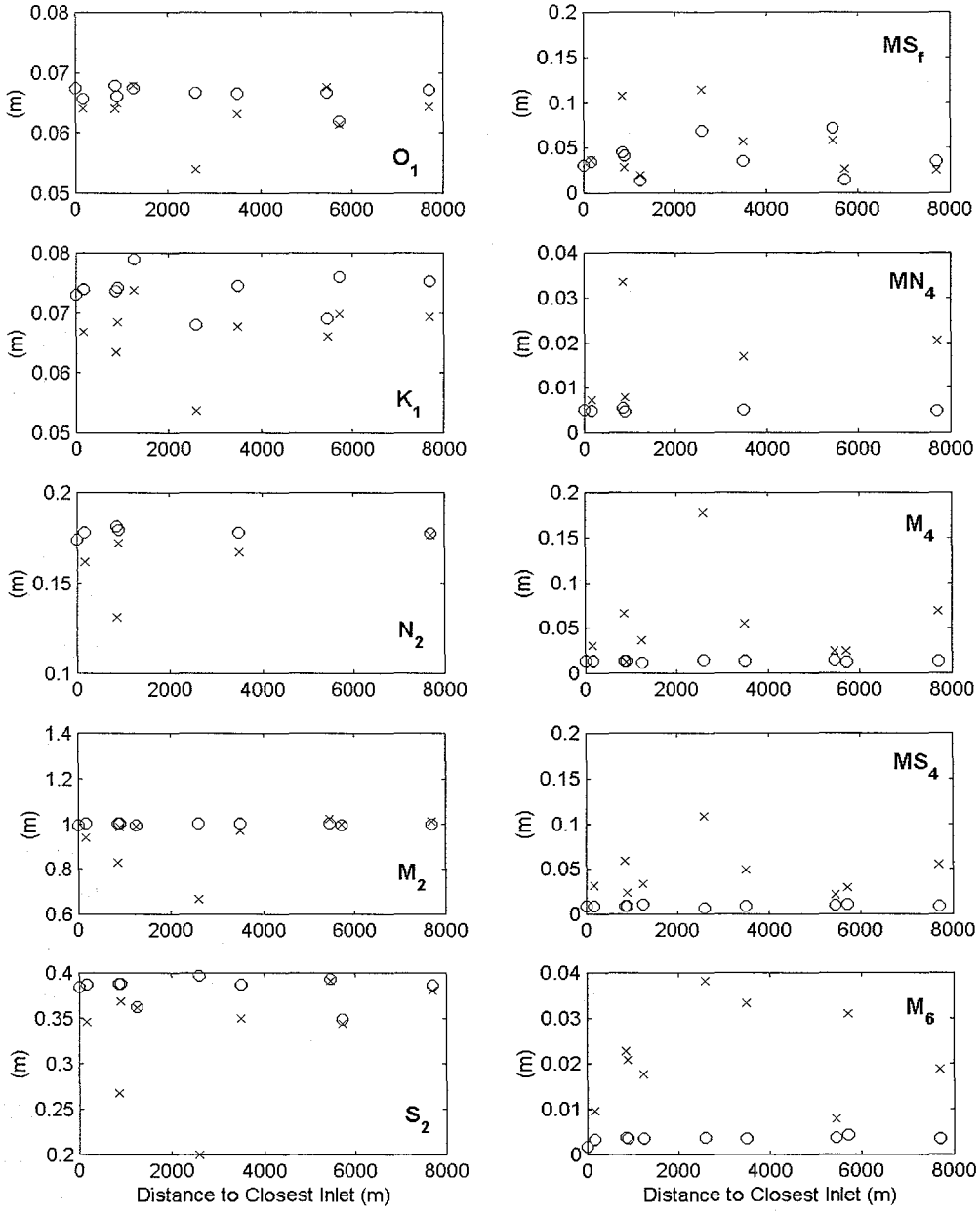

Figure 4-5. Amplitudes of selected tidal constituents from each station (*crosses*), and the corresponding truncated offshore tidal record (*circles*).

Given that the tidal asymmetry is mainly produced by the interaction of the predominant tide and its even harmonics (see, e.g., Fry and Aubrey, 1990; van de Kreeke and Robaczewska, 1993), the focus is on the semi-diurnal tide and the M_4 and M_6 overtides. In Ría Formosa the sixth-diurnal tide M_6 is one order of magnitude smaller than M_4, and therefore the major contributor to tidal distortion is M_4. Figure 4-6 shows the amplitude ratio of M_4 over M_2 and the phase of M_4 relative to M_2.

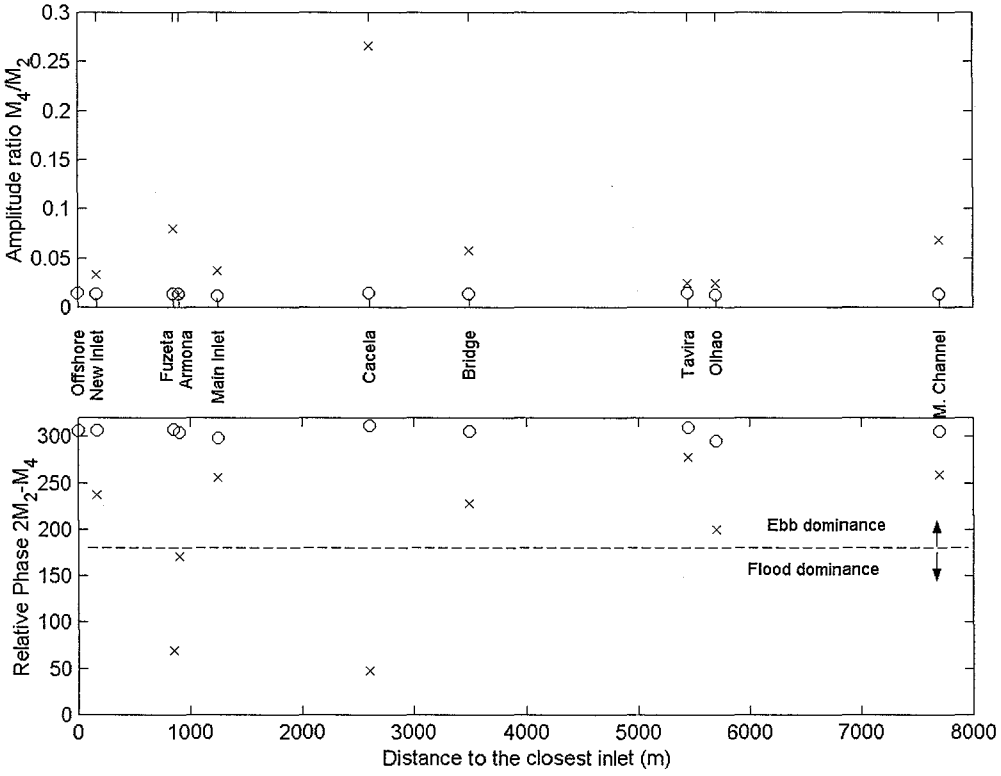

Figure 4-6. Amplitude ratio (M_4 / M_2) and relative phase ($2M_2$-M_4). Results from each station (*crosses*), and the corresponding truncated offshore tidal record (*circles*).

Neither parameter show a definite trend but it can be seen that (a) in general the growth of the M_4/M_2 amplitude ratio is significant (from 0.01 offshore to 0.03 for New Inlet, and up to 0.27 for Cacela), except for Armona, Tavira and Olhão, and (b) that the phase decreases inside the lagoon, suggesting a clear flood dominance in Fuzeta and Cacela, almost symmetry in Armona and Olhão, and ebb dominance in the other stations (following the intervals for flow dominance suggested in Figure 2-6. This finding is also confirmed in Table 4-10, where the average durations of flood and ebb for each station are listed. In Ría Formosa the amplitude of the M_4

overtide is comparable to the amplitude of the MS_4 compound tide and since these two components have similar frequencies, the large amplitude of MS_4 may affect the flow dominance suggested by the Figure 4-6.

Table 4-10. Average Flood and Ebb durations at each station (determined from the water surface elevation fluctuations).

Station	Flood Duration (h)	Ebb Duration (h)
Offshore (1000)	6:18	6:05
New I. (5078)	6:32	5:55
Fuzeta (8709)	5:41	6:45
Armona (8712)	6:17	6:10
Main I. (8711)	6:30	5:58
Cacela (5081)	4:15	8:13
Bridge (8096)	6:39	5:48
Tavira (8713)	6:25	6:02
Olhão (8710)	6:23	6:03
Main Ch. (3853)	6:45	5:42

Finally, the system filtering response is also evident in the change of flood and ebb duration as the tide enters the lagoon, as shown in Figure 4-7. The figure shows that the large high frequency fluctuations in the duration of flood and ebb at the offshore site are removed in the other stations. At some stations, a modulation of the signal to lower frequencies exists. In particular, Cacela and Fuzeta stations (and to a lesser extent Tavira, Main Channel and Main Inlet stations) show a fluctuation with a period of two weeks, which corresponds to the MS_f and the spring/neap cycle periods. In fact, comparing Figure 4-7 and Figure 4-4, the large difference between flood and ebb durations occur during spring tide, and this difference becomes small (and even reversed in some stations), during neap tide, similar to what was found by Aubrey and Speer (1985). This is an indication that the nonlinear distortion varies considerably throughout the monthly tidal cycle, which in turn can lead to considerable variability in patterns of sediment

transport. The actual sediment transport patterns depend on the velocity field, for which no long records containing both spring and neap tides were available. The numerical simulations (chapter 5) will assist in understanding the variability in the velocity field over the spring/neap cycle.

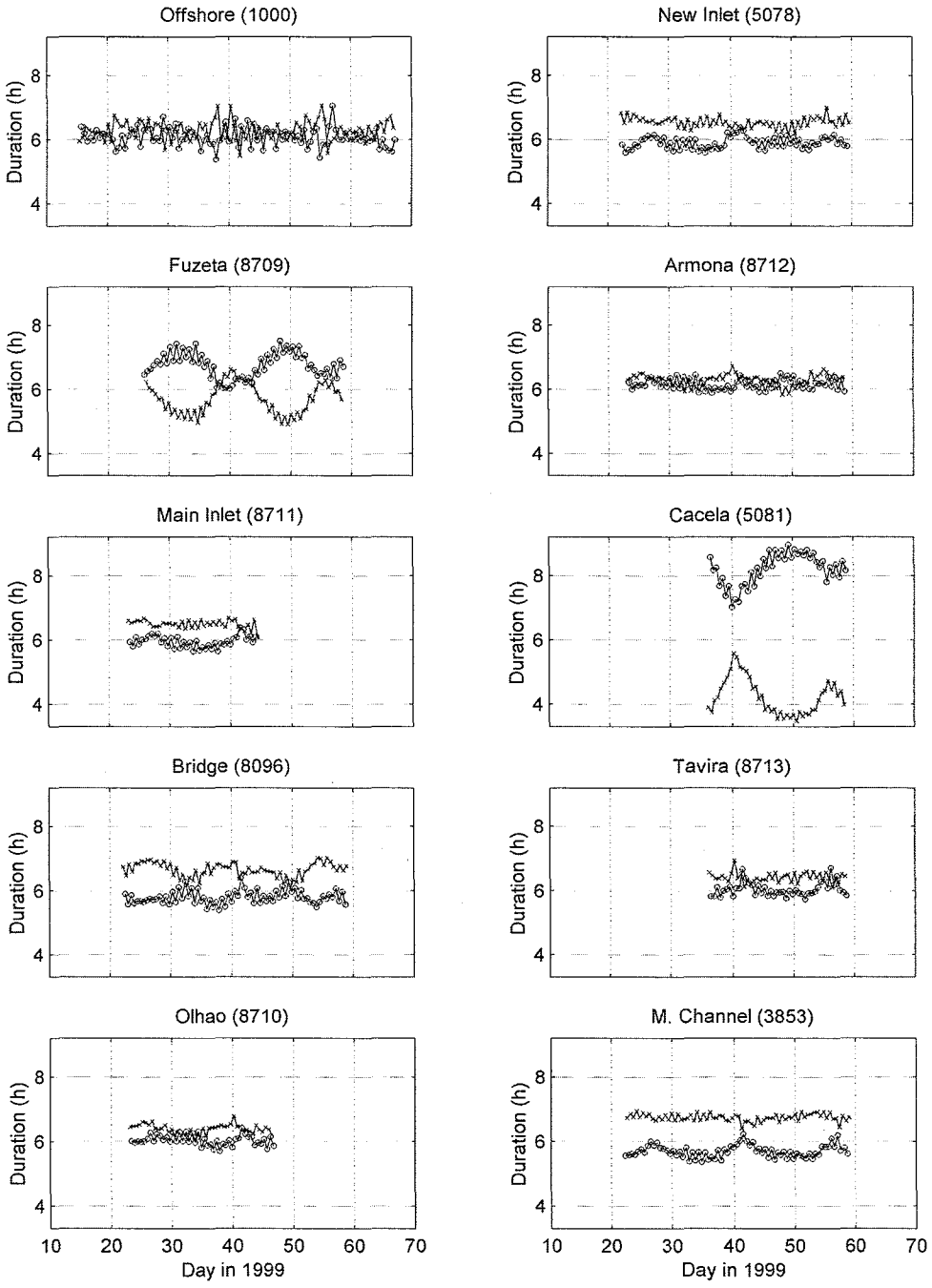

Figure 4-7. Flood (*crosses*) and Ebb (*circles*) durations for each station (determined from the water surface elevation fluctuations).

4.5. References

Aubrey, D. G. and Speer, P. E., 1985. A Study of Non-Linear Tidal Propagation in Shallow Inlet/Estuarine Systems. Part I: Observations. *Estuarine, Coastal and Shelf Science,* **21**: pp 185-205.

Emery, W. J. and Thomson, R. E., 1998. Data Analysis Methods in Physical Oceanography. Pergamon.

Filloux, J. H., 1971. Deep-Sea Tide Observations from the Northeastern Pacific. *Deep-Sea Research,* **18**: pp 275-284.

Foreman, M. G. G., 1977. *Manual for Tidal Heights Analysis and Prediction.* Pacific Marine Science Report, 77-10. Institute of Ocean Sciences. Sidney, BC, Canada.

Fry, V. A. and Aubrey, D. G., 1990. Tidal Velocity Asymmetries and Bedload Transport in Shallow Embayments. *Estuarine, Coastal and Shelf Science,* **30**: pp 453-473.

Godin, G., 1976. *The Use of the Admittance Function for the Reduction and Interpretation of Tidal Records.* Manuscript Report Series, 41. Marine Sciences Directorate, Department of the Environment. Ottawa, Canada.

Morlock, S. E., 1996. *Evaluation of Acoustic Doppler Current Profiler Measurements of River Discharge.* Water-Resources Investigations Report, 95-4218. U.S.G.S. Indianapolis, IN.

Pugh, D. T., 1987. Tides, Surges and Mean Sea Level, a Handbook for Engineers and Scientists. John Wiley & Sons.

R.D.Instruments, 1996. *Adcp Principles of Operation: A Practical Primer. 2nd Edition for Broadband Adcps.*

R.D.Instruments, 1998. Workhorse Acoustic Doppler Current Profiler Technical Manual.

Salles, P., O'Malley, S. P., Voulgaris, G. and Aubrey, D. G., 2000. *Tidal Observations at Ria Formosa, Algarve, Portugal.* Technical Report, WHOI-2000-04. Woods Hole Oceanographic Institution. Woods Hole.

Uncles, R. J., 1981. A Note on Tidal Asymmetry in the Severn Estuary. *Estuarine, Coastal and Shelf Science,* **13**: pp 419-432.

van de Kreeke, J. and Robaczewska, K., 1993. Tide-Induced Residual Transport of Coarse Sediment; Application to the Ems Estuary. *Netherlands Journal of Sea Research,* **31**(3): pp 209-220.

4.6. Appendix

ADCP Survey: designed transect Lines for each inlet

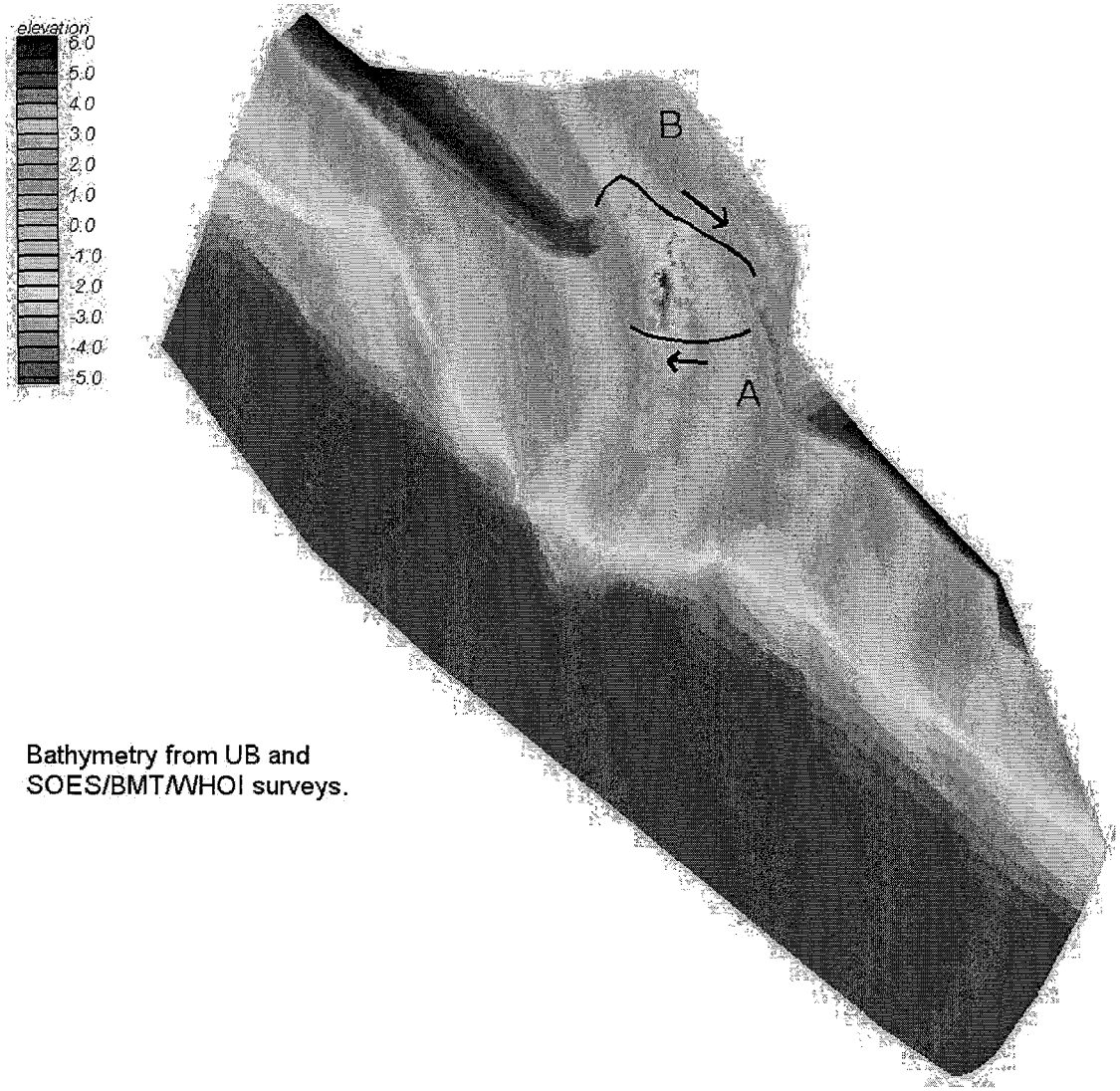

Figure 4-8. New Ancão Inlet ADCP Survey Transects.

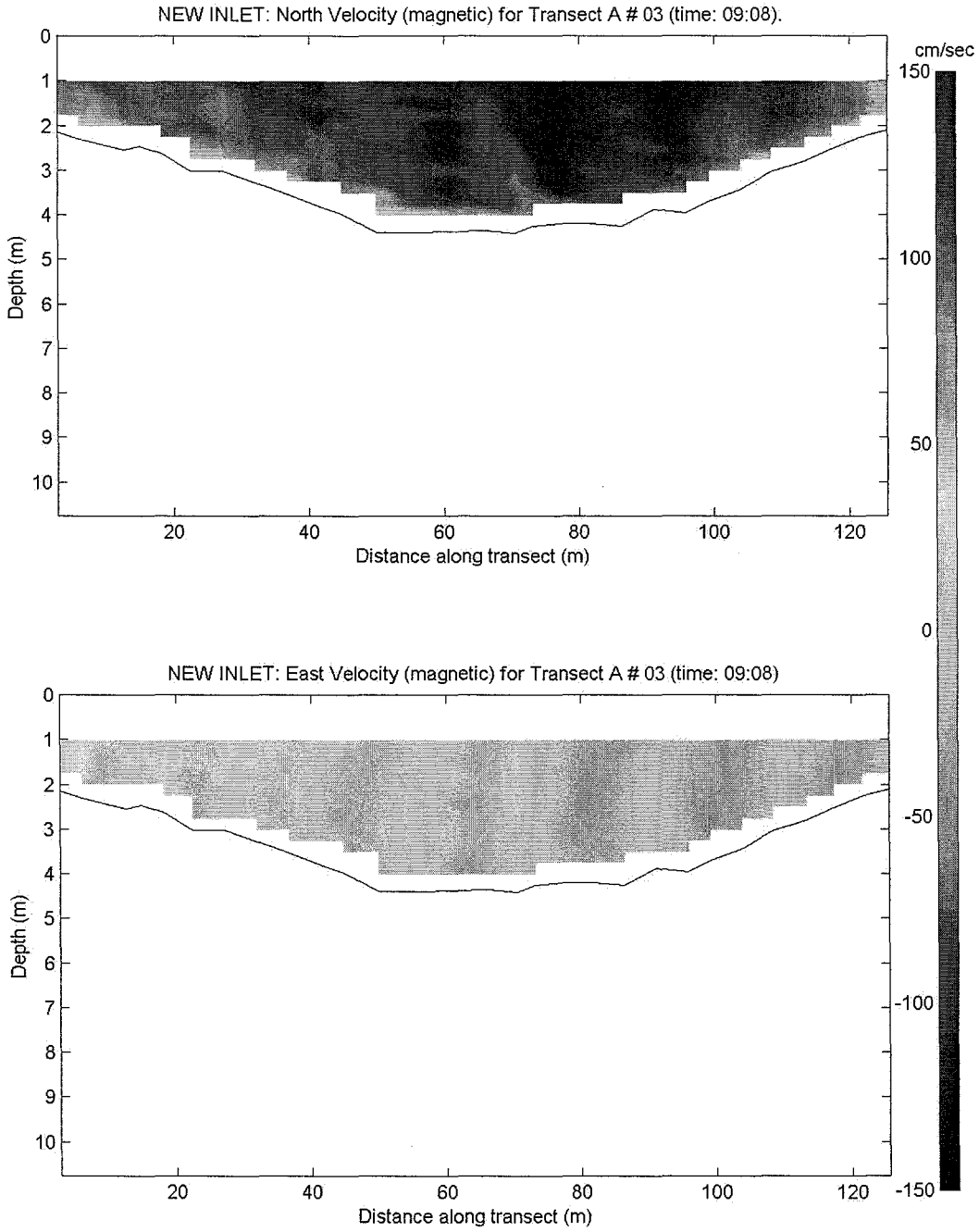

Figure 4-9. Selected Velocity Profile, Transect A, New Ancão Inlet.

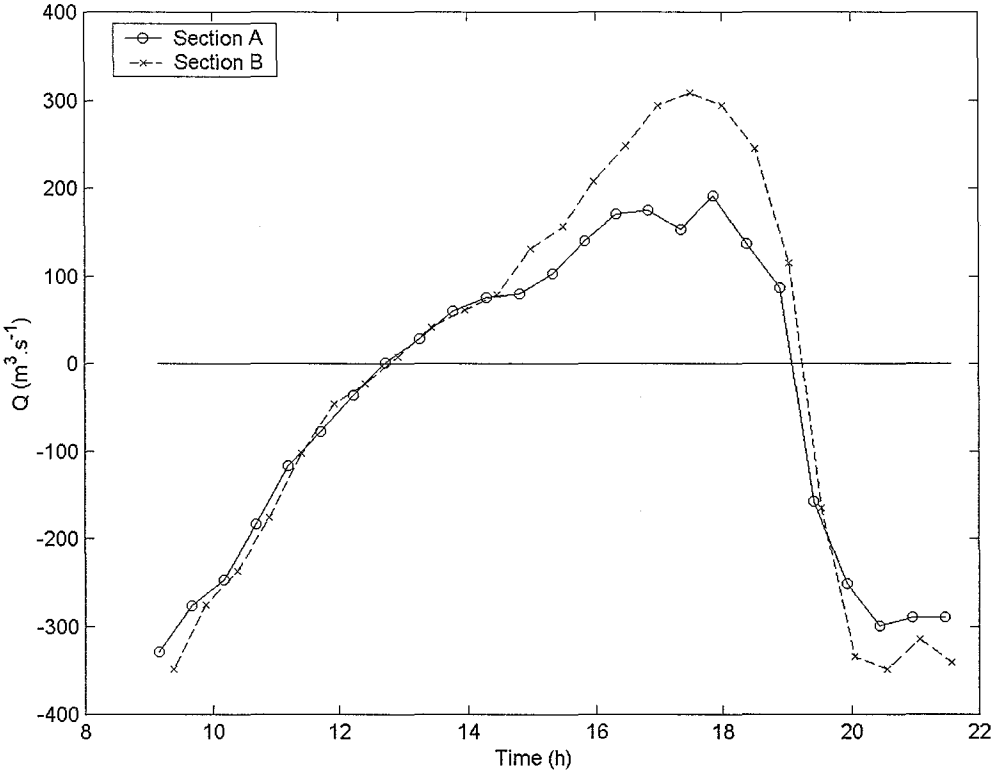

Figure 4-10. Cross-sectional discharge through New Inlet.

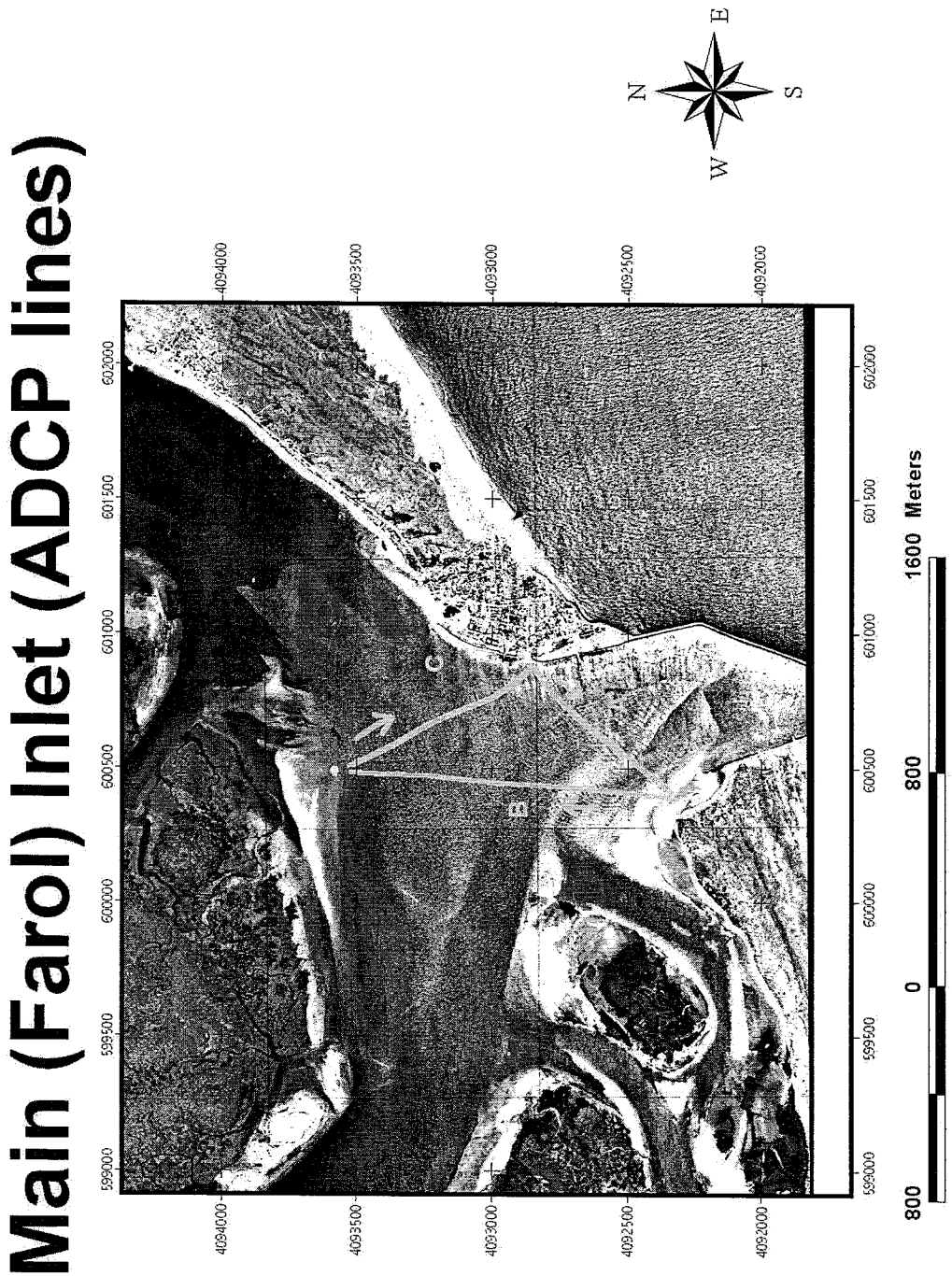

Figure 4-11. Main Inlet ADCP Survey Transects.

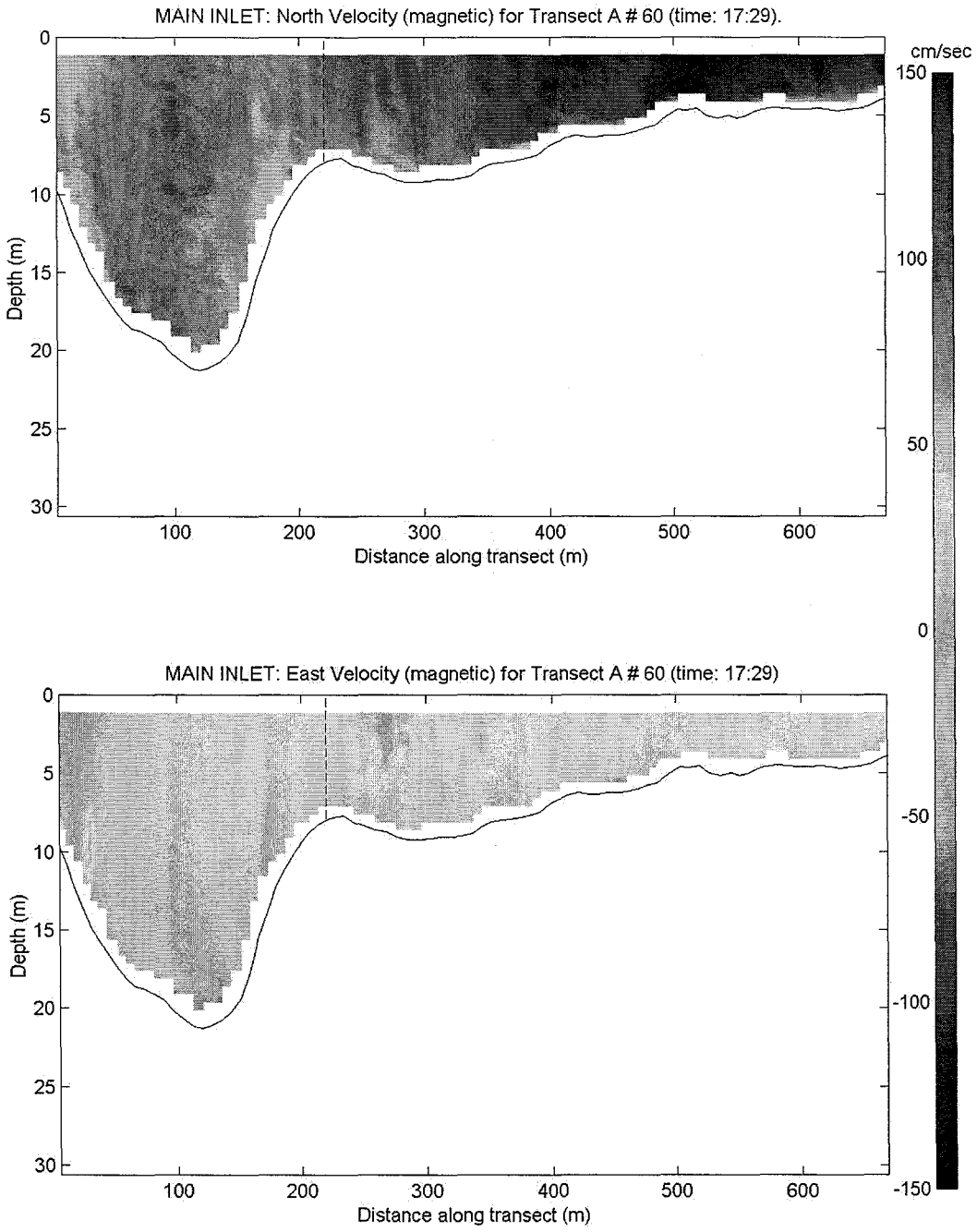

Figure 4-12. Selected Velocity Profile, Transect A, Main Inlet.

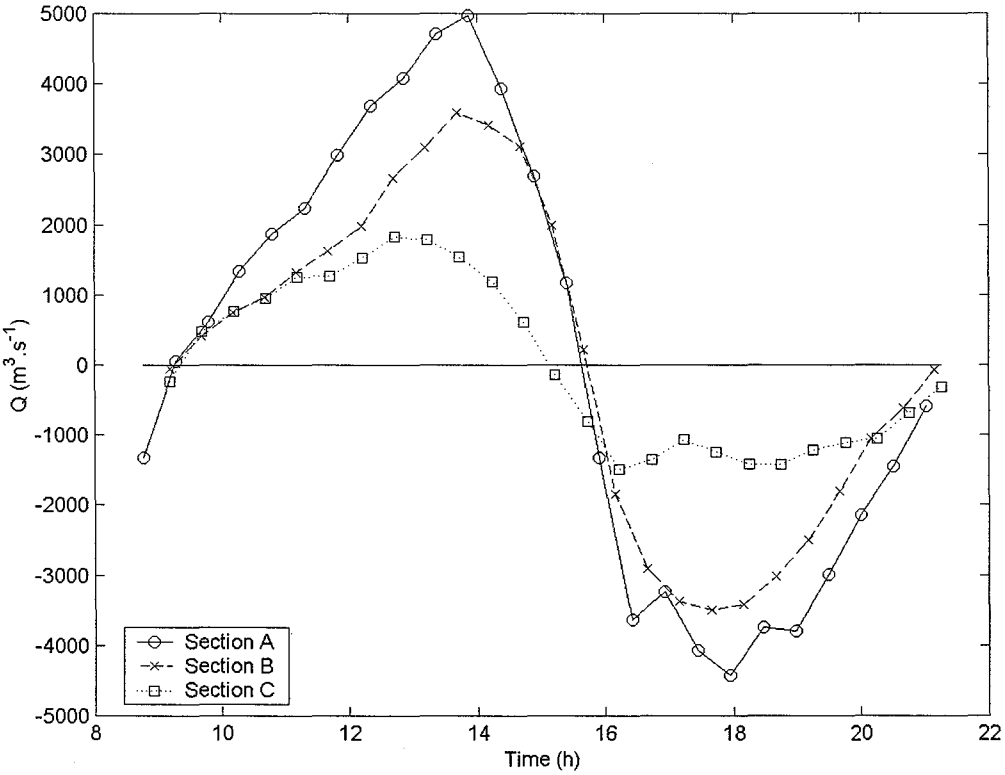

Figure 4-13. Cross-sectional discharge through Main Inlet.

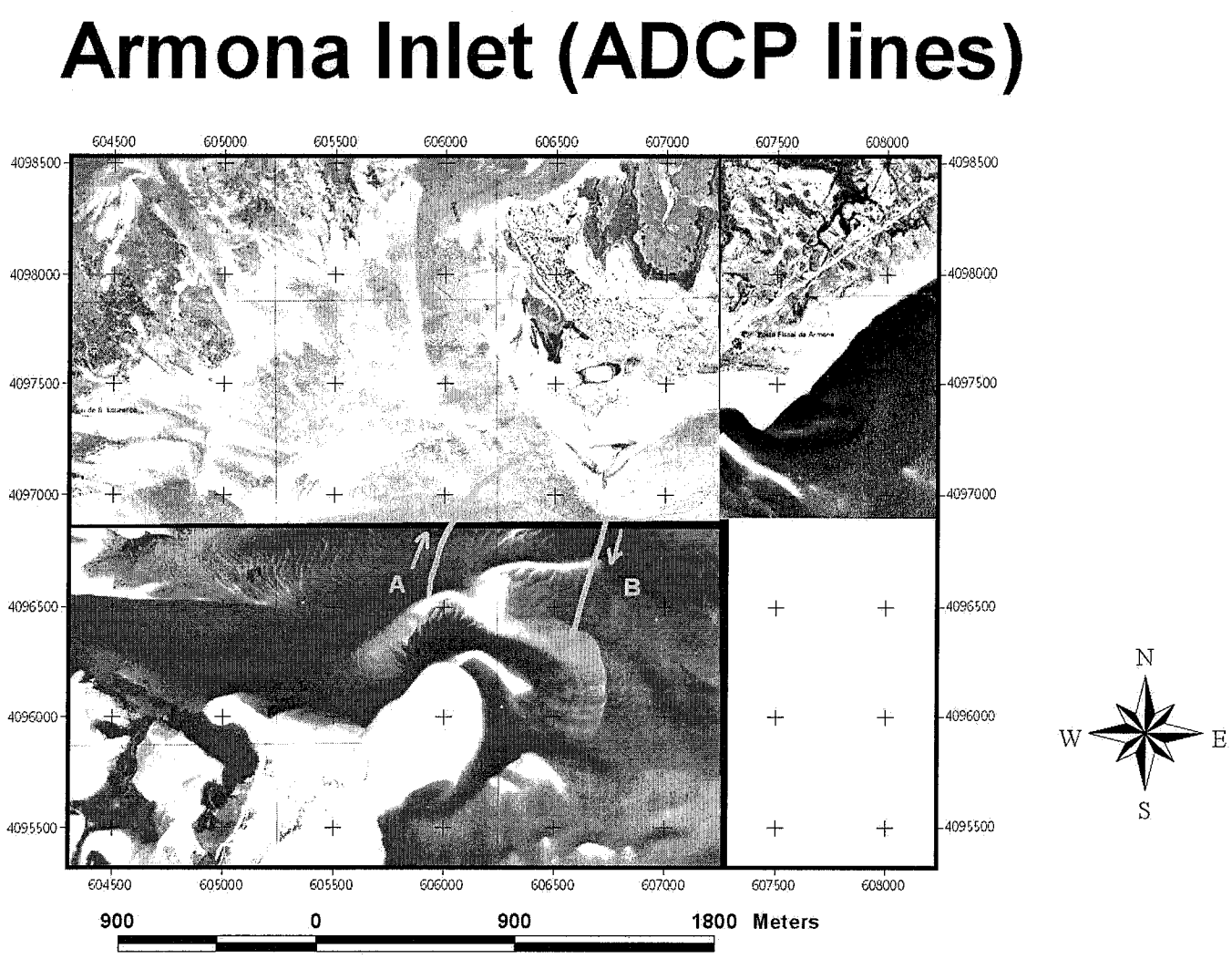

Figure 4-14. Armona Inlet ADCP Survey Transects.

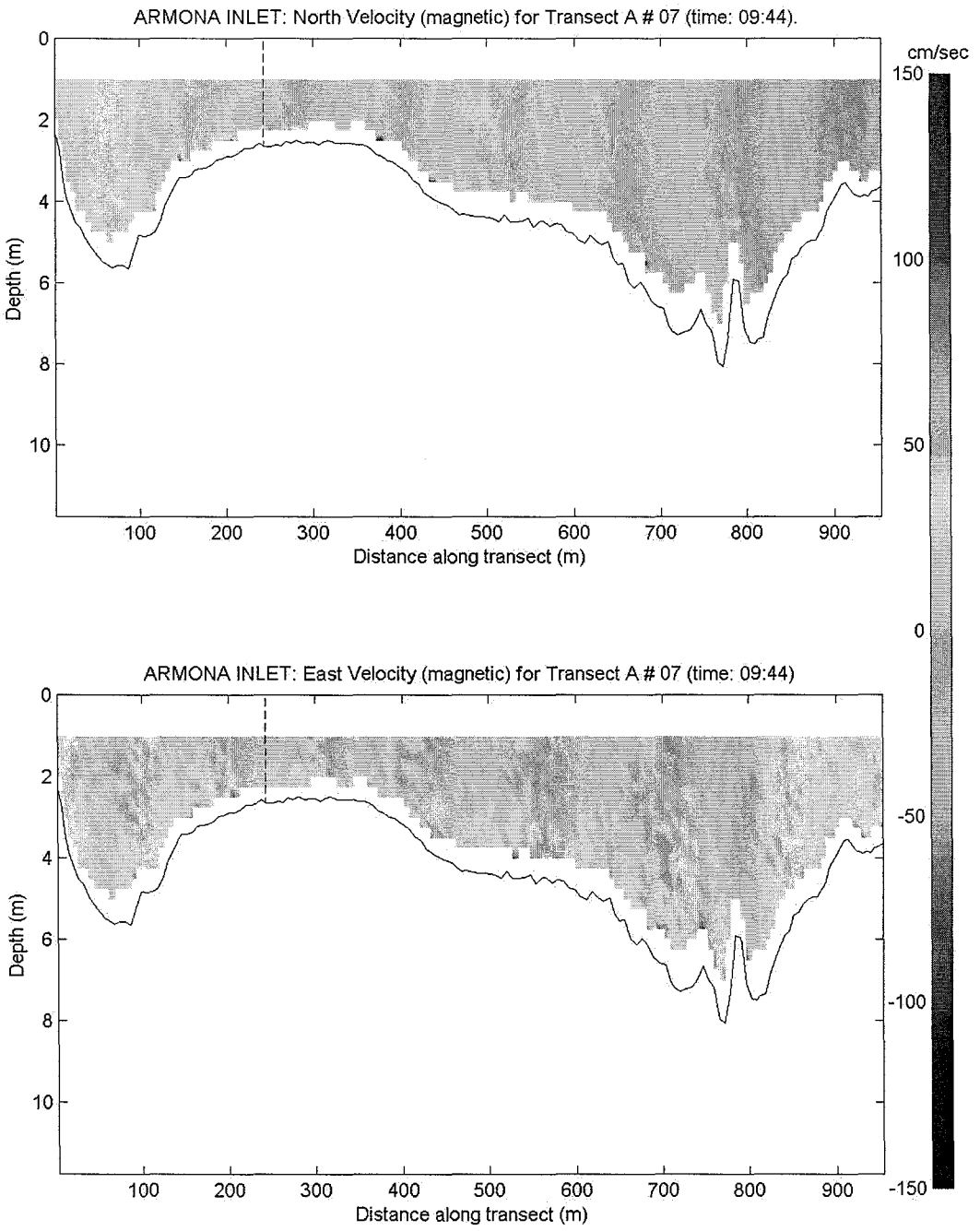

Figure 4-15. Selected Velocity Profile, Transect A, Armona Inlet.

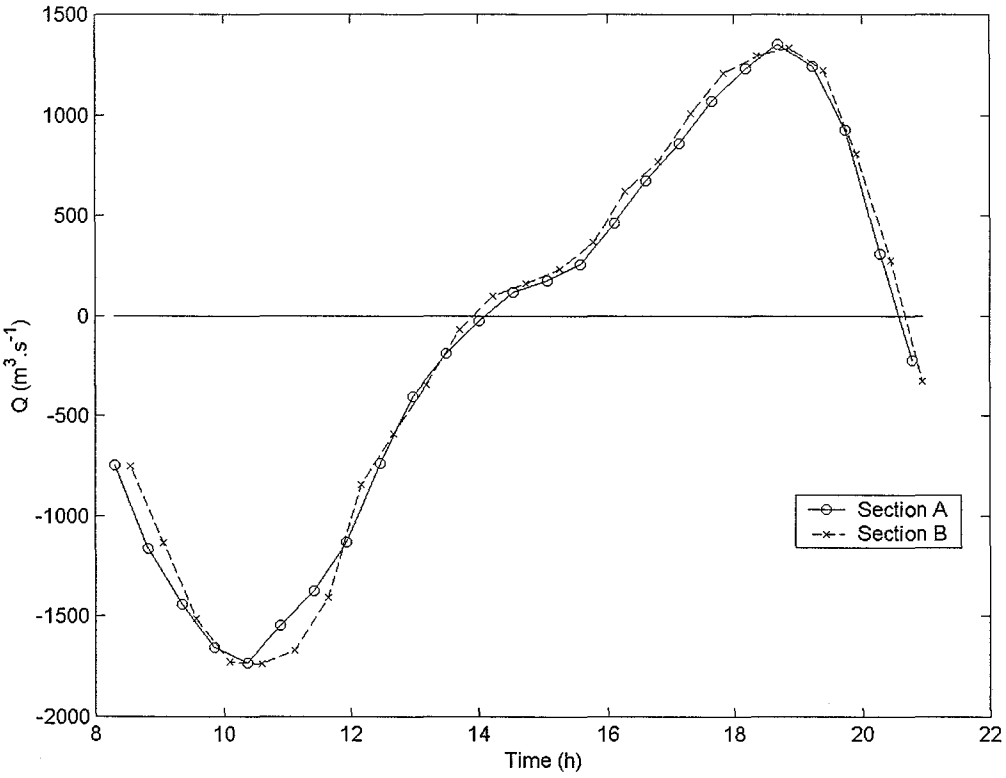

Figure 4-16. Cross-sectional discharge through Armona Inlet.

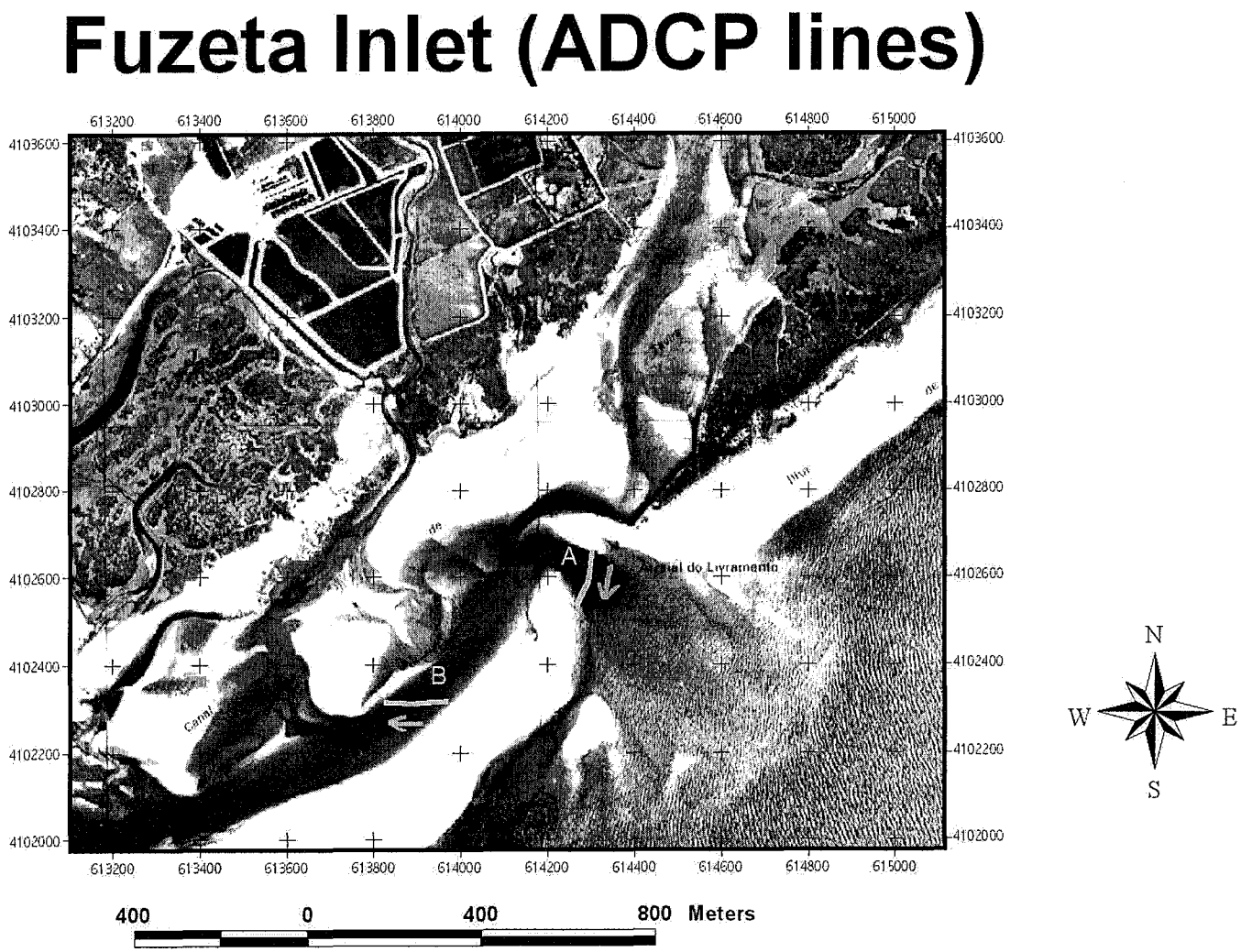

Figure 4-17. Fuzeta Inlet ADCP Survey Transects.

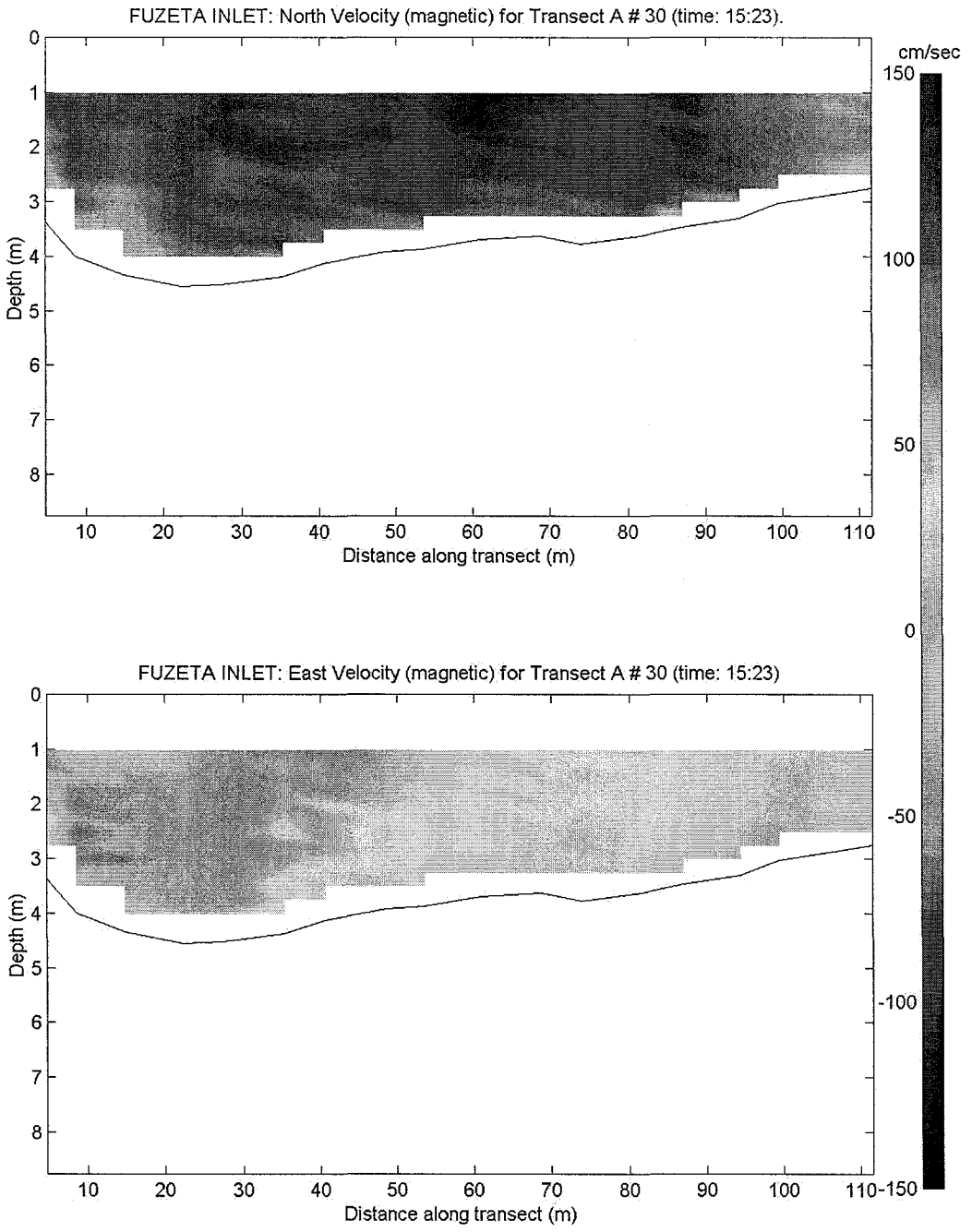

Figure 4-18. Selected Velocity Profile, Transect A, Fuzeta Inlet.

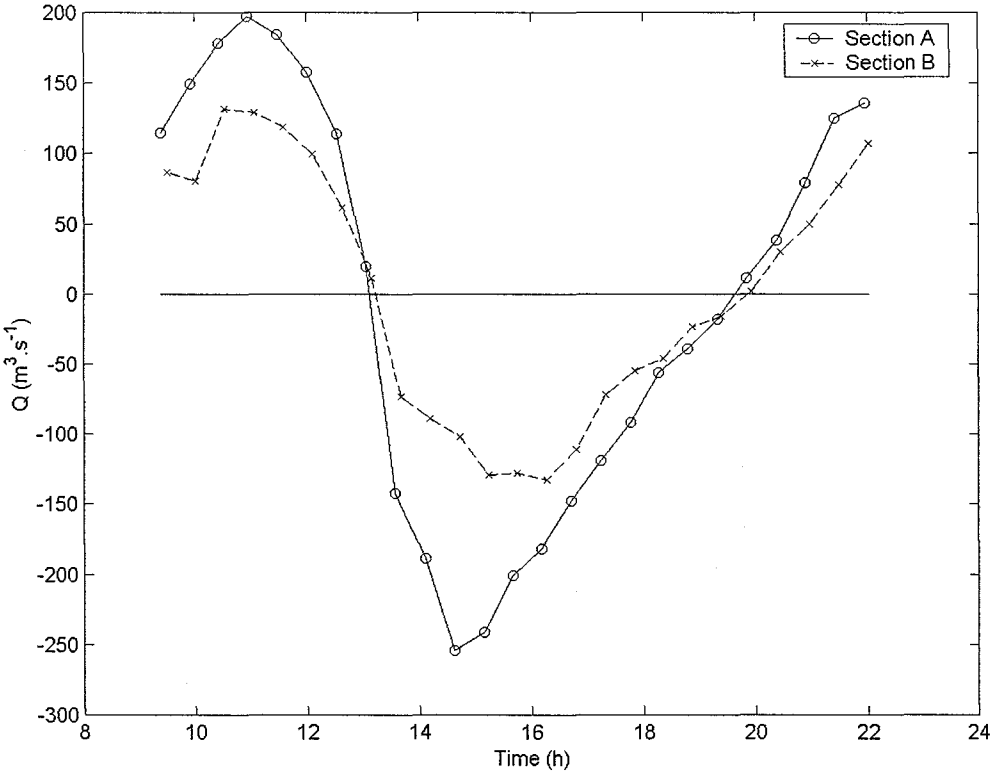

Figure 4-19. Cross-sectional discharge through Fuzeta Inlet.

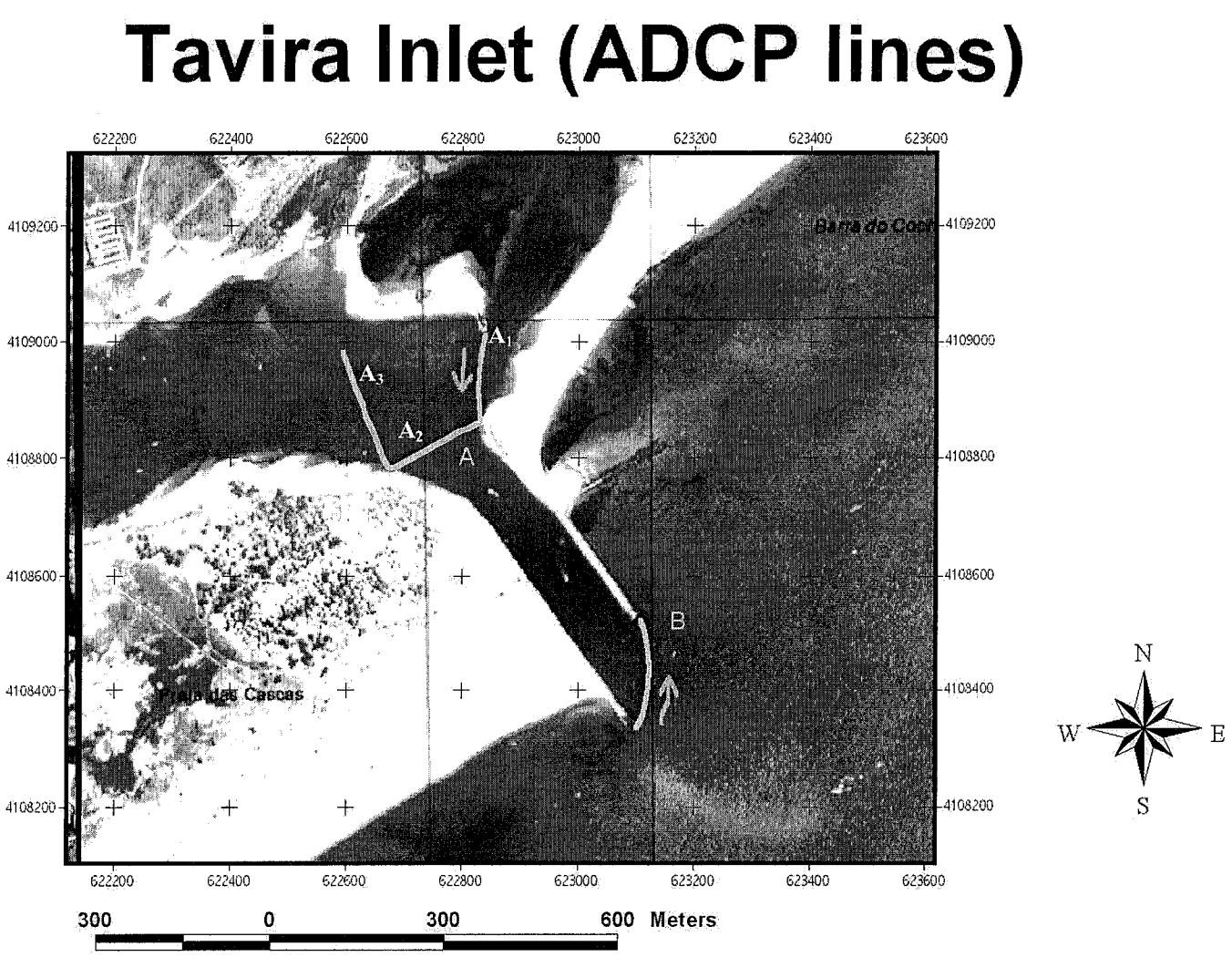

Figure 4-20. Tavira Inlet ADCP Survey Transects.

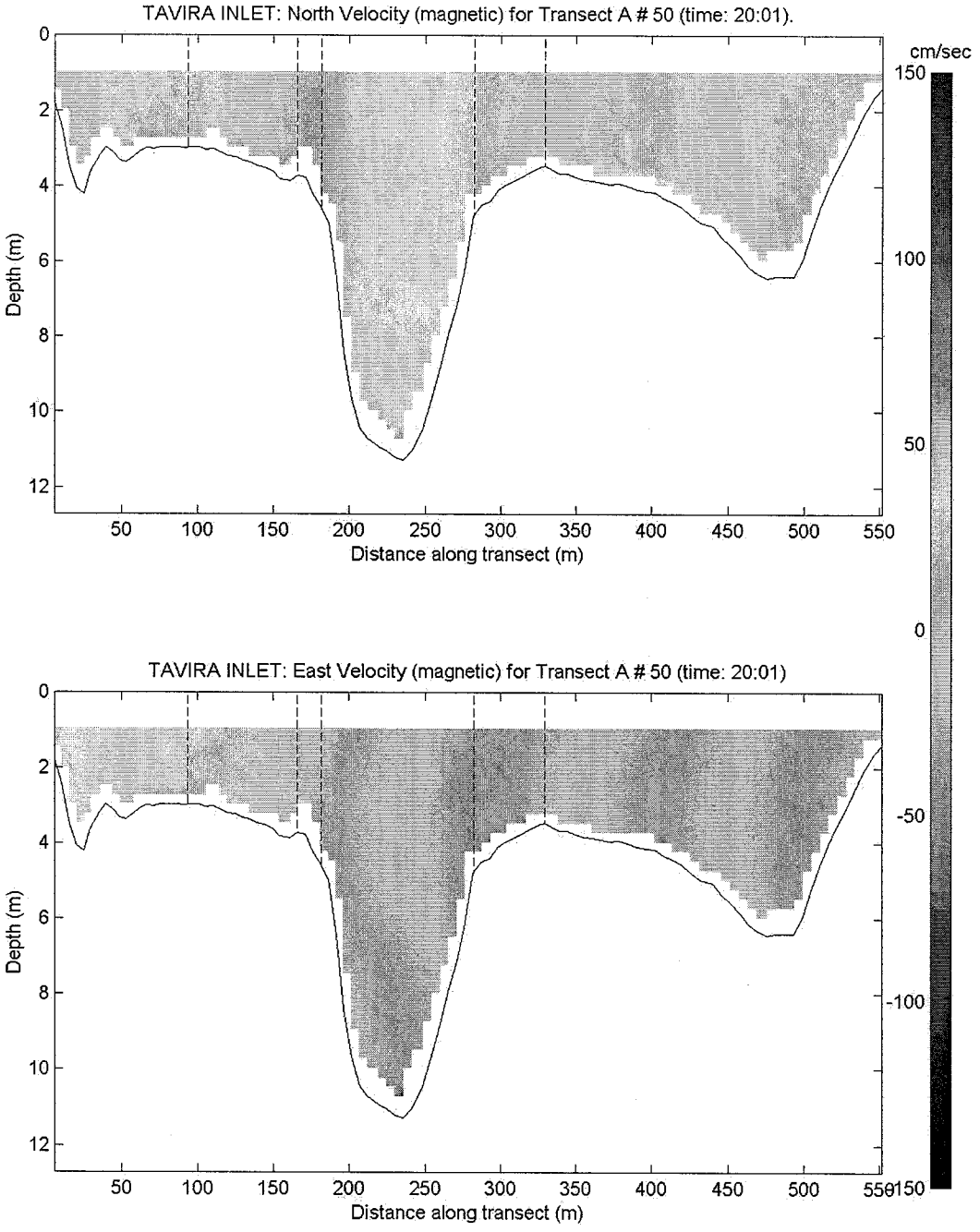

Figure 4-21. Selected Velocity Profile, Transect A, Tavira Inlet.

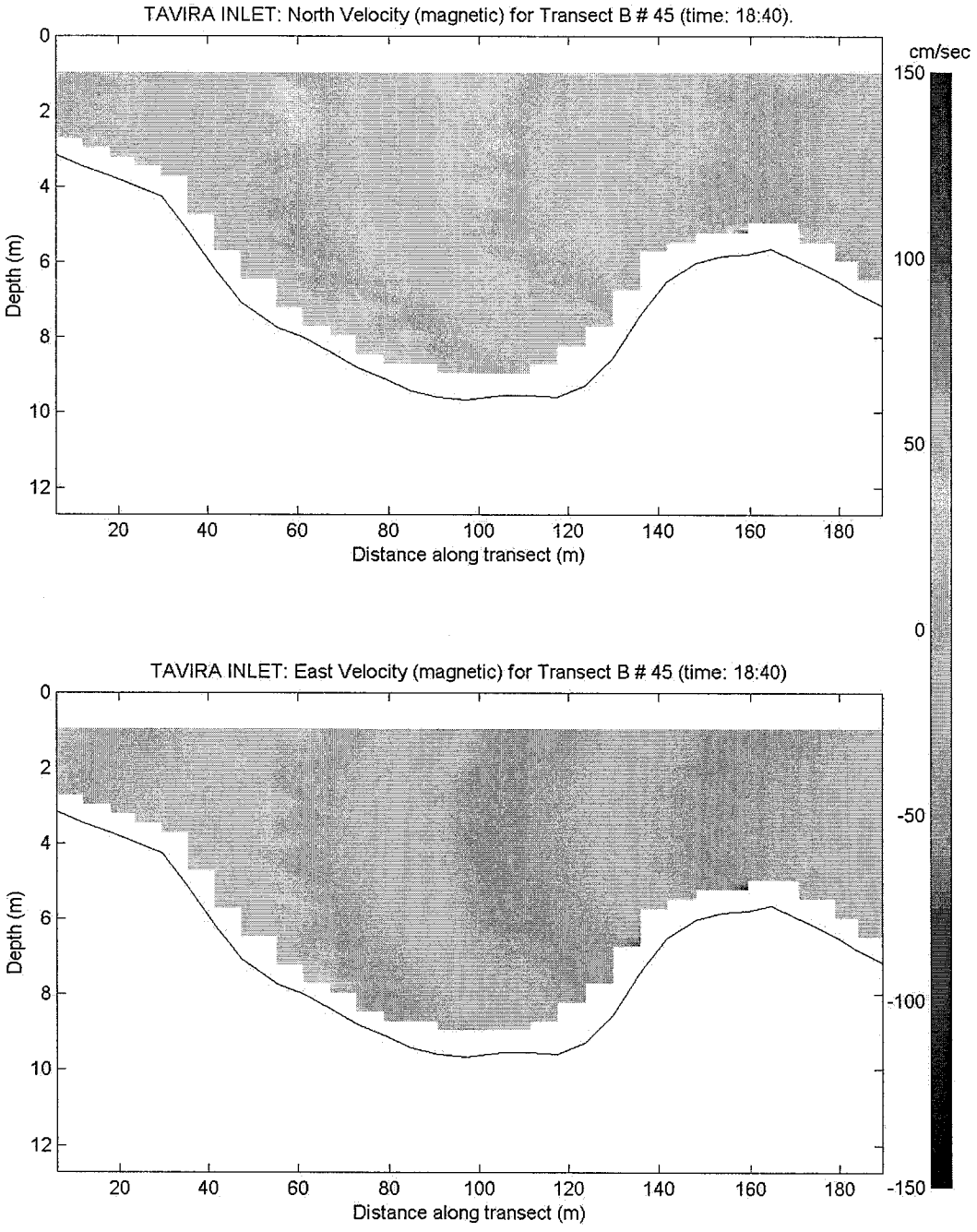

Figure 4-22. Selected Velocity Profile, Transect B, Tavira Inlet.

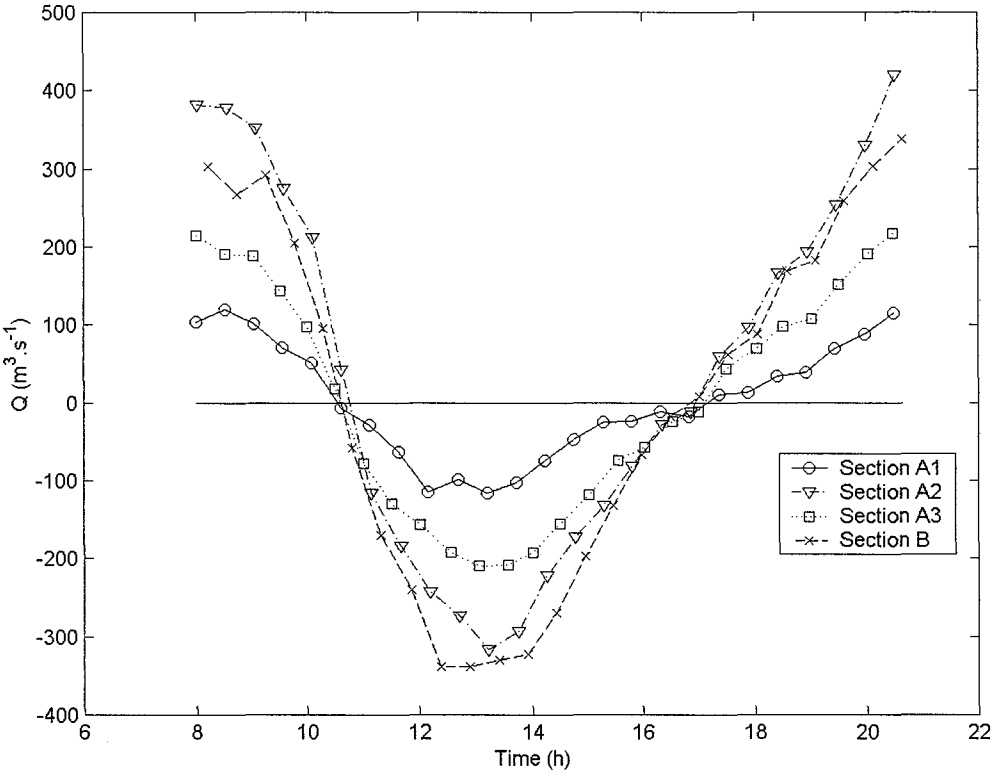

Figure 4-23. Cross-sectional discharge through Tavira Inlet. A1 is the eastern section of transect A (running north-south), A2 is the section running east-west, and A3 is the section running south-north (see Figure 4-20).

Chapter 5

Hydrodynamic Modeling and Results

For the purpose of identifying and analyzing the hydrodynamic processes contributing to multiple inlet persistence, a numerical hydrodynamic model was used to quantify the water circulation inside Ría Formosa, the exchange of estuarine water with open seawater, the tidal discharge in each inlet, and general tidal dynamics. More specifically, the flow characteristics and hydrodynamic processes relevant for this study are: a) maximum cross-sectionally averaged velocity through the inlets, b) flow (flood/ebb) dominance, c) tidal distortion, d) sediment transport capacity, and e) residual circulation. The main approach was to create perturbations in the established geometric configuration of the inlets, through the modification of the computational mesh describing the lagoon bathymetry, and to analyze the results of a series of numerical simulations, in terms of the lagoon hydrodynamic response to these disturbances.

These exercises assisted to determine to what extent i) hydrodynamic interaction between inlets sharing a single embayment is significant, ii) changes in the morphology of one inlet lead to changes in the morphology of adjacent inlets, and iii) to what extent changes in non-linear hydrodynamic processes due to inlet morphological perturbations play an important role in maintaining inlets open.

Given the negligible fresh water input into the system (see section 3.1), a two-dimensional, vertically averaged model was selected for this study. The characteristics of the model used to perform the hydrodynamic simulations are presented in section 5.1. Data obtained from the 1999 field campaign and other sources were used to setup, calibrate, and verify the model prior to simulation (section 5.2). The preparation of the different scenarios for simulation

involved modifying the computational mesh of the model in the inlet areas, as shown in section 5.3. The results of the simulations, as well as a discussion of the relevant findings in terms of changes in various hydrodynamic processes and characteristics as a response to inlet disturbance, are presented in section 5.4.

5.1. Numerical Model Selection and Description

5.1.1. Model Selection

The model selected, RMA-2V, is a finite element, two-dimensional depth-averaged hydrodynamic model. It was first developed in the early 1970s (Norton *et al.*, 1973), and has experienced several improvements and enhancements, culminating in the current version of the code supported by the United States Army Corps of Engineers (Donnell *et al.*, 1997).

The main reasons for the selection of RMA-2V for this study are:

- RMA-2's finite-element structure is flexible, allowing the construction of an irregular mesh (i.e., network of nodes joined to form elements) and the specification of varying element sizes, shapes, and dimensions (one- and two-dimensional elements). This flexibility allows an accurate modeling of the lagoon's irregular shoreline configuration and bathymetry. In addition, relatively coarse grid spacing can be used where spatial gradients are weak, without the need for implementing nested grids, as is often the case in the finite-difference models.
- The model provides an advanced marsh module, which has the capability to simulate alternately wet and dry marsh areas throughout the tidal cycle. This feature contributes to maintain numerical stability by using an algorithm that retains the dry areas in its computations, as will be explained later.
- The model's implicit solution scheme allows for the use of relatively long time steps, reducing significantly the computational time for each simulation. This is particularly convenient in this study, given the large number of simulations performed.

- The source code is available, allowing the inspection of the different routines, as well as the modification of the model output, and the improvement of the model's performance.
- RMA-2V has been used widely in research institutions, government agencies, and consulting firms worldwide, and is well supported by the developers and the users themselves.
- A pre- and post-processing application called Surface-Water Modeling System (SMS) is available and has been used to assist in the generation of the input data and in the formatting and interpretation of the output results.

SMS version 7.0 and RMA-2V version 4.35 were used for this study.

5.1.2. Model Theory

RMA-2V computes a finite element solution of the Reynolds form of the Navier-Stokes equations for turbulent flows. The model incorporates friction losses (approximated either by a Chezy or Manning formulation), Coriolis effects, surface wind stresses, rainfall, and evaporation. All coefficients associated with these terms are allowed to vary in time and space. The Coriolis effects were tested in preliminary model runs, and it was found that this term was negligible, given the dimensions of the system modeled. Wind, rainfall, and evaporation were assumed to play a negligible role in the water balance and lagoon hydrodynamics compared to the tidally-driven flow through the multiple inlets, and therefore were not taken into account. The derivation of the two-dimensional conservation of momentum equations as used by the model is presented below.

The momentum equation in the x direction in this case is:

$$\rho\left(\frac{\partial u}{\partial t}+u\frac{\partial u}{\partial x}+v\frac{\partial u}{\partial y}+w\frac{\partial u}{\partial z}\right)=-\frac{\partial p}{\partial x}+\mu\left(\frac{\partial^2 u}{\partial x^2}+\frac{\partial^2 u}{\partial y^2}+\frac{\partial^2 u}{\partial z^2}\right) \tag{5.1}$$

where ρ is the water density, u, v, and w are the velocity components in x, y, and z, respectively, and p is the hydrostatic pressure. Assuming w negligible and integrating Equation (5.1) over the depth h results in

$$h\left(\frac{\partial u}{\partial t}+u\frac{\partial u}{\partial x}+v\frac{\partial u}{\partial y}\right)+gh\left(\frac{\partial a}{\partial x}+\frac{\partial h}{\partial x}\right)-\frac{h}{\rho}\left(E_{xx}\frac{\partial^2 u}{\partial x^2}+E_{yx}\frac{\partial^2 u}{\partial y^2}\right)-\frac{\tau_{zx}}{\rho}=0 \tag{5.2}$$

where g is the acceleration of gravity, a is the bottom elevation (keeping the RMA notation), E_{xx} and E_{yx} are eddy viscosity coefficients, and τ_{zx} is the shear stress, which is assumed to vary linearly over depth. The last term is the friction term, which involves the x-component of the bottom shear stress, and can be expressed in terms of Manning's n. On one hand, assuming uniform steady flow (during a given time step) and negligible bed slope, the bottom shear stress can be written as in open channel flow theory as

$$\tau=\rho gRS \tag{5.3}$$

where R is the channel hydraulic radius and S is the slope of the water surface. On the other hand, Manning's equation reads

$$V=\frac{1}{n}R^{2/3}S^{1/2} \tag{5.4}$$

where V is the channel vertically averaged flow velocity, whose magnitude is in this case $(u^2+v^2)^{1/2}$. Solving for S in Equation (5.4) and substituting in Equation (5.3), and assuming $R\cong h$, leads to

$$\tau=\rho g\frac{V|V|n^2}{h^{1/3}} \tag{5.5}$$

The bottom shear stress in the x-direction can then be written as

$$\tau_{zx}=\rho gn^2\frac{u\sqrt{u^2+v^2}}{h^{1/3}} \tag{5.6}$$

Substituting Equation (5.6) in Equation (5.2), results in the x-momentum equation

$$\boxed{h\left(\frac{\partial u}{\partial t}+u\frac{\partial u}{\partial x}+v\frac{\partial u}{\partial y}\right)+gh\left(\frac{\partial a}{\partial x}+\frac{\partial h}{\partial x}\right)-\frac{h}{\rho}\left(E_{xx}\frac{\partial^2 u}{\partial x^2}+E_{yx}\frac{\partial^2 u}{\partial y^2}\right)-\frac{gun^2}{h^{1/3}}\sqrt{u^2+v^2}=0} \tag{5.7}$$

Similarly, the momentum equation in the y direction reads

$$\boxed{h\left(\frac{\partial v}{\partial t}+u\frac{\partial v}{\partial x}+v\frac{\partial v}{\partial y}\right)+gh\left(\frac{\partial a}{\partial y}+\frac{\partial h}{\partial y}\right)-\frac{h}{\rho}\left(E_{xy}\frac{\partial^2 v}{\partial x^2}+E_{yy}\frac{\partial^2 v}{\partial y^2}\right)-\frac{gvn^2}{h^{1/3}}\sqrt{u^2+v^2}=0} \tag{5.8}$$

The continuity equation in two dimensions is

$$\boxed{\frac{\partial h}{\partial t}+h\left(\frac{\partial u}{\partial x}+\frac{\partial v}{\partial y}\right)+u\frac{\partial h}{\partial x}+v\frac{\partial h}{\partial y}=0} \tag{5.9}$$

Equations (5.7), (5.8), and (5.9) are the equations solved by the finite element method using the Garlekin method of weighted residuals. Integration in space is performed by Gaussian integration, and derivatives in time are replaced by a nonlinear finite difference approximation. The solution is fully implicit and the set of simultaneous equations is solved by Newton-Raphson nonlinear iteration (Donnell *et al.*, 1997). The final estimates of the velocities and water surface elevation for each node at each time step are obtained by solving the equations iteratively until the convergence criteria is met.

5.1.3. Modeling of the shallow areas

Given the relatively small depth to tidal range ratio in Ría Formosa, the wetting and drying of the shallow areas during the different stages of the tidal cycle is an important tool. The model has two ways of handling these events: "element elimination" and "marsh porosity." The first technique eliminates from the computation an element when any of its nodes has a depth less than a prescribed value, and reactivates the element when all its nodes are below the water surface. The "marsh porosity" allows each element to transition gradually between wet and dry states lowering the ability of the element to hold water until it becomes dry. Either of these methods may be used alone or in combination.

The "element elimination" technique often presents problems during the elimination and reactivation of large intertidal elements around low slack water, inducing numerical shocks in the simulation. Moreover, this technique can isolate some areas of the mesh when large flat intertidal areas are present, creating numerical instabilities. The "marsh porosity" technique is often the best approach for the dynamic simulations of systems having large areas that can potentially become dry. The residual water volume existing on a partially wet element is calculated by vertically integrating a wetted area curve associated with each node of the element. The wetted area curve defines the surface area of water as a function of water surface elevation, and is equivalent to a local hypsometric curve. An example of an empirical wetted area curve is shown in the left

panel of Figure 5-1. The data required to construct a wetted area curve are frequently unavailable, so that the model requires the specification of three parameters (A_1, A_2, and A_3) for each node. The nodal elevation in Figure 5-1-b is A_0. The capacity of a given node to carry water is reduced gradually as the water surface elevation decreases from $A_0+A_2/2$ to $A_0-A_2/2$. Below that elevation, the node will hold a small fraction (A_3) of the total volume it can hold when the wetted area is 100%, until the water surface falls below A_4, for which the node becomes dry. Partially wet elements are retained until all associated nodes become dry. Dry elements re-enter the computations as soon as one associated node is "re-wet" (Donnell *et al.*, 1997). Although elements may also be eliminated with this technique (depending on the value of A_1), the storage of the element decreases gradually, and the likelihood of numerical shock is drastically reduced.

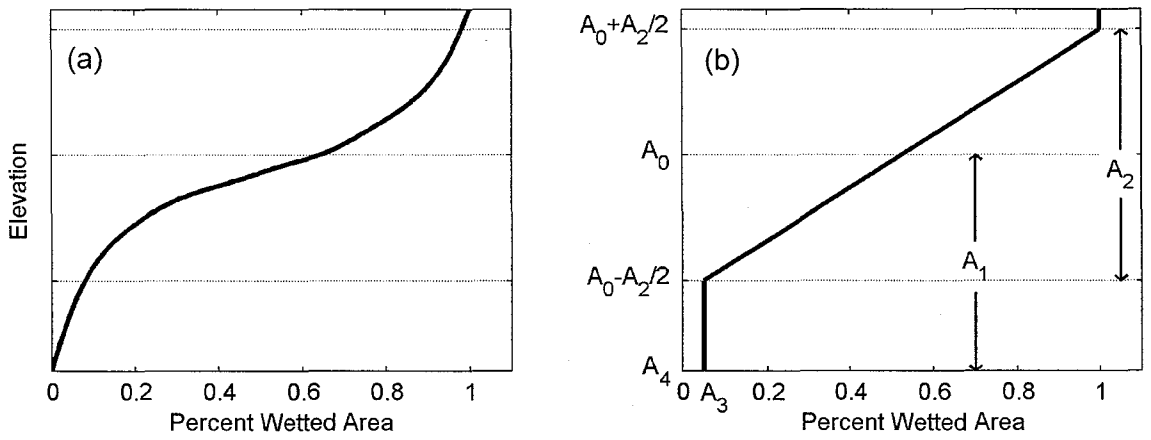

Figure 5-1. Marsh porosity parameters; (a): hypothetical nodal wetted area curve obtained from field data; (b): wetted area curve obtained with parameters A_1, A_2, and A_3. A_0 is the nodal elevation.

5.2. Model Setup, Calibration and Verification

5.2.1. Model Setup

The model setup consisted of creating the computational mesh describing the main features of the Ría Formosa lagoon (shoreline, inlets, primary channels, tidal flats), assigning elevation to the nodes of the mesh, assigning initial values of friction and eddy viscosity, and assigning boundary and initial conditions.

Mesh Generation

The physical features of the lagoon were provided as input to the model in the form of an irregular grid (i.e., network of nodes joined to form elements) extending over the entire model domain. The mesh was designed considering the tradeoffs of spatial resolution and computational capabilities. On one hand the model has to be able to reproduce the hydrodynamics of the system, but on the other hand a mesh that is too fine may require a simulation time too long, which is not practical given the number of simulations to be performed in this study. For that reason, the mesh was designed to reproduce accurately only the areas of greatest interest (inlets and main channels). The tidal flats were simplified, eliminating the secondary channels and the small features, which allowed the use of a coarse grid size in these areas.

The lagoon shoreline and the main channels were digitized from a mosaic generated with 13 orthophotomaps of the area (scale 1:10,000; aerial survey: 1991), obtained from the Portuguese Cartographic Institute. The elevation of each node of the computational mesh was assigned by interpolation from different sets of bathymetric data:

- The bathymetry of the main channels and bodies of water in Ría Formosa system was provided in the form of raw bathymetric charts, which showed both sounding values along the survey tracks and contours. In total 72 charts were acquired in November 1997 (69 charts scale 1:2,000, 2 charts scale 1:1,000, and one at scale 1:5,000), and digitized at the Woods Hole Oceanographic Institution. The maps contain information corresponding to surveys conducted in October/November 1994, which are the latest comprehensive bathymetric surveys performed in the area.
- The elevation of the intertidal areas, which represent more than $^2/_3$ of the total area of the lagoon, was estimated using a 1982 topo-bathymetric grid of the entire lagoon (grid resolution: 75 m), as well as temporary benchmarks established during the deployment in 1999 of the WHOI tide gauges (Chapter 4).
- The bathymetric data from the survey performed in 1999 in the inlets and the Main Channel by WHOI (Chapter 4), as well as the detailed bathymetry of the New Ancão Inlet channel, banks and tidal deltas performed by University of Bordeaux within the InDIA project, were used to update the 1994 bathymetry in these areas.

Due to numerical instabilities around the tips of the jetties, the open boundary at Main and Tavira inlets was constructed along a small semi-circle between the jetties, as opposed to the large fan-shaped offshore mesh at the natural inlets.

The final mesh, shown in Figure 5-2, consisted of 12,800 elements and 32,843 nodes. The bathymetry used for the computations is shown in Figure 5-3.

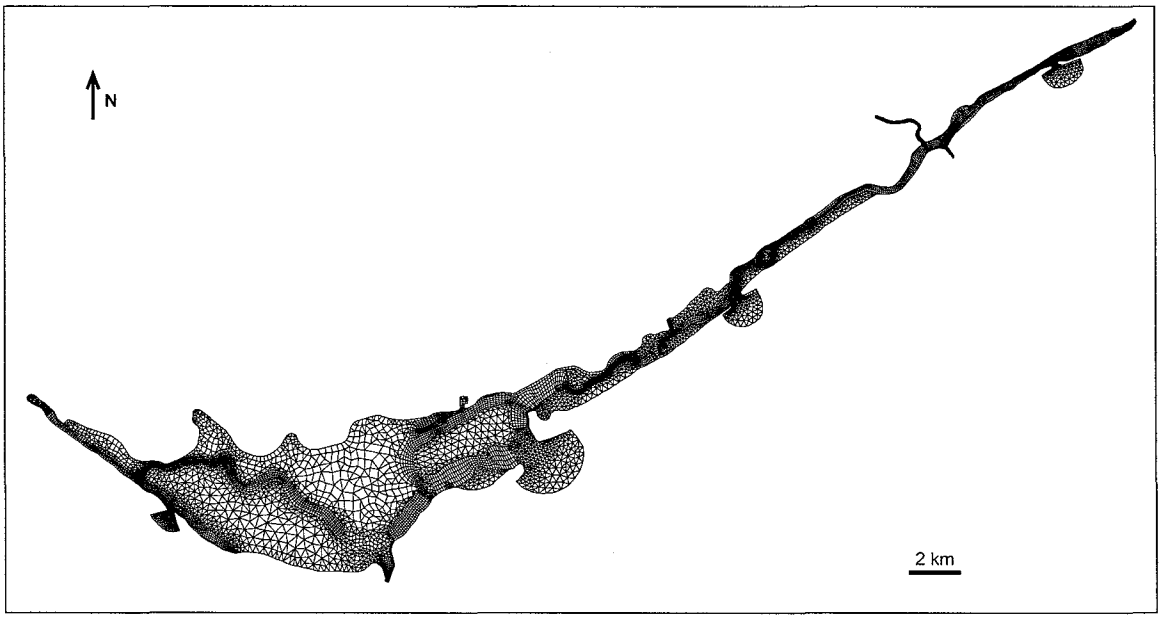

Figure 5-2 Computational mesh of Ría Formosa (12,800 elements).

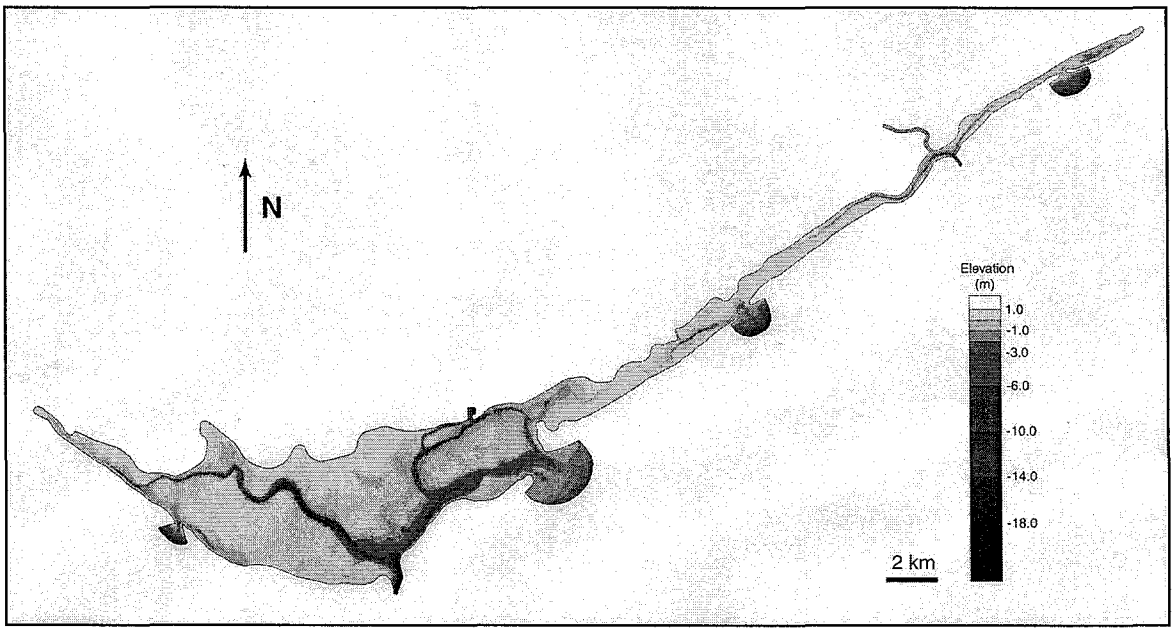

Figure 5-3 Bathymetry used for the numerical model.

Bottom Roughness Coefficients

The Ría Formosa system is composed by a network of channels and large intertidal areas, as shown in Figure 5-3 above. The subtidal channel beds are constituted of fine sand and silt in the middle and upper reaches of the lagoon, and increasing sediment size near the inlets (Bettencourt, 1994). The channels are moderately vegetated with *Zostera marina* in the deeper areas, gradually replaced by *Zostera noltii* in the shallow areas.

The tidal flats and salt marshes represent more than $^2/_3$ of the total area of the lagoon and are composed of different sedimentary environments, which have particular characteristics (elevation, vegetation, roughness) relevant for the hydrodynamic model, and can be qualitatively subdivided into four areas according to elevation and type of vegetation:

e) Low stage (-1.5 to -0.5 m relative to Mean Sea Level): this area represents roughly 15% of the surface of the lagoon.

f) Intermediate stage (-0.5 to 0.5 m relative to MSL): This sector is formed by large tidal flats ranging from silty to sandy texture. It occupies around 30% of the area of the lagoon.

g) Transition stage (0.5 to 1.0 m relative to MSL): this zone corresponds to approximately 20% of the surface of the lagoon.

h) high stage (1.0 to 1.5 m relative to MSL): this stage corresponds to the higher salt marshes and it surface is less than 5% of the surface of the lagoon.

A detailed description of the different morphologic environments was presented in section 3.1.1 (from Bettencourt, 1994).

Flow resistance in vegetated intertidal areas is dominated by form resistance due to vegetation stand, rather than solely by the bed shear as in open channel flows. Although there have been limited experimental studies of flow resistance through salt marshes, in particular focusing on the estimation of Manning's coefficient, numerous studies have been done on flow through other types of vegetation, such as those found in flood plains and agricultural fields (e.g., Chow, 1959; Ree and Crow, 1977). Studies on flow over salt marsh vegetation have focused on (a) determining the vertical variation in drag caused by plant stem wakes and canopy layers (Jackson and Winant, 1983; Ward *et al.*, 1984; Leonard and Luther, 1995), analyzing the effects of (b) canopies on the velocity profile and horizontal diffusivity (Nepf *et al.*, 1997), and (c) of eelgrass

on flow dynamics and turbulent mixing (Fonseca *et al.*, 1982; Gambi *et al.*, 1990; Worcester, 1995).

Since no previous studies have focused on estimating Manning's coefficient for the vegetation types found in salt marshes, and in particular in Ría Formosa, previous studies of flow resistance due to similar vegetation can be used to estimate realistic coefficient values. However, given that the spatial resolution of friction in RMA-2V is limited by the size of the mesh elements, an accurate representation of the various frictional environments listed above would require a large number of small elements. This approach was impractical given the computational resources available. Instead, a simplified approach was adopted prior to calibration, in which the intertidal areas were considered homogeneous and the friction parameterized by a single Manning's n coefficient. Therefore, the computational mesh was divided only into two different morphological units: channels and intertidal areas, for which different values of roughness and eddy viscosity were assigned.

The initial values for the roughness coefficients (Manning's n) were obtained from previous studies in (a) inlet hydrodynamics (Escoffier, 1977; Bruun, 1978), which used n = 0.022-0.025, (b) open channel flows (Chow, 1959; Henderson, 1966), which suggest n = 0.020-0.040 for channels ranging from "clean and straight" to "winding with pools and shoals", and (c) in studies of flow over flood plains and agricultural fields (Henderson, 1966; Ree and Crow, 1977), which estimated Manning friction coefficients ranging from 0.025 to up to 0.425 for a wide range of flow velocities and depths, and depending of the vegetation characteristics (size, height, stem strength, density). Following the estimations from these studies, and considering that the intertidal areas in Ría Formosa are generally composed of patches of vegetations surrounded by a vast networks of secondary and tertiary shallow channels, the estimates of Manning's friction factor for the model calibration ranged from 0.020 to 0.030 for the channels (including inlets), and from 0.030 to 0.120 for the intertidal areas.

Eddy Viscosity Coefficients

The eddy viscosity coefficient is the parameterization of the turbulent exchange in the flow. This coefficient is empirical and its exact value in shallow water is unknown. Previous studies have assigned a broad range of values to it. For instance, Okubo (1971) collected data from several dye-release experiments in the upper mixed layer of the sea, and presented a diagram of diffusivity versus the scale of diffusion in which the diffusivity was approximated by

$$K = 5.16 \cdot 10^2 \ell^{1.15} \tag{5.10}$$

where K is the apparent diffusivity (in Pa.s) and ℓ is the scale of diffusion (in meters). Thus, assuming the length scale of diffusivity to be of the order of 10-100 meters, K would range from $7 \cdot 10^3$ to 10^5 Pa.s. In another study, Tee (1976) used three values of E ranging from 10^3 to 10^5 Pa.s for the hydrodynamic modeling of the Minas Basin at the head of the Bay of Fundy. Kowalik and Murty (1993) suggest that an average eddy viscosity coefficient along the horizontal direction ranges from 10^4 to 10^6 Pa.s. In turn, the RMA-2V technical manual suggests $2.5\ 10^3 < E < 10^4$ Pa.s for tidal flow in a marshy estuary. A test run of the model was performed with a large value of eddy viscosity ($E = 5 \cdot 10^4$ Pa.s), and the distortion of the tide inside the lagoon resulted unrealistically large, evidencing the large sensitivity of the model to this parameter. As a first estimate prior to calibration, a value of $5.5\ 10^3$ Pa.s for the eddy viscosity coefficient was assigned uniformly to the entire system. Moreover, given the irregularity of the system, there is not a preferential direction of the flow in the Cartesian coordinate system used by the model, and therefore the eddy viscosity was considered isotropic.

Marsh Porosity Coefficients

The approach adopted for the simulation of flow over the intertidal areas was to set the "marsh porosity" parameters such that all the elements remained active throughout the tidal cycle. This approach precluded the reactivation of inactive elements during the simulation, with the consequent possibility of numerical instabilities, and resulted in areas remaining active even with the computed water surface elevation below the node elevation. Given the spring tidal range in Ría Formosa ($\cong$ 3.00 m) and the maximum nodal elevation in the mesh (+0.8 m above MSL), the parameter A_1 (see Figure 5-1) was set to 2.3 m. Considering that (i) the salt marsh zones occupy the upper region of the intertidal area (Freire de A., 1990), which roughly corresponds to the elevation range 0-1.5 m above MSL, and (ii) that *Spartina maritima* and *salicornia* stand 30-120 cm and 5-40 cm tall, respectively, the parameter A_2 was set to 1.5 m. Finally, A_3 was set to 0.02, which means that when the water surface elevation is below A_0-A_2, the nodal wetted area is reduced 2% of the area corresponding to full submergence.

This approach was not detrimental to the model's accuracy, specifically to the mass conservation, because the velocities and the volumes of water carried by these artificially wet elements were negligible (section 5.2.3).

Boundary and Initial Conditions

Two types of boundary conditions were applied to the model: 1) open boundary condition, applied at the inlet, where the tidal forcing was prescribed, and 2) parallel flow (or closed) boundary condition, prescribed at the nodes defining the limits of the computational mesh. The boundary condition for the nodes at the edge of the computational mesh places a constraint of zero velocity perpendicular to the boundary and a "slip" boundary condition in the shore parallel direction.

The boundary condition applied at the open edges of the mesh consists of water level fluctuations, and corresponds to the tidal forcing that drives the flow in and out of the lagoon. The tidal forcing applied to the model for the spin-up determination corresponded to a simple harmonic M_2 tide, in order to compare the model output from consecutive tidal cycles. The tidal forcing used for the calibration and verification of the model consisted of the measured offshore forcing, allowing the comparison of the model output with the water surface elevation and velocity measurements. For the simulations, both types of forcing were used.

In addition to the boundary conditions, the dependent variables at all the nodes must be assigned an initial value. Since the initial conditions throughout the system are not available, the simulations are started with an arbitrary assignment of a) an artificially high and uniformly flat water surface elevation, to assure that all the elements start "wet" and the effects of the marsh porosity scheme are not large, and b) zero-velocity throughout the system.

To determine the time steps for the model, there is no unique answer as to how the time step of an implicit scheme has to be chosen. Short time steps may not be practical in instances where large periods have to be modeled or several model runs have to be performed, and long time steps may result in quite large rounding-off errors. According to Kowalik and Murty (1993), comparison of the explicit and implicit numerical equations used to describe the same phenomenon gives a tentative indication that the time step of an implicit numerical scheme can be chosen 10-20 times larger than the time step of an explicit scheme. In this study, the time steps were chosen to be 30 minutes for the spring tide forcing and a multiple of the M_2 period close to 30 minutes (i.e., 0.517 h) for the simulations using single harmonic forcing.

5.2.2. Spin-up time determination

The model solutions are, for a period of time, dependent on the initial conditions and may not be sufficiently reliable since the initial water surface elevation is arbitrarily set throughout the model domain. The model has to be run long enough to achieve independence from the initial conditions, i.e., until the transient effects are negligible. The spin-up time is defined as the time required by the model to provide a solution (water surface elevation and velocity) that repeats itself within some percentage for two consecutive tidal cycles.

A test model run for nine nodes distributed throughout the system (Figure 5-4) was performed using a simple harmonic (M_2) forcing during four tidal cycles.

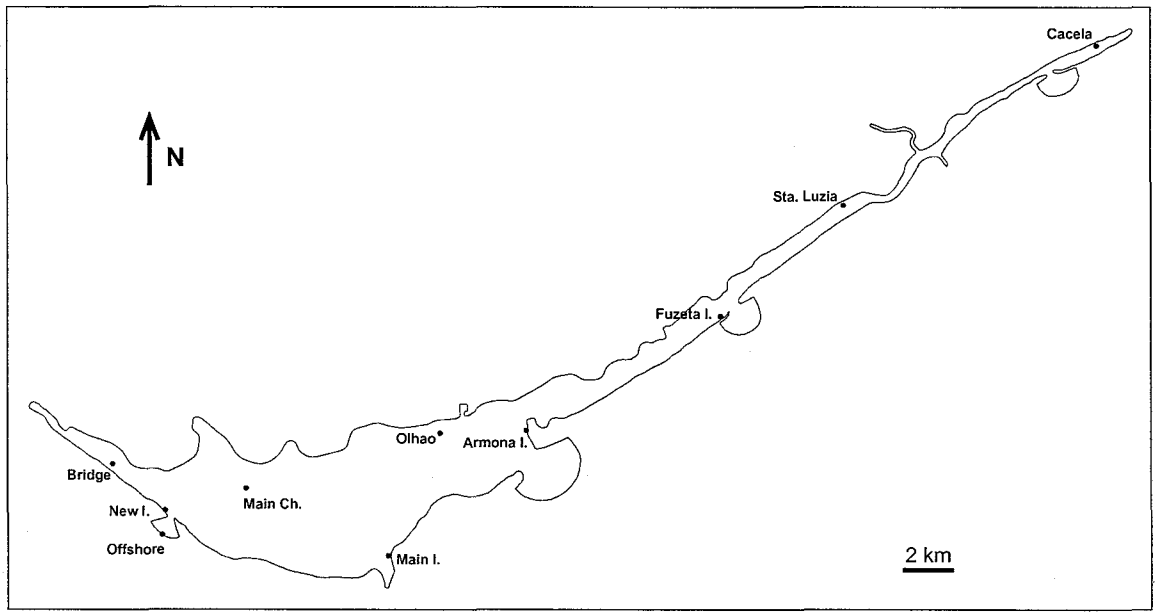

Figure 5-4. Location of stations for spin-up determination and calibration.

The modeled water surface elevation difference between consecutive tidal cycles was computed as

$$\varepsilon_\eta(t) = \left|\eta(t) - \eta(t - T_{M_2})\right| \tag{5.11}$$

where $\eta(t)$ is the water surface elevation at time t, and T_{M_2} is the M_2 period.

The results (Figure 5-5) show that the difference is of the order of 10 cm at t =14.33 h (this is the first time step repeated from the first tidal cycle given the artificially high initial condition; see section 5.2.1), decreases to less than 10^{-2} cm by the end of the second tidal cycle, and remains small for the rest of the simulation.

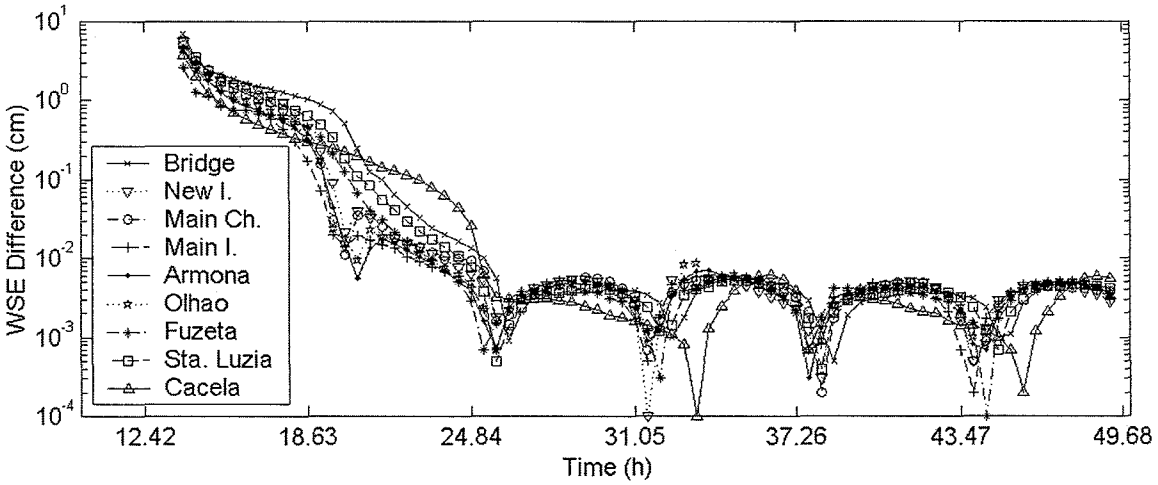

Figure 5-5. Water surface elevation difference between modeled and measured values at the 9 stations shown in Figure 5-4.

It can also be noticed that the curves in Figure 5-5 present a cycle of variation with a period of roughly half the tidal period, and that $\varepsilon(t)$ is smaller around both slack waters, which is when the smaller variations in water surface elevation between time steps occur. This cyclic fluctuation of the error is related to the numerical rounding of the simple harmonic forcing function, and ranges roughly from 10^{-2} to 10^{-4} cm.

In addition to this detailed analysis in specific locations in the lagoon, a more general, lagoon-wide analysis of the velocity magnitude and water surface elevation differences between two consecutive tidal cycles in all the nodes of the mesh was performed, and a sample of the results are shown as contour plots in Figure 5-6. The maximum differences in velocity and water surface elevation between t =1.91 h and t = 14.33 h (panels a-1 and b-1) are 1.5 cm.s^{-1}, and 1.2%, respectively. These values are reduced by two orders of magnitude when looking at the difference between the beginning of the second and third tidal cycles (t =12.42 h and t = 24.84 h), as shown in panels a-2 and b-2.

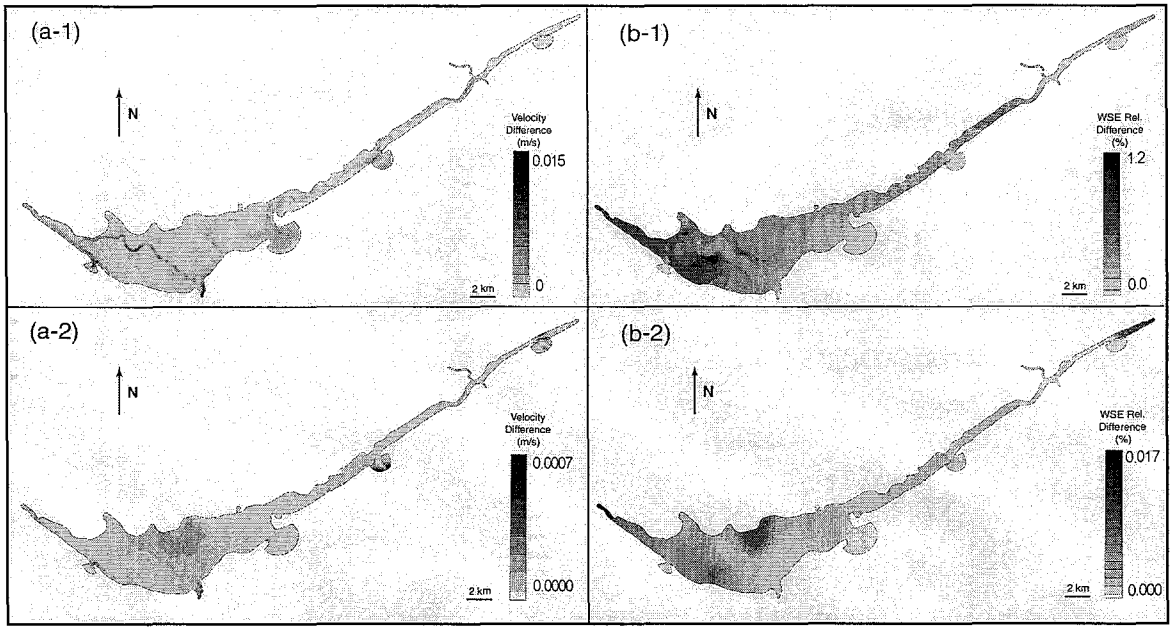

Figure 5-6. Velocity and water surface elevation (WSE) errors between consecutive tidal cycles throughout the lagoon. For velocity, the error is simply the difference between velocity magnitude at different times, and for WSE the error is the difference between the elevation at t_0 and at t_1, relative to the elevation at t_0.Velocity (a-1) and WSE (b-1) errors between t_0=1.91 and t_1=14.33 h; Velocity (a-2) and WSE (b-2) differences between t_0=12.42 and t_1=24.84 h (a-2).

Given the above, it was concluded that the model output of the second and third tidal cycles are identical for practical purposes, suggesting that the model has to be run for only two tidal cycles. This guideline is used for all the calibration and verification simulations.

5.2.3. Mass Conservation

Numerical models, and in particular finite element models such as RMA-2, are susceptible to have problems with conservation of mass due to numerical approximations when solving the governing equations. This problem is likely to be significant if the computational mesh is not implemented properly (inadequate smoothing of sharp elements, steep bathymetry). Therefore, prior to calibration, the model was run and the output was checked for conservation of mass, in order to detect potential problems of "leakage." The forcing consisted of four M_2 tidal cycles (1 m amplitude), and the friction and eddy viscosity coefficients used were: $n_{channels}$ = 0.022, n_{flats} = 0.12, and E = 5,500 Pa.s. Figure 5-7 shows the time series of the sum of discharges through all the inlets (solid line), and the offshore tide (dotted line) superimposed. The results show that the total flood and ebb tidal prisms (computed as the average for three tidal cycles) differ only by 1%.

In other words, there is not significant numerical mass "loss" or "gain," and the model results are reliable for analysis.

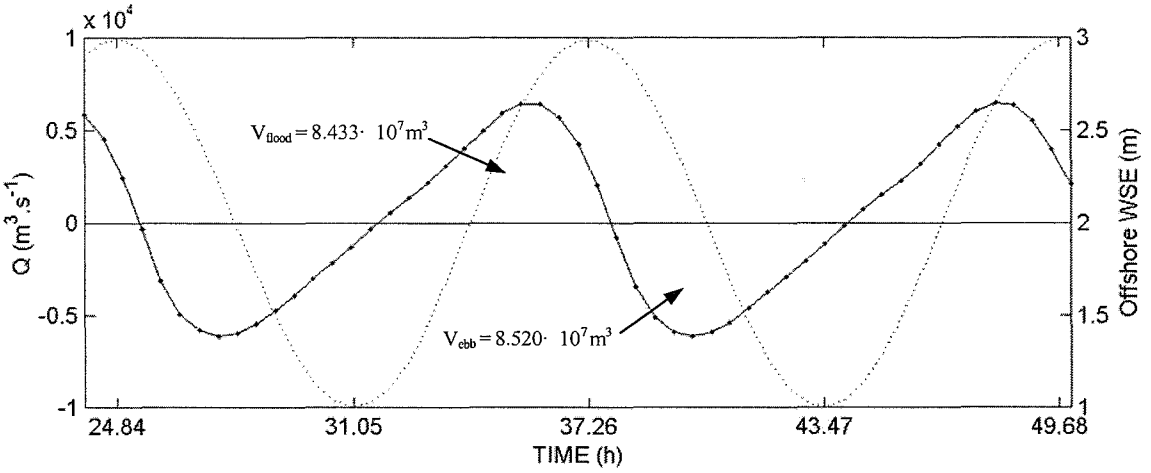

Figure 5-7. Total discharge through the inlets. Discharge (solid line); offshore WSE (dotted line).

5.2.4. Sub-embayments

The mass conservation analysis also revealed the possible existence of sub-embayments. In fact, with the assistance of the post-processing SMS application, animations of the velocity field evolution and flow trace in different areas of the lagoon were created, and it was found that zones of flow convergence and divergence developed throughout the tidal cycle in specific areas of the narrow back-barrier lagoon between Armona and Fuzeta inlets, as well as between Tavira and Cacela inlets, in which the net cross-flow was small (see Figure 5-9 for the Armona-Fuzeta case). This suggests that the system consists of three hydrodynamically quasi-independent sub-embayments: a sub-embayment with 3 inlets (New Ancão, Faro, and Armona) in the wide western area of the lagoon; a central sub-embayment with two inlets (Fuzeta and Tavira) and an eastern sub-embayment serviced by Cacela Inlet.

Therefore, given that the main purpose of this numerical modeling study is to identify and analyze the hydrodynamic interaction between inlets and the hydrodynamic processes contributing to the persistence of multiple inlets, the two eastern sub-embayments (which are serviced by one and two inlets) were not used, and only the western sub-embayment was considered for the simulations.

The zone where the hydrodynamic divide between the western sub-embayment and the rest of the system occurs is a shallow vegetated area, in which the narrow channel extending east from Armona Inlet suddenly widens, becomes poorly-defined across the intertidal zone, and shoals to a maximum depths of –0.25 m relative to MSL (Figure 5-8).

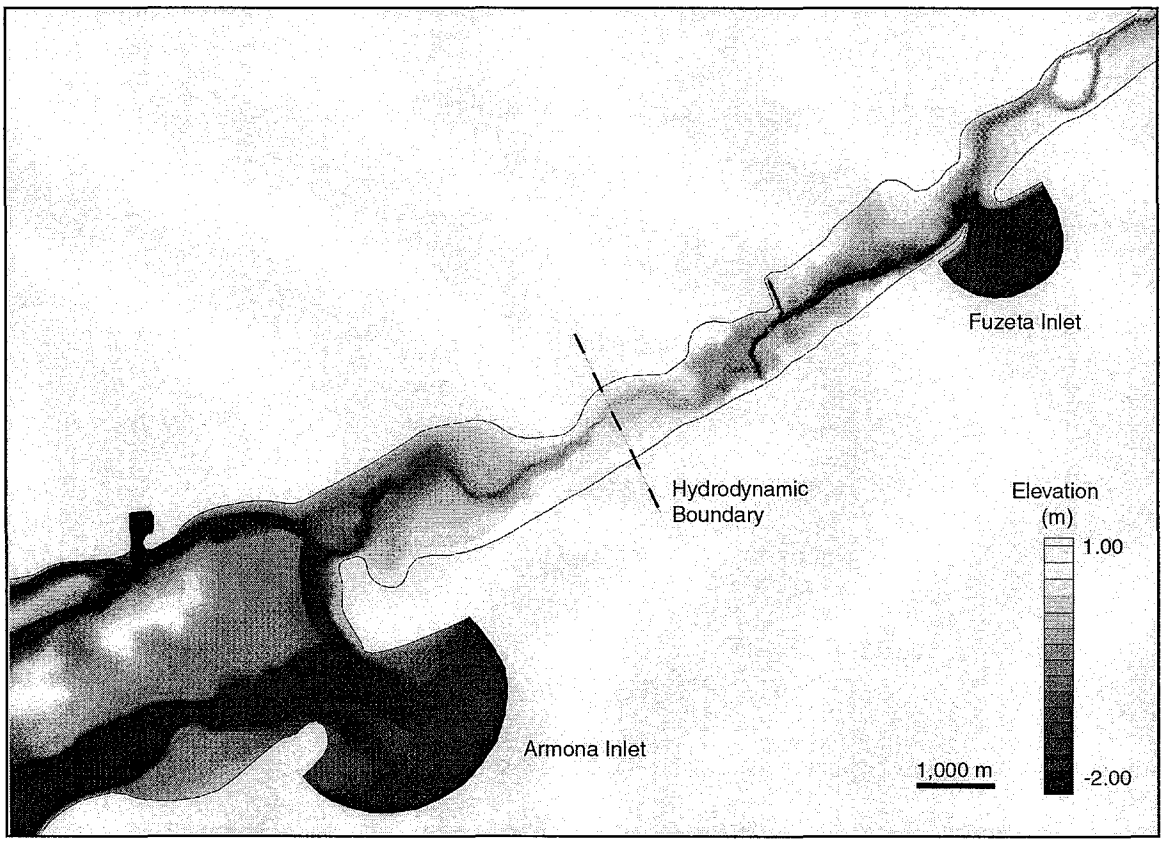

Figure 5-8. Hydrodynamic divide between Armona and Fuzeta inlets.

The velocity field west of this cross-section is mainly directed to the east during flood and west during ebb, whereas the direction is reversed in the region between the divide and Fuzeta Inlet. The flow through the divide has a peak of roughly 7 $m^3.s^{-1}$, which is small compared to the peak flows through Armona Inlet (1,840 $m^3.s^{-1}$), and Fuzeta Inlet (510 $m^3.s^{-1}$). During flood, the net flow across the divide is from Fuzeta to Armona and equivalent to 1.4% of the Fuzeta flood tidal prism, whereas during ebb the net flow is directed from Armona to Fuzeta and equivalent to 0.5% of the Fuzeta ebb tidal prism.

Given the above, the area east of the Armona-Fuzeta hydrodynamic divide was removed from the computational mesh for the subsequent analysis of the hydrodynamics in the 3-inlet western sub-embayment of Ría Formosa.

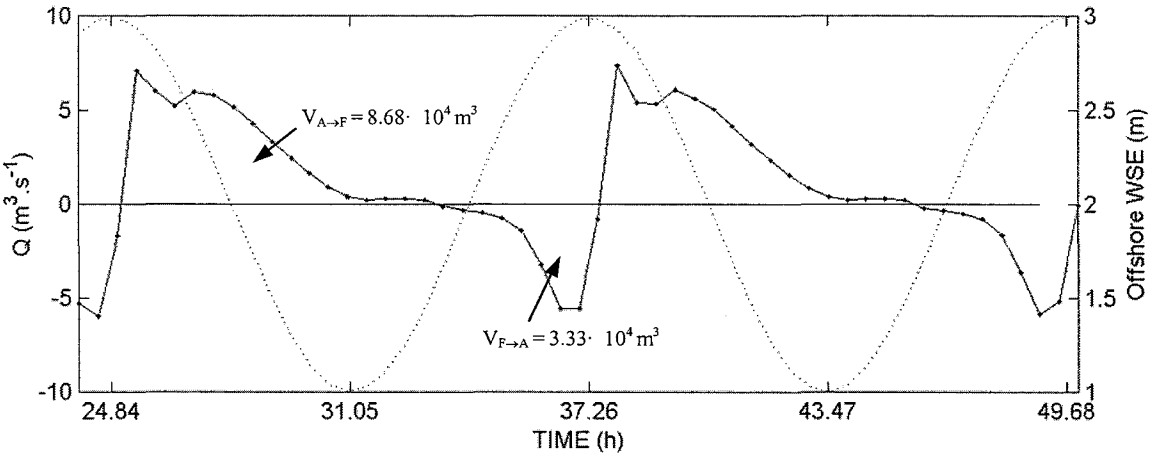

Figure 5-9. Discharge time series through the "hydrodynamic divide" between Armona and Fuzeta inlets ($V_{A\rightarrow F}$: volume of flow in Armona-Fuzeta direction; $V_{F\rightarrow A}$: volume of flow in Fuzeta-Armona direction). The dotted line is the Offshore water surface elevation.

5.2.5. Calibration

In general terms, the model calibration is an iterative process in which the model inputs (physical attributes of the lagoon, friction, and eddy viscosity coefficients) are refined and adjusted to assure that the model can reproduce the field observations with an acceptable level of agreement. The model was calibrated using the water surface elevation measured during the field campaign in January-March 1999 in six stations located in the western sub-embayment of the lagoon: Armona, Bridge, Main Channel, Main Inlet, New Inlet and Olhão (Figure 5-4). More specifically, the calibration iterative process consists of the following steps:

1. Run the model using as forcing the measured tide, using assigned values of the friction and eddy viscosity coefficients,
2. Obtain from the model output the time series of tidal elevations at the nine locations where the tide gauges were deployed (or at the nearest nodes), and perform harmonic analysis to ex-

tract amplitude and phase information for the dominant semi-diurnal signal (M_2) and its first sub-harmonic (M_4),

3. Check if the model reproduces the observations (harmonic analysis of the tidal records obtained in the field) with an acceptable level of agreement, and
4. Modify the model as needed by (i) reconfiguring the mesh (i.e., changing the number, size and types of elements to obtain better spatial resolution, to enhance or remove some physical features and to improve mass conservation), and/or (ii) assigning new values to the friction and eddy viscosity coefficients.

These steps were repeated until the check in item c) indicates that a reasonable agreement was found between model results and observations. In order to automate this process, several numerical runs were performed with varying friction and eddy viscosity coefficients, and the simulations with smaller differences between modeled and measured data were identified. Assuming that the friction and turbulent energy loss coefficients are independent, the calibration was first performed for the friction factor keeping the eddy viscosity coefficient constant, followed by the eddy viscosity calibration using the previously calibrated friction coefficients.

Friction coefficient calibration:

Following the guidelines from section 5.2.1, the following model runs were performed varying the "channel" and the "intertidal" Manning's friction coefficients (n_c and n_i, respectively), where $n_c = 0.02$, 0.022, 0.025 and 0.03, and $n_i = 0.03$, 0.045, 0.06, 0.075, 0.09, and 0.12.

A sample of the model output (using the measured spring tidal forcing and the four combinations of smaller and larger n_c and n_i) is shown in Figure 5-10, where the field data are plotted for comparison (thick line). A visual inspection of this figure shows that the model is able to reproduces reasonably well the gross features of the tidal fluctuation (amplitude and phase of the oscillations). However, a more detailed examination of the model's ability to reproduce the measurements requires an analysis of the major tidal harmonic constituents.

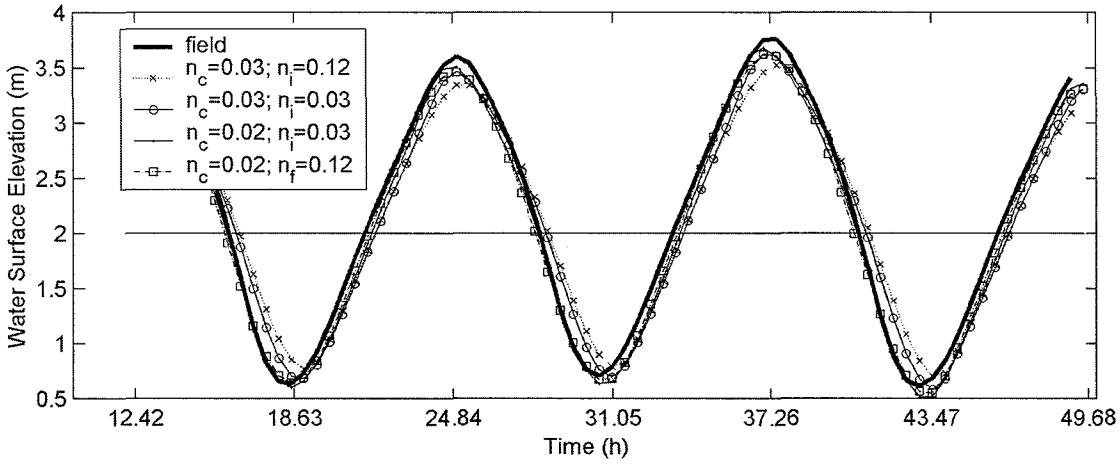

Figure 5-10. Field and modeled (selected runs) water surface elevation at "Main Channel" station (the offshore MSL is +2.00m).

The harmonic analysis was performed on the resulting 126 water surface elevation time series and the results in terms of the M_2 and M_4 amplitude and phase differences between model output and measurements are summarized in the appendix, section 5.6.1 (Figure 5-29 to Figure 5-32).

Based on examination of these figures, the following observations can be made regarding the model response to changes in the friction coefficient:

a) There is not a specific combination of friction factors that clearly produces a consistent improvement at all the stations.

b) The model is more sensitive to variations in the channel friction factor than in the intertidal friction factor.

c) The error variations show trends that in general suggest better agreement between model output and measurements for small channel friction factor (n_c=0.02-0.022). In some cases, small n_i gives better agreement (e.g., "Main Channel" M_2 amplitude, "New Inlet" and "Bridge" M_4 amplitude and phase), but in most cases large n_i produces better numerical results.

d) The largest disagreement occurs in the "Bridge" station. This large difference between model output and measurements is associated with recent changes in the bathymetry in the channel behind Ancão Peninsula, due mainly to dredging before the opening of the New

Ancão Inlet, and to the opening of the inlet itself. The model was not modified to take into account these changes due to lack of bathymetric data in that area.

Given the above, the combination of friction coefficient chosen for the simulations was n_c= 0.022 and n_i = 0.075. This point is marked by a cross in the corresponding Figures in the appendix.

Eddy viscosity coefficient calibration

The model calibration for the eddy viscosity coefficient was performed with the assistance of 24 runs, using the friction coefficients found above and varying the eddy viscosity coefficients in the channel and intertidal areas as $E_c = 3 \cdot 10^3$, $5 \cdot 10^3$, $7 \cdot 10^3$, and 10^4 Pa.s, and $E_i = 10^3$, $2 \cdot 10^3$, $3 \cdot 10^3$, $5 \cdot 10^3$, $7 \cdot 10^3$, and 10^4 Pa.s (smaller values of E_c produced numerical instabilities in the inlet mouths, even after smoothing and simplifying the mesh, and were therefore discarded in the calibration). The differences between model results and measurements, in terms of a) water surface elevation, and b) M_2 and M_4 amplitudes and phase, are shown in the appendix, section 5.6.2 (Figure 5-33 to Figure 5-37).

The main conclusions based on the examination of the figures are:

a) There is no specific combination of eddy viscosity coefficients that clearly produces better overall model results.

b) Similar to the friction coefficient calibration results, these results shown that the model is more sensitive to changes in the "channel" than in the "intertidal" eddy viscosity coefficient.

c) The sensitivity to changes and the error ranges (i.e., maximum-minimum error) are in general large in the three westernmost stations (Bridge, New Inlet and Main Channel), and small in the easternmost stations (Main Inlet, Olhão, and Armona).

d) Small values of E_c produce in general better model results in the stations where the errors (and the error ranges) are large. Moreover, the Main Channel station, which is the station presenting the largest error range, suggests consistently that small values of both eddy viscosity coefficients produce the best agreement between model results and measurements.

e) The parameters presenting the largest disagreements between model results and measurements are the M_4 amplitude and phase. Figure 5-36 and Figure 5-37 suggest that M_4 is bet-

ter modeled when small values of both eddy viscosity coefficients are used. Optimizing this parameter is important since it is one of the major components in the determination of the flow dominance regime, as shown in section 2.3.1, which in turn is a relevant hydrodynamic characteristic for this study. Based on the observations presented above the eddy viscosity coefficients chosen for the simulations were: $E_c = 3{,}000$ Pa.s, and $E_i = 1{,}000$ Pa.s.

5.2.6. Verification

The verification follows the general approach used for the calibration. The data used for the verification are the measured velocities through each inlet (in the form of tidal prisms and discharge time series).

For each inlet's tidal prism and velocity verification, the model was forced with the tide corresponding to the time during which the ADCP survey was performed in that inlet. The resulting velocity records through each inlet's cross section were then used to compute the modeled discharges and tidal prisms, which in turn were compared with the corresponding measured and processed data. The field data used for the verification corresponded to transect B for New Inlet, A for Main Inlet, and B for Armona Inlet (see Figures 4.8, 4.11 and 4.14 for the transect locations).

The discharges computed from the modeled and measured velocities are plotted in the appendix, section 5.6.3 (Figure 5-38). This figure shows that the model results are consistently larger than what was measured in the field for the three inlets of the western sub-embayment. The largest differences occur during peak flood: 162 $m^3.s^{-1}$ for New Ancão Inlet (50% of the corresponding measured discharge); 950 $m^3.s^{-1}$ for Main (Faro) Inlet (25 % of the corresponding measured discharge); and 235 $m^3.s^{-1}$ for Armona Inlet (18% of the corresponding measured discharge) The main reason for this disagreement is the inability of the field crew to measure the entire inlet cross-sections, given i) the large shallow banks on each side of the inlet channels (at New and Armona inlets, and at the western bank of Main Inlet), and ii) the gentle slope of the boat ramp that was used as eastern limit of the Main Inlet transect. In fact, the shallow banks were completely flooded during high tide, but the surveys were designed to keep the same transect throughout the tidal cycle, independently of the stage of the tide (see section 4.2.2 for the survey transect design). The results suggest that the flow through the banks is large, and represents a significant portion of the total inlet flow during peak flood and ebb discharges.

5.3. Simulations

In order to analyze the hydrodynamic response of the western sub-embayment of Ría Formosa to perturbations in the cross-sectional area of the three inlets, a series of 151 simulations (approximate computational time = 1,360 h) was performed with a range of different inlet cross-sectional areas, and two different tidal forcing curves.

For the analysis of inlet stability based on the changes in residual flow, flow dominance (flood/ebb flow volume, duration, and intensity), tidal distortion (M_2 and M_4 amplitude and phase), and sediment transport capacity, the forcing used was a simple harmonic function with a period of 12.42 h (M_2) and 1 m amplitude (equivalent to the measured M_2 amplitude). Similar to the simulations for the model calibration, the water surface elevation of the M_2 forcing was initially raised to a level that assured all elements were wet during the first iteration.

To analyze the hydrodynamic response to extreme tidal conditions, the measured spring tide was used as forcing. These simulations were used to obtain estimates of spring-maximum cross-sectional averaged flow velocity through the inlets with the current and hypothesized geometries, allowing the stability analysis with closure curve arguments. Given that in the spring period there is not a specific tidal cycle during which both the maximum rising and falling tides occur, the model was run for four tidal cycles (49.68 hours including 12.42 hours for spin-up). Both spring and M_2 forcing curves are shown in Figure 5-11.

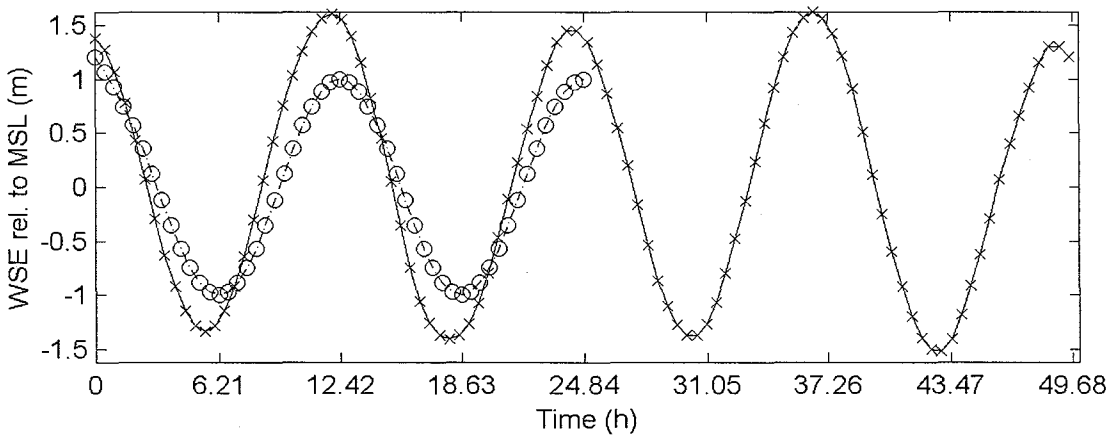

Figure 5-11. Forcing used for the numerical simulations. Both records include a spin-up cycle.

The modification of the areas was done following the known behavior of evolution of the inlets (Esaguy, 1984; Freire de A., 1990; Bettencourt, 1994; Vila *et al.*, 1999): a) narrowing and widening Armona Inlet, b) keeping constant the width in Main Inlet (since it is stabilized with

jetties), and c) keeping constant the aspect ratio (ratio of width over depth) in New Inlet. The numerical simulations were divided in two groups:

I. Simulations varying the cross-sectional areas of New Ancão and Armona inlets, which are the unjettied inlets in the western sub-embayment, and keeping Main Inlet cross-sectional area constant (1,610 m^2, i.e., present day cross-sectional area), as shown in Table 5-1.

Table 5-1. Simulations varying New Inlet and Armona Inlet cross-sectional areas.

		Area $_{New\ I.}$ (m^2)						
Area $_{Armona\ I.}$ (m^2)	Id Type	230 (A - -)	340 (B - -)	470 (C - -)	**595**$^+$ (X - -)	900 (D - -)	1,175 (E - -)	1,575 (F - -)
395	(- - S)	AXS[1]	BXS[1]	CXS[1]	XXS[1]	DXS[1]	EXS[1]	FXS[1]
950	(- - A)	AXA[1,2]	BXA[1,2]	CXA[1,2]	XXA[1,2]	DXA[1,2]	EXA[1,2]	FXA[1,2]
1,480	(- - B)	AXB[1,2]	BXB[1,2]	CXB[1,2]	XXB[1,2]	DXB[1,2]	EXB[1,2]	FXB[1,2]
2,210	(- - C)	AXC[1,2]	BXC[1,2]	CXC[1,2]	XXC[1,2]	DXC[1,2]	EXC[1,2]	FXC[1,2]
2,965$^+$	(- - X)	AXX[1,2]	BXX[1,2]	CXX[1,2]	**XXX**[1,2]	DXX[1,2]	EXX[1,2]	FXX[1,2]
3,940	(- - D)	AXD[1,2]	BXD[1,2]	CXD[1,2]	XXD[1,2]	DXD[1,2]	EXD[1,2]	FXD[1,2]
5,030	(- - E)	AXE[1,2]	BXE[1,2]	CXE[1,2]	XXE[1,2]	DXE[1,2]	EXE[1,2]	FXE[1,2]
5,925	(- - F)	AXF[1,2]	BXF[1,2]	CXF[1,2]	XXF[1,2]	DXF[1,2]	EXF[1,2]	FXF[1,2]

$^+$: present-day cross-sectional areas. ^{1}: simulation forced with M_2 tide.
^{2}: simulation forced with the measured spring tide.

II. Simulations varying the cross-sectional areas of Main and Armona inlet, which are the major inlets in Ría Formosa and are adjacent, keeping the New Inlet cross-sectional area constant (595 m^2, i.e., present-day cross-sectional area), as shown in Table 5-2.

Table 5-2. Simulations varying Main Inlet and Armona Inlet cross-sectional areas.

		Area $_{Main\ I.}$ (m^2)				
Area $_{Armona\ I.}$ (m^2)	Id Type	785 (- A -)	1,345 (- B -)	**1,610**$^+$ (- X -)	2,280 (- E -)	2,680 (- F -)
950	(- - A)	XAA[1,2]	XBA[1]	XXA[1]	XEA[1]	XFA[1]
1,480	(- - B)	XAB[1,2]	XBB[1]	XXB[1]	XEB[1]	XFB[1]
2,210	(- - C)	XAC[1,2]	XBC[1]	XXC[1]	XEC[1]	XFC[1]
2,965$^+$	(- - X)	XAX[1,2]	XBX[1]	**XXX**[1]	XEX[1]	XFX[1,2]
3,940	(- - D)	XAD[1,2]	XBD[1]	XXD[1]	XED[1]	XFD[1]
5,030	(- - E)	XAE[1,2]	XBE[1]	XXE[1]	XEE[1]	XFE[1]
5,925	(- - F)	XAF[1,2]	XBF[1]	XXF[1]	XEF[1]	XFF[1]

$^+$: present-day cross-sectional areas. ^{1}: simulation forced with M_2 tide.
^{2}: simulation forced with the measured spring tide.

For each different cross-sectional area, the computational mesh was modified in the cross-section itself to reach each targeted area shown in the tables above. The resulting cross-sectional areas are plotted in the appendix (section 5.6.5). In addition, the regions immediately seaward and landward were also modified to assure a smooth transition between these areas and the newly enlarged or reduced inlet cross-sectional area. The extent of these modified regions varied from inlet to inlet, being larger for simulations in which the change in cross-sectional area was large. Test runs were performed with both broader and smaller modified areas adjacent to the inlet cross-sections, and no significant change in the model output was observed.

In addition to these numerical simulations, another model run was performed to verify the spin-up time (obtained prior to calibration as one tidal cycle; see section 5.2.2), in terms of the capacity of the model to give reliable estimates of the residual current through each inlet. For this simulation, the model was forced with four M_2 tidal cycles and the inlet configuration was BXA (see Table 5-1). The cross-sectionally averaged residual current was computed as

$$V_{res}(t) = \frac{1}{T} \int_{t-T/2}^{t+T/2} V(t)\, \mathrm{dt} \tag{5.12}$$

where T is the M_2 period, and V is the cross-sectionally averaged velocity at time t.

The results (Figure 5-39 in the Appendix, section 5.6.4) show that the residual discharge estimate reaches a state (roughly after 16 hours of simulation) where it fluctuates about a mean value. Moreover, it was found that these fluctuations are periodic, with a period corresponding to the forcing period (T_{M2} = 12.42 h). No attempt was made to explain this cyclic behavior, and the residual discharge was computed as the average of these fluctuations, i.e., the average of the residual estimates from $t=3/2\ T_{M2}$ to $t=5/2T_{M2}$. Therefore, a reliable estimate of the residual discharge required a simulation for at least three tidal cycles. However, since the modeled velocities after t=12.42 h are reliable within $7 \cdot 10^{-2}$ cm.s^{-1} (see Figure 5-6), instead of running the model for three tidal cycles, the model results for the second tidal cycle were simply repeated for two additional M_2 periods, and the resulting model output record used for the residual computation.

5.4. Results and Discussion

The results are first presented and discussed in terms of the changes in the different hydrodynamic characteristics and processes analyzed individually and for each inlet: flow volume and duration, residual circulation, and near-bed sediment transport capacity (section 5.4.1); tidal distortion (section 5.4.2), and maximum velocities through the inlets (section 5.4.3). A summary of the most relevant findings and a discussion of the overall hydrodynamic response to changes inlet cross-sectional area in multiple tidal inlets are presented in section 5.4.4. Finally, the specific implications of changes in inlet cross-sectional area to Ría Formosa are discussed in section 5.4.5.

5.4.1. Tidal prisms, residual circulation, and sediment transport capacity.

General remarks about tidal prisms

The tidal prisms through New, Main, and Armona inlets vary widely as a function of changes in the inlet cross-sectional areas, ranging from 8 to 12.5%, 40 to 80%, and 12 to 50% of the total tidal prism, respectively, as shown in the appendix (section 5.6.6, Figure 5-43 to Figure 5-45). Panels (g) and (h) of these figures are contour plots of the total flood and ebb tidal prisms, where it can be seen that both tidal prisms vary depending on the inlet's cross-sectional areas. In fact, these panels show that the total volume of water entering and exiting the lagoon increases as the Main Inlet and New Inlet cross-sectional areas increases: 3-4% for the M_2-forced simulations varying A_{Armona} and A_{New} (Figure 5-43-g and -h), 6-8% for the M_2-forced simulations varying A_{Armona} and A_{Main} (Figure 5-44-g and -h), and 4-5% for the spring tide-forced simulations (Figure 5-45-g and -h), which can be regarded as an increase in the inlets' efficiency to exchange water between the ocean and the lagoon. In turn, Armona Inlet does not show a clear trend of increase in efficiency, but the results suggest that the hydraulic efficiency improves for specific cross-sectional areas (1,480, 2,210,and 5,030 m^2). This change in hydraulic efficiency has to be taken into account in the analysis of the overall response of the system to changing cross-sectional areas. However, the general tendencies of tidal prism variation shown in panels (a) to (f) in these figures, which are the flood (ebb) contour plots normalized by the total flood (ebb) tidal prism, are fully preserved in the non-normalized version of these plots (panels (a) and (b) in the figures below).

In addition, the comparison of the volumes shown in these panels indicates that for each simulation the flood and ebb tidal prisms differ by ± 1% when forcing the model with an M_2 tide (Figure 5-43-g and –h, and Figure 5-44-g and -h). This discrepancy is small and falls within the model's ability to conserve mass (see section 5.2.3).

In the case of the simulations forced with the measured spring tide, the tidal period cannot be defined, given that the tide is composed by several constituents with different periods of oscillation. Therefore, the tidal cycles were considered the time intervals between two consecutive positive "zero-crossings" in the discharge time-series, and the tidal prisms were obtained as the average of the tidal prisms over three tidal cycles (Figure 5-45). Panels (g) and (h) in that figure show that the total ebb volume is 5-7% larger than the total flow for each simulation. This difference between flood and ebb volumes is in part due to the existence of the low frequency signal in the measured spring tide (MS_f fortnightly component), which, for the portion of the spring tide selected, confers a net seaward flow to the lagoon hydrodynamics. This large net outflow is of the order of some of the hydrodynamic processes analyzed, and makes the identification of small variations in these processes difficult. Given the above, the results from the simulations forced with the measured spring tide are not considered for further analysis in this particular section.

The following discussion is divided into inlets (New, Main, and Armona), and into types of simulation (varying A_{Armona} and A_{New}, and varying A_{Armona} and A_{Main}). The figures below (Figure 5-12 to Figure 5-18) summarize the relevant results for this section in the form of contour plots of each variable as a function of the inlet cross-sectional areas:

- panels (a) and (b) show the flood and ebb tidal prisms, respectively (in m^3),
- panel (c) shows the residual discharge (in $m^3.s^{-1}$), computed as the mean discharge over a tidal period, similar to the residual current computation presented in section 5.3. The residual discharge is in fact equivalent to the difference between flood and ebb tidal prisms, divided by the tidal period, which in some instances is a useful way to look at the net inflow or outflow.
- panel (d) presents the difference between the flood and ebb durations (in minutes), where negative values mean longer ebb,
- panel (e) shows residual current (in $cm.s^{-1}$), computed as explained in section 5.3, and

- panel (f) is the difference between flood and ebb near bed sediment transport, relative to the smallest of these quantities (in %). The computation of the sediment transport is based on the Meyer-Peter and Müller (1948) empirical equations relating sediment transport rate to shear stress. The predicted sediment transport is assumed to be proportional to V^3, integrated over the flood and ebb portions of the tidal cycle, in an idealized case of zero critical shear stress required for initiation of motion. On one hand, this assumption results in an overestimation of the predicted near-bed sediment transport, but on the other hand it underestimates the potential transport asymmetry. However, these estimates of the sediment transport capacity are a useful indicator of the sediment transport system response (Aubrey, 1986).

In all cases, negative values correspond to seaward direction. Based on the examination of the data in these figures, the following observations can be made:

New Inlet

A. Simulations varying A_{Armona} and A_{New}, with $A_{Main} = 1{,}610\ m^2$ (Figure 5-12)

1) Both flood and ebb tidal prisms (Ω_{flood} and Ω_{ebb}) through New Inlet consistently increase as its cross-sectional area increases (panels a and b), and Ω_{ebb} is in general larger than Ω_{flood} (except when A_{New} has its current size, 595 m^2, in which case the flood volume is 1-2% larger than the ebb volume). The tidal prism being larger during ebb than during flood indicates that a flow circulation exists from the other inlets to New Inlet, as confirmed by the residual discharge predictions shown in panel (c). This panel also shows that the residual discharge (or, equivalently, the difference between flood and ebb tidal prisms) is not constant throughout the simulations, which in turn indicates that the circulation pattern between inlets responds actively to changing inlet cross-sectional areas.

   For instance, as A_{New} decreases from its current size (595 m^2) to 230 m^2, the flood tidal prism decreases on average $1.17 \cdot 10^6$ m^3 and the ebb tidal prism decreases on average only $0.49 \cdot 10^6$ m^3. The difference between these two values represents a volume of water captured by New Inlet from the other inlets' flood flows.

   Similarly, as A_{New} increases (from 595 m^2 to 1,575 m^2), the flood tidal prism experiences a smaller increase than the ebb tidal prism ($0.89 \cdot 10^6$ m^3 versus $1.28 \cdot 10^6$ m^3), indicating that part of the flow that exists the lagoon through New Inlet under these large cross-sectional area conditions is captured from the flow entering the lagoon through the other inlets.

Therefore, the response, in terms of the flow volume, to both an increase and a decrease in New Inlet cross-sectional area is the same, namely an increase in the seaward residual discharge (panel c).

As opposed to the residual discharge, the predicted residual current and sediment transport capacity do not show a landward direction for the present-day New Inlet cross-sectional area. Instead, they appear to be consistently directed seaward throughout all the simulations: the residual velocity ranges from -2 to -16 $cm.s^{-1}$ (panel e), and the ebb sediment transport ranges from being 20% to 110% larger than the flood sediment transport (panel f). This suggests that, at least in that location, New Inlet has a marked tendency to flush near-bottom sediment seaward. Moreover, it is found that this tendency is enhanced as the New Inlet cross-sectional area decreases from its present value, which can be regarded as a response against closure.

2) The flood and ebb durations for these simulations (panel d) show that in all cases the flood portion of the tide is significantly shorter than the ebb phase. This implies that when the flood tidal prism is larger than the ebb tidal prism, which only occurs for A_{New}= 595 m^2, the inlet would normally be considered flood dominant (stronger and shorter flood), since a larger volume enters the system in a shorter time. This is in agreement with the maximum velocity through the inlet being larger during flood for this cross-sectional area (see Figure 5-24-b, section 5.4.3). However, both the residual current and the sediment transport plots (panels e and f) are seaward, indicating a tendency to flush material offshore.

Items 1) and 2) suggest that ebb is longer and in general carries more volume than flood. Since no alternate source of water inflow is considered besides the tidally driven flow, this scenario is only attainable in a multiple inlet system, where water exchange between inlets can occur. Therefore, the determination of flow dominance from information about flood and ebb durations is not possible in cases where the assumption of equal flood and ebb tidal prisms cannot be made. In fact, when the New Inlet cross-sectional deviates from its current value (595 m^2), the inlet can be said to be ebb dominant since the residual discharge, the residual current, and the maximum velocity are directed seaward, in spite of the duration of the ebb portion of the tide being longer. This suggests that the flow and transport dominance should be differentiated.

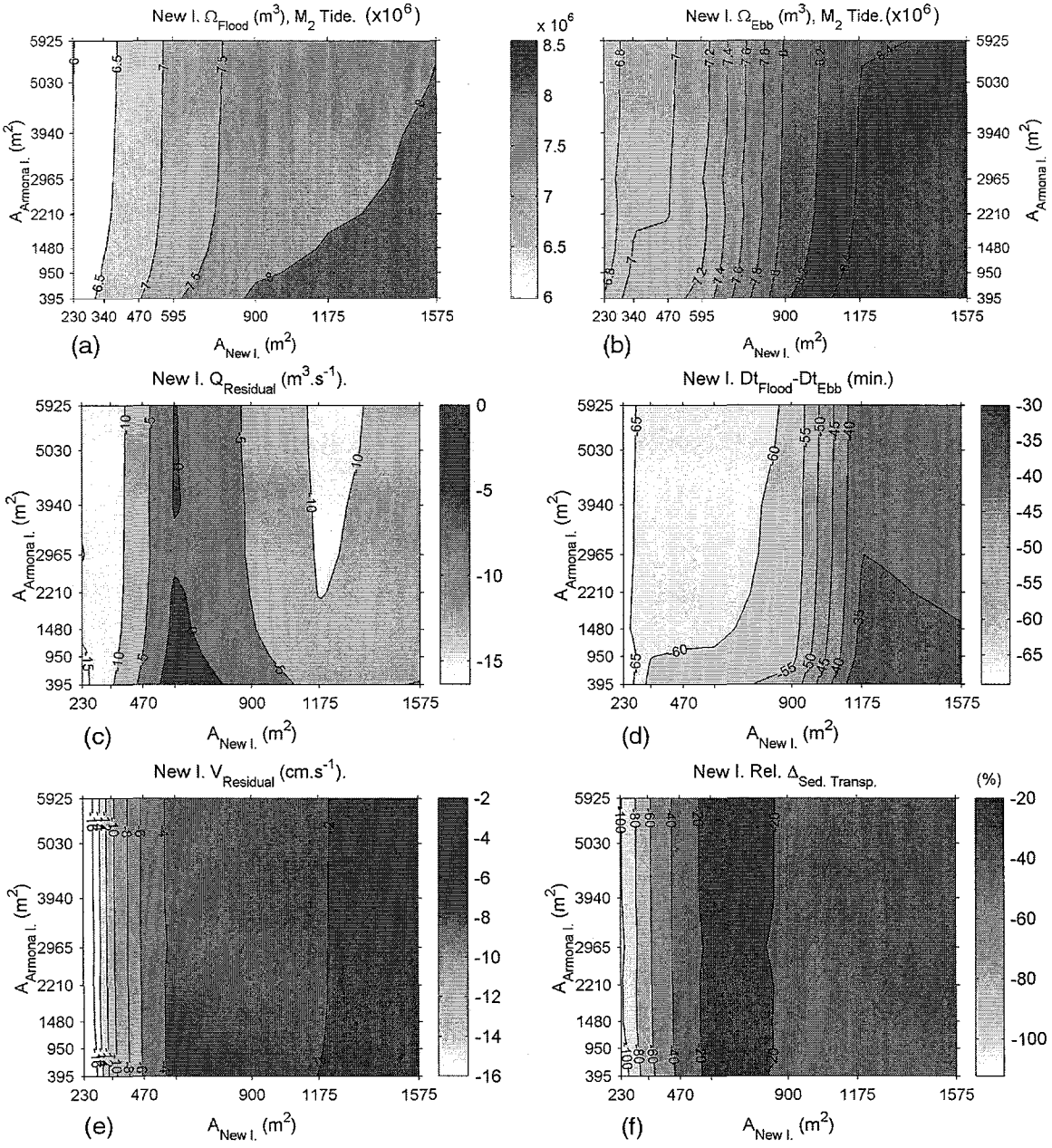

Figure 5-12. Results at New Inlet from simulations with M_2 forcing, varying A_{Armona} and A_{New} (A_{Main}=1,610 m^2). Flood and ebb tidal prisms (a and b); Residual discharge (c); Difference between flood and ebb durations (d); Residual current (e); and flood – ebb near-bed sediment transport difference, relative to the flood sediment transport (f).

3) For a given New Inlet cross-sectional area, changes in A_{Armona} have a non-negligible impact on the New Inlet tidal prism. As A_{Armona} increases from 350 to 5,925 m^2, $\Omega_{New\ I.}$ (flood and ebb) decreases on average 1-4%. This reduction in tidal prism is small since these two inlets are distant and the cross-sectional area of the inlet between them (Main Inlet) is kept constant

in these simulations, but suggests that as Armona cross-sectional area increases, its tidal prism increases, and to a small extent affects the New Inlet tidal prism.

B. Simulations varying A_{Armona} and A_{Main}, with $A_{New} = 595\ m^2$ (Figure 5-13)

4) The tidal prisms through New Inlet decrease as both Main Inlet and Armona Inlet cross-sectional areas increase (Panels a and b), implying that the New Inlet tidal prism is partially captured by the other inlets as their cross-sectional areas increase.

5) The New Inlet tidal prism response to changes in Main Inlet cross-sectional area is greater than the response to changes in Armona Inlet cross-sectional area. As A_{Main} increases (from 785 to 2680 m^2), New Inlet Ω_{flood} decreases 7-14%, whereas the reduction is only of 1-7% when A_{Armona} increases (from 950 to 5,925 m^2).

6) Contrary to the simulations where A_{New} varied, these simulations show that on average the changes in the circulation pattern between New Inlet and the rest of system as A_{Main} and A_{Armona} vary are not very large (Figure 5-13-c). Indeed, both flood and ebb tidal prisms through New Inlet increase (decrease) similarly as A_{Main} or A_{Armona} increase (decrease), with the exception of the simulation with smallest cross-sectional areas in both Main and Armona inlets (785 m^2 and 950 m^2, respectively). This simulation shows a considerable increase in New Inlet flood volume (from 7.4 to $7.8 \cdot 10^6$ m^3; panel a), without a corresponding increase in the ebb volume (panel b), indicating the generation of a net circulation from New Inlet to areas of the lagoon otherwise serviced by the other inlets (panel c). Although this response, in which the flood volume becomes roughly 6% larger than the ebb volume, is accompanied by an increase in the flood duration (panel d), the ebb duration remains larger, which would normally imply flood dominance. In spite of this apparent flood dominance, the residual velocity (panel e), the near-bed sediment transport (panel f), and the maximum velocity (see Figure 5-24-c) are directed seaward. The opposite direction exhibited by the residual discharge and current in this simulation happens because of the nonlinear distortion of the tidal flow, which results in the occurrence of the peak flood discharge at higher waters (i.e., larger cross-sectional area), than the peak ebb discharge. This in turn leads (V=Q/A) to higher velocities during ebb than during flood, and a net ebb residual current, as shown in Figure 5-14. This hydrodynamic behavior shows that a larger flood discharge in a shorter period does not necessarily lead to stronger flood currents, and in fact the inlet appears to be ebb dominant (in terms of its current intensity).

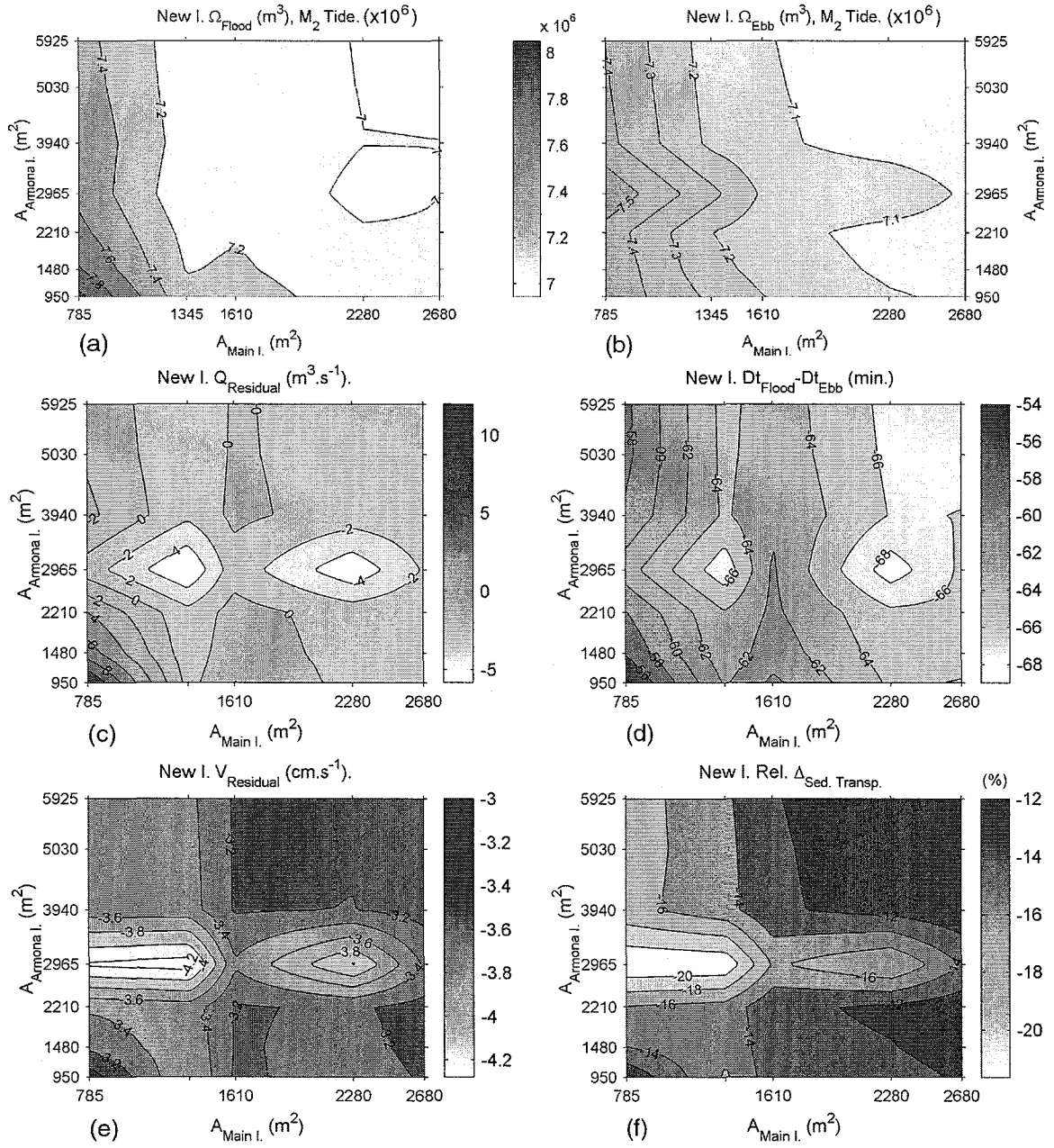

Figure 5-13. Results at New Inlet from simulations with M_2 forcing, varying A_{Armona} and A_{Main} (A_{New}=595 m^2). Flood and ebb tidal prisms (a and b); Residual discharge (c); Difference between flood and ebb durations (d); Residual current (e); and flood – ebb near-bed sediment transport difference, relative to the flood sediment transport (f).

7) Panels (c) to (f) show the existence of two combinations of Main-Armona inlets cross-sectional areas, namely (1,345 m^2; 2,965 m^2) and (2,280 m^2; 2,965 m^2), for which the New Inlet hydrodynamics tend to a more efficient seaward flushing, and in general confer a

stronger long-term stability to the inlet. These specific areas correspond to the present-day Armona cross-sectional area, and both a smaller and a larger Main Inlet cross-sectional area (relative to current size).

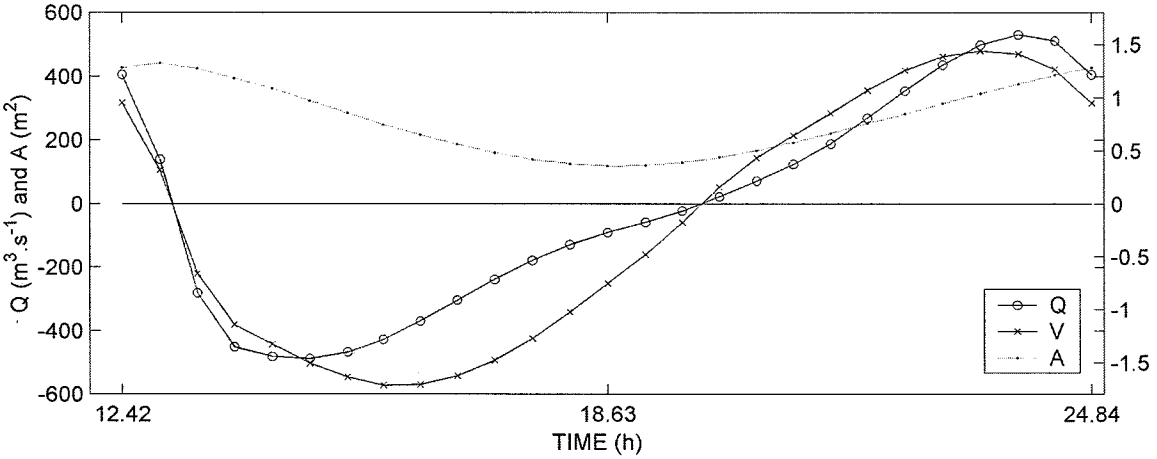

Figure 5-14. Discharge, velocity and cross-sectional area time series at New Inlet for simulation XAA, showing maximum discharge occurring during flood (positive) and maximum velocity occurring during ebb.

8) Comparing Figure 5-12-a and Figure 5-13-a, it can be seen that, in terms of changes in New Inlet Ω_{flood}, a reduction in A_{Main} from its current size (1,610 m^2) to 785 m^2 has a similar effect as an increase in A_{New} from its current size (595 m^2) to 1,575 m^2. In both cases, the flood tidal prism increases from $7.2 \cdot 10^6$ m^3 to $8.1 \cdot 10^6$ m^3. In other words, the effect of changes in Main Inlet cross-sectional area on New Inlet tidal prism can be comparable to the effects of changes in New Inlet itself. This shows how important the effects of the changes in one inlet's cross-sectional area on other inlets can be.

Main Inlet

A. Simulations varying A_{Armona} and A_{New}, with $A_{Main} = 1{,}610$ m^2 (Figure 5-15)

9) These simulations show that, when keeping the Main Inlet cross-sectional area constant, the changes in that inlet hydrodynamics are primarily controlled by changes in A_{Armona}, and to a smaller extent controlled by changes in A_{New}. This is due to i) Armona Inlet being closer to Main Inlet than New Inlet, ii) the existence of a channel running adjacent to Culatra Island's lagoon shoreline, and communicating directly Armona Inlet and Main Inlet, and iii) to the fact that Armona flow volume is in all cases significantly larger than the flow through New Inlet (see Figure 5-43, in appendix 5.6.6, p254).

10) In all simulations, the flood tidal prism remains larger (3-9%) than the ebb tidal prism, conferring a consistent landward residual discharge through Main Inlet (panel c), showing that this inlet consistently acts as importer of water to the entire system. In addition, both the residual current and the residual discharge being landward and increasing as A_{Armona} increases, shows that Main Inlet is flood dominant, in spite of the fact that the duration of the flood is longer than that of the ebb.

11) As A_{Armona} increases, both flood and ebb tidal prisms at Main Inlet decrease (panels a and b). Similar to the behavior of New Inlet tidal prism, item 1), the rate of increase (decrease) of the tidal prism through Main Inlet is not constant as A_{Armona} decreases (increases), as evidenced by the strong variations in the residual discharge (panel c). This suggests again that significant changes in the circulation pattern between inlets occur as their cross-sectional area vary.

For instance, by decreasing A_{Armona} from its current size, 2,965 m^2, to 395 m^2, it is found (panel a) that the Ω_{flood} in Main Inlet increases on average $13.8 \cdot 10^6$ m^3 (from $44.8 \cdot 10^6$ m^3 to $58.3 \cdot 10^6$ m^3, i.e., a 31% increase at a rate of $5.37 \cdot 10^3$ m^3/m^2), whereas Ω_{ebb} (panel b) increases on average $15.4 \cdot 10^6$ m^3 (from $40.9 \cdot 10^6$ m^3 to $56.3 \cdot 10^6$ m^3, i.e., a 38% increase at a rate of $6.03 \cdot 10^3$ m^3/m^2). An increase of $13.8 \cdot 10^6$ m^3 in both flood and ebb tidal prisms at Main Inlet means that the inlet captures a larger tidal prism as A_{Armona} decreases. The additional increase in the ebb flow volume indicates that the Main Inlet also is capturing part of the other inlets flood flows (mainly from Armona inlet, as shown by the decrease in seaward net flow in Figure 5-17-c for $A_{Armona}=395m^2$), modifying the circulation within the lagoon.

Interestingly, a significant decrease in A_{Armona} also leads to dramatic changes in the other hydrodynamic parameters shown in Figure 5-15: The landward residual discharge and the net near-bed sediment transport decrease significantly (panels c and f), the residual current changes direction to become seaward-oriented (panel e), and the ebb duration increases, exceeding the flood duration (panel d). These are all processes that contribute to an enhancement of the Main Inlet stability, considering that ebb-oriented net current and a practically zero net transport are related to a tendency for a more effective seaward flushing. Thus, the Armona reduction in cross-sectional area results in a hydrodynamic response of the Main Inlet that has two effects: i) enhances the seaward transport at Armona Inlet and setup favorable conditions for the restoration of a larger cross-sectional area, and ii) contributes to an en-

hanced stability for the Main Inlet itself, through the suppression of its "lagoon-infilling" capability.

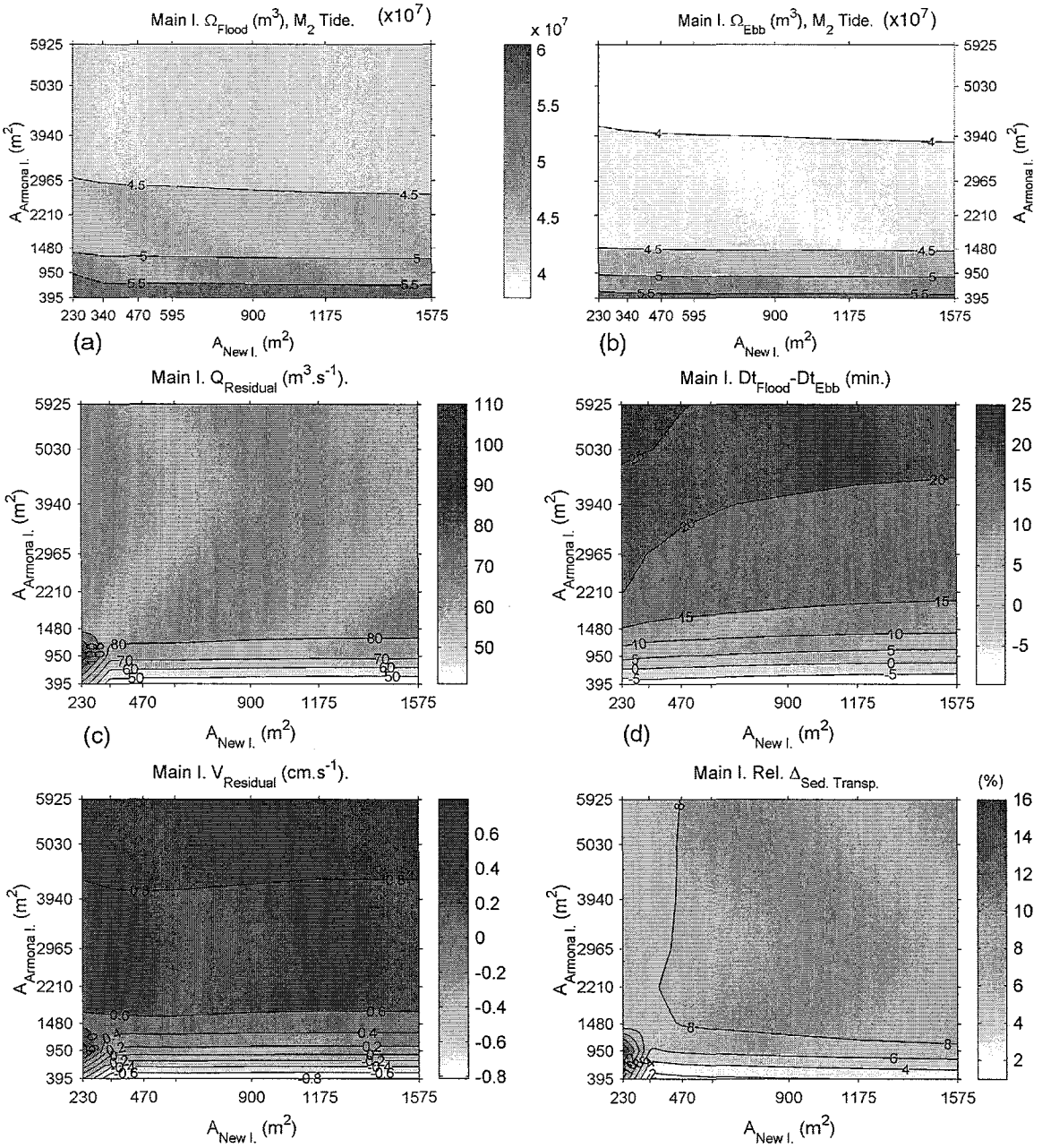

Figure 5-15. Results at Main Inlet from simulations with M_2 forcing, varying A_{Armona} and A_{New} (A_{Main}=1,610 m^2). Flood and ebb tidal prisms (a and b); Residual discharge (c); Difference between flood and ebb durations (d); Residual current (e); and flood – ebb near-bed sediment transport difference, relative to the ebb sediment transport (f).

When A_{Armona} increases from its current size to 5,935 m^2, both tidal prisms decrease the same amount, indicating only a reduction in the volume of water entering and exiting through Main Inlet, with no significant change in the water circulation between inlets.

12) Figure 5-15 also shows that the effects of varying New Inlet cross-sectional on Main Inlet flow volumes is small (~1%), except when both A_{New} and A_{Armona} become small (230 m^2 and 950 m^2, respectively) in which case the hydrodynamic response in Main Inlet is larger: a sudden increase of the flood tidal prism (of the order of 5%), and consequently an increase in the landward residual discharge, current, and sediment transport. This response is coupled with an opposite response at Armona Inlet, as shown in Figure 5-17 and discussed in (15). Although this scenario is beneficial for Armona in the sense that it contributes to maintain and enhance the already established seaward flow and transport at that inlet, it is definitely detrimental for Main Inlet's own stability, given that it triggers a significant increase in the landward flow and transport.

Items (11)and (12) suggest that if A_{Armona} decreases alone, the flow through Main Inlet is able to adjust and contribute to the restoration of the original area, without hampering (and even improving) its own stability. However, if both Armona and New inlets experience a reduction in their cross-sectional areas, a situation can arise in which flow through Main Inlet is not able to counteract satisfactorily such reductions, potentially affecting its own stability. This is a clear example of hydrodynamic interaction between the three inlets. Moreover, it shows that, even if Main Inlet tidal prism is almost an order of magnitude larger than that of New Inlet, a large reduction of New Inlet cross-sectional area can lead to unstabilizing hydrodynamic processes at Main Inlet.

B. Simulations varying A_{Armona} and A_{Main}, with A_{New} = 595 m^2 (Figure 5-16)

13) In these simulations, the changes in both flood and ebb tidal prisms through Main Inlet depend to a similar extent on changes in both Armona Inlet and Main Inlet cross-sectional areas (panels a and b). The Main Inlet tidal prisms are larger when A_{Main} is large and A_{Armona} small, than when A_{Main} is small and A_{Armona} large.

14) As for the previous simulations, the tidal prism is in all cases larger during flood than during ebb, as shown by the consistently landward residual discharge and current (panels c and e), and in general Main Inlet can be said to be flood dominant.

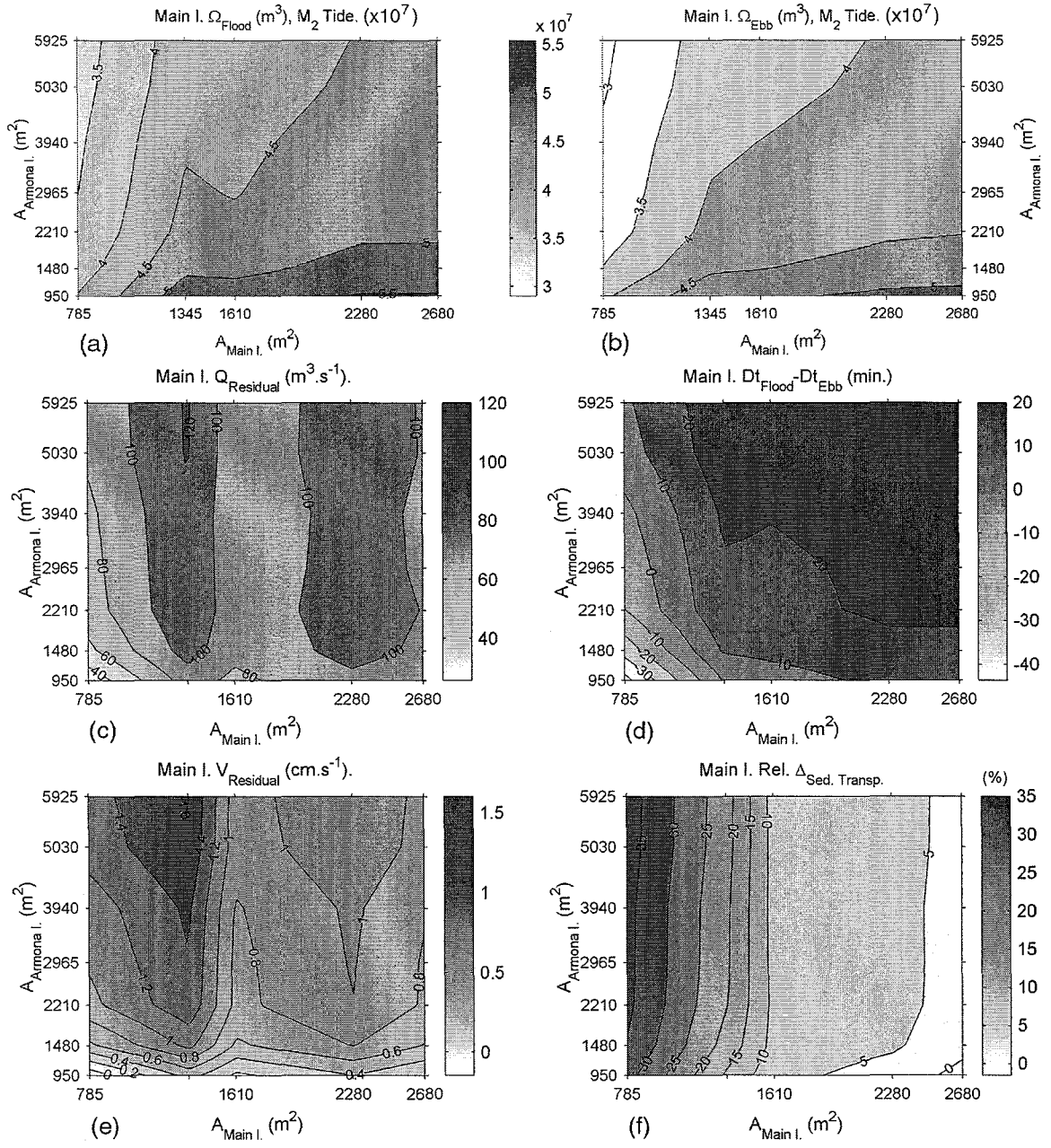

Figure 5-16. Results at Main Inlet from simulations with M_2 forcing, varying A_{Armona} and A_{Main} (A_{New}=595 m^2). Flood and ebb tidal prisms (a and b); Residual discharge (c); Difference between flood and ebb durations (d); Residual current (e); and flood – ebb near-bed sediment transport difference, relative to the ebb sediment transport (f).

Both residual discharge and residual current appear to decrease as a result of the reduction in A_{Armona}, suggesting a decrease of the net flow from Main Inlet to Armona. This trend is enhanced when both A_{Armona} and A_{Main} are small (950 m^2 and 785 m^2, respectively), in which case the residual discharge decreases substantially (panel c), the residual current becomes seaward

(panel e), and the ebb becomes longer than flood (panel d). However, the difference between flood and ebb sediment transport capacity at Main Inlet, which does not appear to depend on changes in A_{Armona} (panel f), increases landward as A_{Main} decreases, enhancing the infilling of the lagoon with coarse sediment.

Moreover, a closer examination of panels (e) and (f) reveal that the direction of the residual velocity is opposite to the direction of the net near-bed sediment transport in some inlet scenarios:

- When A_{Armona}= 950 m^2 and A_{Main} = 785 m^2, the residual velocity appears to be seaward, and the net sediment transport is shown to be strongly landward (flood sediment transport 32% larger that that of ebb). This is due to the fact that the flood maximum velocity is significantly larger than the ebb maximum velocity, which overshadows both the weakly seaward residual velocity, and the moderately distorted velocity field (see Figure 5-20-c).
- When A_{Armona}= 950 m^2 and A_{Main} = 2,680 m^2, the residual is weakly landward, and the net sediment transport appears to be weakly seaward. In this case, the flood maximum velocity is only slightly larger than the ebb maximum velocity, and is in turn overshadowed by the strongly distorted velocity field.

This response of the Main Inlet hydrodynamics to a reduction in both Main Inlet and Armona Inlet cross-sectional areas, which decreases the landward flow but increases the landward sediment transport, is associated with a response in New Inlet (see Figure 5-13-c to -f, and item 6), in which both the landward residual discharge and sediment transport are enhanced, with possible instability implications for that inlet, as the lagoonal area adjacent to New Inlet will have the tendency to accumulate sediment and eventually reduce the hydraulic efficiency.

Armona Inlet

A. Simulations varying A_{Armona} and A_{New}, with A_{Main} = 1,610 m^2 (Figure 5-17)

15) Figure 5-17 shows that changes in Armona Inlet flood and ebb flow volumes and durations are practically independent of the variations in New Inlet cross-sectional area (for a given A_{Armona}, the tidal prism varies less than 0.5% as A_{New} changes), except when A_{New} = 230 m^2, in which case the Armona flood volume and duration decreases significantly faster as A_{Armona} decreases (Panels a and d). This rapid decrease in the flood tidal prism, and in general an increase in the seaward net flow, current, and sediment transport (panels c, e and f), is associ-

ated with a corresponding increase in the net landward flow at Main Inlet, as mentioned in (12).

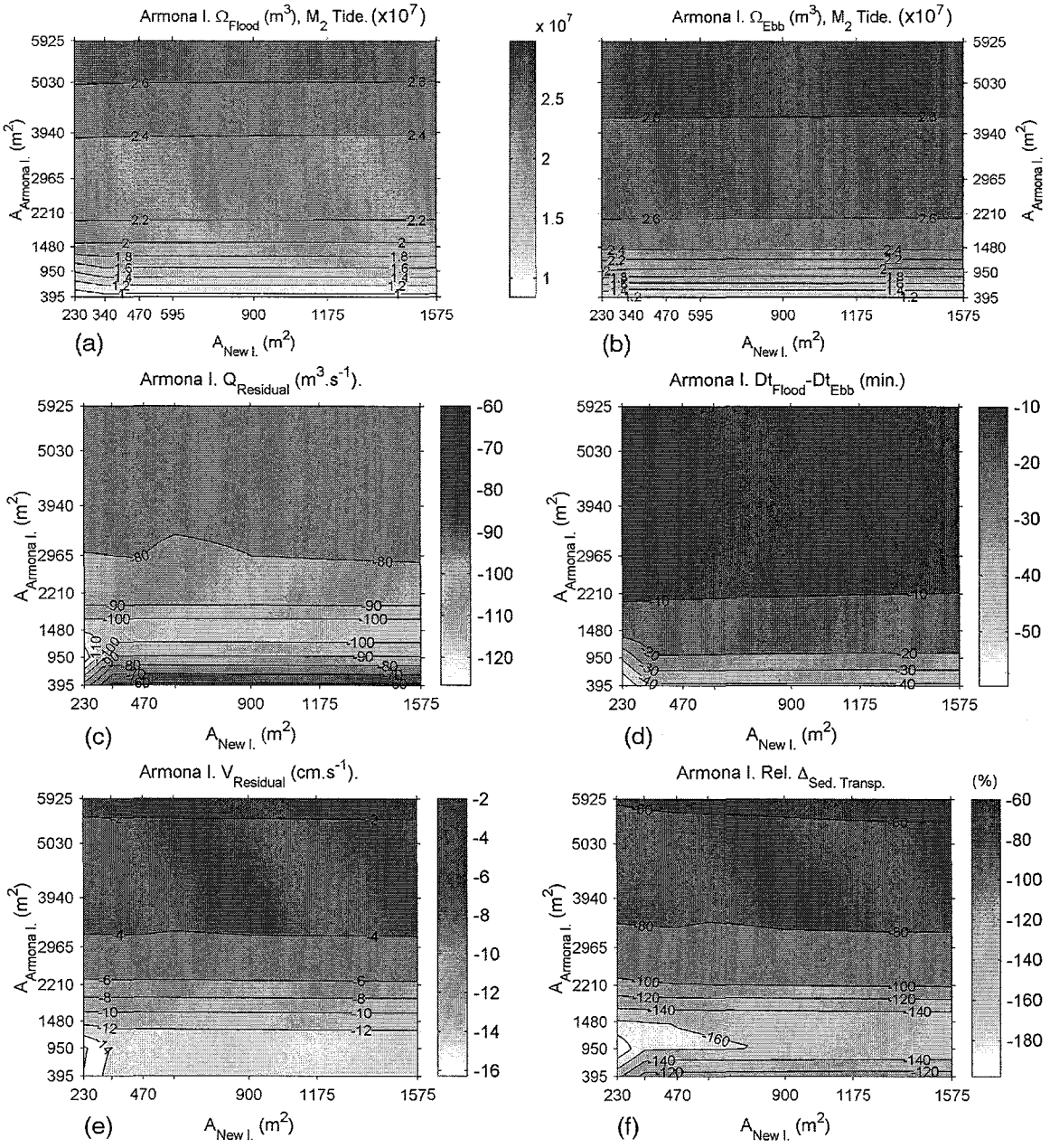

Figure 5-17. Results at Armona Inlet from simulations with M_2 forcing, varying A_{Armona} and A_{New} (A_{Main}=1,610 m^2). Flood and ebb tidal prisms (a and b); Residual discharge (c); Difference between flood and ebb durations (d); Residual current (e); and flood – ebb near-bed sediment transport difference, relative to the flood sediment transport (f).

16) In all cases, including the present-day inlet configuration, the ebb volume is significantly larger than the flood volume (as shown by the residual discharge in panel c), and the residual current and sediment transport are seaward (panels e and f), implying that this inlet is a net "exporter" of water and coarse sediment from the lagoon to the ocean, no matter what its own stability condition may be. As its cross-sectional area increases from its current size, the difference between ebb and flow decreases (panel c), meaning that the net circulation from Main Inlet to Armona decreases, and implying a potential reduction in its seaward-flushing capacity (panels e and f). As the cross-sectional area decreases, the residuals (flow and velocity) tend to increase (except for A_{Armona}=395 m^2, as discussed in item16), meaning that the ebb dominance becomes stronger.

17) Examination of panels (c), (e) and (f) suggest that the areas for which Armona Inlet experiences the greatest seaward net flow, current, and sediment transport, independently of the New Inlet cross-sectional area, are 950 m^2 and 1,480 m^2, which are roughly one third and one half of the present-day size. Keeping in mind the fact that Armona inlet has historically been involved in a process of significant reduction in size, this suggests that, even if at present Armona Inlet already experiences an ebb dominant stability, this state would be enhanced in the case of a continuing reduction. This in turn may be an indication of a decrease in the rate of area reduction, which is in agreement with the historical data analysis (Figure 3-26).

18) Similarly to (6), the duration of ebb being longer that that of flood is not a determining factor in the flow dominance. In fact, the ebb dominance is determined by the seaward-directed residual discharge and current, as well as by the maximum velocity occurring during ebb (see Figure 5-28).

B. Simulations varying A_{Armona} and A_{Main}, with A_{New} = 595 m^2 (Figure 5-18)

19) Panels a and b show that the flood and ebb tidal prisms at Armona exhibit the inverse trend than the tidal prisms at Main Inlet for the same simulations (Figure 5-16-a and -b). Namely, the changes in both flood and ebb tidal prisms through Armona Inlet depend to a similar extent on changes in both Armona Inlet and Main Inlet cross-sectional areas, and they are larger when A_{Armona} is large and A_{Main} small, than when is A_{Armona} small and A_{Main} large. This may be due to the proximity of these two inlets and to the fact that the lagoonal areas they service are likely to overlap to a large extent.

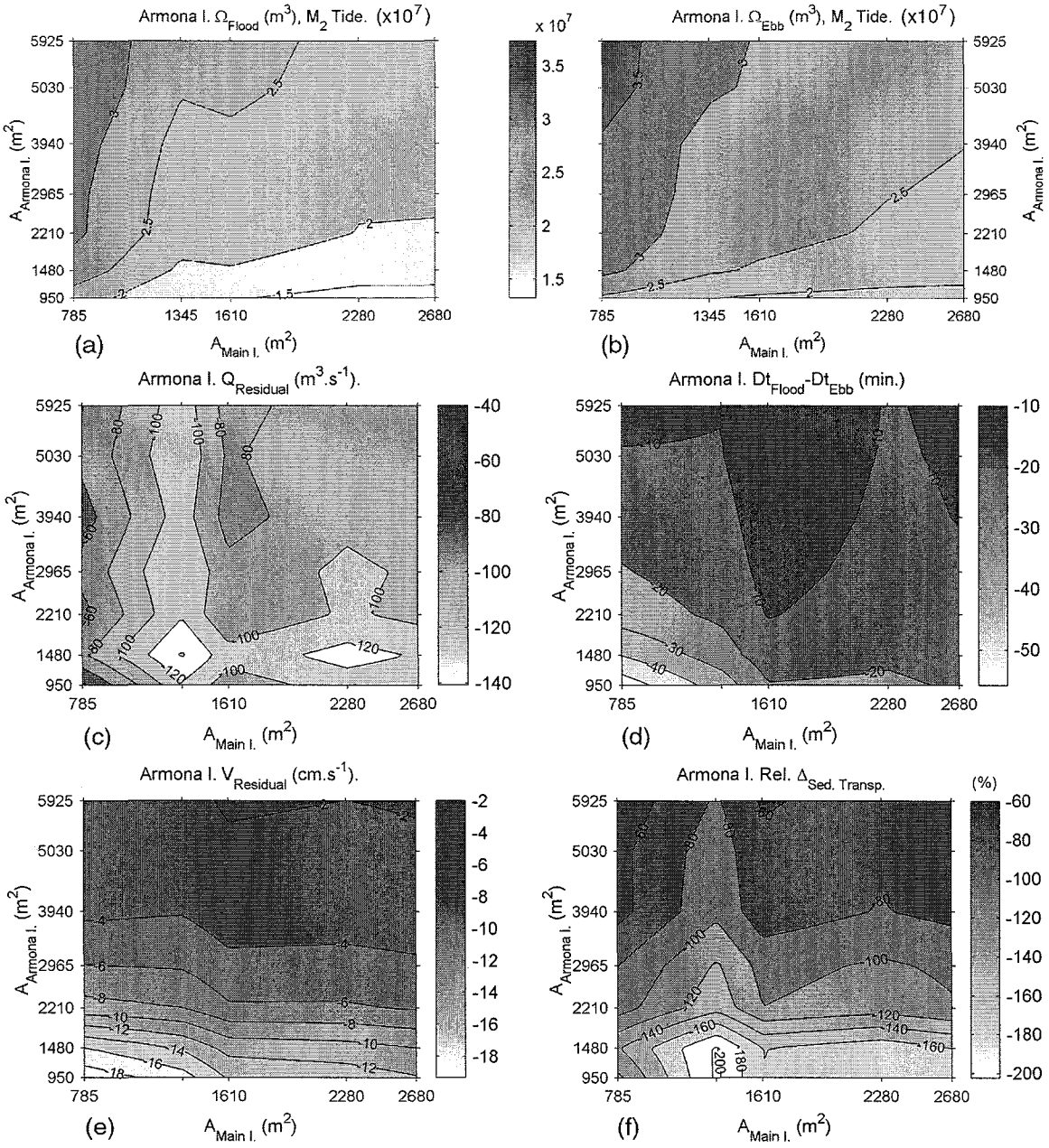

Figure 5-18. Results at Armona Inlet from simulations with M_2 forcing, varying A_{Armona} and A_{Main} (A_{New}=595 m^2). Flood and ebb tidal prisms (a and b); Residual discharge (c); Difference between flood and ebb durations (d); Residual current (e); and flood – ebb near-bed sediment transport difference, relative to the flood sediment transport (f).

20) Similar to the simulations varying A_{Armona} and A_{New} (item 16), the ebb volume is in all cases significantly larger than the flood volume, as can be seen by the residual discharge being consistently seaward and ranging from 40 to 120 $m^3.s^{-1}$ (panel c), implying again that this inlet is

a net "exporter" of water and sediment from the lagoon to the ocean. Moreover, the residual current, the maximum velocity (Figure 5-28), and the near-bed sediment transport are all directed seaward throughout the simulations.

21) When Armona Inlet experiences a reduction in its cross-sectional area (relative to its current size, i.e., 2,965 m^2), the hydrodynamic response is such that it tends to restore the original size: the seaward net flow and current, as well as the near-bed sediment transport, increase, similar to item (16). Inversely, when the cross-sectional area increases, the intensity of the seaward net flow and transport decrease, showing that the capacity of the inlet to maintain its cross-sectional area decreases. Therefore, these elements suggest that Armona Inlet may be in a condition of stable equilibrium (as supported by the historical data analysis, section 3.3.3), given that it exhibits consistently ebb dominance and appears to be able to counteract disturbances. Thus, instability may only be caused by events and processes not analyzed in this study (for instance, changes in sediment supply and wave climate during storms).

22) Similar than for New Inlet (item 7), panels (c) and (f) show the existence of a combination of Main and Armona cross-sectional areas, namely (1,345 m^2; 1,480 m^2), for which the Armona Inlet hydrodynamics tend to a more efficient seaward flushing, and in general confer a stronger stability to the inlet. These specific areas are in both cases smaller than the present-day cross-sectional areas. Since this scenario appears to happen only with this specific combination of areas, it is unlikely that this may have occurred, in spite of the fact that these two inlets have a history of growth.

5.4.2. Tidal Distortion

Harmonic analysis was performed to i) the simulated water surface elevation (WSE) time series at six stations (Bridge, New Inlet, Main Channel, Main Inlet, Olhão, and Armona; see Figure 5-4 for location), as well as to ii) the simulated times series of cross-sectionally averaged velocities through the inlets. Asymmetries in tidal velocity rather than water surface control directly net sediment transport patterns (Friedrichs and Aubrey, 1988).

The information extracted from these analyses corresponds to the amplitude and phase of the M_2 and M_4 tidal constituents, which are, as mentioned in section 2.3.1, used to estimate the tidal distortion. The surface elevation and velocity M_4 to M_2 amplitude ratios (a_{M4}/a_{M2} and

v_{M4}/v_{M2}) and relative phases ($2\varphi_{M2}$-φ_{M4} and $2\phi_{M2}$-ϕ_{M4}) quantify the nature and degree of tidal distortion in the system (Aubrey and Speer, 1985; Speer and Aubrey, 1985).

Given that the boundaries in which the forcing is applied in RMA-2 are non-radiating, the distorted water surface elevation signal generated in the lagoon is gradually deformed by the model as it propagates through the inlets to the offshore model boundary, to comply with the prescribed forcing function at the boundary. This effect is usually minimized by constructing the mesh offshore such that the forcing boundary is far from the area of interest (i.e., the inlet gorge), which is the case for New and Armona inlets. However, at Main Inlet, preliminary simulation runs with a large fan-shaped offshore mesh resulted in numerical instabilities around the tips of the jetties. Numerical stability was only obtained by constructing a smaller offshore computational domain at Main Inlet, in which the forcing boundary was close to the inlet gorge, i.e., close to the cross-section where the modeled flow velocity was extracted for analysis (see Figure 5-19). Therefore, an analysis was done to assess the potential influence of this non-radiating condition in the M_4 tidal signal near the Main Inlet mouth. More specifically, the M_4 water surface elevation results from the RMA-2V model, $\eta_{M4,\ model}$, were compared with the results a purely reflective boundary would produce in terms of the tide, at eight nodes along the inlet channel (lagoonward from the boundary, see Figure 5-19).

In a purely reflective boundary, the simple harmonic M_2 forcing would prescribe a zero M_4 amplitude (i.e., a_{M4}= 0) at the boundary, and the free M_4 tide generated inside the lagoon should behave as a standing wave in the vicinity of the forcing boundary, with the boundary itself being a node of the standing wave. Using linear wave theory for a standing wave, the maximum water surface elevation due to the M_4 signal, $\eta_{M4,\ s.\ wave}$, is related to the M_4 velocity, u_{M4}, by

$$\eta_{M4,\ s.\ wave} = a_{M4} \sin kx = u_{M4} \sqrt{\frac{h}{g}} \sin kx \tag{5.13}$$

where h is the water depth, g is the acceleration of gravity, k is the wave number at each depth for an M_4 tidal wave (obtained with the dispersion relationship), and x is the distance away from the boundary. Both the RMA-2 results and the linear standing wave model results are shown in Table 5-3.

Table 5-3. RMA-2V and linear standing wave model results of water surface elevation at selected nodes at Main Inlet (see Figure 5-19).

Node	$\eta_{M4,\ model}$ (cm)	u_{M4} (cm.s^{-1})	h (m)	x (m)	k (m^{-1})	a_{M4} (cm)	$\eta_{M4,\ s.\ wave}$ (cm)
(1)	**(2)**	(3)	(4)	(5)	(6)	(7)	**(8)**
1	**0.0**	17.3	15.0	0	$2.3 \cdot 10^{-5}$	21.4	**0.0**
2	**0.6**	19.9	14.0	27	$2.4 \cdot 10^{-5}$	23.8	**0.015**
3	**3.8**	25.0	11.0	56	$2.7 \cdot 10^{-5}$	26.5	**0.040**
4	**8.3**	30.7	9.2	89	$3.0 \cdot 10^{-5}$	29.7	**0.078**
5	**7.6**	29.8	9.0	114	$3.0 \cdot 10^{-5}$	28.6	**0.097**
6	**6.4**	29.5	9.0	148	$3.0 \cdot 10^{-5}$	28.2	**0.125**
7	**4.1**	26.6	9.0	179	$3.0 \cdot 10^{-5}$	25.4	**0.136**
8	**3.1**	24.9	9.0	209	$3.0 \cdot 10^{-5}$	23.8	**0.149**

The water surface elevation along the inlet obtained with the linear standing wave model (column 8) appears to be 1 to 2 orders of magnitude smaller than the results from RMA-2V (column 2), which means that the standing wave only accounts for a small fraction of the water surface elevation obtained with RMA-2V.

Similarly, if the modeled water surface elevation ($\eta_{M4,\ model}$, column 1), is assumed to be mainly a product of a standing wave, the corresponding velocity would be 1 to 2 orders of magnitude larger than the values obtained with the model (column 3), suggesting again that a standing wave contribution in the velocity obtained with RMA-2V is negligible.

Although the effects of channel contraction and expansion along the Main Inlet entrance are not taken into account in this analysis, the results above are an indication that the lack of radiation in the forcing boundary in RMA-2V does not have an important effect on the modeled M_4 signal, and therefore may not hamper significantly the validity of the data for tidal distortion analysis.

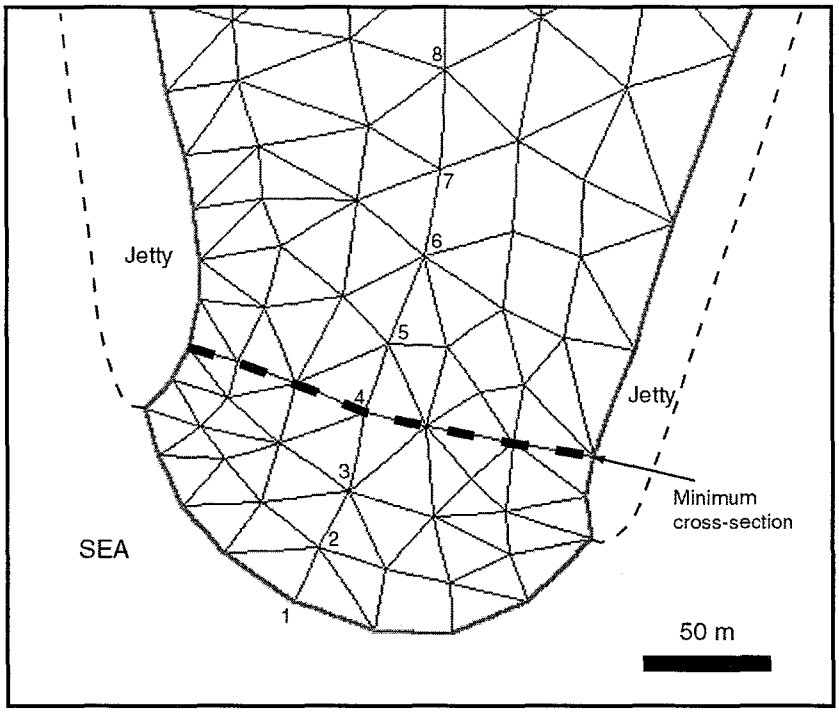

Figure 5-19. Computational mesh at Main Inlet and nodes at which the model results are compared with the linear standing wave model (Table 5-3).

The water surface elevation distortion results are presented in the appendix (section 5.6.7, p 257). The water surface M_4 to M_2 amplitude ratio (a_{M4}/a_{M2}), and the phase of M_4 relative to M_2 ($2\varphi_{M2}-\varphi_{M4}$), are plotted in Figure 5-46 (for the simulations varying A_{Armona} and A_{New}), and in Figure 5-47 (for the simulations varying A_{Armona} and A_{Main}). The velocity distortion results are plotted for each simulation type in Figure 5-20 and Figure 5-21 below.

Based on the examination of these figures, the following observations can be made:

A. Simulations varying A_{Armona} and A_{New}, with $A_{Main} = 1{,}610\ m^2$

23) The results of velocity M_4/M_2 amplitude ratio (Figure 5-20-a, -c and -e) show that the non-linear distortion in the tidal velocity at the inlets is large. This distortion is particularly important at New Inlet, where the velocity M_4/M_2 reaches values exceeding 0.45 for large values of the cross-sectional area. This suggests that the portion of the lagoon serviced by that inlet produces a stronger distortion than the areas serviced by the other inlets.

In fact, New Inlet is in a zone of the lagoon where the channels are narrow and relatively shallow, and where the ratio of intertidal to channel surface areas is the largest in the system. Therefore, as the cross-sectional area at New Inlet becomes larger, and the tidal prism in-

creases, more intertidal areas get flooded, causing a delay of high waters (i.e., ebb dominance), and increased distortion of the tidal velocity (as found by Friedrichs and Aubrey, 1988). However, the degree of ebb dominance appears to be inversely related to the velocity distortion. This is due to a decrease in the average water depth (i.e., an increase in the average tidal amplitude to water depth ratio) as larger intertidal areas get flooded, which in turn increases the frictional interaction between the tide and the lagoon bottoms. This effect compensates and even overcomes the nonlinear effects of the additional water storage, favoring flood dominance, or in this case, reducing the ebb dominance.

At Armona Inlet, which is also ebb dominant, a similar relationship is found between the ebb dominance and the velocity M_4/M_2 amplitude ratio. At Main Inlet, which is flood dominant, the opposite relationship exist for these simulations: as A_{Armona} increases, the flood dominance increase with the velocity distortion.

24) Panels (b) and (d) in Figure 5-20 show that New and Main Inlets display a velocity $2\phi_{M2}-\phi_{M4}$ relative phase within ± 10° of a perfectly symmetric tide (for which the relative phase is 270°; see Figure 2-5). This is mainly because of the forcing being simple harmonic (i.e., no offshore tidal distortion) and the inlet gorges being close to the open boundaries.

Panel (f) shows that at Armona Inlet, where the open boundary was constructed farther offshore to capture the effects of the existing large ebb tidal delta on the hydrodynamics of the system, the relative phase varies significantly throughout the simulations, and suggests that this inlet is in most cases ebb dominant ($90°<2\phi_{M2}-\phi_{M4}<270°$; see Figure 2-5). Moreover, this panel shows that the smaller relative phase (i.e., the stronger ebb dominance) occurs for A_{Armona}= 950 m^2 and 1,480 m^2, which is in agreement with what was found from the tidal prism and residual circulation analysis (item 16).

25) Given the above and looking at panel (e) in Figure 5-20, it can be said that strong ebb dominance is associated with small velocity M_4/M_2 amplitude ratio, suggesting that these quantities are inversely proportional. Besides, the results at Main Inlet show that both flood dominance (Figure 5-15-e, item 10) and tidal distortion (Figure 5-20-c) increase as A_{Armona} increases. Therefore, the simulations in which A_{Main} remains unchanged suggest that an increase in velocity M_4/M_2 amplitude ratio is an indication of increased landward transport (i.e., an increase in flood dominance for Main Inlet or a decrease in ebb dominance for Armona and New inlets).

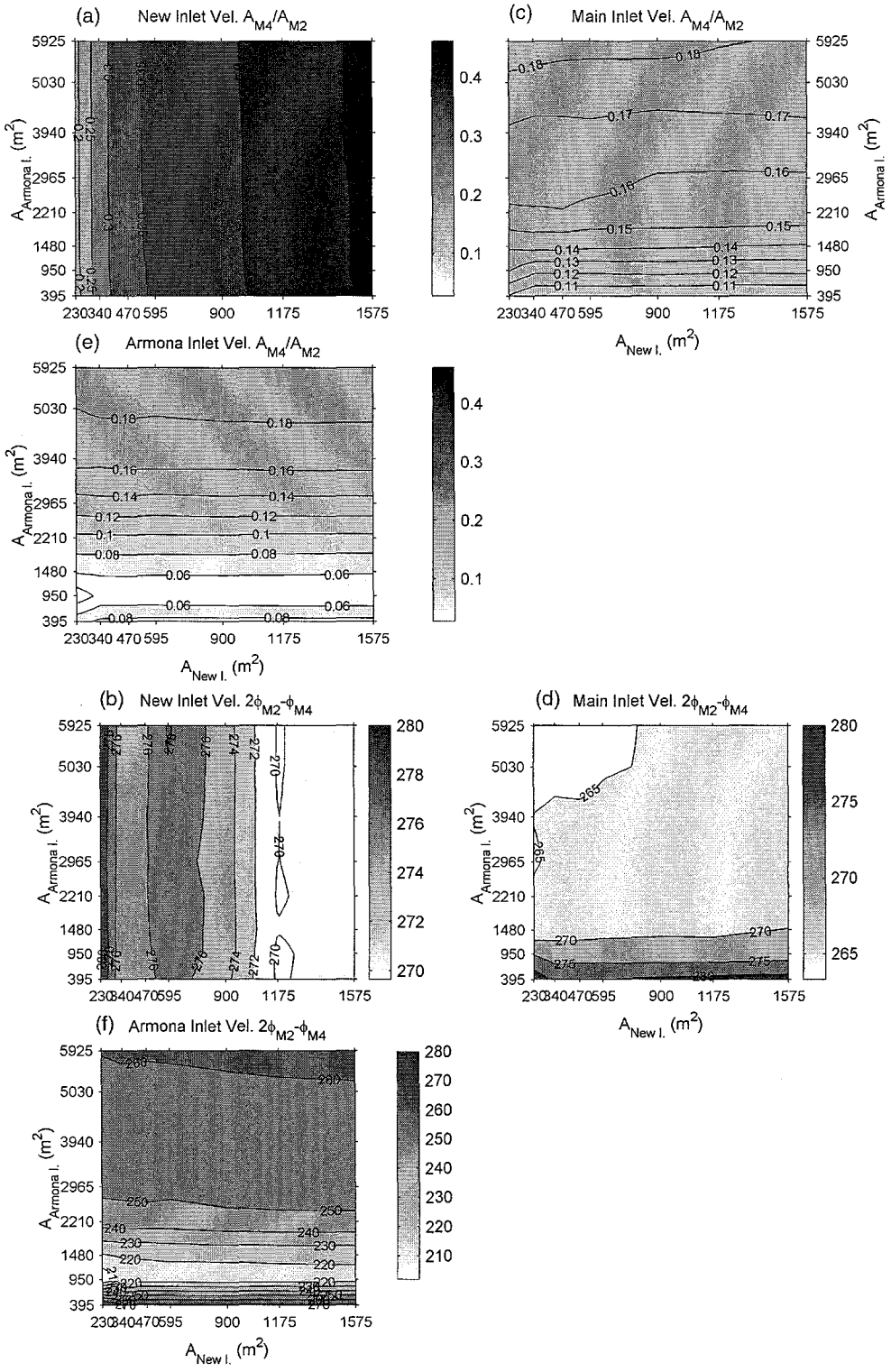

Figure 5-20. Velocity M_4 to M_2 amplitude ratio and phase of M_4 relative to M_2 for New Inlet (a and b), Main Inlet (c and d), and Armona (e and f). Simulations varying A_{Armona} and A_{New} (A_{Main} = 1,610 m^2).

26) Examination of the water surface elevation harmonic analysis results (Figure 5-46, p 257) reveals that the nonlinear distortion in sea-surface differs significantly from tidal velocity distortion, and the following observations can be made:

- The water surface tidal distortion is consistently lower than the velocity distortion.
- Interestingly, the water surface nonlinear distortion exhibits the opposite trend than that of the tidal velocity distortion. In fact, at New and Armona inlets, an increase in the water surface distortion (Figure 5-46, panels a and e) is associated with an increase in net seaward transport (items 1 and 16), whereas at Main Inlet (Figure 5-46, panel c) it is associated with a decrease in landward transport (item 10).
- The relative phases at Armona Inlet and Main Inlet (Figure 5-46, panels b and d) suggest, for most of the simulations, flood and ebb dominance at these inlets, respectively, which is the opposite to what the results from the tidal prism and residual circulation analysis suggest (see item 30 for comments).

B. Simulations varying A_{Armona} and A_{Main}, with $A_{New} = 595\ m^2$ (Figure 5-21)

27) Panel (a) shows that at New Inlet the velocity M_4/M_2 amplitude ratio is large (0.36 on average, similar to the results shown in Figure 5-20 for the simulations with $A_{New} = 595\ m^2$). The velocity $2\phi_{M2}-\phi_{M4}$ relative phase at that inlet (panel b) indicates that the tidal velocity signal is almost symmetric, due to the proximity of the cross-section to the open boundary. It can also be seen that variations in both amplitude ratio and relative phase are small (less than 1%) due the fact that the cross-sectional area at New Inlet remains unchanged in these simulations. This suggests that changes in the tidal prisms and residual circulation, which have been shown to be important in some simulations –items (4) to (8)–, are not necessarily coupled to changes in the tidal distortion.

28) The distortion of the tidal velocity at Main and Armona exhibits an increase as both inlet cross-sectional areas increase (panels c and e). This increase in tidal velocity distortion is associated with a decrease in both flood dominance (Main Inlet), and ebb dominance (Armona Inlet).

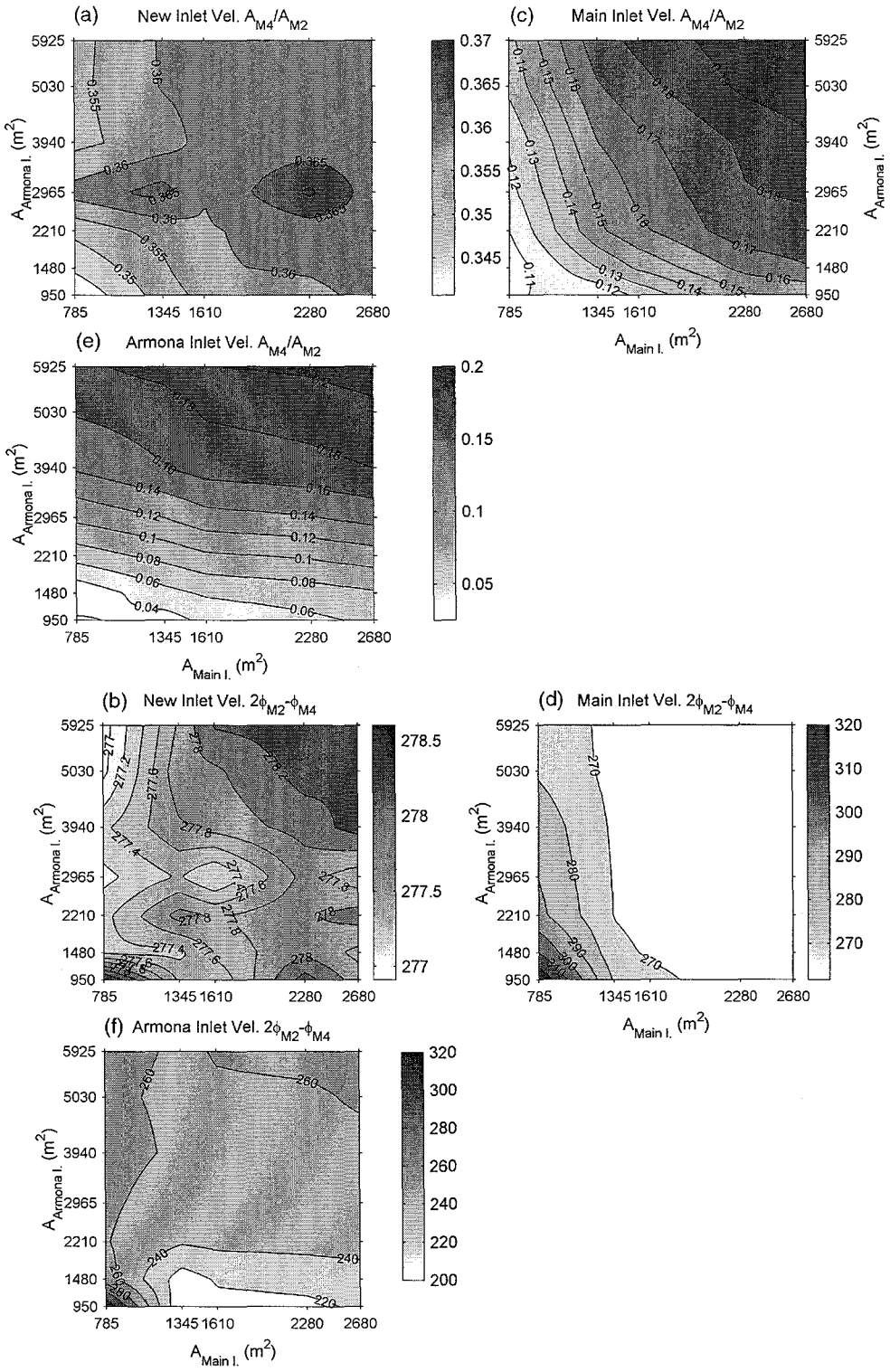

Figure 5-21. Velocity M_4 to M_2 amplitude ratio and phase of M_4 relative to M_2 for New Inlet (a and b), Main Inlet (c and d), and Armona (e and f). Simulations varying A_{Armona} and A_{New} (A_{Main} = 1,610 m^2).

29) The velocity $2\phi_{M2}$-ϕ_{M4} relative phase at Main Inlet (panel d), suggest that the flow is either quasi-symmetric (for large A_{Armona} and A_{Main}), or increasingly flood dominant as these areas decrease, which is in agreement with what the residual analysis suggests (item 14). Although not so clear, a similar conclusion can be drawn from the analysis of the relative phase at Armona Inlet (panel f), compared to the residual current trend.

30) The analysis of the water surface M_4/M_2 amplitude ratio and $2\varphi_{M2}$-φ_{M4} relative phase suggest that:

- Similar to the results from the simulations varying A_{Armona} and A_{New}, the water surface nonlinear distortion at all three inlets exhibits the opposite trend than that of the tidal velocity distortion.
- The water surface distortion at Armona Inlet (Figure 5-47-a) is not only dependent on the changes on its cross-sectional area, but also on disturbances in Main Inlet. This is an additional evidence of the strong effects Main Inlet disturbances can cause on Armona Inlet.
- Inversely, the effects of changes in A_{Armona} on the water surface distortion and the degree of flood dominance at Main Inlet are small. However, as A_{Main} increases, both the water surface distortion and the net landward sediment transport decrease significantly. The water surface distortion at Main Inlet is, in these simulations, proportional to the degree of flood dominance, as opposed to the results suggested by the simulations where A_{Main} remained unchanged. This different result is due to the fact that the effects (on Main Inlet) of disturbances in Main Inlet itself seem to overshadow the effects of the disturbances in Armona Inlet.

Similar to the velocity relative phase, the water surface relative phase at Armona and Main Inlet suggest flow and ebb dominance, respectively, which is in disagreement with results obtained from the residual and transport analysis. This, added to the observations in items (26) and (29), suggests that the relative phase may in some cases not be an evident and reliable diagnostic indicator of the flow dominance. This apparent discrepancy, in terms of flow dominance, between what the relative phase suggests and what the analysis of residuals (flow and current) indicates, is mainly due to the existence of strong net flows between inlets. In fact, the flow dominance arguments, which are derived from the water surface and velocity examination in terms of the magnitude and phases of the primary and forced harmonic tidal

constituents, are based on the assumption of negligible freshwater inflow in single-inlet systems (Aubrey, 1986), limiting the generality of the results. Although single-inlet systems can exhibit consistently stronger flows during some periods of the tidal cycle, i.e., be ebb or flood dominance due to nonlinear tidal distortion, the net flow through the inlet is zero. However, the existence of multiple inlets servicing a single embayment confers an additional characteristic to the global hydrodynamics, which is the potential existence of residual discharges and currents through the inlets. These added processes, together with the magnitude and direction of the maximum velocity, are in fact the characteristics that ultimately determine the flow dominance in a given inlet of a multiple inlet system.

5.4.3. Maximum velocities through the inlets.

The maximum velocity through the inlet is a parameter that has been often used for inlet stability analysis, mainly through the closure curve model and related theories (see Chapter 2), since this velocity corresponds to the highest sediment transport rate throughout the tidal cycle. In addition to the magnitude of the maximum velocity through the inlet gorge, its direction is also important, i.e., whether it occurs during flood or during ebb, since it can be an indication of the flushing capacity of the inlet.

New Inlet

Figure 5-22 shows the changes in maximum velocity at New Inlet, for all the simulations.

31) Changes in Armona cross-sectional area have minor effects in the New Inlet maximum velocity, as revealed by panels (a), (c) and (e). For fixed New Inlet and Main Inlet cross-sectional areas, the changes in New Inlet maximum velocity as a function of changes in A_{Armona} are small (V_{max} at New Inlet decreases 1-3% as A_{Armona} increases from 395 to 5,925 m^2).

32) Panels (b) and (d) are the curves of maximum velocity as a function of A_{New} for different values of A_{Armona}, and for spring (i.e., closure curve) and M_2 tidal forcing, respectively. These curves show that the maximum velocity decreases dramatically as the cross-sectional area increases (from 230 to 1575 m^2). This behavior corresponds to the monotonically decreasing section of the theoretical Escoffier (1940) closure curve (Figure 2.1), indicating that New Inlet may be at present in equilibrium, as found in item (1). However, the maximum velocity at New Inlet does not decrease as A_{New} becomes small, at least for the cross-sectional areas used in these simulations.

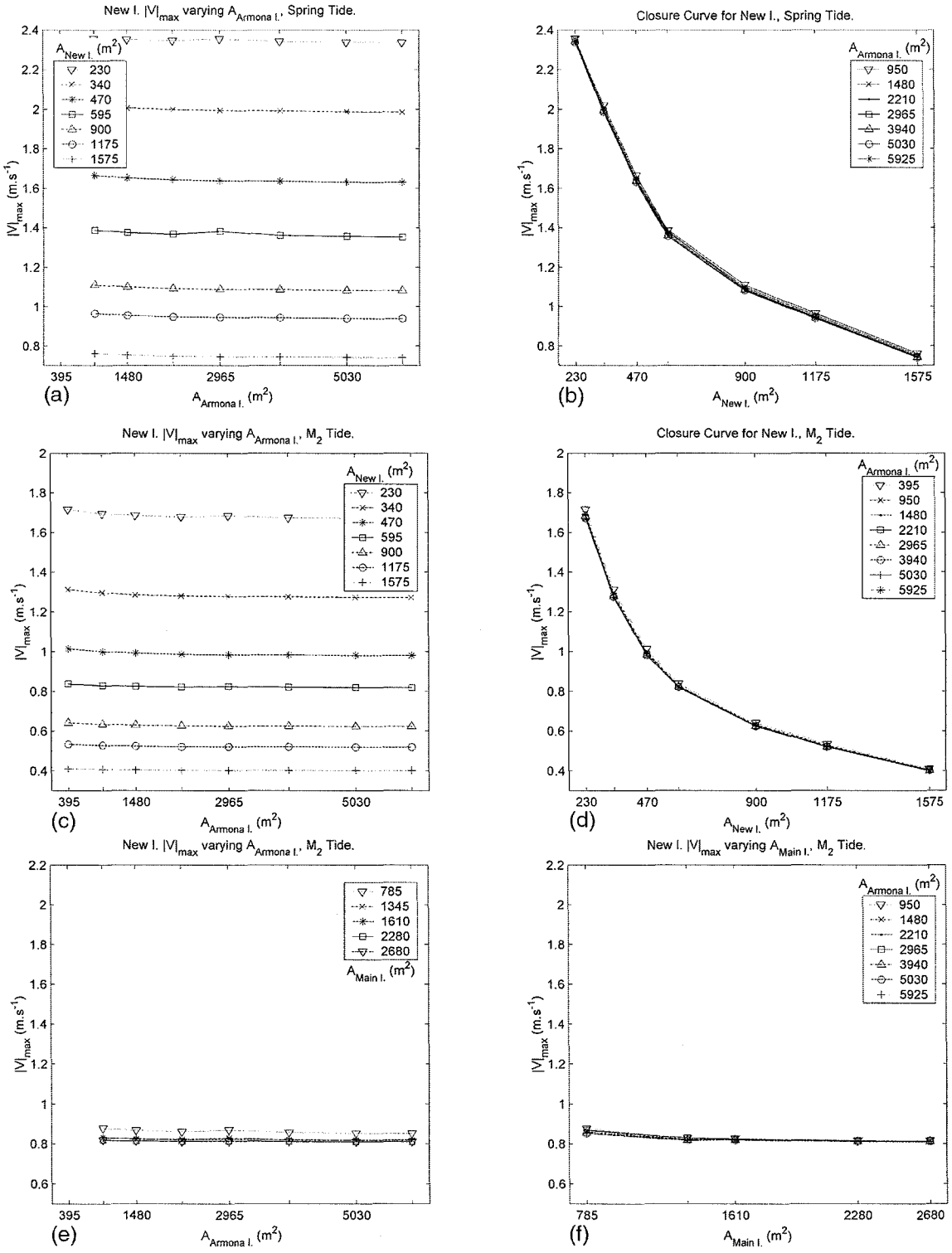

Figure 5-22. Maximum Velocities through New Inlet. Spring tidal forcing, varying A_{Armona} and A_{New} (a and b); M_2 forcing varying A_{Armona} and A_{New} (c and d), and varying A_{Armona} and A_{Main} (e and f). For a, b, c, and d: A_{Main}=1,610 m^2. For e and f, $A_{New.}$=595 m^2. All the plots are at the same scale.

In order to investigate the trend of the maximum velocity for small cross-sectional areas, additional model runs were performed, whose characteristics are shown in Table 5-4.

Table 5-4. Model runs with small New Inlet cross-sectional areas.

Run	A_{New}	A_{Main} (m^2)	A_{Armona} (m^2)	Forcing Type
S_2XA	85 m^2	1,610 m^2	950 m^2	M_2
S_1XA	122 m^2	1,610 m^2	950 m^2	M_2

33) The results of these simulations (Figure 5-23) show that the absolute maximum velocity (dashed line) through New Inlet for these small cross-sectional areas persists in increasing. However, these maximum velocities occur during flood, as opposed to the maximum velocities for the larger areas, which occur during ebb. Furthermore, the figure shows that the maximum ebb velocity, which can be regarded as the maximum velocity during the "seaward flushing" phase of the tide, does decrease for the smaller cross-sectional areas, implying a decrease in the inlet's capacity to transport sediment seaward.

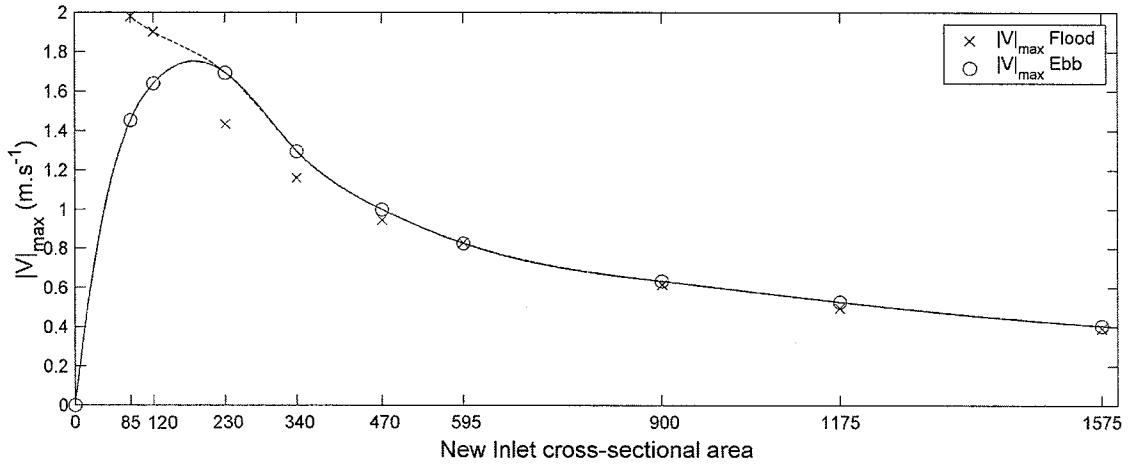

Figure 5-23. Maximum Flood and Ebb cross-sectionally averaged velocity magnitudes through New Inlet for runs [S_2XA, S_1XA, AXA, BXA, CXA, XXA, DXA, EXA, FXA].

Even if the absolute maximum velocity does not follow the behavior of a "typical" closure curve in the region of small cross-sectional areas, the combination of a) the change from ebb to flood in the occurrence of the maximum velocity, and b) the decrease in ebb maximum velocity, may be an indication of instability in the long term, since the higher sediment transport rate becomes landward, and the seaward sediment transport rate decreases, independently of what the velocity needed to remove the sediment deposited in the inlet gorge (equilibrium velocity)

may be. These scenarios with small areas, in which the maximum velocities exceed 1.8 $m.s^{-1}$ and may be greater than the so-called equilibrium velocity, will indeed have the tendency to promote the infilling of the back-barrier areas adjacent to the inlet (shoaling of channels, creation or enlargement of flood deltas), which may eventually lead to inlet closure. Therefore, given that the occurrence of the maximum velocity during flood or ebb can be determinant for the long-term stability of the inlet, the use of the closure curve for inlet stability arguments has to take into account not only the magnitude, but also the direction of the maximum velocity.

34) The closure curve (panel b) also shows that the maximum velocity under present conditions is approximately 1.35 $m.s^{-1}$, which is large if compared to the widely used equilibrium velocity of 1 $m.s^{-1}$. This in principle suggests that the inlet is at present in a phase of growth.

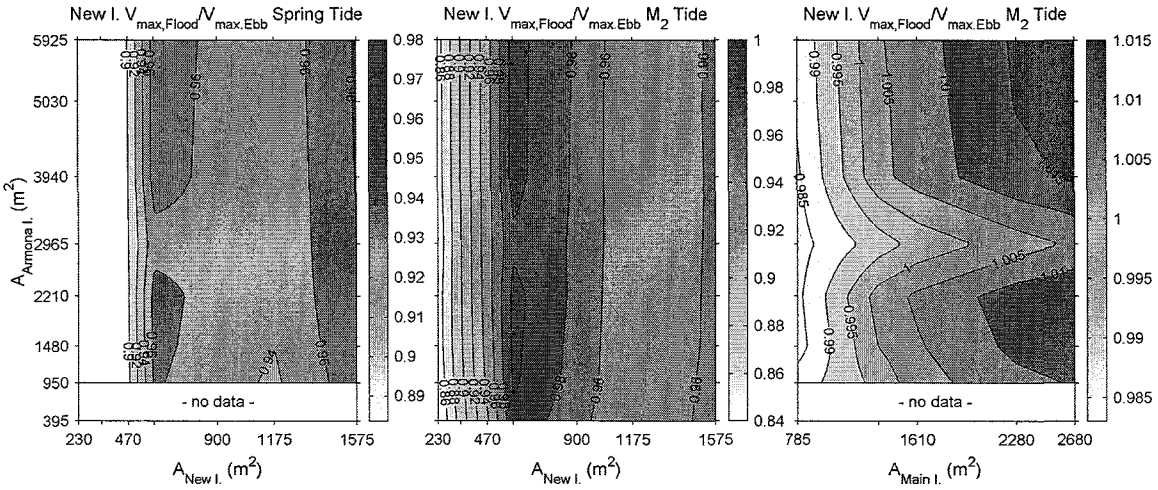

Figure 5-24. Flood / Ebb New Inlet maximum velocity ratio. Spring forcing varying A_{Armona} and A_{New} (a); M_2 forcing varying A_{Armona} and A_{New} (b), and A_{Armona} and A_{Main} (c).

35) When looking at the portion of the tide (flood or ebb) in which the maximum New Inlet velocity magnitude occurs, in terms of the flood to ebb maximum velocity ratio (Figure 5-24), it is found that:

- For the runs keeping Main Inlet cross-sectional area constant (panels a and b), the ebb maximum velocity is in general greater than the flood maximum velocity. The ebb maximum velocity is of the order of 10% (spring forcing) and 15% (M_2 forcing) larger than the flood maximum velocity, for small A_{New} (230 m^2). The difference between flood and ebb maximum velocities decreases rapidly to 2-4% (spring forcing) and 0-4% (M_2 forcing) as A_{New} increases

to 595 m^2. For larger cross-sectional areas, the ebb maximum velocity becomes the largest again, by 2-4%. This suggests that the tendency to transport sediment seaward increases as the cross-sectional area either increases or decreases, relative to its current value, which can be interpreted as a stabilizing hydrodynamic response to the cross-sectional area disturbance. This trend is similar to the residual discharge behavior for the same simulations, as show in Figure 5-12, and implies that the present-day New Inlet cross-sectional area is stable, and that the hydrodynamics would respond against disturbances in it's actual cross-sectional area.

- In the case of changes of Main Inlet cross-sectional area keeping A_{New} constant (panel c), the maximum velocity through New Inlet occurs during ebb for A_{Main} small (780 m^2), and during flood for A_{Main} larger. This is an indication that New Inlet has a tendency to flush the sediment seaward more effectively when the adjacent inlet's cross-sectional area is small, as confirmed by the residual current and the near-bed sediment transport (Figure 5-13-e and -f).

Main Inlet

Figure 5-25 and Figure 5-26 show the maximum velocity through Main Inlet, and the flood-to-ebb maximum velocity ratio, respectively, for all the simulations. Based on these figures, the following observations can be made:

36) Figure 5-26 shows that the occurrence of maximum velocity is always during flood, which supports the flood dominance arguments presented in item (10).

37) When keeping A_{Main} constant (Figure 5-25, panels a, b, c, and d), the changes in the maximum velocity through Main Inlet are almost solely controlled by changes in the Armona Inlet cross-sectional area, with the exception of the simulations where both New and Armona inlets have their smallest area, in which case the maximum velocity exhibits a sudden increase of 13% (spring tide forcing) and 4% (M_2 forcing). This response is clearly shown in Figure 5-26-a and -b, where the maximum flood velocity is shown to increase dramatically (relative to the ebb maximum velocity). This is associated with the rapid increase (decrease) in flood tidal prism and landward (seaward) residuals at Main Inlet (Armona Inlet), as discussed in items (12) and (15), and shows the rapid response of the entire system to specific cross-sectional area conditions.

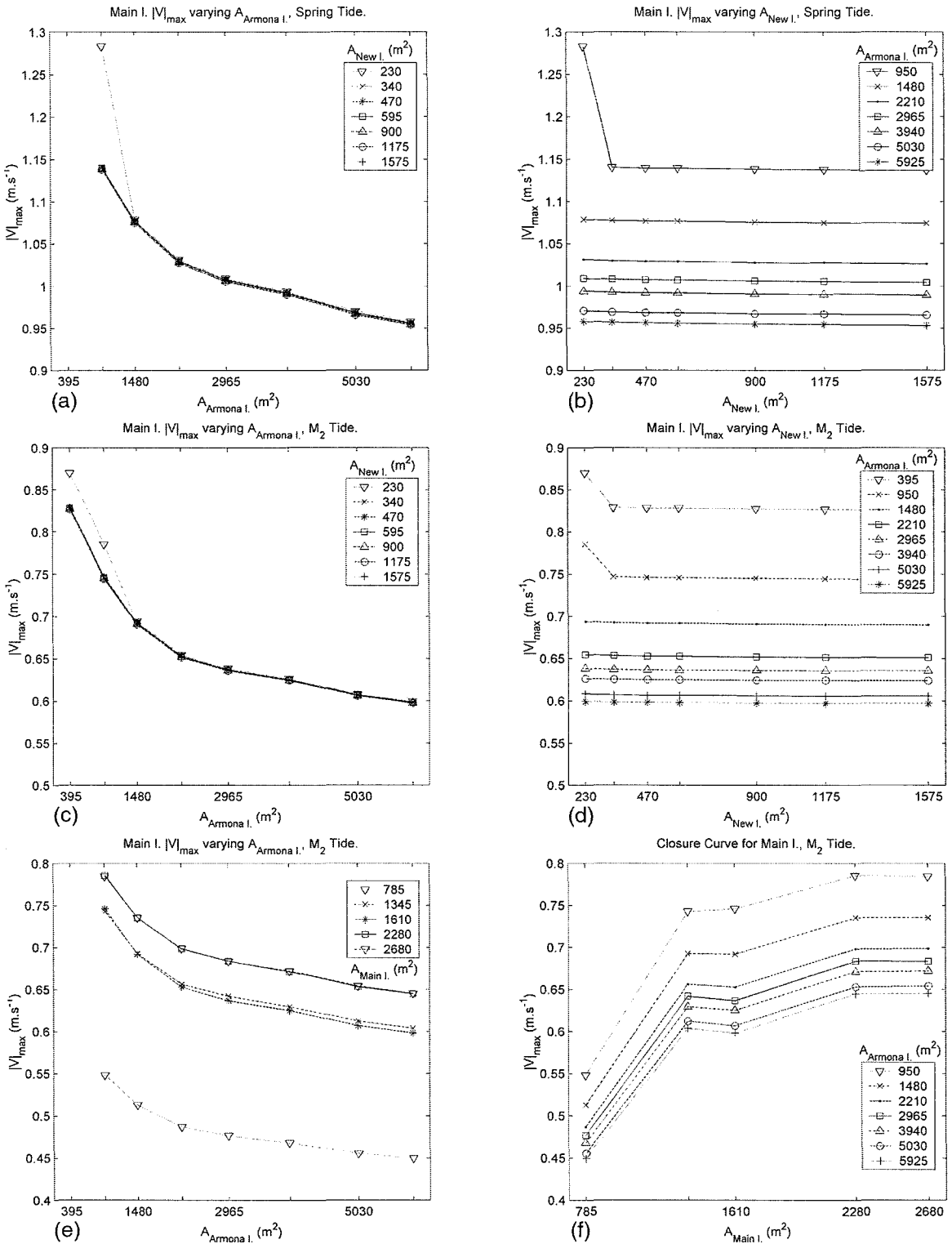

Figure 5-25. Maximum Velocities through Main Inlet. Spring tidal forcing, varying A_{Armona} and A_{New} (a and b); M_2 forcing varying A_{Armona} and A_{New} (c and d), and varying A_{Armona} and A_{Main} (e and f). For a, b, c, and d: $A_{Main\ I.}$=1,610 m^2. For e and f, $A_{New\ I.}$=595 m^2. All the plots are at the same scale.

For the rest of the simulations, as A_{Armona} increases, the maximum velocity through Main Inlet decreases. Panel (a) shows that, at present, the maximum velocity through Main Inlet is approximately 1.02 $m.s^{-1}$, which, compared to the 1 $m.s^{-1}$ suggested by many authors (e.g., Escoffier, 1940; Bruun, 1968; see section 2.1.2) to be the equilibrium velocity, would indicate that Main Inlet is in equilibrium, i.e., having a zero rate of deposition/erosion in the inlet. This agrees with the historical data analysis (section 3.3.3), where it was found that the maximum depth of the inlet seems to have stabilized, implying that the cross-sectional area has also stabilized since the width is fixed. Therefore, the stability suggests that the net landward residuals and sediment transport (shown to exist in Figure 5-15-c, -e, and -f) are primarily moving sand from offshore to the lagoon, without interfering (on average) in the inlet region.

38) The closure curve for Main Inlet (Figure 5-25-f) shows that, as A_{Main} increases (decreases), the maximum velocity is expected to increase (decrease), which corresponds to the monotonically increasing portion of the theoretical closure curve. When looking at this aspect of the flow in isolation, this implies that changes in Main Inlet would trigger further changes. Given that the historically data analysis (section 3.3.3) showed that the present geometry represents either an equilibrium cross-sectional area for the average hydrodynamic conditions, or a configuration in which the inlet has a tendency to grow, the closure curve results suggest that Main Inlet would grow if unjettied. This may have implications in the stability of the other inlets, as will be analyzed in section 5.4.4.

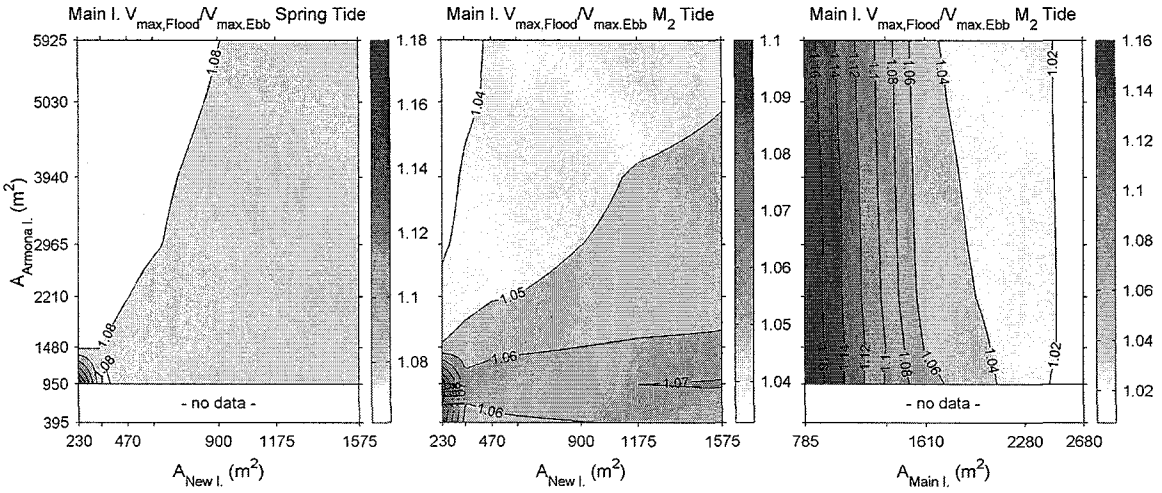

Figure 5-26. Flood / Ebb Main Inlet maximum velocity ratio. Spring forcing varying A_{Armona} and A_{New} (a); M_2 forcing varying A_{Armona} and A_{New} (b), and A_{Armona} and A_{Main} (c).

Armona Inlet

The maximum velocities through Armona Inlet, and their occurrence in the tidal cycle, are shown for all the simulations in Figure 5-27 and Figure 5-28, respectively. The most relevant observations that can be extracted from these figures are:

39) The maximum velocities through Armona Inlet occur consistently during ebb (Figure 5-28), supporting the previous observations indicating that that this inlet is ebb-dominant.

40) The maximum velocities through Armona Inlet are virtually independent of the changes in New Inlet cross-sectional area, exhibiting only 1-2% decrease as A_{New} increases (Figure 5-27-b and -d).

41) Figure 5-27-a, which is the closure curve (i.e., simulations with spring tide forcing) for Armona Inlet, shows a monotonically decreasing trend. This, in combination with the residual and transport results (item 41), suggests that the flow response tends, in all cases, to counteract disturbances in the cross-sectional area, and that the present-day maximum velocity can be considered to be the equilibrium velocity. However, this stabilizing flow response has to be taken in perspective when multiple inlets are present, since changes in other inlets may affect the response capacity of Armona Inlet. Indeed, Figure 5-27-e and -f show that the maximum velocity through Armona increases (decreases) as A_{Main} is reduced (enlarged), relative to its current size, indicating the profound effect disturbances in Main Inlet may have over Armona Inlet stability. For instance, for any given A_{Armona}, an enlargement of Main Inlet would decrease the maximum velocity through Armona Inlet, which then could change from being larger to being smaller than the required velocity for equilibrium.

42) In addition, this panel shows that the maximum velocity under present conditions (A_{Armona}=2,965 m^2) is approximately 1.05 $m.s^{-1}$, which is close to the "universal" equilibrium velocity. If the inlet is considered to be in equilibrium due to that, equilibrium would be associated in this case with a net seaward flow and transport, as shown in Figure 5-17 and discussed in item (16).

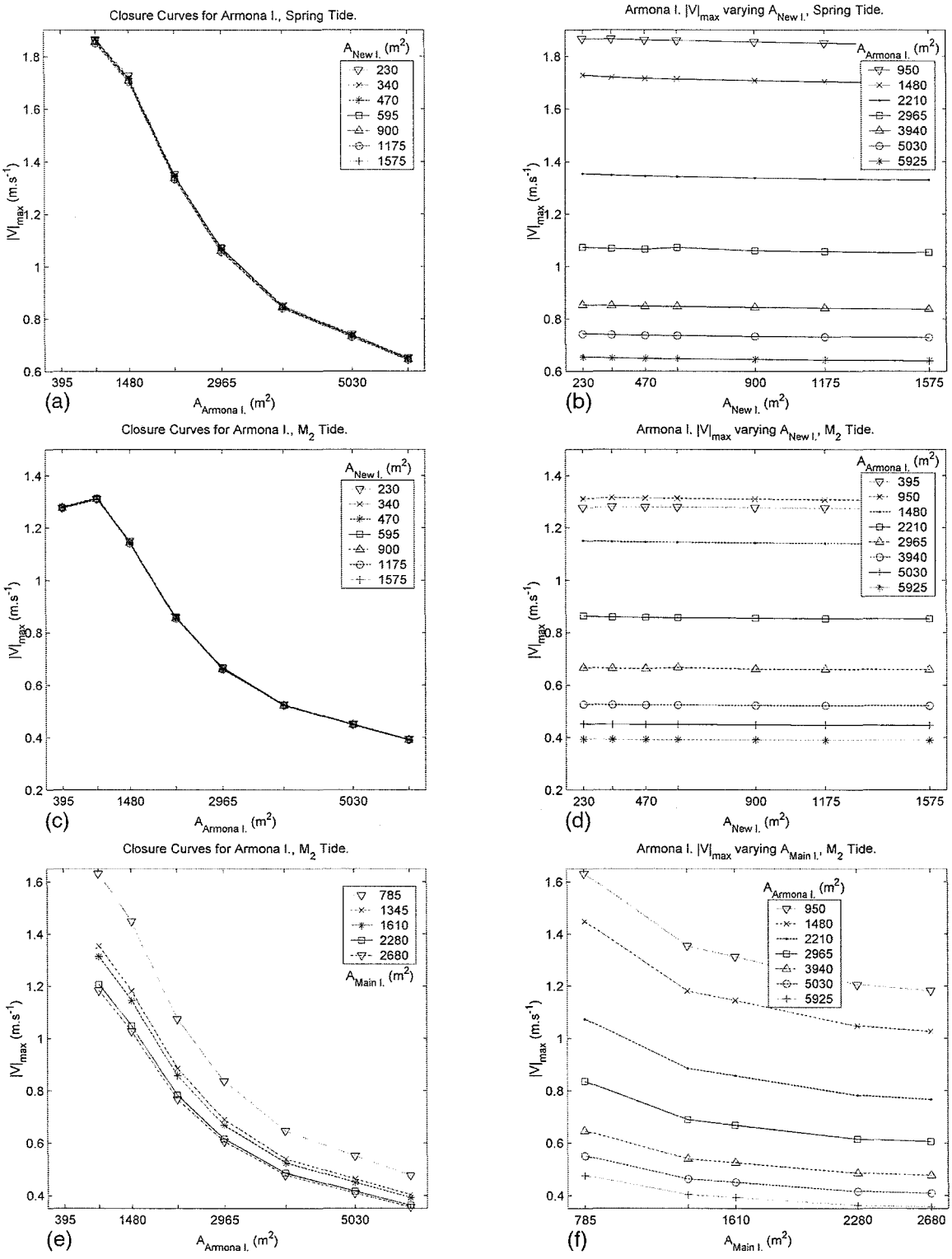

Figure 5-27. Maximum Velocities through Armona Inlet. Spring tidal forcing, varying A_{Armona} and A_{New} (a and b); M_2 forcing varying A_{Armona} and A_{New} (c and d), and varying A_{Armona} and A_{Main} (e and f). For a, b, c, and d: $A_{Main\ I.}$=1,610 m^2. For e and f, $A_{New\ I.}$=595 m^2. All the plots are at the same scale.

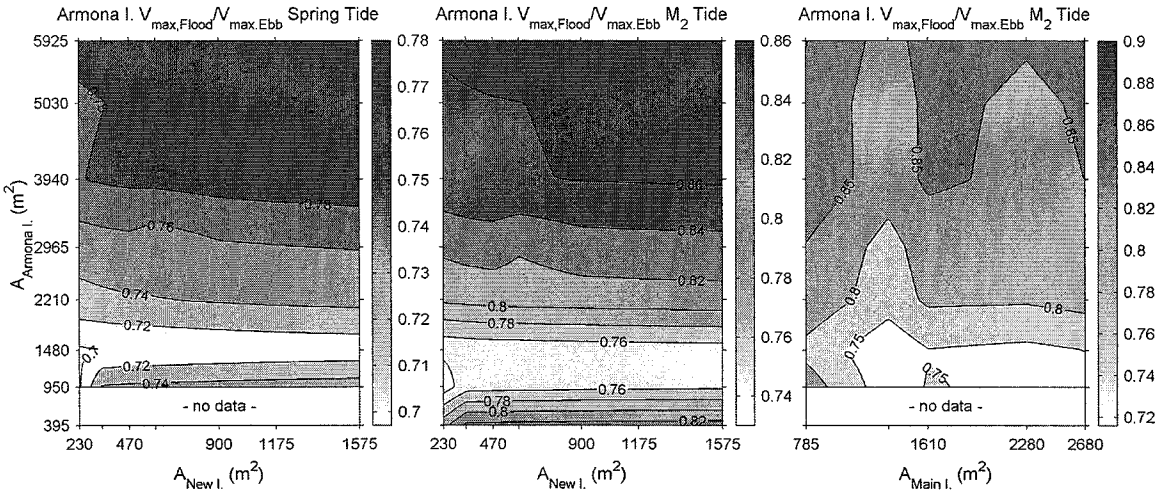

Figure 5-28. Flood / Ebb Armona Inlet maximum velocity ratio. Spring forcing varying A_{Armona} and A_{New} (a); M_2 forcing varying A_{Armona} and A_{New} (b), and A_{Armona} and A_{Main} (c).

43) Figure 5-27-c shows that the peak in the closure curve is reached for an area between 395 m^2 and 1,480 m^2. According to the closure curve model, this peak corresponds to the highest sediment transport rates within the inlet zone, which is in agreement with the sediment transport results shown in Figure 5-17, and discussed in item (16). Therefore, the maximum velocity appears in this case to be a reliable indicator of the tidally-averaged hydrodynamic conditions.

5.4.4. Summary and overall hydrodynamic response

The simulations performed, varying the cross-sectional area of the three inlets in a multiple inlet system, served to analyze the hydrodynamic response of the system, and in particular of the inlets, to such disturbances, and identify the potential effects on inlet stability.

General inlet hydrodynamic interdependence

First, the strong hydrodynamic interaction between inlets was evidenced. Given that the total mass in the system has to be conserved between tidal cycles, changes in flow volume through an inlet necessarily lead to changes in the flow volumes through the other inlets. It was found that the hydrodynamic characteristics and response to change at a given inlet (flow volumes, intensities, residuals and distortion) not only depend on disturbances at that inlet, but also on disturbances at the other inlets. For instance, situations can arise, in which the hydrodynamics

through a given undisturbed inlet can be strongly affected by disturbances on other inlets (e.g., distortion in Armona, item 29), resulting in the inability to counteract such disturbances, leading to potentially profound and irreversible changes in its stability condition (items 11 and 14), even if the flow volume through the disturbed inlet is an order of magnitude smaller than that of the affected inlet (item 12). Moreover, the degree of hydrodynamic interdependence can be strong, to an extent in which the response in a given inlet "A" to disturbances in another inlet "B" is comparable to the response to disturbances in "A" itself (item 8).

In addition, it was found that, although the variations in various hydrodynamic parameters follow in general well-defined trends, specific combinations of cross-sectional areas can lead to abrupt deviations from these trends (items 6, 7, 12, 14, 22) which in turn confer substantially different hydrodynamic behavior to the inlets. The identification of these particular responses through modeling can serve a predictive tool to i) assist in the determination of the optimal disturbances (in the case of desired or needed anthropogenic modifications of the inlets and the system in general), and ii) to identify the worst-case scenarios, and recommend actions to prevent them to happen.

Flow duration and flow dominance

Strong nonlinear distortion in water surface elevation and velocity fields can lead to different responses of the residual discharge, currents, and near-bed sediment transport capacity. The results of the simulations show that, as opposed to the behavior in single-inlet systems, the duration of flood or ebb is not a determinant factor for flow dominance. Longer flood (ebb) may be associated with flood (ebb) dominance, due to the existence of strong residual circulation between inlets (items 2, 6 10 and 18). In fact, larger flood (ebb) discharge in a shorter period does not necessarily lead to stronger flood (ebb) currents (item 7). Moreover, a distorted velocity field can produce residual velocities and net sediment transport in opposite directions (item 14). The direction of the net sediment transport (flood or ebb) is not only dependent on the direction of the average velocity, but also on the shape (distortion) of the velocity, and on the flood to ebb maximum velocity ratio.

It is suggested here that, at least for multiple inlets exhibiting strong hydrodynamic interaction and distortion, a distinction should be made between flow dominance (larger flow), and transport dominance. The former is important globally, as it determines the degree of inlet interaction and the overall system response capacity to inlet disturbances, and the latter is more useful

in a local sense, to estimate the seaward-flushing or landward-infilling ability of a particular inlet in a given scenario.

Tidal distortion

The model results show that, in terms of tidal distortion response at a given inlet, the effects of disturbances in adjacent inlets are small compared to the effects of disturbances in its cross-sectional area (item 26 and 30). Moreover, simulations keeping a given inlet unchanged suggest that its hydrodynamic response to disturbances in other inlets in terms of residual circulation and sediment transport capacity, are not necessarily coupled to changes in the tidal distortion (e.g., item 27). Therefore, the analysis of the relationship between tidal distortion and flow dominance has to rely on the hydrodynamic response at each inlet due to disturbance in their own cross-sectional areas.

The hydrodynamic response at a given inlet to disturbances in its own cross-sectional area indicates in all cases that:

- The water surface M_4/M_2 amplitude ratio, which is an direct measure of the degree of nonlinear tidal distortion, is proportional to the flow dominance: an increase in surface distortion is associated with an increase in either flood transport dominance (in flood dominant inlets) or ebb transport dominance (in ebb dominant inlets).
- The velocity M_4/M_2 amplitude ratio is inversely proportional to the flow dominance: an increase in velocity distortion is associated with a decrease in both flood dominance or ebb dominance (item 28).

No explanation has been given to why the water surface an tidal velocity distortions exhibit opposite responses to changes in inlet cross-sectional area.

The simulation results suggest that the velocity and water surface relative phase are not, in most cases, an evident and reliable diagnostic indicator of the flow dominance (items 26, 29, and 30). This apparent discrepancy, in terms of flow dominance, between what the relative phase suggests and what the analysis of residuals (flow and current) and transport indicate, is mainly due to the existence of strong net flows between inlets. In fact, the flow dominance arguments, which are derived from the water surface and velocity examination in terms of the magnitude and phases of the primary and forced harmonic tidal constituents, are based on the assumption of negligible freshwater inflow in single-inlet systems (Aubrey, 1986), limiting the generality of the

results. Although single-inlet systems can exhibit consistently stronger flows during some periods of the tidal cycle, i.e., be ebb or flood dominant due to nonlinear tidal distortion, the net flow through the inlet is zero on average. However, the existence of multiple inlets servicing a single embayment confers an additional characteristic to the global hydrodynamics, which is the potential existence of residual discharges and currents through the inlets. These added processes, together with the magnitude and direction of the maximum velocity, are in fact the processes and characteristics that ultimately determine the flow dominance and the sediment flushing capacity in a given inlet, and can outweigh the effects of tidal distortion.

Maximum velocities, closure curves and equilibrium

Model results revealed that the occurrence (flood or ebb) of the maximum velocity is an important parameter in the analysis of inlet stability. Large flood maximum velocities are in general associated with landward net sediment transport and indicate a tendency to lagoon infilling, whereas maximum velocities occurring during ebb suggest a tendency to increased efficiency in flushing sediment seaward. Moreover, a stable condition may in fact exhibit smaller maximum absolute velocities than an unstable condition, provided that these high velocities occur during ebb. This characteristic of the flow is often disregarded in closure curve stability arguments.

In addition, the model results show different responses and stability conditions for each inlet. In some cases, the equilibrium velocity can be determined from the analysis of various hydrodynamic processes and characteristics of the flow (items 32 ad 41). For instance, model results and historical analysis suggest that the present-day New and Armona inlet cross-sectional areas are stable, and that the hydrodynamics would respond against disturbances in its cross-sectional area to reestablish the original configuration. This suggests that the actual maximum velocity can be considered to be the equilibrium velocity (1.35 $m.s^{-1}$ for New Inlet and 1.05 $m.s^{-1}$ for Armona Inlet), eliminating the need to rely on the value of 1 $m.s^{-1}$, which has been shown not to be universal (see section 2.1.2). This significant difference between the equilibrium velocities is in part attributed to the fact that the sediment grain size at New Inlet is larger than at Armona, due to the latter being closer to the Guadiana River, which provides large amounts of finer material (Freire de A., 1990). The results also show that these inlets are consistently ebb dominant, which is often regarded as a contributing factor for stability, and that instability may only be caused by events and processes not analyzed in this study, such as abrupt changes in sediment supply and wave climate.

In other cases, the model results indicate that the equilibrium velocity is associated with a net landward transport (item 37). Although flood transport dominance is often associated with potential inlet instability, these results show that the apparent "lagoon infilling" process and the inlet stability operate at different time scales, in particular when the landward transport does not affect the inlet immediate vicinity.

Finally, the simulations varying the inlet cross-sectional areas show that the equilibrium state in a given inlet, as well as its response capacity to disturbances on the inlet itself, have to be taken in perspective when multiple inlets are present, since changes in other inlets may modify the overall stability conditions and requirements. For instance, the maximum velocity through an inlet is likely to decrease as the cross-sectional area of other inlets increase, in which case it could change from being larger to being smaller than the required velocity for equilibrium.

Overall Stability using the closure curve approach

The overall stability of the system can be analyzed in terms of the maximum velocity response to inlet disturbances.

On one hand, disturbances in inlet cross-sectional areas produce changes in the maximum velocity through the inlets, which can be written as

$$\boldsymbol{\delta V} = \boldsymbol{T}\,\boldsymbol{\delta A}, \text{ or } \quad \begin{bmatrix} \delta V_{11} & \delta V_{12} & \delta V_{13} \\ \delta V_{21} & \delta V_{22} & \delta V_{23} \\ \delta V_{31} & \delta V_{32} & \delta V_{33} \end{bmatrix} = \boldsymbol{T} \begin{bmatrix} \delta A_1 \\ \delta A_2 \\ \delta A_3 \end{bmatrix} \tag{5.14}$$

where δA_i are the changes in cross-sectional area at each inlet, δV_{ij} are the resulting changes of maximum velocity, $\boldsymbol{T}$ is a matrix of coefficients, which correspond to the slope of the A-V_{max} curves (Figures 5-22, 5-25, and 5-27), and the sub-indexes 1, 2 and 3 correspond to New, Main, and Armona inlets, respectively.

On the other hand, although the maximum velocity through the inlet is a complicated function of the cross-sectional area, as shown by the closure curve, the closure curve concept can locally be expressed in terms of the cross-sectional area rate of change, in which case the change in maximum velocity after a disturbance is proportional to the rate of change of the cross-sectional area, i.e.,

$$\delta V = \beta \frac{d}{dt} \delta A \tag{5.15}$$

where δA and δV are the matrices from equation (5.14), and β a constant. Combining equations (5.14) and (5.15), the equation for the change in area becomes

$$\frac{d}{dt}\delta A = \frac{1}{\beta} T \delta A \tag{5.16}$$

The solution of the previous equation is of the form

$$\delta A = \xi e^{\alpha t} \tag{5.17}$$

where the eigenvalues α and the constant vector ξ are to be determined. Substituting for δA equation (5.17) in equation (5.16), we obtain the system of algebraic equations

$$\left(\frac{1}{\beta} T - \alpha I\right)\xi = 0 \tag{5.18}$$

Nontrivial solutions of equation (5.18) exist if and only if

$$\det\left(\frac{1}{\beta} T - \alpha I\right) = 0 \tag{5.19}$$

For the present Ría Formosa configuration (i.e., A_{New} = 595 m^2, A_{Main} = 1,610 m^2, and A_{Armona} = 2,965 m^2), the matrix T is

$$T = \begin{bmatrix} -0.9901 & -0.0015 & -0.0054 \\ -0.0146 & 0.0767 & -0.1067 \\ -0.0010 & -0.0134 & -0.1910 \end{bmatrix} \cdot 10^{-3} \tag{5.20}$$

whose coefficients are the slopes of the A-V_{max} curves.

The corresponding eigenvalues are -0.9901, 0.0819, and -0.1962, and the general solution of (5.16) is

$$\begin{bmatrix} \delta A_1 \\ \delta A_2 \\ \delta A_3 \end{bmatrix} = c_1 \begin{bmatrix} 0.9999 \\ 0.138 \\ 0.0014 \end{bmatrix} \exp^{-0.9901 \cdot 10^{-3} t} + c_2 \begin{bmatrix} 0.0011 \\ -0.9988 \\ 0.0490 \end{bmatrix} \exp^{0.0819 \cdot 10^{-3} t} + c_3 \begin{bmatrix} -0.0070 \\ 0.3639 \\ 0.9314 \end{bmatrix} \exp^{-0.1962 \cdot 10^{-3} t} \tag{5.21}$$

where c_1, c_2 , and c_3 are arbitrary constants.

The first and third terms in solution (5.21) have negative exponents, which indicates that the changes in cross-sectional areas will decay with time. However, the exponent in the second

term is positive, suggesting that the changes in the cross-sectional areas will increase with time. More specifically, this second term shows that Main Inlet will grow (decrease) fast, while New and Armona inlets decrease (grow) slowly, depending on the sign of c_2.

A sensitivity analysis with different combinations of cross-sectional areas indicates that this inlet behavior, in which Main Inlet would grow (decrease) rapidly with time while New and Armona inlets would decrease (grow) slowly, occurs consistently as long as $T(2,2)$ is greater or equal to zero. In other words, as long as the slope of the Main Inlet closure curve is greater or equal to zero (i.e., its area lies in the portion of the closure curve where V_{max} increases with A_{Main}), the system is apparently unstable, if all the inlets were free to evolve. However, if Main Inlet cross-sectional increases such that the slope of its closure curve becomes negative, $\alpha_i < 0$ (i = 1, 2, 3), and the system would become stable.

According to the maximum velocity curves and the historical data analysis, this new stable configuration would be possible if Main Inlet were free to evolve. In fact:

- examination of Figure 5-25-f suggests that the peak of the Main Inlet closure curve lies between A_{Main}= 2,280 m^2 and 2,680 m^2, and therefore a negative slope exists for A_{Main}< 2,680 m^2, and
- the historical data analysis showed that Main Inlet experienced a phase of rapid growth until its cross-sectional area stopped increasing. Since the inlet has maintained approximately a constant cross-sectional area for more than 20 years, it is reasonable to believe that Main Inlet has either reached a stable configuration, or its growth (until a new equilibrium size) is limited by the jetties and possibly by the unavailability of erodible material on the bottom of the channel in the inlet gorge (see section 3.3.3).

This approach to analyze the overall system stability does not take directly into account the so-called equilibrium maximum velocity. However, it was shown above that equation (5.21) suggests that a persistent inlet configuration would be reached after a large increase of Main Inlet cross-sectional area and a small decrease of both New and Armona inlets cross-sectional areas. At Armona Inlet, for instance, its maximum velocity would decrease after the growth of Main Inlet (large growth but small $|dV_{Armona}/dA_{Main}|$, Figure 5-27-f), which would be balanced by an increase

in velocity due the decrease of Armona Inlet itself (small decrease but large $|dV_{Armona}/dA_{Armona}|$, Figure 5-27-e).

Therefore, this analysis suggests that the present-day inlet configuration is artificially stable, and that a likely natural overall stability would be reached after the growth of Main Inlet and a corresponding slight decrease of Armona and New inlets. The closure curve condition for overall stability is

$$\frac{dV_i}{dA_i} < 0, \text{ for } i = 1,2,3 \tag{5.22}$$

5.4.5. Specific implications to Ría Formosa

Several observations specific for the Ría Formosa system can be made from the analysis of the simulation results:

- At present conditions, Main Inlet is the inlet that carries more flow. In fact, 60% of the total tidal prism of the western sub-embayment of the lagoon enters through Main Inlet, whereas Armona and New Inlet contribute with 31% and 9%, respectively.
- Numerical simulations of the hydrodynamics of the system with various inlet configurations allows the identification of the best combination of cross-sectional areas for the overall stability of the system. These optimal combinations may not be practical since Main Inlet is artificially stabilized, but in some instances they can serve as recommendations for future engineering projects in the existing inlets. Moreover, these types of simulations can be extended to study the effects of closure, opening, or migration of inlets, as well as changes in the lagoon size and geometry, in the overall stability of the system, which, in the case of Ría Formosa, could be applied to New Inlet or the Inlets in the eastern sector of the system.
- The hydrodynamic response at New Inlet, in terms of the flow volume, to both an increase and a decrease in New Inlet cross-sectional area is the same, namely an increase in the seaward residual discharge (item 1). On one hand, the tendency to flush more effectively sediment seaward is enhanced as the New Inlet cross-sectional area decreases from its present value, which can be regarded as a response against closure. On the other hand, as A_{New} increases, the residual discharge increases seaward, but the residual current and maximum velocity (which are also directed seaward) decrease, meaning that the ebb transport dominance

decreases. Therefore, from a tidal hydrodynamic point of view, New Inlet seems to be at present in a stable condition.

- Main inlet acts as a net importer of water to the system. Its flood tidal prism is consistently larger than that of ebb. In addition, that inlet is always flood dominant, in spite of the flood duration being consistently longer than ebb duration.

- The hydrodynamics in Main Inlet can vary significantly as the Armona cross-sectional area is disturbed, even when keeping A_{Main} constant (item 9). This scenario is possible if, for instance, a strong storm results in the reduction of the Armona and New inlets cross-sectional areas, that would in turn result in a significant increase in flood dominance (in flow and transport) at Main Inlet (item 12). If only A_{Armona} is reduced, the flood dominance at Main Inlet appears to decrease and even be reversed to ebb transport dominance (item 11). However, these disturbances in the Armona cross-sectional area have also the effect of creating a hydrodynamic response at Armona itself that will tend to restore its original cross-sectional area, and therefore the effects on Main Inlet may decrease gradually. The hydrodynamic analysis alone is not capable to determine the time scales of the responses and their ultimate morphologic effects, and therefore no conclusions can be drawn as to whether the disturbances in Armona would have permanent unstabilizing effects or if the overall stability of the system would be recovered.

- Changes in Armona Inlet flood and ebb flow volumes and durations are practically independent of the variations in New Inlet cross-sectional area (for a given A_{Armona}, the tidal prism varies less than 0.5% as A_{New} changes), except when $A_{New} = 230$ m^2, in which case the Armona flood volume and duration decreases significantly faster as A_{Armona} decreases. This rapid decrease in the flood tidal prism, and in general an increase in the seaward net flow and sediment transport, is associated with a corresponding increase in the net landward flow at Main Inlet, as mentioned in (12). This is a clear example of the importance of the existence of New Inlet in the overall hydrodynamics in the system. This suggests that, prior to the opening of that inlet in 1998, the flow through both Main and Armona inlets had significantly different characteristics.

- On one hand, Armona is a net exporter of water and sediment, in all cases. This trend decreases as its area increases. On the other hand, a reduction in its cross-sectional area would result in an increase in ebb flow and transport dominance. This two responses suggest that

Armona is at present in a state of equilibrium (item 20), which is in agreement with the historical data analysis, and that instability may only be caused by events and processes not analyzed in this study (for instance, changes in sediment supply and wave climate during storms).

- The closure curve of New Inlet shows that the maximum velocity under present conditions is approximately 1.35 $m.s^{-1}$, which in principle indicates that the inlet is in a phase of growth, if compared to the widely used equilibrium velocity of 1 $m.s^{-1}$. According to Vila *et al.*(1999), the width of New Inlet has reached a state of relative stability (230 m referred to MSL). Therefore, the large maximum velocity may be responsible for either increasing the cross-sectional area by increasing the depth of the inlet, or triggering other processes known to occur in natural inlets, such as enlargement of the ebb tidal delta or, in particular in New Inlet, inlet migration. In fact, given that various elements indicate that the present-day New Inlet cross-sectional area is stable, and that the hydrodynamics would respond against disturbances in its cross-sectional area, the "surplus" in maximum velocity may well trigger other morphologic processes.

- At present, the maximum velocity through Main Inlet is approximately 1.02 $m.s^{-1}$ (Figure 5-25-a), which, compared to the 1 $m.s^{-1}$ suggested by many authors (e.g., Escoffier, 1940; Bruun, 1968; see section 2.1.2) to be the equilibrium velocity, would indicate that Main Inlet is in equilibrium, i.e., having a zero rate of deposition/erosion in the inlet. However, it was found that Main Inlet is a net importer of sediment, as evidenced by the net landward residuals and sediment transport observed in the simulation results, which are primarily moving sand from offshore to inner areas in the lagoon the frequent dredging that takes places in the lagoon side of the inlet. Moreover, the historical data analysis (section 3.3.3) showed that the inlet has had a tendency of growth, and that the cross-sectional area has reached a maximum, limited not only by the existence of the jetties, but also by the unavailability of erodible material in the bottom due to the existence of a hard stratum. Therefore, the maximum velocity close to 1 $m.s^{-1}$ does not correspond in this case to an equilibrium state, and this apparent Main Inlet stable configuration (V_{max} = 1.02 $m.s^{-1}$) is artificial, caused mainly by the underlying geology and the existence of the jetties. If unjettied, Main Inlet would grow until reaching roughly 2,500 m^2, and this would be accompanied by a small reduction in Armona and New inlets.

- The closure curve for Main Inlet shows that, as A_{Main} increase (decreases), the maximum velocity is expected to increase (decrease), which corresponds to the monotonically increasing portion of the theoretical closure curve. When looking at this aspect of the flow in isolation, this implies that changes in Main Inlet would trigger further changes, which could in the short term either generate the need for dredging or increased damage of the jetties foundations.

5.5. References

Aubrey, D. G., 1986. Hydrodynamic Controls on Sediment Transport in Well-Mixed Bays and Estuaries, in: J. van de Kreeke, Ed.: *Physics of Shallow Estuaries and Bays*. Coastal and Estuarine Studies, **16**. Springer-Verlag, New York, NY, pp 245-258.

Aubrey, D. G. and Speer, P. E., 1985. A Study of Non-Linear Tidal Propagation in Shallow Inlet/Estuarine Systems. Part I: Observations. *Estuarine, Coastal and Shelf Science,* **21**: pp 185-205.

Bettencourt, P., 1994. *Les Environements Sédimentaires De La Côte Sotavento (Algarve, Sud Portugal) Et Leur Évolution Holocène Et Actuelle.* PhD thesis, Université de Bordeaux I.

Bruun, P., 1968. Tidal Inlets and Littoral Drift. Oslo University Book Company.

Bruun, P., 1978. Stability of Tidal Inlets, Theory and Engineering. Development in Geotechnical Engineering, **23**. Elsevier.

Chow, V. T., 1959. Open-Channel Hydraulics. McGraw-Hill. New York, NY

Donnell, B. P., Finnie, J. I., Letter, J. V., McAnally, W. H., Roig, L. C. and Thomas, W. A., 1997. *User's Guide to Rma2 Wes Version 4.3*. US Army Corps of Engineers - Waterways Experiment Station Hydraulics Laboratory.

Esaguy, A. S., 1984. *Ría De Faro, "Barra De Armona", Evolução 1873-1983*. Direcção Geral de Portos, Divisão de Costas Marítimas e Estuários.

Escoffier, F. F., 1940. The Stability of Tidal Inlets. *Shore and Beach,* **8**: pp 114-115.

Escoffier, F. F., 1977. *Hydraulics and Stability of Tidal Inlets*. General Investigation of Tidal Inlets (GITI) Report, 13. USACE.

Fonseca, M. S., Fisher, J. S., Zieman, J. C. and Thayer, G. W., 1982. Influence of the Seagrass, *Zostera Marina* L., on Current Flow. *Estuarine, Coastal and Shelf Science,* **15**: pp 351-364.

Freire de A., C., 1990. *O Ambiente De Barreira Da Ría Formosa, Algarve - Portugal.* Ph. D. thesis, University of Lisbon.

Friedrichs, C. T. and Aubrey, D. G., 1988. Nonlinear Tidal Distortion in Shallow Well-Mixed Estuaries: A Synthesis. *Estuarine, Coastal and Shelf Science,* **27**: pp 521-545.

Gambi, M. C., Nowell, A. R. M. and Jumars, P. A., 1990. Flume Observations on Flow Dynamics in *Zoostera Marina* (Eelgrass) Beds. *Marine Ecology Progress Series,* **61**: pp 159-169.

Henderson, F. M., 1966. Open Channel Flow. MacMillan. NY

Jackson, G. and Winant, C., 1983. Effect of a Kelp Forest on Coastal Currents. *Continental Shelf Research,* **2**: pp 75-80.

Kowalik, Z. and Murty, T. S., 1993. Numerical Modeling of Ocean Dynamics. Advanced Series on Ocean Engineering, **5**. World Scientific.

Leonard, L. and Luther, M., 1995. Flow Hydrodynamics in Tidal Marsh Canopies. *Limnology and Oceanography,* **40**: pp 1,474-1,484.

Nepf, H., Sullivan, J. A. and Zavistosky, R. A., 1997. A Model for Diffusion within Emergent Vegetation. *Limnology and Oceanography,* **42**: pp 1,735-1,745.

Norton, W. R., King, I. P. and Orlob, G. T., 1973. *A Finite Element Model for Lower Granite Reservoir*. Report prepared by Water Resources Engineers, Walnut Creeke, California, for U.S. Army Corps of Engineers, Walla Walla,Washington,

Okubo, A., 1971. Ocean Diffusion Diagrams. *Deep-Sea Research,* **18**: pp 789-802.

Ree, W. O. and Crow, F. R., 1977. *Friction Factors for Vegetated Waterways of Small Slope.* Model of Tidal Numerical Propagation, Report No. ARS-1-151.F. U.S. Department of Agriculture.

Speer, P. E. and Aubrey, D. G., 1985. A Study of Non-Linear Tidal Propagation in Shallow Inlet/Estuarine Systems. Part 2: Theory. *Estuarine, Coastal and Shelf Science,* **21**: pp 207-224.

Tee, K. T., 1976. Tide-Induced Residual Current, a 2-D Nonlinear Numerical Tidal Model. *Journal of Marine Research,* **34**: pp 603-628.

Vila, A., Dias, J. M. A., Ferreira, Ó. and Matias, A., 1999. Natural Evolution of an Artificial Inlet. Proc. of the Coastal Sediments 1999, Long Island, NY., pp 1478-1488.

Ward, L., Kemp, W. and Boynton, W., 1984. The Influence of Wave and Seagrass Communities on Suspended Particles in an Estuarine Embayment. *Marine Geology,* **59**: pp 85-103.

Worcester, S. E., 1995. Effects of Eelgrass Beds on Advection and Turbulent Mixing in Low Current and Low Shoot Density Environments. *Marine Ecology Progress Series,* **126**: pp 223-232.

5.6. Appendix

5.6.1. Friction Coefficient Calibration Results

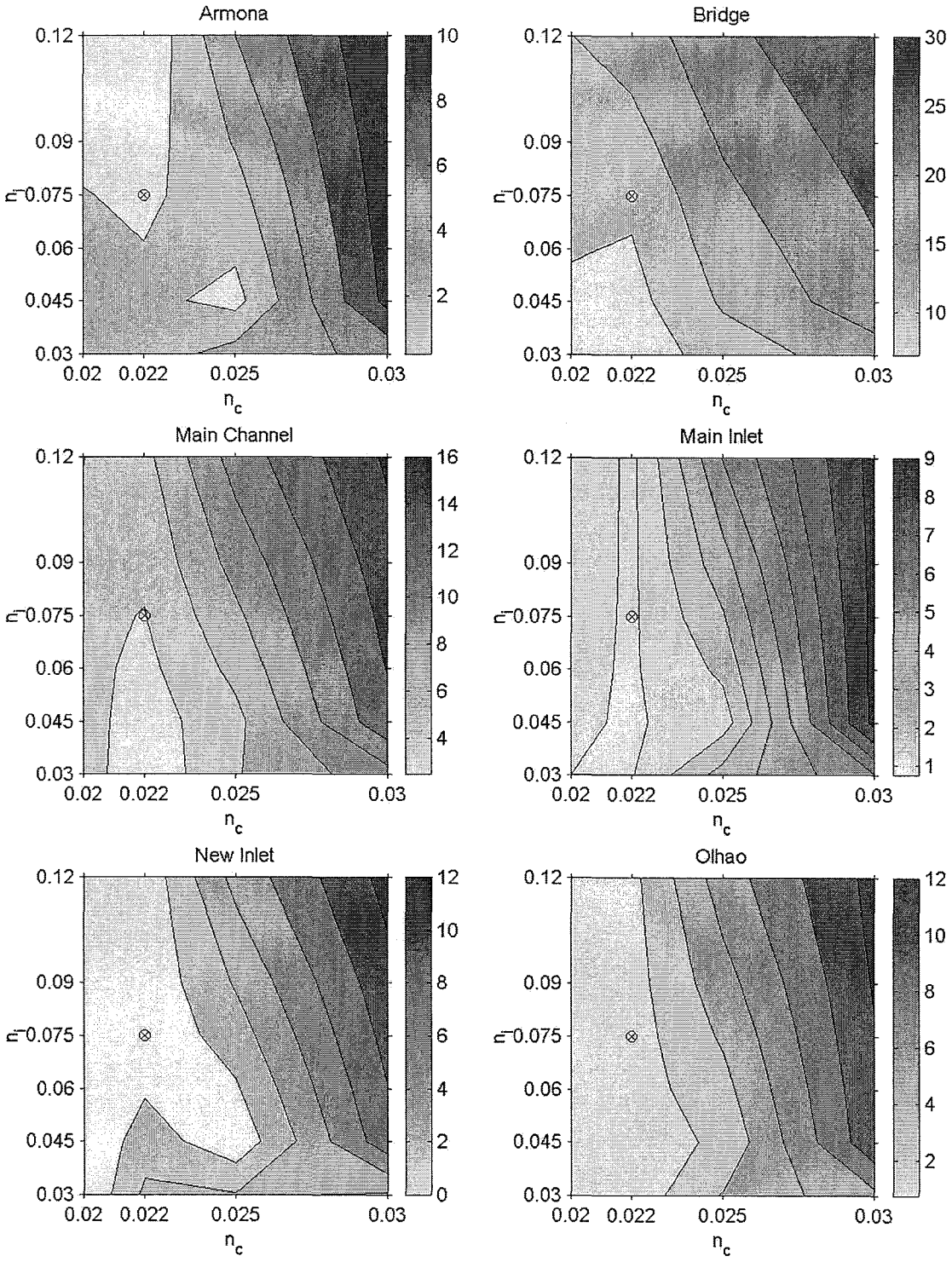

Figure 5-29. Friction Coefficient Calibration: M_2 amplitude absolute difference (cm) between model results and measurements (the circled cross corresponds to the friction coefficients chosen for the simulations).

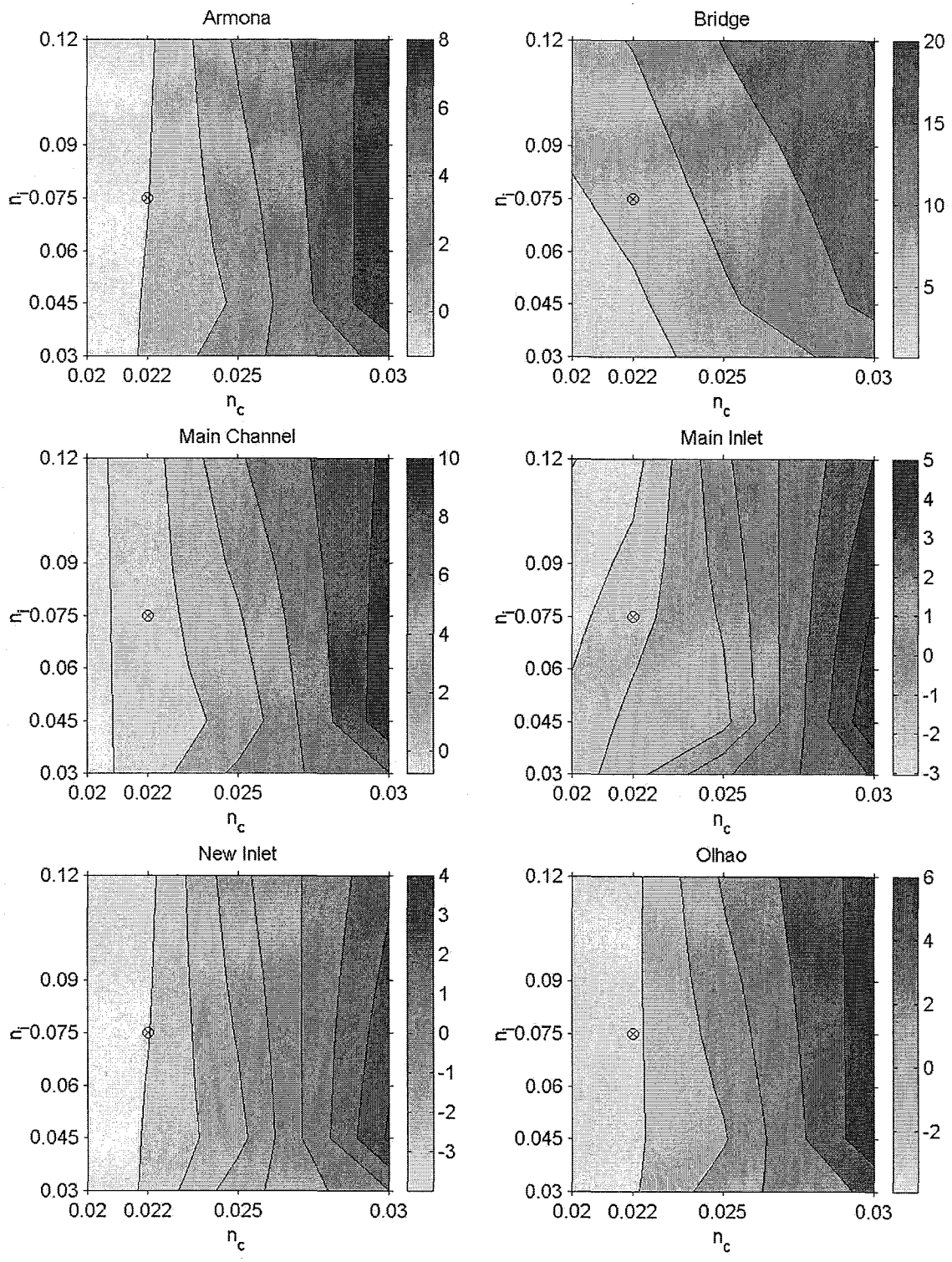

Figure 5-30. Friction Coefficient Calibration: M_2 phase difference (degrees) between model results and measurements (the circled cross corresponds to the friction coefficients chosen for the simulations).

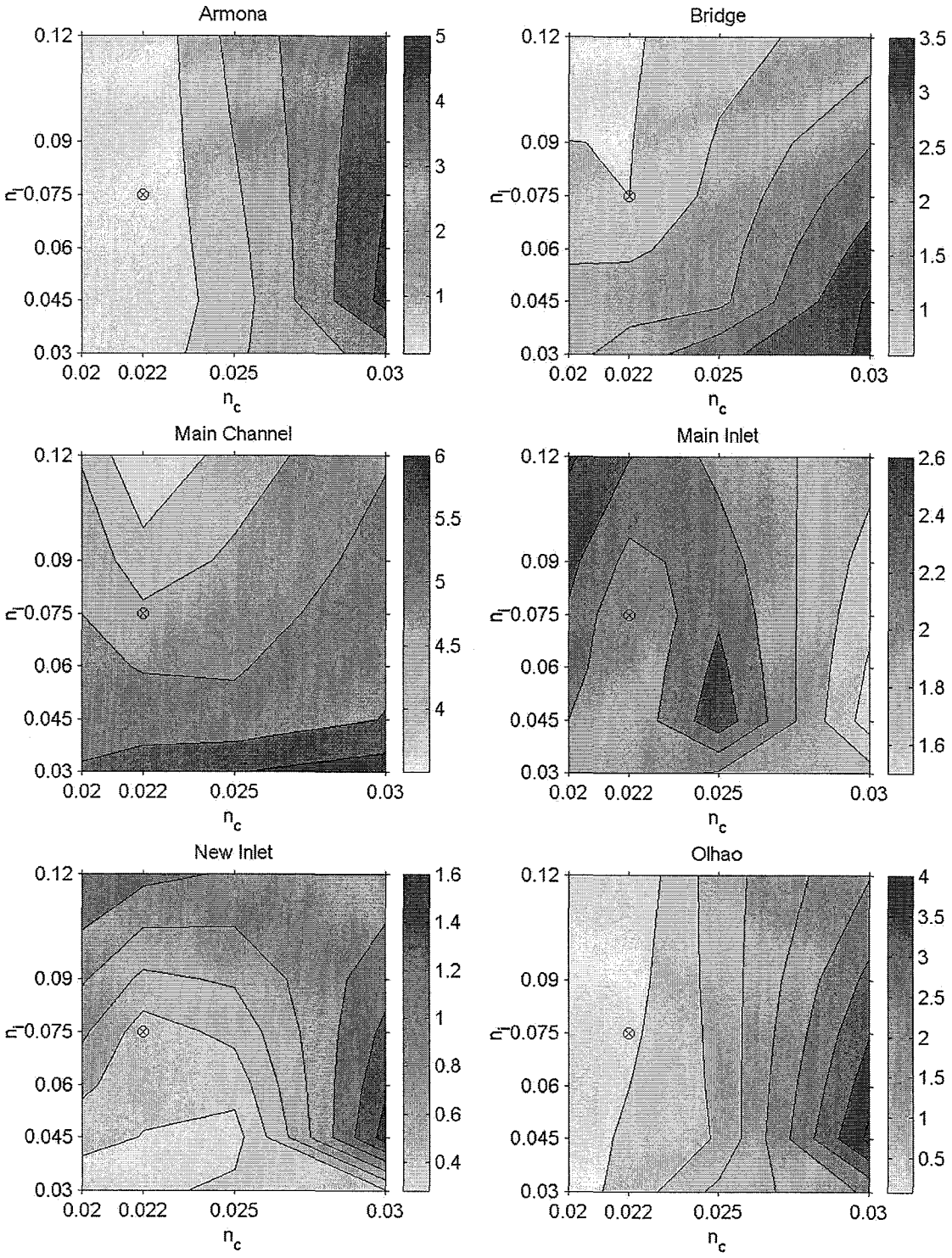

Figure 5-31. Friction Coefficient Calibration: M_4 amplitude absolute difference (cm) between model results and measurements (the circled cross corresponds to the friction coefficients chosen for the simulations).

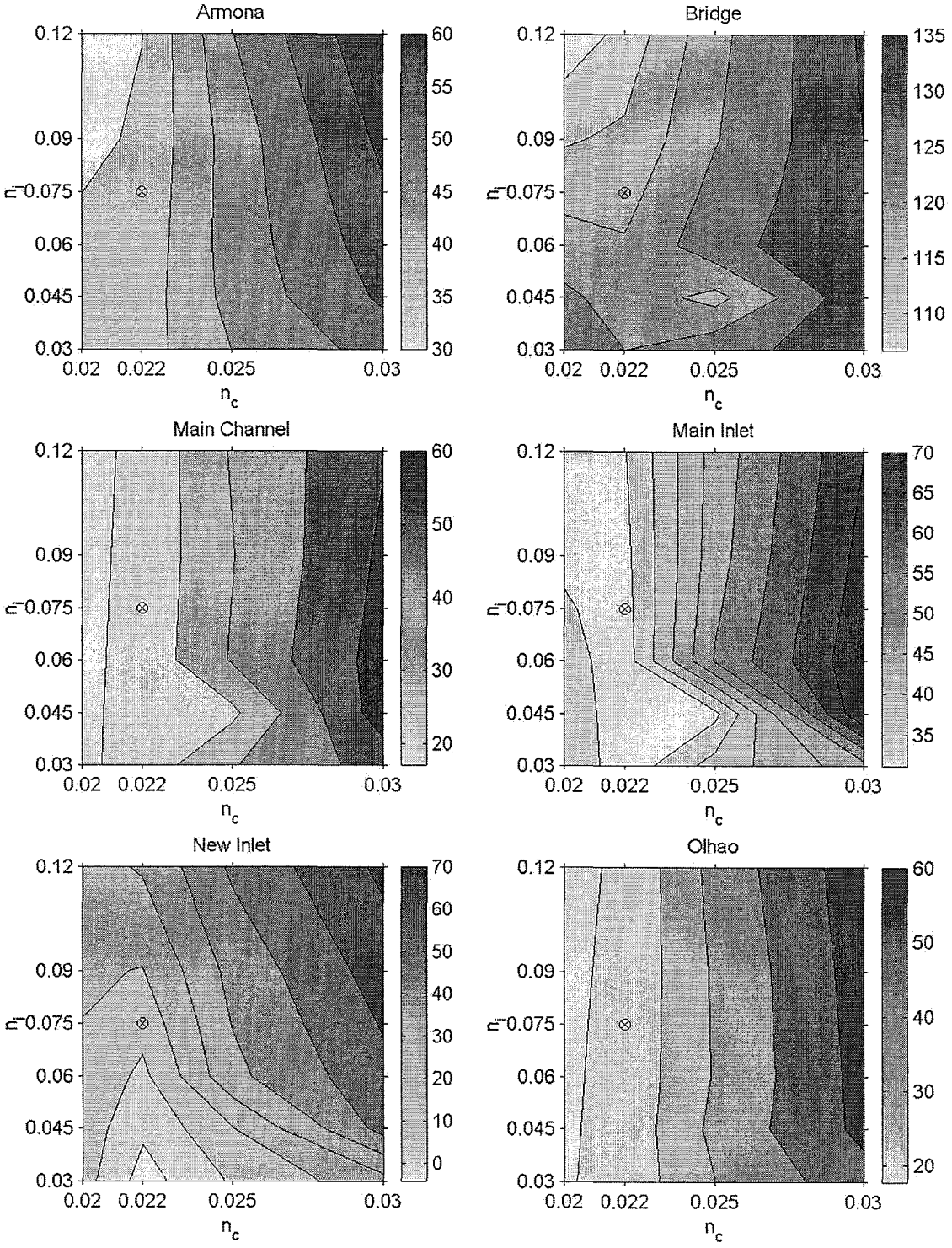

Figure 5-32. Friction Coefficient Calibration: M_4 phase difference (degrees) between model results and measurements (the circled cross corresponds to the friction coefficients chosen for the simulations).

5.6.2. Eddy Viscosity Calibration Results

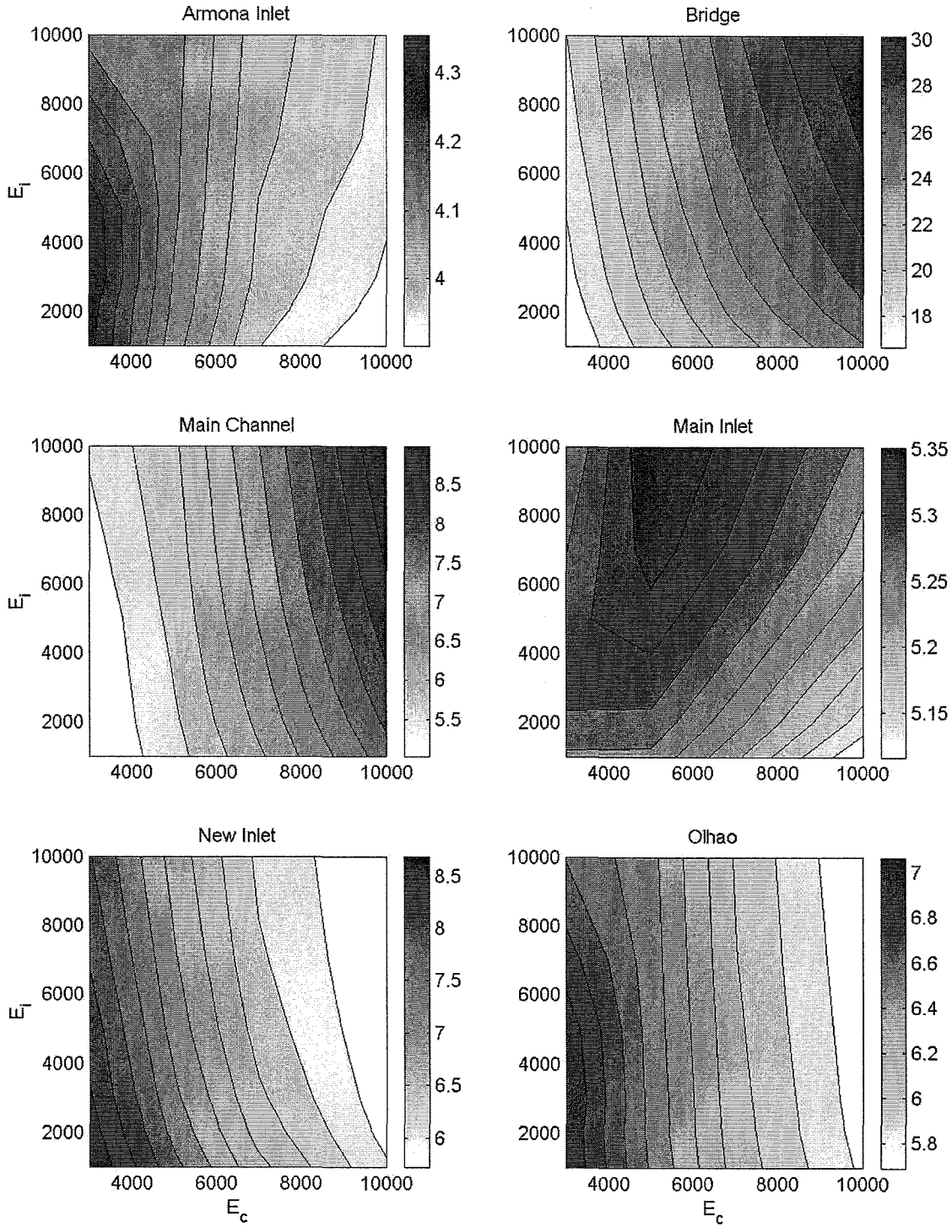

Figure 5-33. Eddy Viscosity Calibration: Water Surface Elevation RMS error (cm) between model results and measurements.

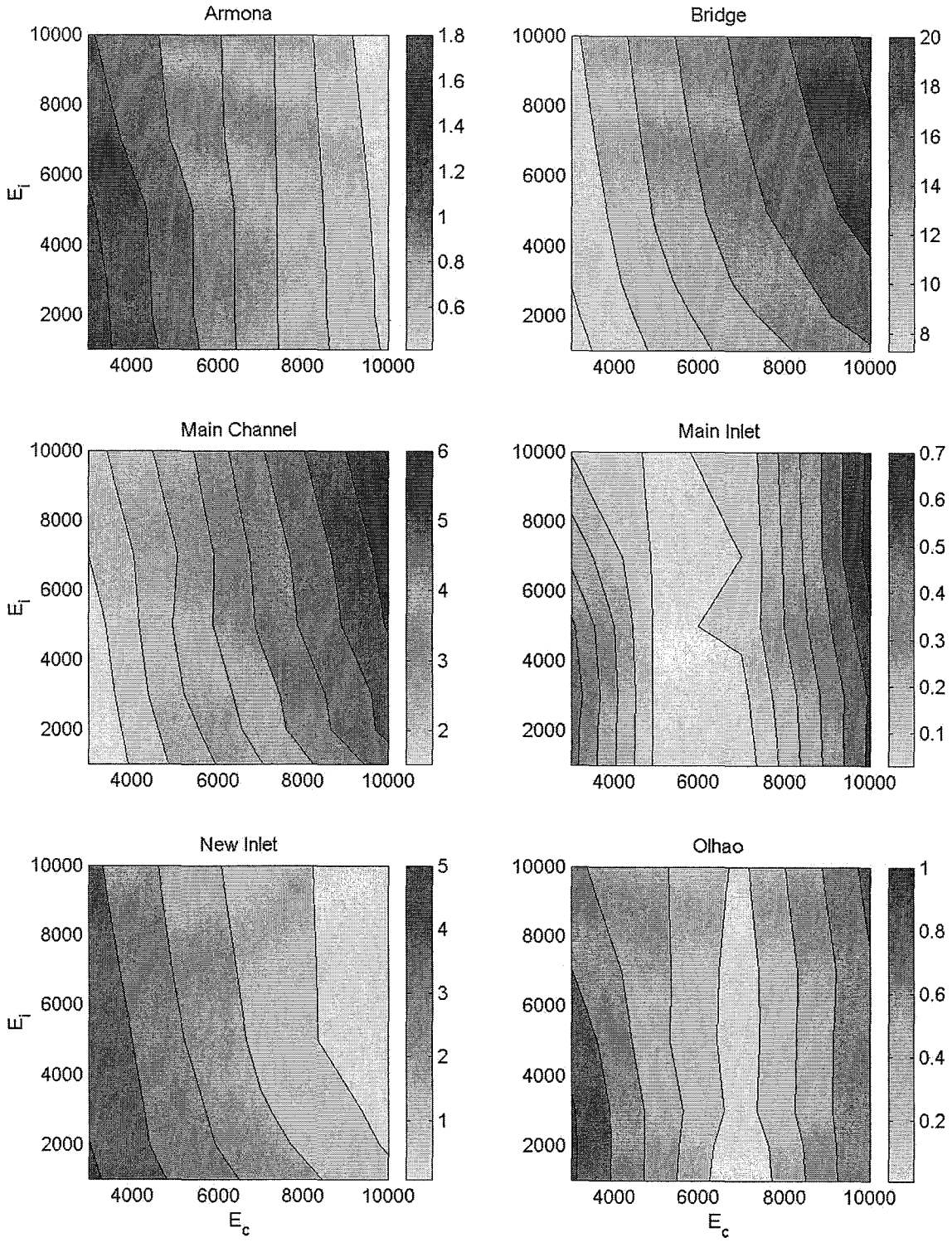

Figure 5-34. Eddy Viscosity Calibration: M_2 amplitude absolute difference (cm) between model results and measurements.

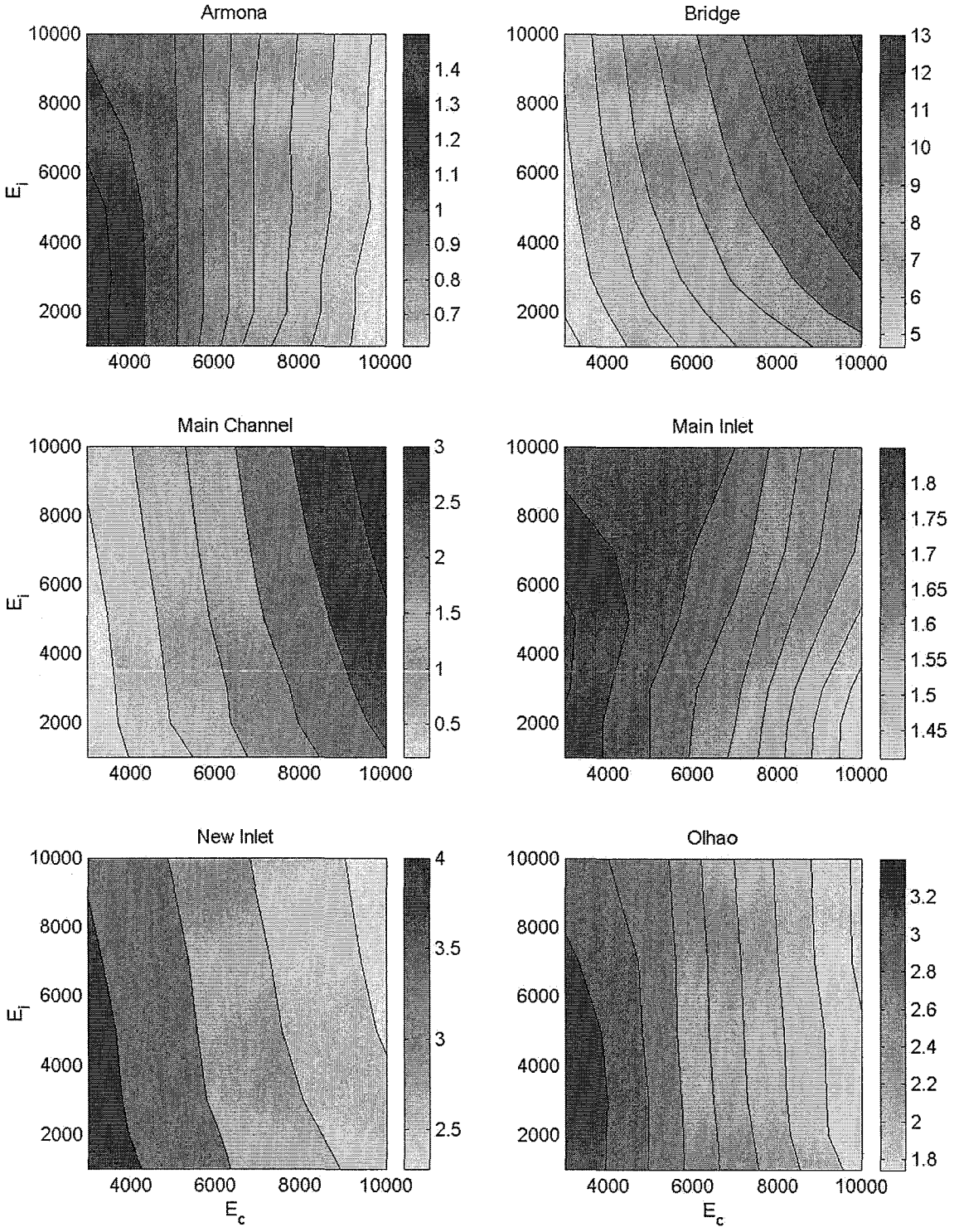

Figure 5-35. Eddy Viscosity Calibration: M_2 phase difference (degrees) between model results and measurements.

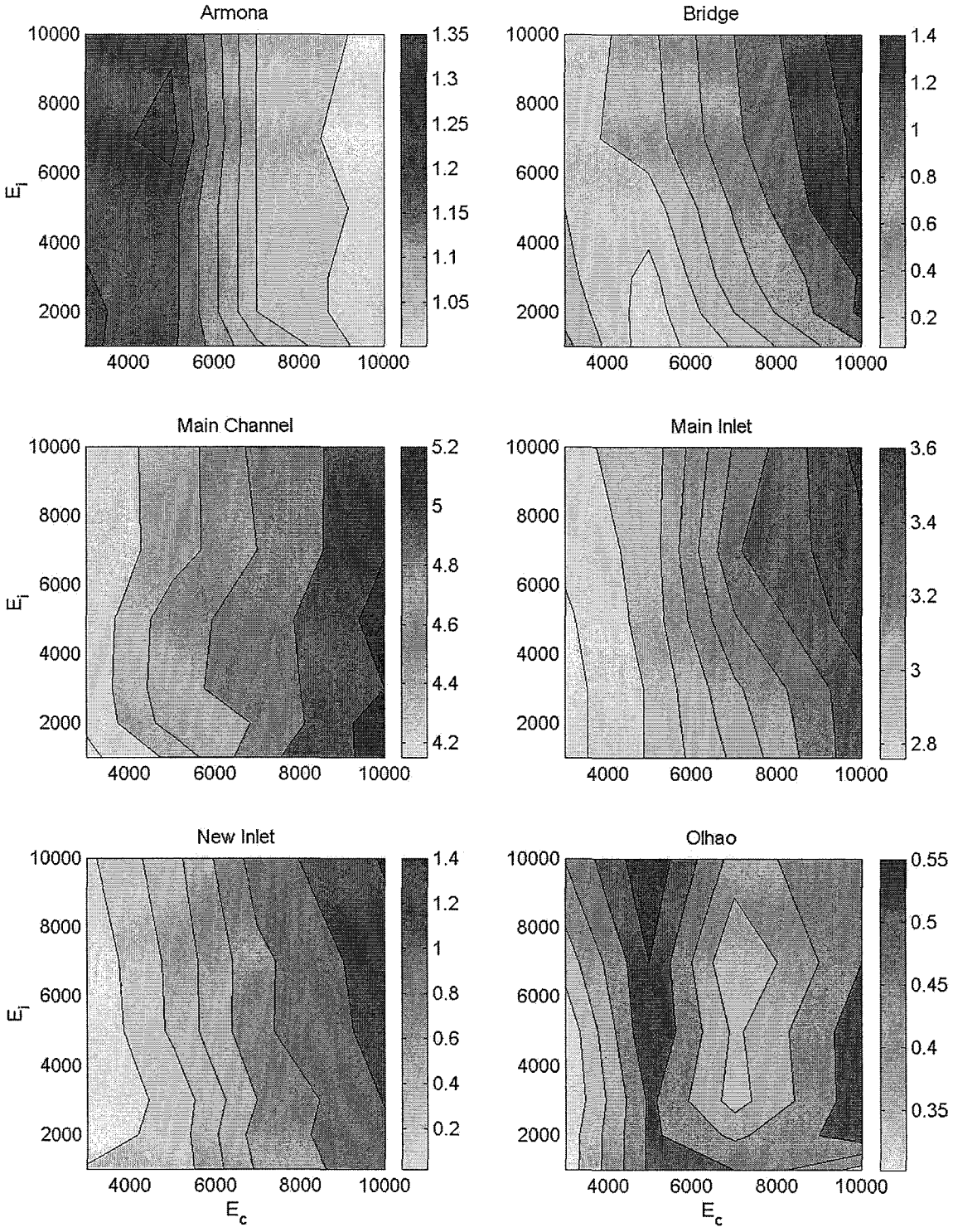

Figure 5-36. Eddy Viscosity Calibration: M_4 amplitude absolute difference (cm) between model results and measurements.

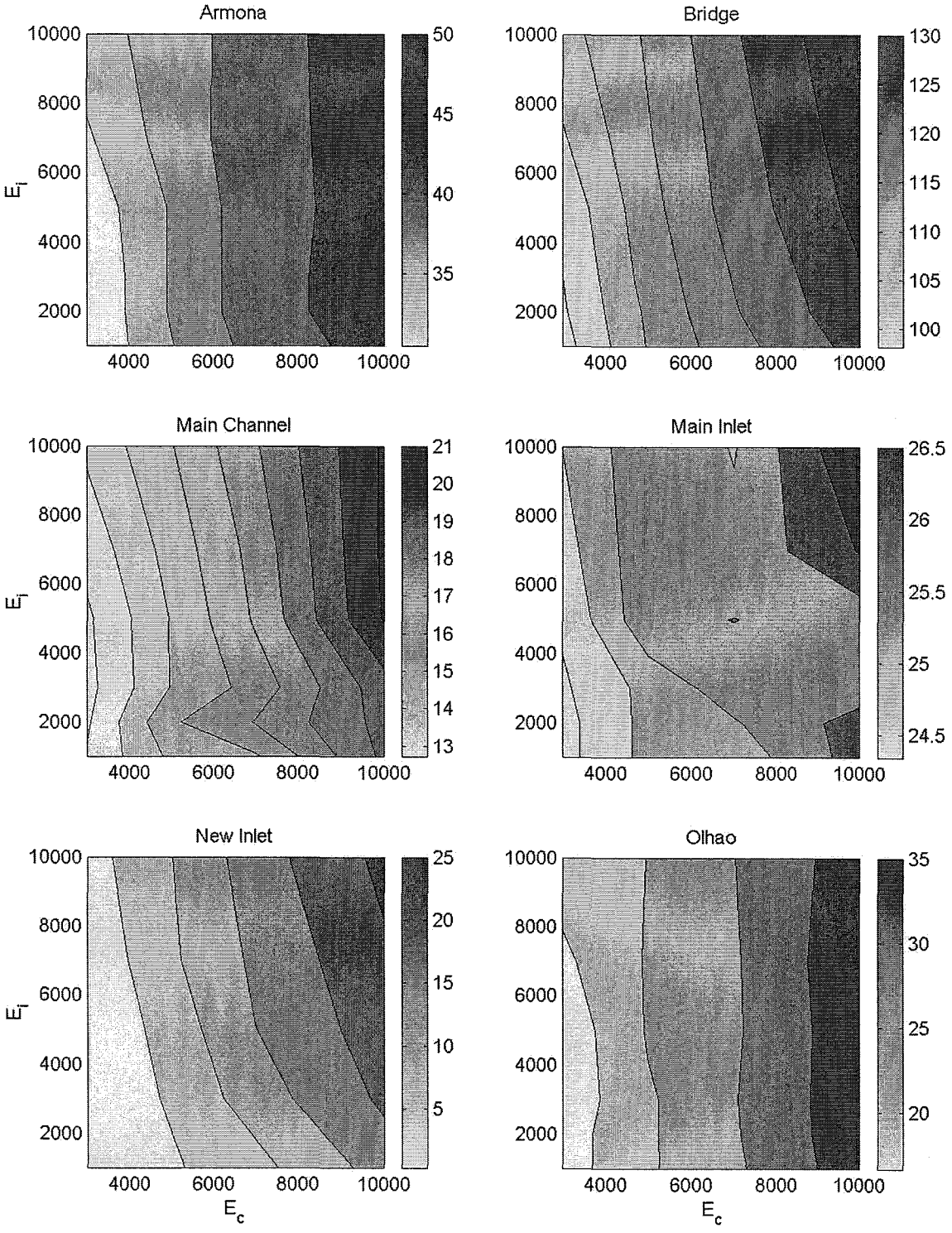

Figure 5-37. Eddy Viscosity Calibration: M_4 phase difference (degrees) between model results and measurements.

5.6.3. Model verification results

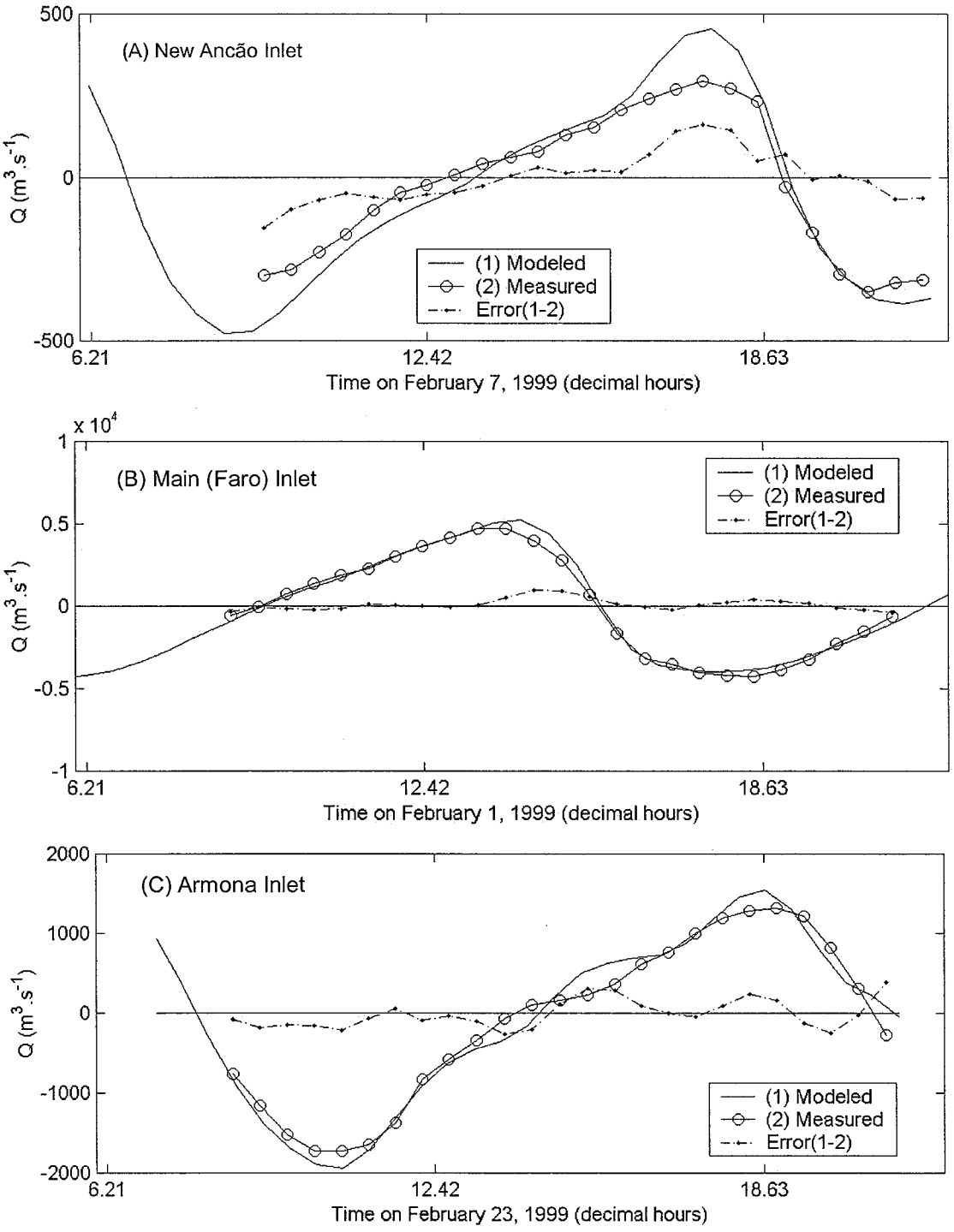

Figure 5-38. Model Verification: modeled and measured discharges through New Ancão Inlet, Main (Faro) Inlet, and Armona Inlet.

5.6.4. Spin-up verification.

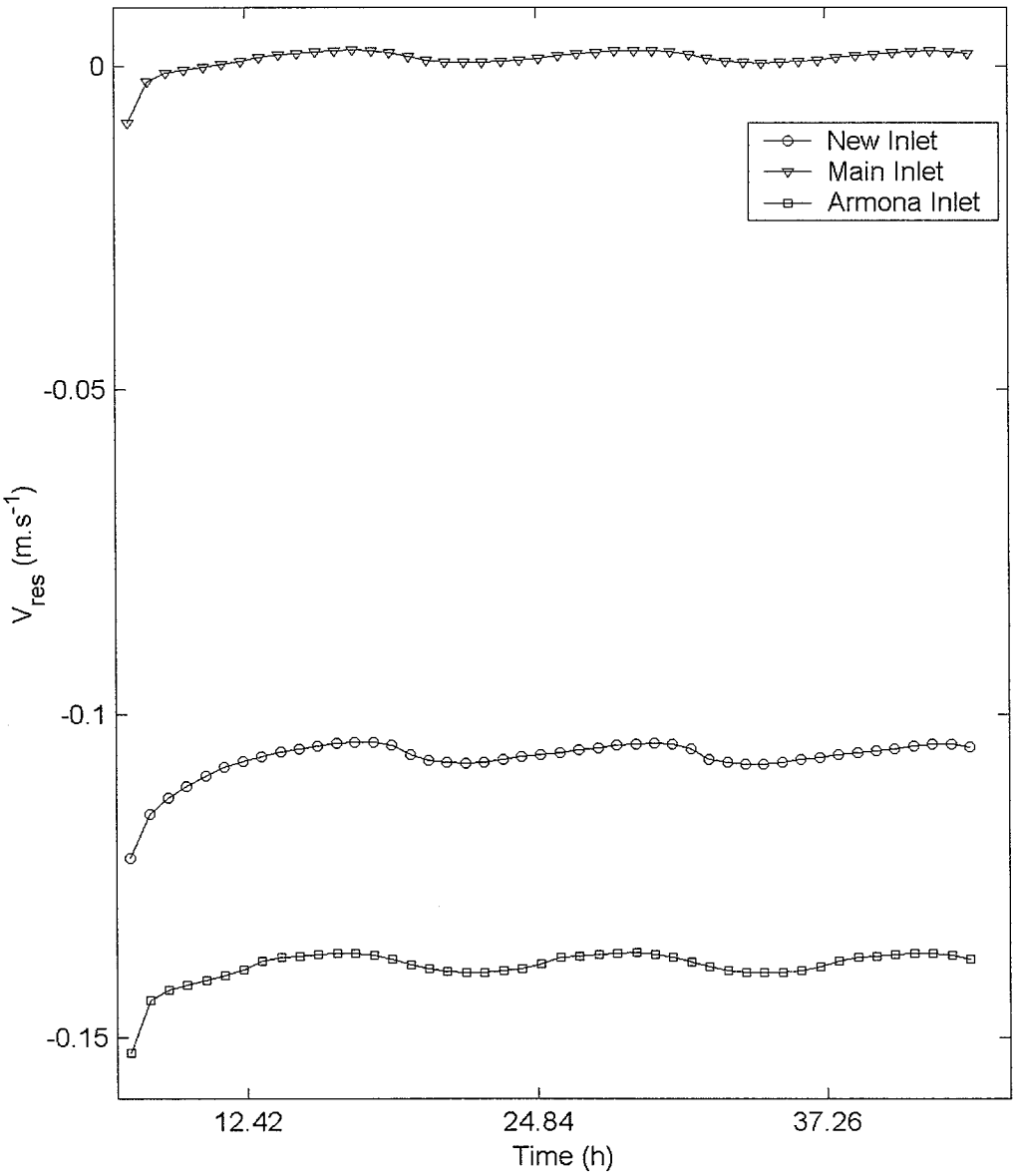

Figure 5-39. Residual current through New Ancão, Main (Faro), and Armona inlets. Model simulation forced with M_2 tide.

5.6.5. Inlet cross-sectional areas used for the simulations

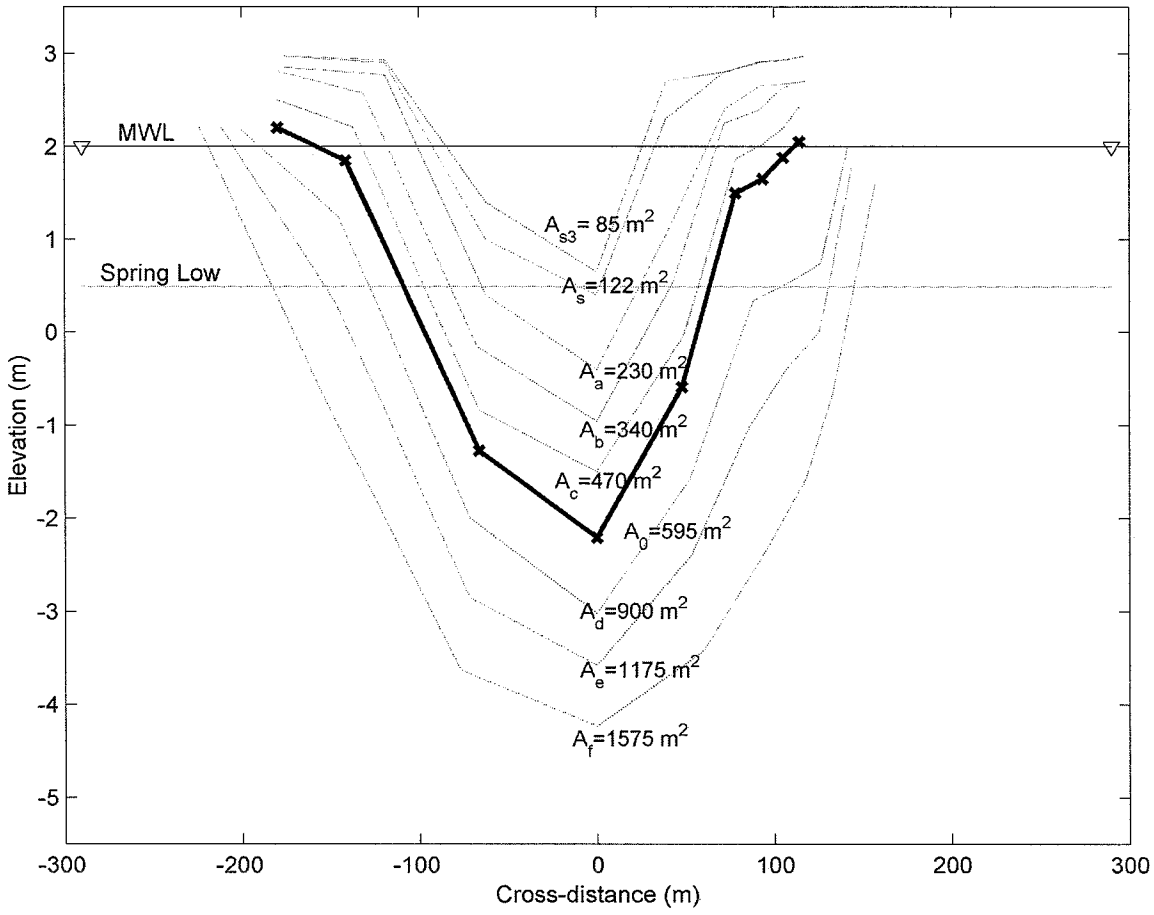

Figure 5-40. New Inlet cross-sectional areas used in the simulations.

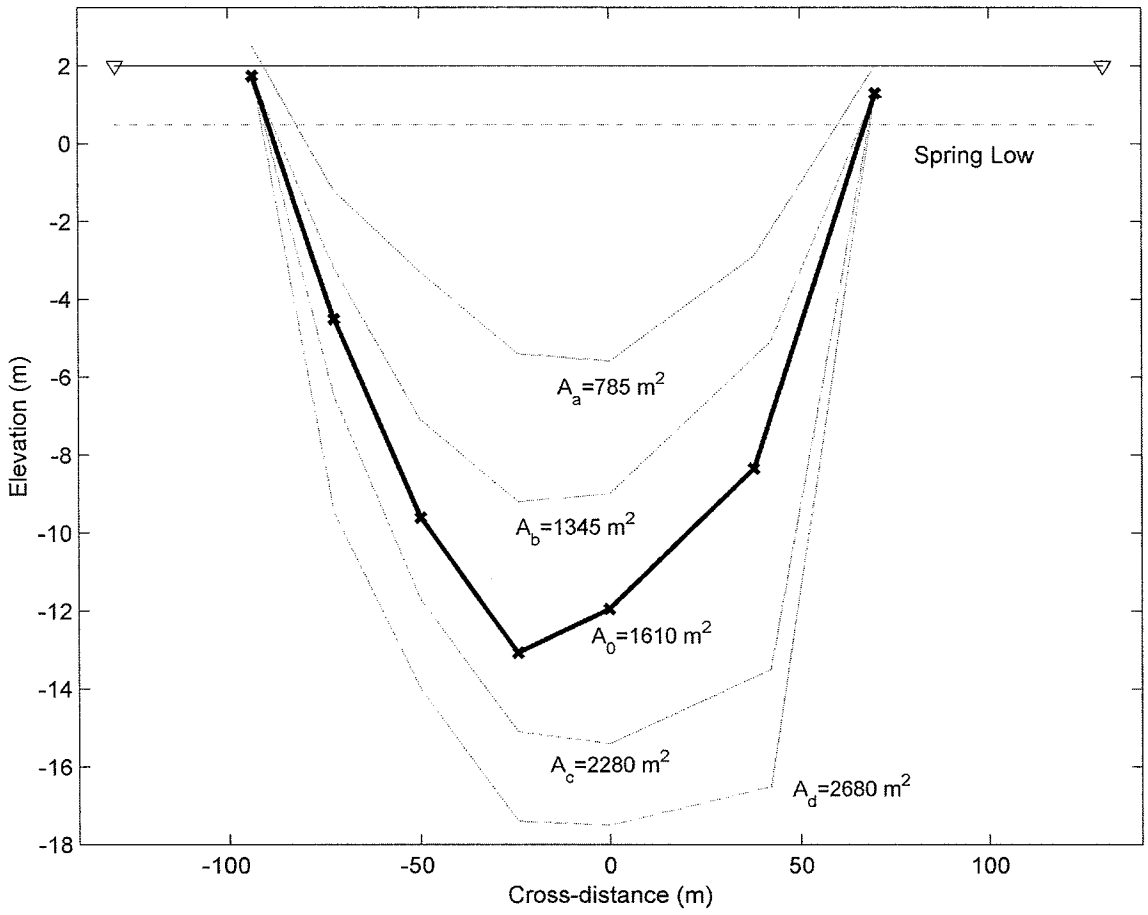

Figure 5-41. Main Inlet cross-sectional areas used in the simulations.

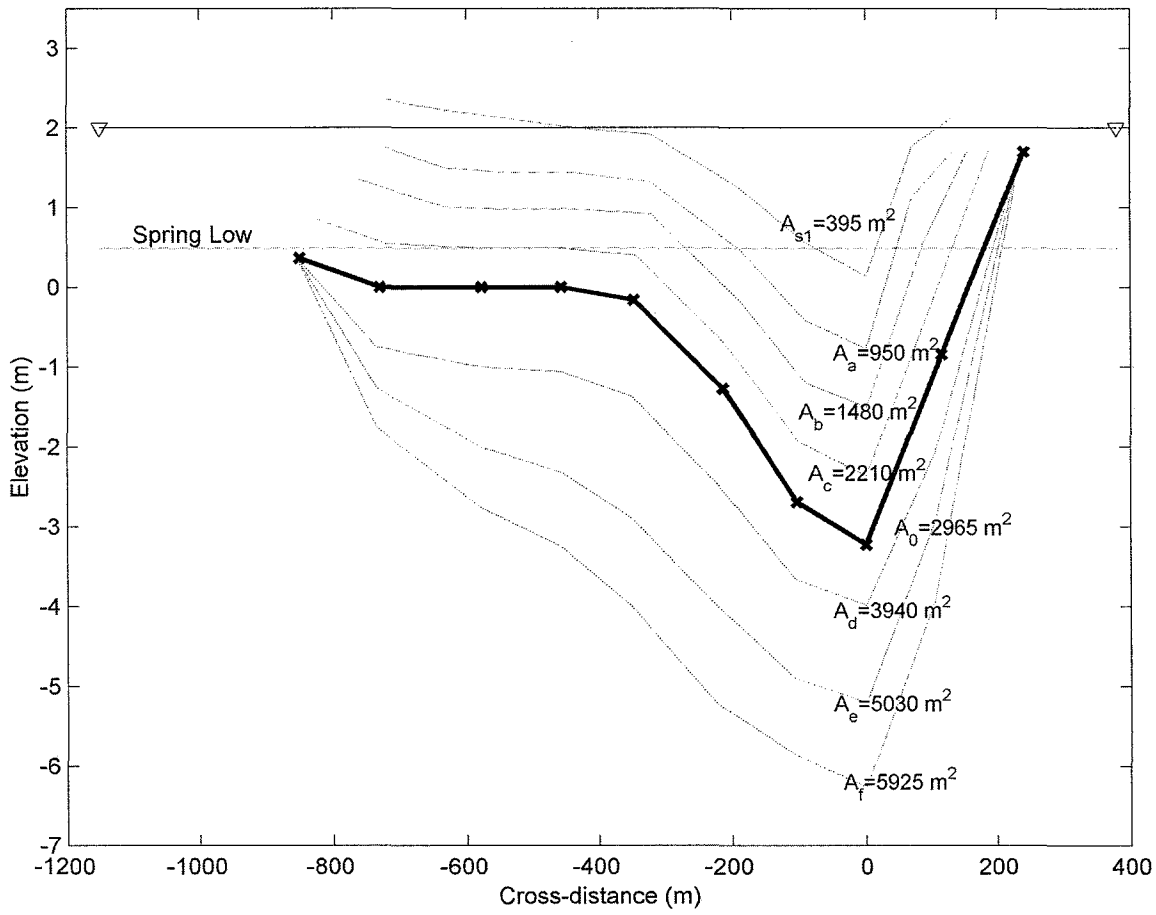

Figure 5-42. Armona Inlet cross-sectional areas used in the simulations.

5.6.6. Tidal prisms relative to total tidal prism

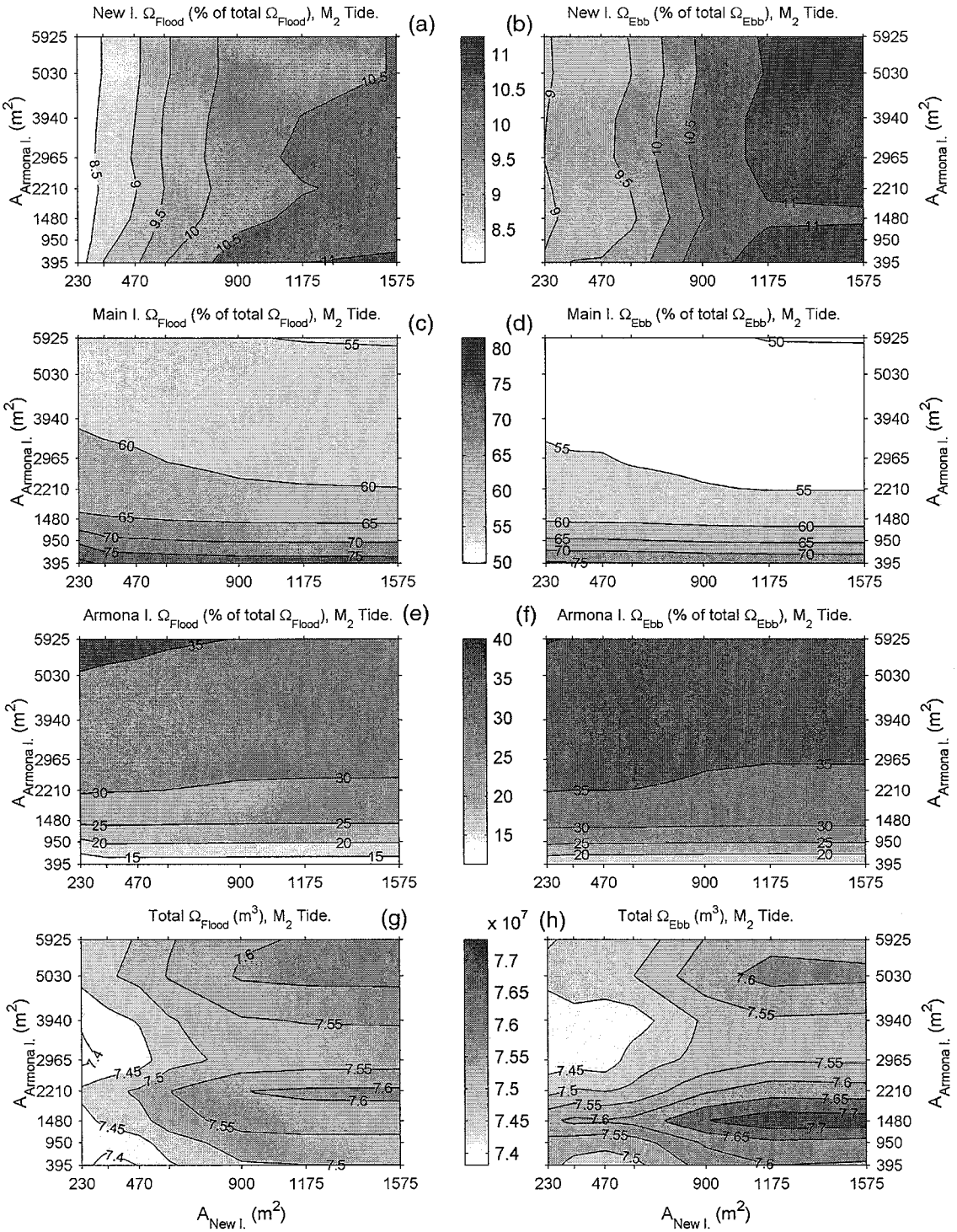

Figure 5-43. Flood and ebb tidal prisms at New, Main, and Armona inlets, relative to total tidal prism. M_2 tide forcing, varying $A_{Armona\ I.}$ and $A_{New\ I.}$.

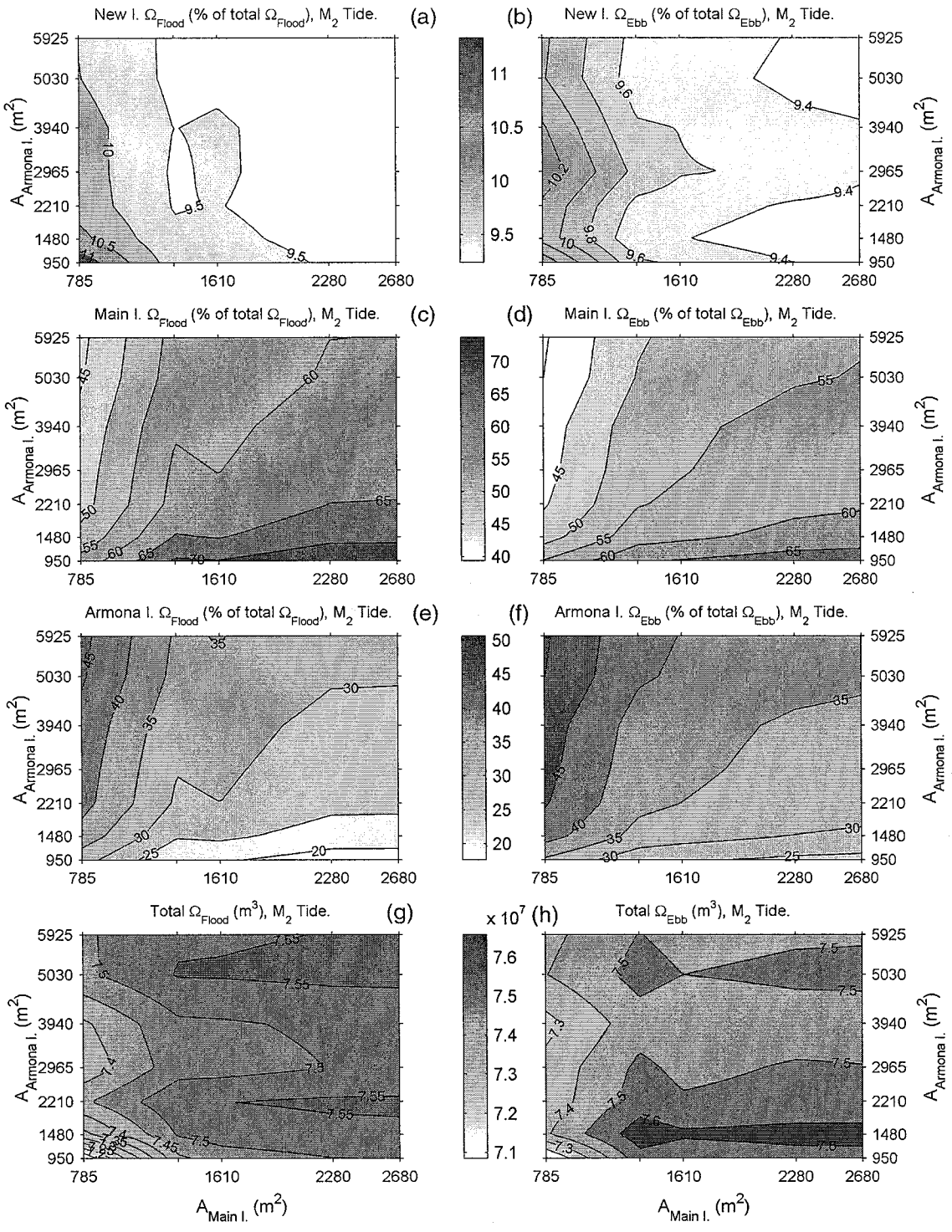

Figure 5-44. Flood and ebb tidal prisms at New, Main, and Armona inlets, relative to total tidal prism. M_2 tide forcing, varying $A_{Armona\ I.}$ and $A_{Main\ I.}$.

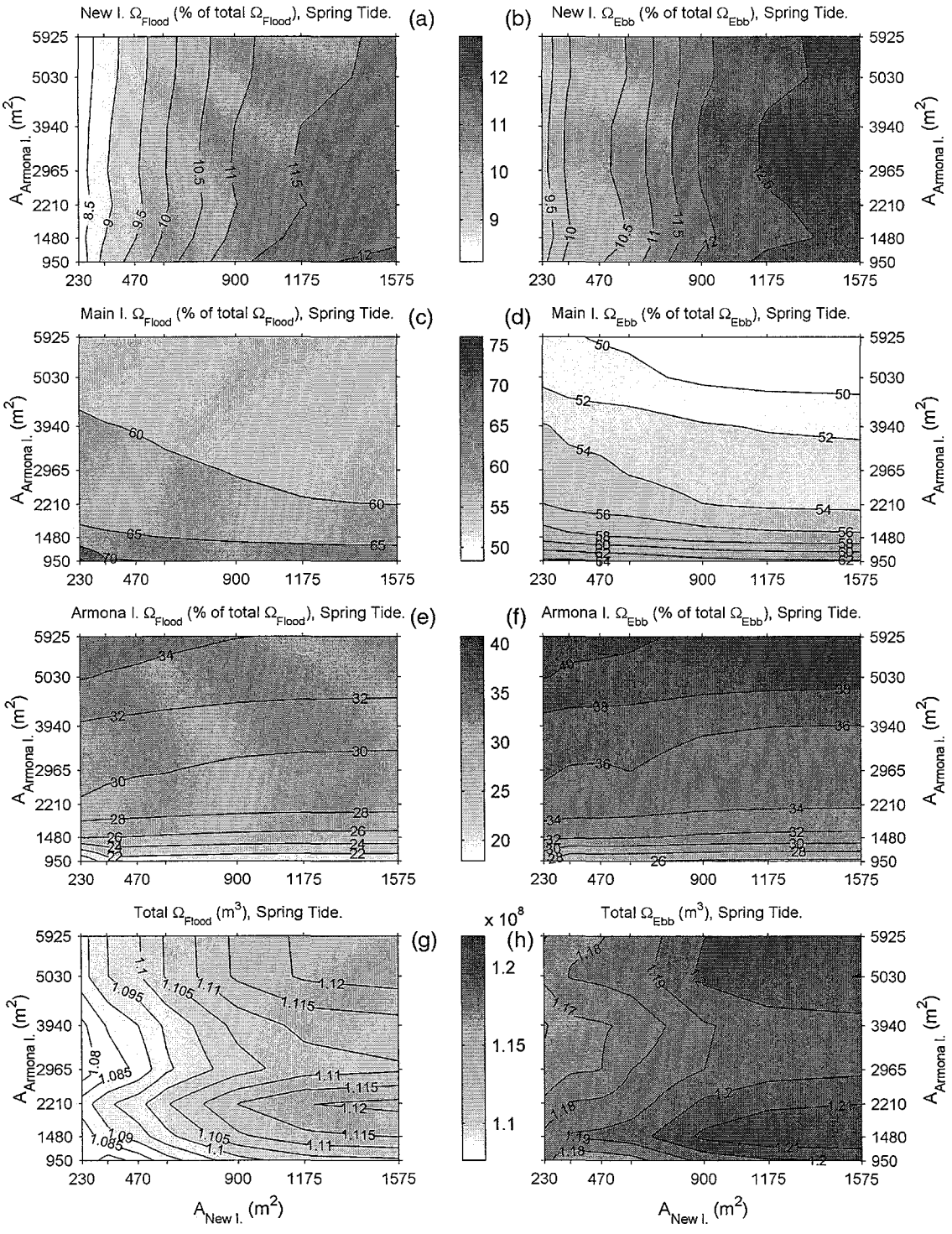

Figure 5-45. Flood and ebb tidal prisms at New, Main, and Armona inlets, relative to total tidal prism. Spring tide forcing, varying $A_{Armona\ I.}$ and $A_{New\ I.}$.

5.6.7. Simulated water surface elevation harmonic analysis results

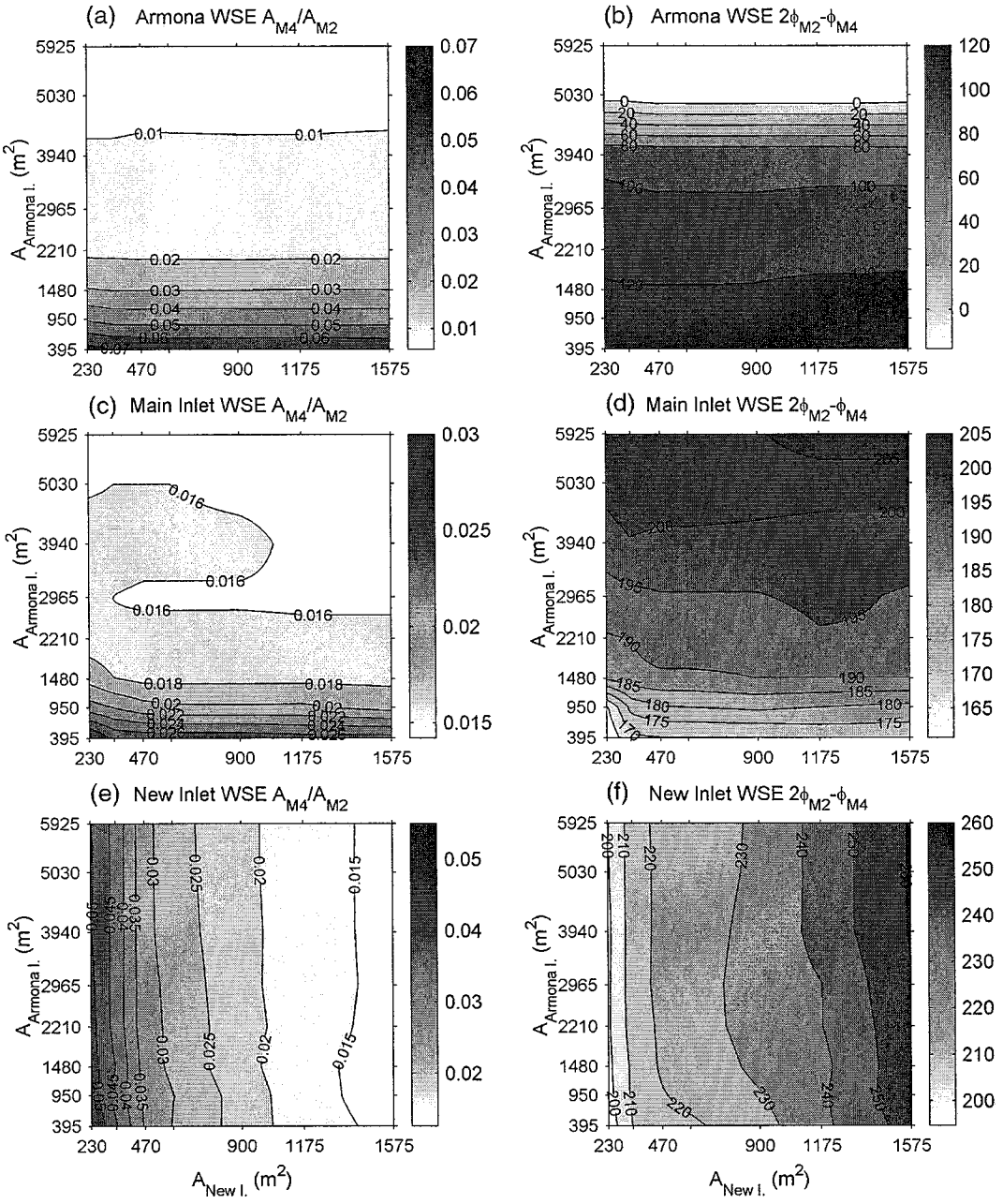

Figure 5-46. M_4 to M_2 water surface amplitude ratio at six stations. Simulations using M_2 forcing, varying A_{Armona} and A_{New} (A_{Main}=1,610 m^2).

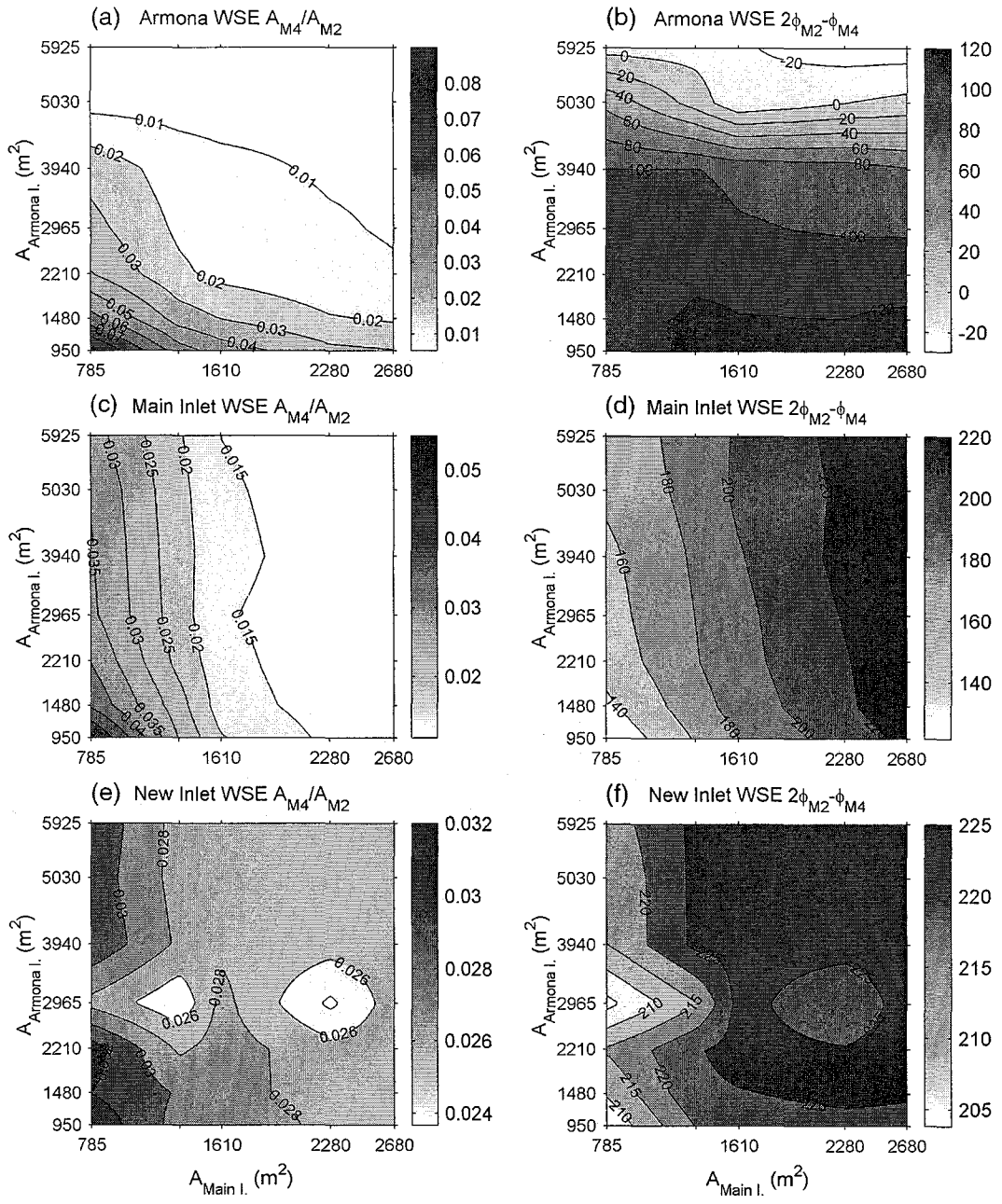

Figure 5-47. M_4 to M_2 water surface amplitude ratio and phase of M_4 relative to M_2 at Armona Inlet, Main Inlet, and New Inlet. Simulations using M_2 forcing, varying A_{Armona} and A_{Main} (A_{New}=595 m^2).

Chapter 6

Summary and Conclusions

6.1. Summary

The importance of the existence and persistence of multiple inlets in coastal systems is fundamental for issues such as water quality, navigability, and beach/barrier stability. In the case of long embayments, having extended residence times, the existence and stability of multiple inlets can be important for more efficient flushing and water exchange between the embayment and the ocean. The capacity of an inlet to stay open depends ultimately on the sediment transport pattern, and in turn sediment transport is locally dependent on many factors related to the flow (such as tidally driven flow, wave action, wave-induced currents, wind-induced circulation, river flow) and to the mechanics of near-bottom flow-sediment interaction. The persistence of multiple inlets servicing a single embayment depends in part on factors not found in single inlet systems. Morphological changes in a given inlet modify the hydrodynamic behavior in the inlet and its "area of influence" inside the lagoon (changes in total flow volumes through the inlet, generation of residual flows and currents, alteration of the nonlinear tidal distortion signal), which in turn affect the hydrodynamics in areas of the lagoon serviced by other inlets, leading ultimately in the establishment of conditions favoring morphological changes in these undisturbed inlets. The identification, quantification, and analysis of these processes are fundamental to understand the hydrodynamic response to natural or anthropogenic disturbances.

Many approaches have been used to analyze inlet stability, such as a) data based models, b) empirical relationships and empirical models, c) semi-empirical long-term models, d) process-

based models, and e) idealized models. In reality most of the studies conducted to present have been of the types (a), (b) and (c), such as the tidal prism-cross-sectional area relationship (O'Brien, 1931), the closure curve approach (Escoffier, 1940) and related criteria (Bruun and Gerritsen, 1960; O'Brien and Dean, 1972; Escoffier, 1977; Skou, 1990), and the Ω/M_{tot} and related criteria for overall stability (Bruun, 1978, 1990). These models have focused on single rather than multiple tidal inlet systems, relying solely on measured data to describe and predict the behavior of tidal inlets and/or suggesting empirical stability relationships between inlet morphology and inlet/bay hydrodynamics.

At present, the only multiple tidal inlet stability model available (van de Kreeke, 1985, 1990) combines a linear analytical model for the flow and an empirical relationship for equilibrium, suggesting that multiple inlet systems are unstable and ultimately all inlets will close or, at best, one will remain open. Van de Kreeke's model assumes an inlet/lagoon geometry such that linearizing simplifications in the mathematical model can be made, and does not take into account the nonlinear processes usually present in shallow coastal systems.

Focusing on shallow multiple tidal inlet systems and in particular on Ría Formosa, a shallow coastal lagoon in the south of Portugal known to have maintained persistently multiple inlets in a historical time scale, the morphodynamic and hydrodynamic response to disturbances in the physical characteristics of the lagoon and inlets was studied through a) the analysis of historical data of the region, b) the analysis of tidal data (velocity and water surface elevation) collected in the field, and c) through the numerical modeling of the system hydrodynamics under various inlet scenarios, with emphasis on the contribution of the hydrodynamic response to maintain the multiple inlets open.

Historical Data Analysis

The Ría Formosa lagoon is a barrier island system that has maintained multiple inlets on a historical time scale. The tide in Ría Formosa is semi-diurnal, and the wave climate is characterized by dominant smooth and moderate sea states, and by the occurrence of two different types of storms – from SW and from SE – that generate sea states with different wave characteristics, and modify temporarily the prevailing west to east longshore sediment transport.

The general shape and morphologic evolution of the barrier island chain result from (1) the geological origin and evolution of the system, and its response to relative sea-level rise, on

time scales of thousands of years, (2) the exposure to different wave and current conditions on each side of the chain (southwest- and southeast-facing sides), on time scales of years, and (3) from the effects of storms and the subsequent adaptation processes, on time scales of weeks.

The system has historically responded to disturbances with significant changes in its morphology, always maintaining multiple inlets open. In some cases, the disturbances have favored the overall stability of the system (Tsunami of 1755, opening and stabilization of Main Inlet), and others (closure of the Ludo estuary, stabilization of Tavira Inlet) have resulted in the adaptation of adjacent areas and inlets to new states of equilibrium.

The most relevant events that occurred in the past centuries are:

- In the second half of the 18th century, the system experienced the attachment of the outer barrier islands to the mainland, apparently due to a Tsunami that hit the Algarvian coast in 1755. This new configuration reduced the infilling and shoaling of the lagoon with sediment from the ocean, and in turn triggered a series of morphodynamic processes that favored the overall stability of the system: the inlets narrowed (in part due to an increase of the littoral drift reaching the inlets), which resulted in an increase of the flow intensity through the inlets, and favored their capacity to flush sediment.
- After experiencing a drastic change in position (either by continuous migration or by closure and opening of another inlet), which apparently was triggered by the closure of the Ludo Estuary and the Bispo Inlet, the Ancão Inlet eventually reached a condition of locational stability in the early 1920's, which lasted almost 60 years. No satisfactory explanation has been given to the last period of migration (1978-1999), which resulted in the inlet closure.
- The opening (1927) and stabilization (1927-1955) of the Main Inlet triggered a series of morphodynamic changes that lead to a new state of equilibrium. After the opening, the consequent trapping and diversion of the littoral drift resulted in significant shoreline retreat in the barrier immediately downdrift, but had no evident effect in inlet behavior downdrift, as suggested by the persistent accretion of the Culatra Island eastern tip. The inlet deepened considerably and its cross-sectional area increased, resulting in the gradual capture of a significant fraction of the Armona Inlet tidal prism. This in turn caused the narrowing of Armona Inlet. This process of enlargement of Main Inlet and the reduction of Armona inlet eventually stopped, suggesting that both inlets ended the phase of adaptation and reached a new stable configuration.

- After showing high rates of inlet mobility, closure and opening of new inlets during most of last century, including several failed attempts to maintain open Tavira Inlet, the eastern sector of Ría Formosa has experienced a period of relative stability in the last 10-15 years. The successful stabilization of Tavira Inlet coincides with the period in which Fuzeta Inlet recovered its original cross-sectional area after a major storm in 1962. Moreover, the increasing uniformity of the inlet separation (between Armona, Fuzeta, and Tavira inlets) may be an indication of a self-adjustment of the system, with which the Fuzeta inlet is moving to the midpoint between Armona and Tavira inlets.

  This process in Fuzeta Inlet is in part controlled by the size of the adjacent inlets. For instance, an increase in Armona Inlet cross-sectional area, and the consequent increase in its tidal prism, would disturb the established hydrodynamic boundary between the western and central sub-embayments (most likely move the boundary east, closer to Fuzeta), resulting in a reduction in the tidal prism through Fuzeta Inlet. This may in turn have implications in the inlet locational and geometrical stabilities. Similarly, disturbances in Tavira Inlet may also affect Fuzeta Inlet stability.

The historical data analysis showed that the Ría Formosa multiple inlet system is a dynamic system that has experienced several changes in its configuration. The persistence of multiple inlets can be explained in part by the capacity of the system to respond to disturbances, which in turn is enhanced by the strong hydrodynamic interaction between inlets.

Field Data Analysis

The field campaign was designed to: (1) obtain hydrodynamic measurements from a persistent multiple inlet system, in order to assist in the identification of processes that may control such persistence, and (2) to provide detailed bathymetric and tidal data (water surface elevation in various locations inside the lagoon and flow velocities through the inlets) for the calibration and validation of the hydrodynamic numerical modeling. Based on the examination of the tidal data, the following conclusions can be drawn:

- In general terms, it can be seen that there is no definite trend of the tidal distortion as a function of the distance from the station to the closest inlet for any of the constituents, as has been observed in other studies for single-inlet systems (e.g., Aubrey and Speer, 1985). However, the figure shows the strong distortion of the tide within the lagoon, which is the result of dis-

sipation due to friction and nonlinear spectral energy transfer. The friction translates in the reduction of the tidal amplitude and creation of phase lags, while the nonlinear distortion translates in (a) the decay of diurnal and semi-diurnal tides, (b) generation of M_2 overtides and compound tides, and (c) in the generation of the forced MS_f fortnightly compound tide.

- The effect of friction on the tide is demonstrated by the decay of all diurnal and semi-diurnal constituents, and by the generation of phase lags. The decay of M_2 is generally small, with the exception of the stations Cacela and Fuzeta (33% and 17%, respectively), which are close the small and shallow inlets. The M_2 phase lag is consistently positive for all the stations and ranges from 8 to 26°. In addition, the semi-diurnal components show larger decay rates than the diurnal components for some stations. While the diurnal decays (averaged over K_1 and O_1) for Cacela and Fuzeta are 20% and 11%, the semi-diurnal decays (averaged over N_2, M_2 and S_2) are 38% and 22%, respectively. The other stations show similar decay rates in the diurnal and semi-diurnal bands, of the order of 5%. The phase is again consistently positive for all the diurnal and semi-diurnal constituents analyzed (with the exception of 0_1 in Tavira), of the order of 18°, ranging from 6 to 34°.

- The effect of the nonlinear growth of the M_2 overtides and its dominant compound tides is important. For all the stations, there is a significant growth of the amplitude of MN_4, M_4, MS_4 and M_6, which are the dominant high frequency components in Ría Formosa. In the offshore station (averaging the results from truncated tidal records), these components have amplitudes of 0.5 cm, less than 1.5 cm, less than 1 cm, and 0.4 cm, respectively. Inside the lagoon, the average amplitudes of these components are 1.7 cm, 4.2 cm (without including a_{M4}=17.7 cm at Cacela), 4.6 cm, and 2.3 cm, respectively.

- The system filtering response is evident in the change of flood and ebb duration as the tide enters the lagoon. Large high frequency fluctuations in the duration of flood and ebb at the offshore site are removed as the tide enters the lagoon. In addition, at some stations, a modulation of the signal to lower frequencies exists. In particular, Cacela and Fuzeta stations (and to a lesser extent Tavira, Main Channel and Main Inlet stations) show a fluctuation with a period of two weeks, which corresponds to the MS_f and the spring/neap cycle periods. The large difference between flood and ebb durations occurs during spring tide, and this difference becomes small and even reversed in some stations, during neap tide. This strong variability in

time asymmetry throughout the spring/neap cycle can potentially cause considerable changes in the sediment transport patterns.

- The analysis of the water surface M_4/M_2 amplitude ratio and $2\varphi_2-\varphi_4$ relative phase shows that neither parameter exhibits a definite trend. However, it can be seen that (a) in general the growth of the M_4/M_2 amplitude ratio is significant (from 0.01 to 0.03 for New Inlet, and up to 0.27 for Cacela), except for Armona, Tavira and Olhão, and (b) that the phase decreases inside the lagoon, suggesting a clear flood dominance in Fuzeta and Cacela, almost symmetry in Armona and Olhão, and ebb dominance in the other stations.

Numerical Simulation Results

The simulations performed, varying the cross-sectional area of the three inlets in a multiple inlet system, served to analyze the hydrodynamic response of the system, and in particular of the inlets, to such disturbances, and identify the potential effects on inlet stability.

General inlet hydrodynamic interdependence

The strong hydrodynamic interaction between inlets was evidenced. Given that the total mass in the system has to be conserved between tidal cycles, changes in flow volume through an inlet necessarily lead to changes in the flow volumes through the other inlets. It was found that the hydrodynamic characteristics and response to changes at a given inlet (flow volumes, intensities, residuals and distortion) not only depend on disturbances at that inlet, but also on disturbances at the other inlets. For instance, situations can arise in which the hydrodynamics through a given undisturbed inlet can be strongly affected by disturbances on other inlets (e.g., distortion in Armona), resulting in the inability to counteract such disturbances, leading to potentially profound and irreversible changes in its stability condition. This "remote" response occurred even if the flow volume through the disturbed inlet is an order of magnitude smaller than that of the affected inlet. Moreover, the degree of hydrodynamic interdependence can be strong, to an extent in which the response in a given inlet "A" to disturbances in another inlet "B" is comparable to the response to disturbances in "A" itself.

Flow duration and flow dominance

Strong nonlinear distortion in water surface elevation and velocity fields can lead to different responses of the residual flow, currents, and near-bed sediment transport capacity. The results of the simulations show that, as opposed to the behavior in single-inlet systems, the duration of flood or ebb is not a determinant factor for flow dominance. Longer flood (ebb) may be associated with flood (ebb) dominance, due to the existence of strong residual circulation between inlets. In fact, larger flood (ebb) discharge in a shorter period does not necessarily lead to stronger flood (ebb) currents. Moreover, a distorted velocity field can produce residual velocities and net sediment transport in opposite directions. The direction of the net sediment transport (flood or ebb) is not only dependent on the direction of the average velocity, but also on the shape (distortion) of the velocity, and on the flood to ebb maximum velocity ratio.

Tidal distortion

The model results show that, in terms of tidal distortion response at a given inlet, the effects of disturbances in adjacent inlets are small compared to the effects of disturbances in its own cross-sectional area. Moreover, simulations keeping a given inlet unchanged suggest that its hydrodynamic response to disturbances in other inlets in terms of residual circulation and sediment transport capacity, are not necessarily coupled to changes in the tidal distortion. Therefore, the analysis of the relationship between tidal distortion and flow transport dominance has to rely on the hydrodynamic response at each inlet due to disturbance in their own cross-sectional areas.

The hydrodynamic response at a given inlet to disturbances in its own cross-sectional area indicates in all cases that:

- The water surface M_4/M_2 amplitude ratio, which is a direct measure of the degree of nonlinear tidal distortion, is proportional to the flow dominance: an increase in surface distortion is associated with an increase in either flood transport dominance (in flood dominant inlets) or ebb transport dominance (in ebb dominant inlets).
- The velocity M_4/M_2 amplitude ratio is inversely proportional to the flow dominance: an increase in velocity distortion is associated with a decrease in either flood dominance or ebb dominance.
- The simulation results suggest that the velocity and water surface relative phase are not, in most cases, an evident and reliable diagnostic indicator of the flow dominance. This apparent

discrepancy, in terms of flow dominance, between what the relative phases suggests and what the analysis of residuals (flow and current) and transport indicate, is mainly due to the existence of strong net flows between inlets. In fact, the flow dominance arguments, which are derived from the water surface and velocity examination in terms of the magnitude and phases of the primary and forced harmonic tidal constituents, are based on the assumption of negligible freshwater inflow in single-inlet systems (e.g., Aubrey, 1986), in which the net flow through the inlet is zero on average. However, the existence of multiple inlets servicing a single embayment confers an additional characteristic to the global hydrodynamics, which is the potential existence of residual flows and currents through the inlets. These added processes, together with the magnitude and direction of the maximum velocity, are in fact the processes and characteristics that ultimately determine the flow dominance and the sediment flushing capacity in a given inlet, and can outweigh the effects of tidal distortion.

Maximum velocities, closure curves and equilibrium

Model results revealed that the occurrence (flood or ebb) of the maximum velocity is an important parameter in the analysis of inlet stability. Large flood maximum velocities are in general associated with landward net sediment transport and indicate a tendency to lagoon infilling, whereas maximum velocities occurring during ebb suggest a tendency to increased efficiency in flushing sediment seaward. Moreover, a stable condition may in fact exhibit smaller maximum absolute velocities than an unstable condition, provided that these high velocities occur during ebb. This characteristic of the flow is often disregarded in closure curve stability arguments.

In addition, the model results show different responses and stability conditions for each inlet. In some cases, the equilibrium velocity can be determined from the analysis of various hydrodynamic processes and characteristics of the flow. For instance, model results and historical analysis suggest that the present-day New and Armona inlet cross-sectional areas are stable, and that the hydrodynamics would respond against disturbances in its cross-sectional area to reestablish the original configuration. This suggests that the actual maximum velocity can be considered to be the equilibrium velocity (1.35 $m.s^{-1}$ for New Inlet and 1.05 $m.s^{-1}$ for Armona Inlet), eliminating the need to rely on the value of 1 $m.s^{-1}$, which has been shown not to be universal (see section 2.1.2). The results also show that these inlets are consistently ebb dominant, which is often regarded as a contributing factor for stability, and that instability may only be caused by events and

processes not analyzed in this study, such as abrupt changes in sediment supply and wave climate.

In other cases, the model results indicate that the equilibrium velocity is associated with a net landward transport. Although flood transport dominance is often associated with potential inlet instability, these results show that the apparent "lagoon infilling" process and the inlet stability operate at different time scales, in particular when the landward transport does not affect the inlet immediate vicinity.

Finally, the simulations varying the inlet cross-sectional areas show that the equilibrium state in a given inlet, as well as its response capacity to disturbances on the inlet itself, have to be taken in perspective when multiple inlets are present, since changes in other inlets may modify the overall stability conditions and requirements. For instance, the maximum velocity through an inlet is likely to decrease as the cross-sectional area of other inlets increase, in which case it could change from being larger to being smaller than the required velocity for equilibrium.

6.2. Conclusions

The Ría Formosa system is a shallow multiple inlet coastal system, which exhibits strong non-linear hydrodynamics. This study served to identify the processes and morphodynamic disturbances that lead to the persistence of multiple inlets in the Ría Formosa system. In addition, it served to analyze the tidal hydrodynamics in a persistent multiple inlet system, to study the response of the system to inlet disturbance, and to identify the hydrodynamic processes that contribute to such persistence. It was found through numerical hydrodynamic modeling that multiple tidal inlet systems can exhibit stable inlet configurations, and that the strong hydrodynamic interaction between inlets, as well as the non-linear distortion of the tide, play a major role in multiple inlet persistence. Some of the results and findings are specific to Ría Formosa, and others can be generalized and used to identify processes contributing to stability in shallow systems with multiple inlets servicing a single embayment.

Based on the results from the historical data analysis, the field measurements, and the numerical hydrodynamic simulations, the following conclusions can be drawn:

a) Observed morphological responses to inlet and lagoon disturbances and the evolution of the physical characteristics of the system can help explain the inlet persistence.

The historical data analysis (Chapter 3) showed that Ría Formosa has been able to adapt and evolve after strong natural and anthropogenic disturbances, exhibiting continuously multiple inlets in a historical time scale. For instance, an abrupt disturbance to the system (Tsunami of 1755), had favorable effects for the overall multiple inlet stability, by attaching the outer barrier islands to the mainland through overwash and infilling of the outermost inlets, which eventually resulted in the narrowing of the other inlets and the generation of a more stable overall configuration. In addition, the artificial opening and stabilization of Faro (Main) Inlet resulted in the modification of the hydrodynamics in the system, and the major adjacent inlet reduced in size and reached a new equilibrium configuration. The persistence of multiple inlets can be explained in part by the capacity of the system to respond to disturbances, and reach new stable configurations.

b) The hydrodynamic interaction between inlets servicing a single embayment, and the capacity of the system to adjust to inlet disturbances by transferring large portions of the tidal prism from one inlet to another, and by modifying the residual flow and sediment transport patterns, contribute to maintain multiple inlets open.

Strong inlet hydrodynamic interdependence was found to exist between inlets servicing a single embayment. Disturbances in a given inlet resulted in the modification of the hydrodynamics through that inlet, which affected the hydrodynamics, and ultimately the stability, at other inlets (sections 5.4.1 and 5.4.2, items 8, 11, 14, 30). In general, the model results showed that the response in undisturbed inlets to disturbances in another inlet was such that they would adjust to the new hydrodynamics, without loosing stability (section 5.4.1, items 1, 11, 12, and 21).

In addition, it was found that, although the variations in the various hydrodynamic parameters analyzed (flow duration, residual discharge and velocities, sediment transport capacity) followed general well-defined trends as a response to inlet disturbances, specific combinations of cross-sectional areas lead to abrupt deviations from these trends, which in turn conferred substantially different inlet hydrodynamic behavior (section 5.4.1, items 6, 7, 12, 14, 22). The identification of these particular responses through modeling can serve a predictive tool to i) assist in the determination of the optimal disturbances (in the case of desired or

needed anthropogenic modifications of the inlets and the system in general), and ii) to identify the worst-case scenarios, and recommend actions to prevent them to happen.

c) The hydrodynamic interaction results in longer flood (or ebb) not necessarily associated with stronger flood (or ebb) flows, nor with larger capacity to transport sediment landward (or seaward), as opposed to the behavior in single-inlet systems (section 5.4.1, items 2, 6, 7, 10, and 18). It is suggested here that, at least for multiple inlets exhibiting strong hydrodynamic interaction and distortion, a distinction should be made between flow dominance (larger flow), and transport dominance. The former is important globally, as it determines the degree of inlet interaction and the overall system response capacity to inlet disturbances, and the latter is more useful in a local sense, to estimate the seaward-flushing or landward-infilling ability of a particular inlet in a given scenario.

d) Nonlinear hydrodynamics are important to multiple inlet persistence in shallow systems. In other words, changes in nonlinear hydrodynamic processes due to inlet morphological disturbances play an important role in maintaining inlets open.

   The strong distortion existing in shallow multiple tidal inlets, together with the inlet hydrodynamic interaction, can produce residual velocities and net sediment transport in opposite directions. For instance, an inlet exhibiting a landward residual velocity can present a seaward sediment transport capacity (section 5.4.1, item 14), suggesting a tendency to flush sediment seaward, which in turn is usually associated with stability. The direction of the net sediment transport (flood or ebb) is not only dependent on the direction of the residual velocity, but also on the distortion of the velocity field, and on the flood to ebb maximum velocity ratio.

   Therefore, the embayment morphology, which controls the degree of nonlinearity, appears to be important for stability in shallow multiple inlet systems such as Ría Formosa, whose hydrodynamics cannot be modeled appropriately with linear models.

e) In the specific case of Ría Formosa, New and Armona inlets were found to be in equilibrium (section 5.4.1, items 1 and section 5.4.5 for New Inlet; section 5.4.1, item 21 for Armona Inlet), and changes in their cross-sectional areas would modify the hydrodynamics such that the inlets would tend to recover their original sizes. In general, it can be said that the western sub-embayment appears to be stable at present, although it may not be in equilibrium. This is because Main Inlet is stable, but according to its closure curve (Figure 5-25-

f), it is not in equilibrium, and changes in its cross-sectional area may trigger further changes.

f) The historical data analysis (section 3.3.3) suggest that Main Inlet has a tendency to grow, and that the growth has stopped either because the inlet reached equilibrium, or because the jetties (and possibly a hard stratum in the bottom) prevent further growth. This, together with the closure curve results, suggest that Main Inlet would grow if unjettied.

g) The analysis of the overall stability using the closure curve approach, suggests that the system at present is not stable, and that stability would be reached only if Main Inlet cross-sectional area increases significantly (from 1,600 to 2,500 m^2). This growth of Main Inlet would be accompanied by a small decrease in size of New and Armona inlets, which in turn may affect stability. However, the residual flow and sediment transport capacity analysis, together with the closure curves, suggest that small changes in cross-sectional area at New and Armona inlets would not hamper their stability.

Therefore, if the jetties at Main Inlet were removed, the western sub-embayment of Ría Formosa would reach natural stability and equilibrium with three inlets.

6.3. Future work

The analysis of the hydrodynamics through the inlets, and the inlet response to disturbances was done with the modeling of the western sub-embayment of Ría Formosa. The hydrodynamic divide separating the western sub-embayment from the rest of the system was found with a preliminary model simulation, using the present-day inlet configuration. However, it is likely that this hydrodynamic divide will move, or even disappear, if the inlets cross-sectional areas (in particular the closest to the divide) are changed, or if the channels between the inlets were dredged (as they were during 2000). Therefore, an analysis of the sensitivity of the sub-embayment separations to inlet or lagoon disturbances, and how this affects the overall stability, should be made.

Besides, as mentioned in the introduction, this study was limited to the analysis of multiple tidal inlet persistence from a tidal hydrodynamic point of view, and to the analysis of the hydrodynamic response to inlet morphological disturbances. However, the wave action and the wave/current interaction play an important role in the sediment transport. Moreover, although the

tidally driven motion may well represent the fair-weather hydrodynamic conditions, storm events are able to modify dramatically the inlet configuration in short periods, through wave action, storm surge, and wind driven motions inside the lagoon. Therefore, a model able to incorporate wave effects, coupled with a sediment transport model to study the evolution of the inlets, would give a more complete picture of the hydrodynamics and the morphological evolution of the inlets, in terms of their response to inlet disturbances and storm events. These types of morphodynamic models are at present in early stages of development, and are not yet reliable in extended time scales.

6.4. References

Aubrey, D. G., 1986. Hydrodynamic Controls on Sediment Transport in Well-Mixed Bays and Estuaries, in: J. van de Kreeke, Ed.: *Physics of Shallow Estuaries and Bays*. Coastal and Estuarine Studies, **16**. Springer-Verlag, New York, NY, pp 245-258.

Aubrey, D. G. and Speer, P. E., 1985. A Study of Non-Linear Tidal Propagation in Shallow Inlet/Estuarine Systems. Part I: Observations. *Estuarine, Coastal and Shelf Science,* **21**: pp 185-205.

Bruun, P., 1978. Stability of Tidal Inlets, Theory and Engineering. Development in Geotechnical Engineering, **23**. Elsevier.

Bruun, P., 1990. Port Engineering, **2**. Gulf Publishing Company.

Bruun, P. and Gerritsen, F., 1960. Stability of Coastal Inlets. North Holland Publishing Co.

Escoffier, F. F., 1940. The Stability of Tidal Inlets. *Shore and Beach,* **8**: pp 114-115.

Escoffier, F. F., 1977. *Hydraulics and Stability of Tidal Inlets*. General Investigation of Tidal Inlets (GITI) Report, 13. USACE.

O'Brien, M. P., 1931. Estuarine Tidal Prism Related to Entrance Areas. *Civil Engineering,* **1**: pp 738-739.

O'Brien, M. P. and Dean, R. G., 1972. Hydraulics and Sedimentary Stability of Coastal Inlets. Proc. of the 13th Conference on Coastal Engineering, (Location?), ASCE., pp 761-780.

Skou, A., 1990. *On the Geometry of Cross-Section Areas in Tidal Inlets*. Series Paper, 51. Institute of Hydrodynamics and Hydraulic Engineering, Technical University of Denmark. Lyngby, Denmark.

van de Kreeke, J., 1985. Stability of Tidal Inlets - Pass Cavallo, Texas. *Estuarine, Coastal and Shelf Science,* **21**: pp 33-43.

van de Kreeke, J., 1990. Can Multiple Tidal Inlets Be Stable? *Estuarine, Coastal and Shelf Science,* **30**: pp 261-273.